

FLORIDA INTERNATIONAL UNIVERSITY
Miami, Florida

NEUTRON MAGNETIC FORM FACTOR G_M^N MEASUREMENT AT HIGH Q^2
WITH CLAS12

A dissertation submitted in partial fulfillment of the
requirements for the degree of
DOCTOR OF PHILOSOPHY
in
PHYSICS
by
Lamy Baashen

2023

To: Dean Michael Heithaus
College of Arts, Sciences and Education

This dissertation, written by Lamy Baashen, and entitled Neutron Magnetic Form Factor G_M^n Measurement at High Q^2 with CLAS12, having been approved in respect to style and intellectual content, is referred to you for judgment.

We have read this dissertation and recommend that it be approved.

David Chatfield

Gerard Gilfoyle

Lei Guo

Misak M. Sargsian

Brian A. Raue, Major Professor

Date of Defense: November 1, 2023

The dissertation of Lamy Baashen is approved.

Dean Michael Heithaus
College of Arts, Sciences and Education

Andrés G. Gil
Vice President for Research and Economic Development
and Dean of the University Graduate School

Florida International University, 2023

© Copyright 2023 by Lamya Baashen

All rights reserved.

DEDICATION

To my parents Latifa Baashen and Abubaker Baashen, whose support has been invaluable for me to accomplish my academic and professional goals. Also, to the physics department at King Saud University.

ACKNOWLEDGMENTS

As a PhD student, it is really hard to find the appropriate words to thank all of those who helped me along the way. I was privileged to be surrounded by supporting family members, friends, and mentors. It is truly overwhelming to try to thank all of them in a few pages.

First and foremost, I would like to begin by expressing my sincere gratitude to my thesis advisor, Prof. Brian A. Raue. His support and trust made this journey possible, and I'm grateful for the freedom he gave me to explore my research independently. One of the most important lessons I've gained from him is his insistence on understanding the results - "Do they make sense? And why?" - I am profoundly thankful for the privilege of having him as my advisor.

Next, I would like to extend my sincere appreciation to Prof. G. P. Gilfoyle, the expert in this analysis. None of this work would've been accomplished without his dedicated time, and guidance. He is a true scientist who is extremely knowledgeable and patient. I learned a lot from him while working together. The discussions with him were always enjoyable and helped clear my confusion about the analysis. Thank you so much for giving me your time and guidance even when you were super busy. Working alongside Prof. Gilfoyle has been a privilege, and I consider myself fortunate to have had this opportunity.

I would also like to express my appreciation to the rest of my thesis committee—Prof. Lei Guo, Prof. Misak M. Sargsian, and Prof. David Chatfield—for their insightful feedback during my annual review.

During my time at Thomas Jefferson Lab, I collaborated with brilliant scientists. I owe a great of debt gratitude to the contributions of staff scientists, including Cole who has been a helpful source of knowledge on NDE work, Raffaella De Vita who has been a helpful source of swimming particles, Latifa Elouadrhiri, Stepan Stepanyan,

and Silvia Niccolai, who provided me with their expertise and assistance during the analysis. Also, a special thanks to Andrey Kim and Stefan Diehl for their invaluable assistance.

I would like also to thank my Florida International University friends and colleagues Achyut, Jose, Mahmoud, Rupesh, Shankar, Taya, and Trevor. I am so grateful that I have such wonderful colleagues and friends as them.

I extend my gratitude to the Department of Physics at King Saud University for providing invaluable opportunities and financial support throughout my academic journey in the USA. Additionally, I would like to thank the Department of Energy (DOE) and Florida International University (FIU) for their generous financial support during my last semester.

Finally, I want to express profound gratitude to my family for their unwavering love, support, encouragement, and guidance. My parents, Abubaker and Latifa, have been my biggest fans and pushed me to pursue what makes me happy. Their sacrifices and investments in my life are immeasurable. I am where I am today because of them. Mom and Dad, you are the best parents one could ever ask for, and I love you dearly. I know thanking you would never do you justice, but I hope to continually make you proud and happy. A special acknowledgment goes to my uncle Hussin, and my brother Fahad for traveling to the USA to attend my defense alongside my parents and sharing these significant moments with me. To the rest of my family who couldn't attend, your spirit was with me, and I am grateful for your support. I also extend sincere thanks to my brother and sisters: Kholud, Huda, Afnan, Abdul-Aziz, Abdullah, Raghad, Lamar, Layan, and my cousin, Saeed, for their unwavering help and support. Your contributions have been invaluable on this journey.

ABSTRACT OF THE DISSERTATION
NEUTRON MAGNETIC FORM FACTOR G_M^N MEASUREMENT AT HIGH Q^2
WITH CLAS12

by

Lamya Baashen

Florida International University, 2023

Miami, Florida

Professor Brian A. Raue, Major Professor

The neutron magnetic form factor, G_M^n , is a fundamental quantity that describes how magnetic properties are distributed within a neutron. This measurement provides insights into the internal structure of the neutron. Furthermore, by measuring G_M^n alongside three other form factors (G_E^n , G_E^p , G_M^p), we can test the predictions of Quantum Chromodynamics (QCD), which is the fundamental theory governing the strong force that binds quarks and gluons. Additionally, these measurements play a significant role in constraining Generalized Parton Distributions (GPDs) and contribute to determining the angular momentum of the quarks within nucleons

The G_M^n was measured using the ratio of quasi-elastic $e - n$ to $e - p$ scattering from a deuteron target. The measurement covered a range of four-momentum transfer squared, Q^2 , from 5 to 12 GeV², using three different beam energies (10.2, 10.4, and 10.6 GeV). The data is compared with previous measurements and several theoretical models. The preliminary results reveal that G_M^n exceeds the predictions of the standard dipole parametrization by 12-20%, based on RG-B pass1 data. It is expected that this deviation from the standard dipole parametrization will diminish as we transition to using RG-B pass2 data, aligning G_M^n more closely with the dipole form factor. The ongoing RG-B pass2 analysis in CLAS12 holds considerable promise for significant improvement. This enhancement is achievable through

collaborative efforts aimed at refining tracking efficiency, momentum correction, calibration, and alignment.

TABLE OF CONTENTS

CHAPTER	PAGE
INTRODUCTION	1
1. Nuclear Form Factors	4
1.1 Elastic Electromagnetic Form Factors	4
1.2 Interpretation of Nucleon Form Factors	8
1.3 Motivation for Measurements of G_M^n	12
1.4 Experimental Measurements of G_M^n	13
1.4.1 Polarized Measurements	14
1.4.2 Unpolarized Measurements	16
1.5 Theoretical predictions of G_M^n	20
1.5.1 Vector Meson Dominance Models	20
1.5.2 Constituent Quark Models	22
1.5.3 Dyson-Schwinger Equations	24
1.5.4 Generalized Parton Distributions (GPD)	25
1.5.5 Chiral Perturbation Theory	26
1.5.6 AdS/QCD Correspondence	28
2. Experimental Setup	30
2.1 The Continuous Electron Beam Accelerator Facility (CEBAF)	31
2.2 Hall B Beamline	31
2.3 CEBAF Large Acceptance Spectrometer (CLAS12)	32
2.3.1 Target	34
2.3.2 Torus Magnets	35
2.3.3 Drift Chambers	36
2.3.4 Cherenkov Counters	38
2.3.5 Time of Flight System	40
2.3.6 Forward Electromagnetic Calorimeter	41
2.4 Data Processing of CLAS12	43
2.4.1 Data Acquisition of CLAS12	43
2.4.2 Reconstruction Software of CLAS12	45
3. Neutron Detection Efficiency	50
3.1 Method of Measuring NDE	50
3.2 Dataset Used	51
3.3 Event Selection	52
3.4 Electron Particle ID	52
3.4.1 Electron Vertex Cut	53
3.4.2 HTCC Photoelectrons Cut	54
3.4.3 PCAL Fiducial Cut	54

3.4.4	DC Fiducial Cuts	55
3.4.5	Calorimeter Cuts	56
3.4.6	Energy Deposited Cuts	59
3.5	π^+ Particle ID	61
3.5.1	Vertex Difference Cut	61
3.5.2	χ^2 PID Cut	62
3.5.3	Fiducial Cuts for DC	63
3.6	Neutron Selection	64
3.6.1	Identification of the Reaction $p(e, e'\pi^+)n$	65
3.6.2	Identification of the Reaction $p(e, e'\pi^+n)$	67
3.7	Efficiency Measurement in the Calorimeter	71
3.8	Background Subtraction	71
3.9	NDE Results	77
3.10	NDE Parameterization	80
4.	Quasi-elastic Ratio Measurement	82
4.1	RGB Run Period	82
4.2	Events Selection	83
4.3	Quasi-elastic Selection	84
4.3.1	Incident Electron Beam Energy Cut	86
4.3.2	$\Delta\phi$ Cut	87
4.3.3	θ_{pq} Cut	88
4.4	Acceptance Matching	92
4.5	Uncorrected Ratio Results	94
5.	Corrections to Quasi-elastic Ratio	97
5.1	NDE Corrections to the Ratio	97
5.2	Correction due to Fermi motion of the Target	98
5.2.1	Simulating Quasielastic Scattering on Deuterium	99
5.2.2	Comparison to Data	100
5.2.3	Fermi-Loss Correction to the Ratio	101
5.3	Radiative Correction	104
6.	G_M^n Results	112
6.1	G_M^n Extraction from Ratio	112
6.2	Systematic Uncertainties	116
6.2.1	Systematic Uncertainty due to Neutron Detection Efficiency	117
6.2.2	Systematic Uncertainty due to Electron Identification Cuts	118
6.2.3	Systematic Uncertainty due to Quasi-elastic Selection Cuts	120
6.2.4	Systematic Uncertainty due to Radiative Effects	123
6.3	Total Systematic Uncertainty	125

7. Preliminary G_M^n result and discussion	128
7.1 Comparison to Previous Measurements and Models	128
7.2 Conclusion	130
Bibliography	133
A. Fit Missing Mass Distribution using Gaussian Function	144
B. Fit Missing Mass Distribution using Crystal Ball Function	154
C. Measured G_M^n Values and Errors	165
VITA	167

LIST OF TABLES

TABLE		PAGE
1	Listing of the electromagnetic form factors of the nucleons experiments.	3
3.1	RG-A taken on Fall 2018 and Spring 2019.	52
3.2	EB electron (PID = 11) assignment requirements.	53
3.3	Parameters for sampling fraction cut on electron identification.	58
3.4	Cuts used for electron identification.	62
3.5	Cuts used for pion identification.	65
3.6	The average χ^2 of both expected and detected neutrons for Gaussian and CB functions.	77
3.7	The fit parameters of the neutron detection efficiency.	81
4.1	RG-B run period conditions.	82
4.2	Cuts used for electron and nucleon identification.	83
5.1	The average radiative correction values for 10.2, 10.4 and 10.6 GeV data set. These values are used to correct the ratio measurement in each Q^2 bin.	110
6.1	Relative systematic uncertainties due to various sources and relative statistic uncertainties at different Q^2 bins.	127
C.1	Measured values of $G_M^n/\mu_n G_D$ and statistical errors for each dataset. The Q^2 values given are the central value of each Q^2 bin.	165
C.2	Measured values of $G_M^n/\mu_n G_D$, statistical and systematic uncertainties from the waighted average. The Q^2 values given are the central value of each Q^2 bin.	166

LIST OF FIGURES

FIGURE	PAGE	
1.1	Feynman diagram for electron-nucleon scattering. The shaded circle on the right side of the diagram represents the structure inside the nucleon while the black dot on the left side represents the electron as a point like particle emitting a virtual photon.	5
1.2	Kelly Fits to nucleon electromagnetic form factors [18].	10
1.3	The charge and magnetization distributions of the proton and the neutron obtained from nucleon form factor data by Kelly [17].	11
1.4	The flavor decomposition of proton form factors shows the behavior of the dependence u and d quarks contributions on Q^2 [8].	13
1.5	The measurements of G_M^n from polarized electron-deuteron experiments. Graph from Ref. [7].	15
1.6	The world data on G_M^n from unpolarized electron-deuteron experiments. Graph from [27].	16
1.7	The world data on G_M^n from polarized and unpolarized electron-deuteron experiments at high Q^2 values. The red band shows the systematic uncertainty for the CLAS6 data. The theory curves are the Miller model (blue) [41], the Gutsche model (yellow) [42], and the Cloet model (green) [43].	18
1.8	Photon-nucleon coupling in the VMD models.	20
1.9	The fit of the extended GK model by Lomon's work for the neutron magnetic form factor G_M^n scaled by $\mu_n G_D$ [49]. Graph from [51] . . .	22
1.10	Comparison of theoretical predictions to G_M^n data. Theory curves are (Diehl05) [22], (Lomon06) [49], (Gross08) [54], and (Santopinto) [56]. Graph from [57] and G_M^n data are from Refs. [8, 26, 40]	24
1.11	The result of predictions of the Faessler's model for the neutron magnetic form factor G_M^n scaled by μG_D [63]	27
1.12	The prediction of soft-wall AdS/QCD model for the neutron magnetic form factor G_M^n . Left: With minimal number of parameters [65]. Right: Extended Gutsche's works [42]	29
2.1	The Jefferson Lab CEBAF accelerator site and four experimental halls [66]. The electrons are emitted from the injector that is marked by the number (1) and accelerated through the two LINACs that are marked by the number (2), connected at each end with recirculating magnets represented by number (4). The electron beam is sent to four different experimental halls A, B, C and D that are marked by the numbers 5, 6, 7, and 8, respectively.	30

2.2	Hall B beamline upstream of the CLAS12 detector showing the tagger magnet yoke (in the left) that is energized during beam tuning and during polarization measurements, quadrupoles and corrector that are used to deliver beam to the target, beam position monitors (BPM) that consist of Radio Frequencies (RF) cavities to provide both the beam position in the $x - y$ plane and the relative beam intensity and wire harps that are used to measure the electron beam profile and position [67].	32
2.3	The CLAS12 spectrometer in Hall B at JLab. The electron beam is incident from the right side of this figure. The CLAS12 Forward (FD) and Central (CD) Detectors are identified [68].	33
2.4	The design rendering of the target cell located within the scattering chamber [67].	35
2.5	Left: The torus magnet in Hall B before the installation of drift chambers between the coils [72]. Right: The torus magnet between the drift chamber regions [74].	36
2.6	The wire layout of one superlayer of the CLAS12 drift chambers. A hexagonal cell is formed by surrounding the sense wire with two layers of field wires. The path of a charged particle detected in the chamber is represented by the red line. The drift distance (calculated from the drift time) between the track to the nearest signal wire (shown by yellow circles) constrains the track fit to reach the required momentum resolution of $\Delta p/p = 1\%$ [74].	37
2.7	Fully assembled High Threshold Cherenkov Counter [75].	39
2.8	Forward Time Of Flight of CLAS12. It consists of three different counters: panel-1b counters (dark blue), panel-2 counters (orange), and panel-1a counters are located immediately downstream of the panel-1b counters which are not shown here [70].	40
2.9	Left: 6 sectors of PCAL [68]. Right: A single PCAL sector located in front of the Sector 5 EC [78].	41
2.10	Visual representation of the PCAL configuration, showing five layers in each view (U, V, and W) and lead sheets placed between each scintillator layer [78].	42
2.11	The DAQ and trigger system of CLAS12 [80].	45
2.12	The CLARA framework for FD reconstruction. The information extracted from the decoded HIPO files is fed into the micro-services (represented by orange ovals) to produce transient information which is then used by the Event Builder (EB) [82].	47

2.13	The schematic flow of analysis trains involves reading event data from HIPO files, applying corrections for the ECAL sampling fraction (SF) and filters through the analysis chain, labeling events based on filter criteria, and storing the labeled events in output files [82].	49
3.1	The front face of the calorimeter with 6 sectors on the left, and on the right is a close-up view of the single sector. The black point shows the electron vertex, the blue point shows the detected neutron measured by the calorimeter, and the gray and green points show the detected and expected neutron intersecting with the front face of the calorimeter. The blue line is the detected neutron's path, which is calculated from the electron vertex in direction of the blue point while the green line is the expected neutron's path starting from the electron vertex and moving in direction of the missing momentum of the neutron.	51
3.2	The electron z-vertex position for three different datasets. The events pass the EB cut that listed in Table 3.2.	53
3.3	Number of photoelectrons produced in the HTCC. The events pass the EB cut that listed in Table 3.2.	54
3.4	Effects of the PCAL fiducial cuts of electrons. Red shows all events. Non-red colors show the hits after applying the fiducial cut. The events pass the EB cut that listed in Table 3.2.	55
3.5	Effects on the three regions of DC fiducial cuts for electrons for each RGA dataset. The red points show the hits before the fiducial cuts and the color points show the hits after the fiducial cuts. The events pass the EB cut that listed in Table 3.2.	56
3.6	The sampling fraction for electron candidates in sector 1 as a function of momentum with the $\pm 5\sigma$ cut applied by the event-builder on SF as a function of E_{dep} . The red lines are the cut on the SF as a function of P_{ele} with the $\pm 3.5\sigma$ and a vertical line indicating the minimum electron momentum cut. The distributions have the EB cut that listed in Table 3.2. The curly tail that appears in the inbending 10.6 GeV dataset was a result of an issue with the parameterization of SF vs. E_{dep} cut, see text for explanation.	58
3.7	The chi2pid distribution of reconstructed electron. The events pass the EB cuts listed in Table 3.2, $\pm 3.5\sigma$ SF cut and the minimum momentum of 2 GeV and 1.5 GeV for 10.6 GeV and 10.2 GeV beam energies, respectively.	59
3.8	The correlation of the sampling fraction using the E_{inner} vs. the PCAL. The events pass the EB cuts listed in Table 3.2 and $P_{ele} > 4.5$ GeV. The diagonal cut removes the events below the red lines, which are pions.	60

3.9	Energy is deposition in $EC_{in} + EC_{out}$ layers versus energy deposited in the PCAL layer. The red line is at 60 MeV. Plot is for all negative tracks for Sector 1.	60
3.10	Top: Energy deposition in $EC_{in} + EC_{out}$ layers versus energy deposited in the PCAL layer. The PCAL > 0.06 GeV cut is defined in the Event Builder. The events pass the EB cuts listed in Table 3.2. Bottom: Same distribution but with $\pm 3.5\sigma$ cut on SF as a function of P_{ele} , diagonal cut, and the minimum momentum of 2 GeV and 1.5 GeV for 10.6 GeV and 10.2 GeV beam energies, respectively.	61
3.11	Vertex difference between the electron and π^+ . The events pass the EB cuts listed in Table 3.2.	61
3.12	Top: The chi2pid vs momentum distribution after the Event Builder applied Δt to assign a particle as the pions.	63
3.13	The effect of fiducial cuts on the three regions of the drift chambers on the π^+ . The red points show the hits before the cuts were applied and the overlaid colored points show the hits that survive the fiducial cut. Top is region 1, middle is region 2 and bottom is region 3.	64
3.14	The missing mass distribution as function of missing momentum of $ep \rightarrow e'\pi^+X_n$	66
3.15	The missing mass distribution of $ep \rightarrow e'\pi^+X_n$	66
3.16	PCAL/ECAL hit position Y vs. X of expected neutrons intersecting with the calorimeters. The red points show the events before applying the fiducial cut. Top row shows an overlay of all sectors rotated by $(s - 1)60^\circ$ and the bottom row shows each sector individually.	67
3.17	The missing mass distribution of the expected neutron $p(e, e'\pi^+)n$ that intersects with the calorimeters and passes the fiducial cut. The red vertical lines show the cut applied within 2σ	68
3.18	Differences in direction cosines ΔC_y vs. ΔC_x . The red circle shows the cut used to eliminate the background.	69
3.19	The missing mass distribution of detected $p(e, e'\pi^+)n$ neutron satisfied $\Delta C_x, \Delta C_y$ cut. From left to right inbending 10.6 GeV, outbending 10.6 GeV and inbending 10.2 GeV.	70
3.20	β_{neut} of neutral particles measured in calorimeters vs. missing momentum that satisfied $\Delta C_x, \Delta C_y$ cut. The red line is the theoretical curve for neutrons.	71
3.21	The missing mass distribution of expected $p(e, e'\pi^+)n$ (top) and detected $p(e, e'\pi^+)n$ (bottom) neutron satisfied above cuts. From left to right, inbending 10.6 GeV, outbending 10.6 GeV and inbending 10.2 GeV.	72

3.22	The missing mass distribution of $p(e, e'\pi^+n)$ for inbending 10.6 GeV, generated from SIDIS MC.	74
3.23	The missing mass distribution of expected (top) and detected (bottom) neutron for three different P_{mm} bins. The distribution is fitted with a Gaussian plus polynomial background. The blue curve is the signal distribution after subtraction of the background distribution, the green is the background, and the red is the sum of the two. The fitting is shown for inbending 10.6 GeV dataset. See Appendix A for other P_{mm} bins and other datasets.	76
3.24	The missing mass distribution of expected (top) and detected (bottom) neutron for three different P_{mm} bins. The distribution is fitted with a Crystal ball polynomial background. The blue curve is the signal distribution after subtraction of the background distribution, the green is the background, and the red is the sum of the two. The fitting is shown for inbending 10.6 GeV dataset. See Appendix B for other P_{mm} bins and other datasets.	76
3.25	Left: The mean values of the signal distribution for both expected and detected neutrons for each P_{mm} bin. Right: The width values of the signal distribution for both expected and detected neutrons for each P_{mm} bin.	77
3.26	A comparison of the neutron detection efficiency in the CLAS12 calorimeters detector between the Gaussian and the Crystal Ball fitting, binned in missing momentum of neutron. The comparison shows inbending 10.6 GeV (Top Left), inbending 10.6 GeV (Top Right) and inbending 10.2 GeV (Bottom).	79
3.27	The neutron detection efficiency in the calorimeter detector was extracted from the Gaussian (Right) and the Crystal Ball function (Left), binned in missing momentum of the neutron, for each dataset and compared with the CLAS6 result.	79
3.28	A fit of the neutron detection efficiency for the Crystal Ball function (top) and the Gaussian (bottom) according to Eq. 3.30. The uncertainty on the fit is shown as a band in the right hand side plots for the Crystal Ball function (top) and the Gaussian (bottom).	81
4.1	The kinematic quantities for $D(e, e'p)/D(e, e'n)$ shows the scattering plane that is defined by the 3-momenta of the incoming and scattered electrons and the reaction plane that is determined by the 3-momentum transfer, $\vec{q} = \vec{p}_{e'} - \vec{p}_e$, and the final proton/neutron 3-momentum, \vec{p}_1 . θ_{pq} is the angle between the direction of the detected nucleon \vec{p}_1 and the direction of the virtual photon \vec{q}	84
4.2	The invariant mass W distribution as a function of θ_{pq} for $D(e, e'p)$ (top) and $D(e, e'n)$ (bottom) for each data set.	85

4.3	The invariant mass W distribution of $D(e, e'p)$ (top) and $D(e, e'n)$ (bottom) for each dataset.	86
4.4	The $E_{\text{beam}}^{\text{angles}}$ vs. $E_{\text{beam}}^{\text{from ele}}$ distributions for $D(e, e'p)$ (top) and $D(e, e'n)$ (bottom) that satisfied $\theta_{pq} < 10^\circ$ cut for each dataset.	88
4.5	The $E_{\text{beam}}^{\text{angles}}$ distributions of $D(e, e'p)$ events that satisfied $0.85 < W < 1.05$ GeV and $\theta_{pq} < 10^\circ$ cut for each sector. The black vertical lines show the cut applied within 1σ	89
4.6	The $E_{\text{beam}}^{\text{angles}}$ distributions of $D(e, e'n)$ events that satisfied $0.85 < W < 1.05$ GeV and $\theta_{pq} < 10^\circ$ cut for each sector. The black vertical lines show the cut applied within 1σ	90
4.7	The $\Delta\phi$ distributions for events passing cut on $0.85 < W < 1.05$ GeV, $\theta_{pq} < 10^\circ$ and $E_{\text{beam}}^{\text{angles}}$ cuts for $D(e, e'p)$ (top) and $D(e, e'n)$ (bottom) for each datasets. The black vertical lines show the cut applied within 1σ	91
4.8	The Q^2 as a function of θ_{pq} distribution for $D(e, e'p)$ (top) and $D(e, e'n)$ (bottom) for each datasets that satisfied $0.85 < W < 1.05$ GeV, $E_{\text{beam}}^{\text{angles}}$ and $\Delta\phi$ cuts. The red curve is the cut used to select the quasi-elastic events.	92
4.9	The W distribution for $D(e, e'p)$ (top) and $D(e, e'n)$ (middle) for each dataset that satisfied $E_{\text{beam}}^{\text{angles}}$, $\Delta\phi$ and θ_{pq} cuts. The bottom plots shows the comparison between $D(e, e'p)$ and $D(e, e'n)$ channels. The counts are scaled by normalizing the peak of the $D(e, e'p)$ and $D(e, e'n)$ events.	93
4.10	Acceptance matching using the “swimming” technique for negative torus polarity “inbending” field, where the electron is bent toward the beam line. By requiring both swum-neutron and swum-proton tracks to hit the calorimeters, the geometric acceptance of $D(e, e'p)$ and $D(e, e'n)$ are equal.	94
4.11	The distribution of the swum neutron (yellow points) and swum proton (red points) in the $x - y$ plane of the ECAL for $D(e, e'p)$ (top) and $D(e, e'n)$ (bottom) for each data set.	95
4.12	The σ_n/σ_p ratio results from different data sets at three different beam energies 10.2, 10.4, and 10.6 GeV binned in Q^2	96
5.1	The σ_n/σ_p ratio results including NDE correction from different data sets at three different beam energies 10.2, 10.4, and 10.6 GeV binned in Q^2	98
5.2	Fermi momentum distribution of nucleons inside the deuteron given by Hulthen model and generated by QUEEG.	100

5.3	The polar angle of the reconstructed electron as a function of the momentum of electron for $D(e, e'p)$ quasi-elastic events for each data set. Top row is the data and bottom is the simulation.	100
5.4	The polar angle of reconstructed electron as a function of the momentum of electron for $D(e, e'n)$ quasi-elastic events for each data set. Top row is the data and bottom is the simulation.	101
5.5	The W distribution for $D(e, e'p)$ (top) and $D(e, e'n)$ (bottom) for both experimental (black) and simulated (red) data that satisfied the quasi-elastic selection cuts and pass acceptance matching. The counts are scaled by normalizing the maximum histogram of both experimental and simulated data. The comparison is shown for incident beam energies of 10.2, 10.4 and 10.6 GeV.	102
5.6	The fraction of nucleons at different Q^2 bins that scattered into the PCAL/ECAL acceptance and satisfied the θ_{pq} cuts and acceptance matching, as determined by simulation. The black points on the plot represent the neutron fraction, while the red points represent the proton fraction. These points were generated using an incident beam energy of 10.2, 10.4 and 10.6 GeV. The error bars on the plot are quite small and may not be easily observed.	103
5.7	The correction factor, $f_{fermi}(Q^2) = \frac{f_{pro}(Q^2)}{f_{neut}(Q^2)}$, to the σ_n/σ_p ratio for Fermi loss in the PCAL/ECAL has been determined for the 10.2, 10.4 and 10.6 GeV data. The error bars on the plot are quite small and may not be easily observed.	104
5.8	The σ_n/σ_p ratio results including NDE and Fermi corrections from data at three different beam energies 10.2, 10.4, and 10.6 GeV binned in Q^2	104
5.9	Feynman diagrams for Born term and lowest order radiative processes for the electron. The p_h and p_u are the momentum of the detected and undetected hadrons, respectively.	105
5.10	A comparison of the radiative correction factor, RC, for $D(e, e'p)n$ (red curve) and $D(e, e'n)p$ (green curve) as a function of ϕ_{pq} . The curves shown were generated for a beam energy of 10.2 GeV and $W = 2.60$ GeV at different Q^2 values.	108
5.11	A comparison of the radiative correction factor, RC, for $D(e, e'p)n$ (red curve) and $D(e, e'n)p$ (green curve) as a function of ϕ_{pq} . The curves shown were generated for a beam energy of 10.4 GeV and $W = 2.60$ GeV at different Q^2 values.	108
5.12	A comparison of the radiative correction factor, RC, for $D(e, e'p)n$ (red curve) and $D(e, e'n)p$ (green curve) as a function of ϕ_{pq} . The curves shown were generated for a beam energy of 10.6 GeV and $W = 2.60$ GeV at different Q^2 values.	109

5.13	The ratio of the radiative correction of $D(e, e'p)n$ to $D(e, e'n)p$ at different Q^2 values for 10.2 GeV (top left), 10.4 GeV (top right) and 10.6 GeV (bottom middle). The average over the ϕ_{pq} values of these radiative correction are used to correct the ratio measurement in each Q^2 point.	109
5.14	The σ_n/σ_p ratio results including NDE, Fermi and radiative corrections from different data sets at three different beam energies 10.2, 10.4, and 10.6 GeV binned in Q^2	111
6.1	Arrington parameterizations of $G_M^p/\mu_p G_D$ (left), G_E^p/G_D (middle) and $G_E^n/\mu_n G_D$ (right) shown as black solid curves. The error band within the dashed curves and highlighted in red represent the fit uncertainty from the parameterization. The plot from Ref. [93].	113
6.2	Arrington parameterizations of G_M^p (left), G_E^p (middle) and G_E^n (right) that correspond to the Q^2 values of our experiment.	114
6.3	The G_M^n as a function of Q^2 for three different beam energies of 10.2, 10.4 and 10.6 GeV. The black line showing $G_M^n = \mu_N G_D$	114
6.4	G_M^n weighted average as a function of Q^2 obtained by combining data from three different beam energy 10.2, 10.4 and 10.6 GeV. The black line shows $G_M^n = \mu_N G_D$	115
6.5	The difference of the neutron detection efficiency between fitting the neutron peak with a Gaussian function and a Crystal Ball function, binned in missing momentum of neutron for inbending and outbending 10.6 GeV and inbending 10.2 GeV datasets.	117
6.6	Left: Comparison of the G_M^n measurements with Crystal Ball (black) and Gaussian (red) functions used to determine the NDE correction. Right: The estimated relative systematic uncertainty on G_M^n due to the NDE fitting procedure.	118
6.7	Left: Comparison of the G_M^n measurements with (black) and without (red) electron vertex cut applied during particle identification. Right: The estimated relative systematic uncertainty on G_M^n due to electron vertex cut.	119
6.8	Left: Comparison of G_M^n measurements with (black) and without (red) fiducial cuts applied during particle identification. Right: The estimated relative systematic uncertainty on G_M^n due to fiducial cuts.	119
6.9	Left: Comparison of G_M^n measurements with different SF cut applied during electron identification. Right: The estimated relative systematic uncertainty on G_M^n due to SF cut.	120
6.10	The estimated relative systematic uncertainty on G_M^n due to electron ID cuts in added quadrature.	120

6.11	Left: Comparison of G_M^n measurements with different $E_{\text{beam}}^{\text{angles}}$ cut applied during quasi-elastic events selection. Right: The estimated relative systematic uncertainty on G_M^n due to $E_{\text{beam}}^{\text{angles}}$ cut.	121
6.12	Left: Comparison of G_M^n measurements with different $\Delta\phi$ cut applied during quasi-elastic events selection. Right: The estimated relative systematic uncertainty on G_M^n due to $\Delta\phi$ cut.	122
6.13	The Q^2 as a function of θ_{pq} distribution for $D(e, e'p)$ (left) and $D(e, e'n)$ (right) for 10.2 GeV dataset. The red curve represents the initial θ_{pq} cut applied to select quasi-elastic events. The black curves represent θ_{pq} cuts that are 10% larger and smaller than the original cut.	122
6.14	Left: Comparison of G_M^n measurements with different θ_{pq} cut applied during quasi-elastic events selection. Right: The estimated relative systematic uncertainty on G_M^n due to a 10% larger than the original θ_{pq} cut.	123
6.15	Left: Comparison of G_M^n measurements with different θ_{pq} cut applied during quasi-elastic events selection. Right: The estimated relative systematic uncertainty on G_M^n due to a 10% smaller than the original θ_{pq} cut.	123
6.16	The estimated relative systematic uncertainty on G_M^n due to the quasi-elastic cuts in added quadrature.	124
6.17	Left: Comparison of G_M^n measurements with smallest and largest value of the ratio of radiative corrections. Right: The estimated relative systematic uncertainty on G_M^n due to the radiative correction.	124
6.18	The estimated relative systematic uncertainty on the weighted average of G_M^n for the individual contributing sources as a function of Q^2 values.	125
6.19	The total estimated relative systematic uncertainty on the weighted average value of G_M^n in added quadrature.	126
7.1	Final G_M^n results scaled to the dipole parametrization. A selection of previous measurements is shown. The grey points indicate the results of this analysis. The weighted average systematic error is shown as a grey band. The black line indicates $G_M^n = \mu_N G_D$. The theory curves are the Miller model (blue) [41], the Gutsche model (yellow) [42], and the Cloet model (green) [43].	129
7.2	Same as Fig.7.1 but with error bars being the quadrature sum of systematic and statistical uncertainty for our results.	129

A.1	The missing mass distribution of expected neutron $p(e, e'\pi^+)n$ for different P_{mm} bin. The distribution is fitted with a Gaussian plus polynomial background. The blue curve is the signal distribution after subtraction of the background distribution, the green is the background, and the red is the sum of the two. The fitting is shown for inbending 10.6 GeV dataset.	145
A.2	The missing mass distribution of detected neutron $p(e, e'\pi^+)n$ for different P_{mm} bin. The distribution is fitted with a Gaussian plus polynomial background. The blue curve is the signal distribution after subtraction of the background distribution, the green is the background, and the red is the sum of the two. The fitting is shown for inbending 10.6 GeV dataset.	146
A.3	Missing mass distribution of expected neutron $p(e, e'\pi^+)n$ for different P_{mm} bin. The distribution is fit with a gaussian + polynomial background. The blue curve is the signal distribution after subtraction of the background distribution, the green is the background, and the red is the sum of the two. The fitting is shown for outbending 10.6 GeV dataset.	147
A.4	Missing mass distribution of detected neutron $p(e, e'\pi^+)n$ for different P_{mm} bin. The distribution is fit with a gaussian + polynomial background. The blue curve is the signal distribution after subtraction of the background distribution, the green is the background, and the red is the sum of the two. The fitting is shown for outbending 10.6 GeV dataset.	148
A.5	Missing mass distribution of expected neutron $p(e, e'\pi^+)n$ for different P_{mm} bin. The distribution is fit with a Gaussian + polynomial background. The blue curve is the signal distribution after subtraction of the background distribution, the green is the background, and the red is the sum of the two. The fitting is shown for inbending 10.2 GeV dataset.	149
A.6	Missing mass distribution of detected neutron $p(e, e'\pi^+)n$ for different P_{mm} bin. The distribution is fit with a Gaussian + polynomial background. The blue curve is the signal distribution after subtraction of the background distribution, the green is the background, and the red is the sum of the two. The fitting is shown for inbending 10.2 GeV dataset.	150
A.7	The χ^2 of the expected (left) and detected (right) neutron as a function of P_{mm} using Gaussian + polynomial background.	151
A.8	The amplitude of the expected (left) and detected (right) neutron as a function of P_{mm} using Gaussian + polynomial background.	151
A.9	The mean of the expected (left) and detected (right) neutron as a function of P_{mm} using Gaussian + polynomial background.	151

A.10	The width of the expected (left) and detected (right) neutron as a function of P_{mm} using Gaussian + polynomial background.	152
A.11	The P_0 parameter of the expected (left) and detected (right) neutron as a function of P_{mm} using Gaussian + polynomial background.	152
A.12	The P_1 parameter of the expected (left) and detected (right) neutron as a function of P_{mm} using Gaussian + polynomial background.	152
A.13	The P_2 parameter of the expected (left) and detected (right) neutron as a function of P_{mm} using Gaussian + polynomial background.	153
A.14	The P_3 parameter of the expected (left) and detected (right) neutron as a function of P_{mm} using Gaussian + polynomial background.	153
A.15	The P_4 parameter of the expected (left) and detected (right) neutron as a function of P_{mm} using Gaussian + polynomial background.	153
B.1	The missing mass distribution of expected neutron $p(e, e'\pi^+)n$ for different P_{mm} bin. The distribution is fitted with a Crystal Ball + polynomial background. The blue curve is the signal distribution after subtraction of the background distribution, the green is the background, and the red is the sum of the two. The fitting is shown for inbending 10.6 GeV dataset.	155
B.2	The missing mass distribution of detected neutron $p(e, e'\pi^+)n$ for different P_{mm} bin. The distribution is fitted with a Crystal Ball + polynomial background. The blue curve is the signal distribution after subtraction of the background distribution, the green is the background, and the red is the sum of the two. The fitting is shown for inbending 10.6 GeV dataset.	156
B.3	Missing mass distribution of expected neutron $p(e, e'\pi^+)n$ for different P_{mm} bin. The distribution is fit with a Crystal ball + polynomial background. The blue curve is the signal distribution after subtraction of the background distribution, the green is the background, and the red is the sum of the two. The fitting is shown for outbending 10.6 GeV dataset.	157
B.4	Missing mass distribution of detected neutron $p(e, e'\pi^+)n$ for different P_{mm} bin. The distribution is fit with a Crystal ball + polynomial background. The blue curve is the signal distribution after subtraction of the background distribution, the green is the background, and the red is the sum of the two. The fitting is shown for outbending 10.6 GeV dataset.	158

B.5	Missing mass distribution of expected neutron $p(e, e'\pi^+)n$ for different P_{mm} bin. The distribution is fit with a Crystal ball + polynomial background. The blue curve is the signal distribution after subtraction of the background distribution, the green is the background, and the red is the sum of the two. The fitting is shown for inbending 10.2 GeV dataset.	159
B.6	Missing mass distribution of detected neutron $p(e, e'\pi^+)n$ for different P_{mm} bin. The distribution is fit with a Crystal ball + polynomial background. The blue curve is the signal distribution after subtraction of the background distribution, the green is the background, and the red is the sum of the two. The fitting is shown for inbending 10.2 GeV dataset.	160
B.7	The χ^2 of the expected (left) and detected (right) neutron as a function of P_{mm} using Crystal ball + polynomial background.	161
B.8	The amplitude of the expected (left) and detected (right) neutron as a function of P_{mm} using Crystal ball + polynomial background.	161
B.9	The mean of the expected (left) and detected (right) neutron as a function of P_{mm} using Crystal ball + polynomial background.	161
B.10	The width of the expected (left) and detected (right) neutron as a function of P_{mm} using Crystal ball + polynomial background.	162
B.11	The P_0 parameter of the expected (left) and detected (right) neutron as a function of P_{mm} using Crystal ball + polynomial background.	162
B.12	The P_1 parameter of the expected (left) and detected (right) neutron as a function of P_{mm} using Crystal ball + polynomial background.	162
B.13	The P_2 parameter of the expected (left) and detected (right) neutron as a function of P_{mm} using Crystal ball + polynomial background.	163
B.14	The P_3 parameter of the expected (left) and detected (right) neutron as a function of P_{mm} using Crystal ball + polynomial background.	163
B.15	The P_4 parameter of the expected (left) and detected (right) neutron as a function of P_{mm} using Crystal ball + polynomial background.	163
B.16	The n parameter of the expected (left) and detected (right) neutron as a function of P_{mm} using Crystal ball + polynomial background.	164
B.17	The a parameter of the expected (left) and detected (right) neutron as a function of P_{mm} using Crystal ball + polynomial background.	164

INTRODUCTION

The modern model of the atom is a dense nucleus surrounded by an electron cloud and revealed by Rutherford's gold foil experiment in 1911 [1]. Later, it was discovered the nucleus itself is made up of smaller objects that we refer to as nucleons (protons and neutrons). The fact that the proton's magnetic moment is $\mu_p = 2.79 \mu_N$ instead of $\mu_p = \mu_N$ for a point-like charged particle with spin 1/2 demonstrates that the proton has a structure. Similarly, the neutron's magnetic moment of $\mu_n = -1.91 \mu_N$ is different from the magnetic moment of a point neutral particle which is $\mu_n = 0$. This is one indication that protons and neutrons are very complicated objects that we now know are made up of fundamental particles called quarks and gluons.

Quarks have six "flavors" known as up (u), down (d), strange (s), charm (c), bottom (b), top (t), and strange and carry color charges (blue (B), red (R), or green (G)). They interact with each other by exchanging massless particles, called gluons through the strong interaction. The strong interaction between the quarks and gluons is described by the theory of Quantum Chromodynamics (QCD) and the strength of the interaction can be determined by the strong coupling constant, α_s , which is dependent on Q^2 according to [2]

$$\alpha_s(Q^2) = \frac{12\pi}{(33 - 2N_f) \ln(\frac{Q^2}{\lambda_{QCD}^2})}, \quad (1)$$

where Q^2 is the four-momentum transfer squared from the incident electron to the nucleon, N_f is the number of quark flavors, and λ_{QCD} is a parameter in QCD (≈ 0.22 GeV) [3, 4]. In the limit of very large values of Q^2 (short distance scale), α_s is small. Therefore, the quarks are weakly interacting, which can be considered to be "free". This is asymptotic freedom. On the other hand, when Q^2 is small (large distance scale), α_s is large and quarks are strongly interacting parties and bind to form

nucleons.

Understanding the quark-gluon dynamics and the nucleon structure is currently the central problem of nuclear physics. The electromagnetic form factors of the nucleons are basic observables that provide insight into the nucleon structure. These observables describe the distribution of charge and magnetization within the nucleon at low Q^2 and the behavior of quarks at high Q^2 . The unique tool to obtain these observables experimentally is through high-energy electron-nucleon scattering.

Many experiments over the last several decades have studied the nucleon form factors at different accelerator facilities [5]. One of these facilities is the Continuous Electron Beam Accelerator Facility (CEBAF) at the Thomas Jefferson National Accelerator Facility (Jefferson Lab or JLab) in the United States. The Jefferson Lab experiments measured the form factors for both the proton and neutron up to $Q^2 = 5 \text{ GeV}^2$ (see [6] and references therein). In 2015, JLab completed the upgrade of CEBAF from 6 GeV to 12 GeV, which has provided the opportunity to extend the measurement of form factors to higher Q^2 . Measuring nucleon form factors at high Q^2 will shed light on many topics related to the nucleon structure such as the behaviors of the up and down quark contributions [7], the orbital angular momentum of the quarks [8], etc. There are several experiments in Hall A to measure all four elastic electric, G_E , and magnetic, G_M , form factors for the proton and neutron at high Q^2 and one experiment in Hall B. The listing of experiments for measuring the elastic electromagnetic form factors in the Jefferson Lab 12-GeV era is shown in Table 1.

In experimental Hall A, a new Super BigBite Spectrometer (SBS) will be used to measure the nucleon form factors and their ratios, G_M^p , G_E^p/G_M^p , G_E^n/G_M^n , and the G_M^n [9], see Table 1. In experimental Hall B, the new CLAS12 spectrometer has measured G_M^n up to $Q^2 = 12 \text{ GeV}^2$.

This dissertation will describe the measurement of G_M^n in Hall B using the CLAS12 detector. The dissertation is organized as follows: Chapter 1 will present the definition and interpretation of the elastic form factors, provide a review of the previous data on G_M^n and describe some of the theoretical models of the form factors. In Chapter 2, we will present the experimental setup to measure G_M^n , which includes a description of the CLAS12 detector and how it work. In Chapter 3, we will explain our method to measure the neutron detection efficiency, which is one of the most important experimental quantities necessary to measure G_M^n and a source of systematic uncertainty. In Chapter 4, will present the procedures that we use to measure the ratio R of quasi-elastic (QE) cross sections for $e - n$ to $e - p$ scattering on a deuteron target. All corrections to the ratio required to extract G_M^n will be presented in Chapter 5. Finally, the preliminary results of G_M^n and the systematic uncertainty on G_M^n will discuss in Chapter 6.

Quantity	Exp.	Method	Target	Q^2 GeV ²	Hall	Status
G_M^p	E12-07-108	Elastic Scattering	LH ₂	2.0 - 15.7	A	PRL ¹
G_E^p/G_M^p	E12-07-109	Polarization transfer	LH ₂	6.4 - 10.5	A	Fall 2023
G_M^n	E12-07-104	$e - n/e - p$ ratio	LD ₂ , LH ₂	5 - 12.0	B	Complete ²
G_M^n	E12-09-019	$e - n/e - p$ ratio	LD ₂ , LH ₂	1.9 - 9.9	A	Complete ²
G_E^n/G_M^n	E12-09-016	Double polarization asymmetry	polarized ³ He	2.1 - 8.4	A	Complete ²
G_E^n/G_M^n	E12-17-004	Polarization transfer	LD ₂	4.3	A	Summer 2023
G_E^n/G_M^n	E12-11-009	Polarization transfer	LD ₂	up to 6.9	A	To be scheduled

Table 1: Listing of the electromagnetic form factors of the nucleons experiments.

¹Phys. Rev. Lett., 128, 102002 (2022)

²Data collection completed but not yet published.

CHAPTER 1
NUCLEAR FORM FACTORS

This chapter describes how elastic electron-nucleon scattering is used to determine the internal structure of the nucleons. We will begin by deriving the differential cross section for elastic electron-nucleon scattering, described by the theory of Quantum Electrodynamics (QED). Then, we will discuss how the electric G_E and magnetic G_M form factors are related to the distribution of charge and current within the nucleon.

This chapter also describes the experimental methods to measure G_M^n and some of the theoretical models describing G_M^n .

1.1 Elastic Electromagnetic Form Factors

Elastic electron scattering off the nucleon is described by Feynman diagram shown in Fig. 1.1 and defined by

$$e(k) + N(p) \rightarrow e(k') + N(p'), \quad (1.1)$$

where the incident and scattered electron has four-momenta $k = (\vec{k}, E)$ and $k' = (\vec{k}', E')$, respectively, and the initial and final nucleon state are $p = (\vec{p}, E_N)$ and $p' = (\vec{p}', E'_N)$, respectively. The four-momentum transfer from the electron is through the exchange of a virtual photon $Q = k - k' = -q$. According to Feynman rules for QED, the amplitude for elastic scattering can be written as a product of an electronic and nucleon currents, j^μ and J^μ , respectively [10]:

$$-i\mathcal{M} = j^\mu \left(\frac{-ig_{\mu\nu}}{q^2} \right) J^\mu, \quad (1.2)$$

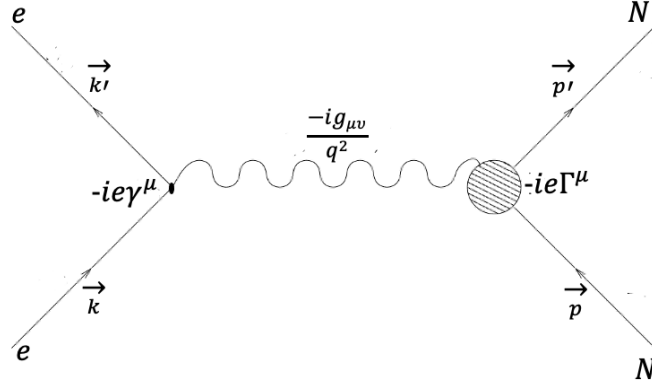


Figure 1.1: Feynman diagram for electron-nucleon scattering. The shaded circle on the right side of the diagram represents the structure inside the nucleon while the black dot on the left side represents the electron as a point like particle emitting a virtual photon.

where

$$j^\mu = \bar{u}(k')(-ie\gamma^\mu)u(k) \quad \text{and} \quad J^\mu = \bar{u}(p')(-ie\Gamma^\mu)u(p), \quad (1.3)$$

where $\left(\frac{-ig_{\mu\nu}}{q^2}\right)$ is the virtual photon propagator, $\bar{u}(k)$, $u(k')$ are four-component Dirac spinors for the initial and final electron states, respectively, while $\bar{u}(p)$, $u(p')$ are Dirac spinors for initial and final nucleon states, respectively. The quantity γ^μ represents the Dirac matrices and $g_{\mu\nu}$ is the Minkowski tensor. The electronic current contains $-ie\gamma^\mu$, which represents the electromagnetic vertex function. On the other hand, the nucleon current involves $-ie\Gamma^\mu$, which is the photon-nucleon vertex function. The factor Γ^μ contains all information about the internal electromagnetic structure of the nucleon and can be defined in terms of Dirac (F_1) and Pauli (F_2) form factors as [10]

$$\Gamma^\mu = \left[\gamma^\mu F_1(Q^2) + i\frac{\kappa\sigma^{\mu\nu}q_\nu}{2M} F_2(Q^2) \right], \quad (1.4)$$

where $\sigma^{\mu\nu}$ is the antisymmetric product of the gamma matrices defined as $\sigma^{\mu\nu} = \frac{i}{2} [\gamma^\mu, \gamma^\nu]$, $\mu \neq \nu$, κ represents the anomalous magnetic moment of the nucleon, and

M is the mass of the nucleon. By using this expression for the nucleon current, the amplitude of elastic scattering becomes

$$\mathcal{M} = \frac{e^2}{q^2} \bar{u}(k') \gamma^\mu u(k) g_{\mu\nu} \bar{u}(p') \left[\gamma^\mu F_1(Q^2) + i \frac{\kappa \sigma^{\mu\nu} q_\nu}{2M} F_2(Q^2) \right] u(p). \quad (1.5)$$

By using the above amplitude we can express the cross section for elastic electron-nucleon scattering in terms of the invariant amplitude \mathcal{M} given by Fermi's Golden Rule [?]

$$d\sigma = \frac{1}{64\pi^2 M^2} |\overline{\mathcal{M}^2}| d\Omega. \quad (1.6)$$

Therefore, the differential cross section for unpolarized elastic electron-nucleon scattering in terms of Dirac F_1 and Pauli F_2 form factors becomes

$$\frac{d\sigma}{d\Omega} = \sigma_{Mott} \left[(F_1^2 + \kappa^2 \frac{Q^2}{2M^2} F_2^2) + \frac{Q^2}{2M^2} (F_1 + \kappa F_2)^2 \tan^2(\frac{\theta}{2}) \right], \quad (1.7)$$

where θ is the electron scattering angle, σ_{Mott} is the Mott cross section for a point-like nucleon

$$\sigma_{Mott} = \frac{\alpha^2 E' \cos^2(\frac{\theta}{2})}{4E_{beam}^3 \sin^4(\frac{\theta}{2})}, \quad (1.8)$$

and $\alpha \approx \frac{1}{137}$ is the fine structure constant. The differential cross section is related to the probability that an electron interacts with a target and scatters into the solid angle $d\Omega$. Equation (1.7) is known as the Rosenbluth formula and contains the interference term of Dirac and Pauli form factors.

The Sachs form factors, G_E and G_M [11], were introduced as

$$G_E(Q^2) = F_1(Q^2) - \tau F_2(Q^2) \quad (1.9)$$

$$G_M(Q^2) = F_1(Q^2) + F_2(Q^2), \quad (1.10)$$

where $\tau = \frac{Q^2}{4M^2}$. The functions G_E and G_M are linear combinations of Dirac F_1 and Pauli F_2 form factors. With this redefinition of the form factors, we can rewrite the

Rosenbluth formula as

$$\frac{d\sigma}{d\Omega} = \sigma_{Mott} \left[\frac{G_E^2(Q^2) + \tau G_M^2(Q^2)}{1 + \tau} + 2\tau G_M^2(Q^2) \tan^2\left(\frac{\theta}{2}\right) \right]. \quad (1.11)$$

The advantage of using the Sachs form factor is that there is no term interference, for example, the cross section in Eq. 1.7 is $\propto F_1 F_2$. In addition, the Sachs form factors are related to charge and magnetic current densities, as discussed below.

The Sachs electric G_E and magnetic G_M form factors depend on Q^2 . In the static limit, where $Q^2 \rightarrow 0$, the virtual photon probe is no longer able to resolve the nucleon's substructure. In this case, the virtual photon should only observe a point-like particle of charge q_N and magnetic moment μ_N of the nucleon.

$$\begin{aligned} G_E(Q^2 = 0) &= q_N, \\ G_M(Q^2 = 0) &= \mu_N. \end{aligned} \quad (1.12)$$

The magnetic moment for a point-like particle is given by [12]

$$\mu_N = g \left(\frac{q}{2M} \right) \frac{\hbar}{2}, \quad (1.13)$$

where g is the g -factor which is close to 2 and \hbar is the Planck constant h divided by 2π . The magnetic moment has been experimentally measured to be $\mu_p = 2.79$ for the proton [13] and $\mu_n = -1.91$ for the neutron [14].

$$\begin{aligned} G_E^p(Q^2 = 0) &= 1, & G_M^p(Q^2 = 0) &= \mu_p = 2.79 \\ G_E^n(Q^2 = 0) &= 0, & G_M^n(Q^2 = 0) &= \mu_n = -1.91. \end{aligned} \quad (1.14)$$

In early measurements, the nucleon form factors could be described, to first order, by a dipole form as

$$G_E^p = \frac{G_M^p}{\mu_p} = \frac{G_M^n}{\mu_n} = G_D, \quad (1.15)$$

where

$$G_D(Q^2) = \left(\frac{1}{1 + \frac{Q^2}{0.71(GeV/c)^2}} \right)^2. \quad (1.16)$$

The dipole model is successful in describing the experimental form factor data at low Q^2 . However, it cannot be used for the neutron electric form factor because at $Q^2 = 0$ the dipole model goes to 1 while the value of G_E^n should go to the charge of the neutron, which is zero. Therefore, the Galster parametrization [15] is usually used to describe the neutron electric form factor

$$G_E^n(Q^2) = -\frac{\mu_n \tau}{1 + 5.6\tau} G_D(Q^2). \quad (1.17)$$

1.2 Interpretation of Nucleon Form Factors

The physical meaning of the Sachs electric G_E and magnetic G_M form factor can be understood in the Breit frame, which is defined as the reference frame where energy transfer is zero. The virtual-photon four-momentum is given by $q = (0, \mathbf{q})$ and $Q^2 = |\mathbf{q}|^2$. In this frame, the four components of the nucleon current, $J^\mu(p', p) = (J^0, \mathbf{J})$, are related to the charge and magnetic moment distributions [16] by

$$\begin{aligned} J^0(p', p) &= -ie\bar{u}(p')G_E u(p), \\ \mathbf{J}(p', p) &= -ie\bar{u}(p') \left[\frac{i\boldsymbol{\sigma} \times \mathbf{q}}{2M} G_M \right] u(p), \end{aligned} \quad (1.18)$$

where $\boldsymbol{\sigma}$ are the Pauli matrices. The nucleon current operator is then given by

$$\hat{J}^\mu(\mathbf{q}^2) = \left(G_E(\mathbf{q}^2), \frac{i\boldsymbol{\sigma} \times \mathbf{q}}{2M} G_M(\mathbf{q}^2) \right). \quad (1.19)$$

Comparing equation 1.19 to the classical current density in \vec{r} space

$$\hat{J}_{cl}^\mu(\mathbf{r}) = (e\rho_{ch}(\mathbf{r}), \boldsymbol{\sigma} \times \nabla\rho_m(\mathbf{r})), \quad (1.20)$$

leads equation (1.19) to the interpretation of G_E and G_M in the Breit frame as Fourier transforms of charge and magnetization distributions given by

$$\begin{aligned} G_E(Q^2) &= \frac{4\pi}{Q} \int r dr \rho_{ch}(r) \sin Qr, \\ G_M(Q^2) &= \frac{4\pi}{Q} \int r dr \mu \rho_m(r) \sin Qr. \end{aligned} \quad (1.21)$$

Therefore, the nucleon charge and magnetization densities can be obtained from the inverse Fourier transformations of experimental data G_E and G_M in the limit of $Q^2 \rightarrow 0$.

At very low Q^2 , G_E and G_M can be related to RMS charge and magnetic radii of the nucleon by using a Taylor series expansion of Eq.(1.21) [2], given by

$$\begin{aligned} G_E(Q^2) &= \int 4\pi r^2 dr \rho_{ch}(r) - \frac{1}{6} Q^2 \int 4\pi r^2 dr r^2 \rho_{ch}(r) + \dots, \\ &= 1 - \frac{1}{6} Q^2 \langle r_E^2 \rangle + \dots, \end{aligned} \quad (1.22)$$

and

$$\begin{aligned} G_M(Q^2)/\mu &= \int 4\pi r^2 dr \rho_m(r) - \frac{1}{3!} Q^2 \int 4\pi r^2 dr r^2 \rho_m(r) + \dots, \\ &= 1 - \frac{1}{3!} Q^2 \langle r_M^2 \rangle + \dots, \end{aligned} \quad (1.23)$$

where μ denotes the nucleon magnetic moment. Hence, the RMS charge and magnetic radii of the nucleon are given as

$$\langle r_E^2 \rangle = -6 \left. \frac{dG_E}{dQ^2} \right|_{Q^2=0}, \quad \langle r_M^2 \rangle = -6 \frac{1}{\mu} \left. \frac{dG_M}{dQ^2} \right|_{Q^2=0}. \quad (1.24)$$

This interpretation of charge and magnetization densities is only valid in the non-relativistic regime. Kelly [17] studied the systematic behavior of the elastic electromagnetic form factors (EEFFs) with Q^2 using various prescriptions taking into account relativistic effects. He related G_E and G_M in equation (1.21) to the rest frame charge and magnetization densities of the nucleon in the Breit frame as

$$\tilde{\rho}_{ch}(k) = G_E(Q^2)(1 + \tau)^{\lambda_E}, \quad (1.25)$$

$$\mu\tilde{\rho}_m(k) = G_M(Q^2)(1 + \tau)^{\lambda_M}, \quad (1.26)$$

where the intrinsic form factors $\tilde{\rho}(k)$ are related to the densities by the Fourier transform:

$$\tilde{\rho}(k) = \frac{2}{\pi} \int_0^\infty dr r^2 j_0(kr) \rho(r), \quad (1.27)$$

and k is the intrinsic spatial frequency defined as

$$k^2 = \frac{Q^2}{1 + \tau}. \quad (1.28)$$

The λ_E and λ_M in Eqs. 1.25 and 1.26 are model-dependent constants. The nucleon form factors G_E and G_M in Eqs. 1.25 and 1.26 can be obtained by fitting the results of the nucleon form factor data available in 2004 [18] as shown in Fig. 1.2. The charge and magnetization densities for both the proton and the neutron are shown in Fig 1.3.

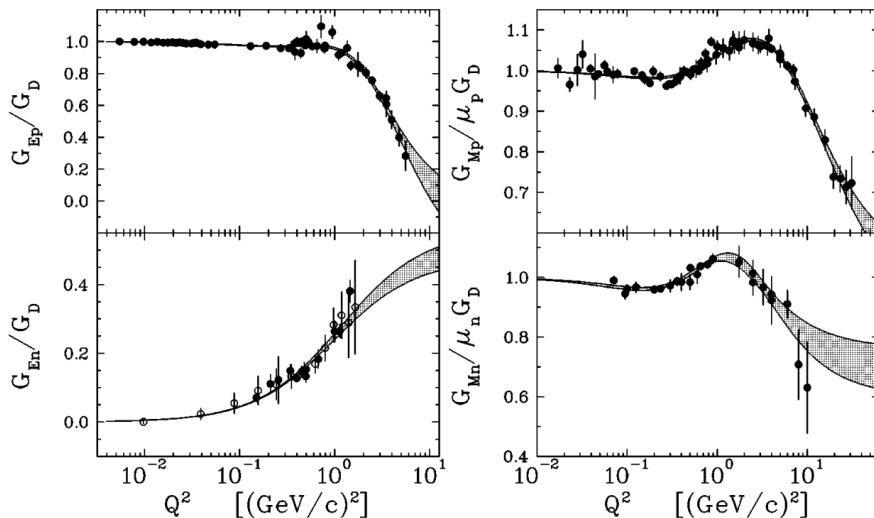


Figure 1.2: Kelly Fits to nucleon electromagnetic form factors [18].

The neutron's magnetization density ρ_m is very similar to that of the proton, despite the interior precision not being as good in the experimental data because of large uncertainties at high Q^2 . The neutron charge distribution has a positive core

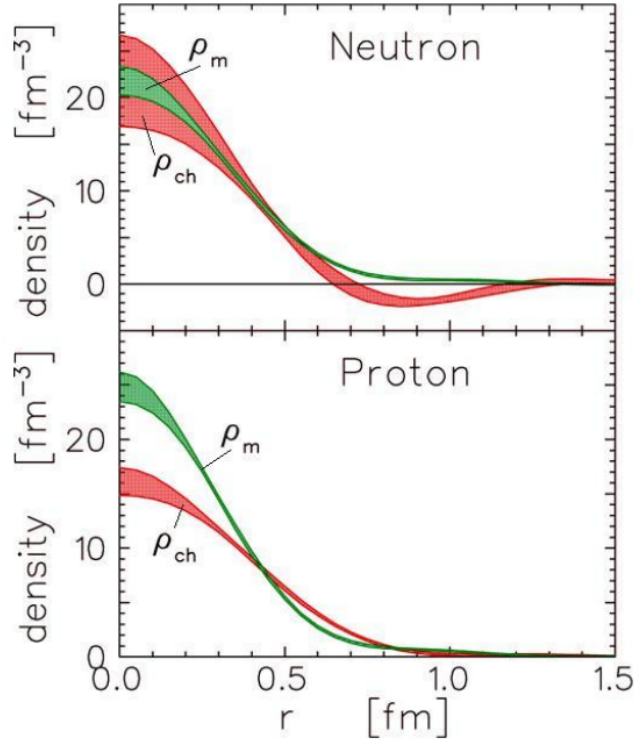


Figure 1.3: The charge and magnetization distributions of the proton and the neutron obtained from nucleon form factor data by Kelly [17].

with an extended negative tail, which can be interpreted as a neutron with a proton core dressed by a π^- cloud. The neutron charge density ρ_{ch} has an error band that is significantly broader due to the limitations in the range and quality of the G_E^n data that were available at the time.

In 2007, Gerald A. Miller [19] introduced a fresh perspective to elastic scattering experiments involving neutrons. His approach provided insight into the spatial distribution of charges within the neutron. Miller's re-evaluation of the data indicated the presence of a negative charge at the neutron's core, situated within its positive region. Meanwhile, inelastic experiments that measure quark momentum consistently indicated that highly energetic quarks, particularly negatively charged

down quarks, are more likely to be located closer to the center of the neutron [19]. Consequently, higher Q^2 data will enhance the precision of neutron densities and provide a deeper understanding of their distribution. The next section will show the available world data of G_M^n and describe methods of measuring G_M^n .

1.3 Motivation for Measurements of G_M^n

The nucleon form factor G_E and G_M are fundamentally important to understand the electric charge and magnetic moment within the neutron at low Q^2 and the behavior of quarks at high Q^2 . Measuring G_M^n at higher Q^2 with the other three form factors (G_E^p , G_M^p and G_E^n) allows extraction of the individual up and down quark contributions. The formula connecting nucleon form factors and the up and down quark contributions are [8]

$$F_{1(2)}^u = 2F_{1(2)}^p + F_{1(2)}^n \quad \text{and} \quad F_{1(2)}^d = 2F_{1(2)}^n + F_{1(2)}^p, \quad (1.29)$$

where $F_{1(2)}$ are the Dirac (Pauli) form factors and there are no contributions from heavier quarks. The result of this process is represented in Fig. 1.4 [8]. It shows the down quark appears to scale roughly as $1/Q^4$ above $Q^2 = 1.5 \text{ GeV}^2$, while the up quark appears to scale as $1/Q^2$. The interpretation of the very different behaviors can possibly be explained through diquark correlations. The current experiment when combined with the other form factors will allow the flavor decomposition at Q^2 up to 10 GeV^2 , where the behaviors of the individual quark contributions, as well as the calculations will be further tested [8].

In addition, the nucleon form factors including G_M^n play a crucial role in the understanding and interpretation of various other quantities. A few examples of this are:

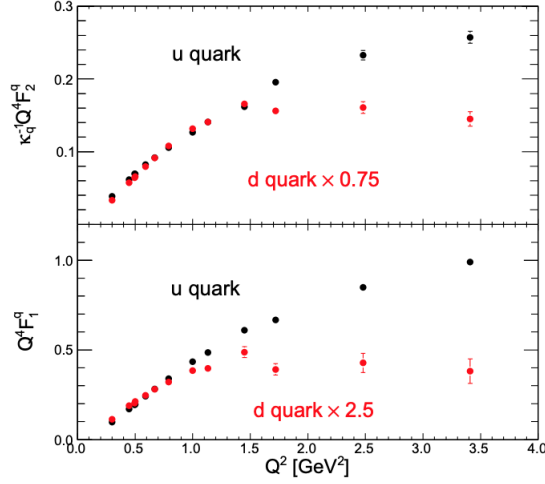


Figure 1.4: The flavor decomposition of proton form factors shows the behavior of the dependence u and d quarks contributions on Q^2 [8].

- Parity-violating electron scattering experiments designed to probe the strange content of the nucleon [20].
- Determining the charge and magnetization radii of nuclei and interpreting electron scattering experiments from nuclei [21].
- First moments of the Generalized Parton Distributions relating to Dirac and Pauli form factors [22].

1.4 Experimental Measurements of G_M^n

Several experiments were performed in order to measure the neutron form factor at different electron accelerators around the world. The data for the neutron form factors are less well known compared to proton form factors due to the lack of a free neutron target, since a free neutron will decay with a half-life of about 14.7 minutes via β^- decay, or $n \rightarrow p + e^- + \nu_e$. Therefore, most neutron experiments were done using deuterium targets, which contain both a proton and a neutron. In

this case, we use a bound neutron as a target so nuclear corrections must be applied to account for the nuclear structure of deuterium. There are two main methods to measure G_M^n ; unpolarized and polarized electron-nucleon scattering.

1.4.1 Polarized Measurements

There are two experiments that have extracted G_M^n using polarized targets, which were both done at low Q^2 . The first experiment was done by Gao *et al.* [23] at the MIT-Bates laboratory by measuring the transverse asymmetry $A_{T'}$ in ${}^3\text{He}(\vec{e}, e')$. Then G_M^n is extracted by fitting the data to theoretical calculations of ${}^3\text{He}$ structure. The experimental asymmetry can be written in terms of electric and magnetic form factors as

$$A_{exp} = P_b P_t \frac{\overbrace{-2\tau v_{T'} \cos \theta^* G_M^2(Q^2)}^{A_{T'}} + 2\sqrt{2\tau(1+\tau)} v_{TL'} \overbrace{\sin \theta^* \cos \phi^* G_E(Q^2) G_M(Q^2)}^{A_{TL'}}}{(1+\tau)v_L G_E^2 + 2\tau v_T G_M^2}, \quad (1.30)$$

where θ^* and ϕ^* are the polar and azimuthal angles of target spin with respect to the virtual photon momentum q , P_b and P_t are the beam and target polarizations, respectively, $v_L = \frac{Q^2}{|q|^4}$, $v_T = \frac{Q^2}{2|q|^2} + \tan^2(\theta/2)$, $v_{TL'} = \frac{1}{\sqrt{2}} \frac{Q^2}{|q|^2} \tan(\theta/2)$, and $v_{T'} = \tan(\theta/2) \sqrt{\frac{Q^2}{2|q|^2} + \tan^2(\theta/2)}$. The asymmetry corresponding to $\theta^* = 0^\circ$ is called the transverse asymmetry, $A_{T'}$, while the asymmetry corresponding to $\theta^* = 90^\circ$ is called the transverse-longitudinal asymmetry $A_{TL'}$. The transverse asymmetry $A_{T'}(G_M^n{}^2)$ can be written as a function of the neutron magnetic form factor $G_M^n{}^2$ as

$$A_{T'}(G_M^n{}^2) = \frac{1 + aG_M^n{}^2}{b + cG_M^n{}^2}, \quad (1.31)$$

where a , b and c are the fit parameters from the calculations of Salme *et al.* and Schulze *et al.* [23]. This experiment obtained G_M^n at $Q^2 = 0.19 \text{ GeV}^2$, see Fig. 1.5 the hollow star point. The large uncertainty on G_M^n is dominated by statistical

uncertainties, with a small contribution from nuclear-model uncertainties.

The second experiment that obtained G_M^n using this technique was done at Jefferson Lab [24, 25, 26] and is represented by the blue points in Fig. 1.5. In this experiment, G_M^n was extracted in the range $Q^2 = 0.1-0.6 \text{ GeV}^2$. The error bars shown in the figure represent both statistical and systematic uncertainties.

The polarized method provides valuable information on G_M^n at lower Q^2 values. However, in this analysis, the main focus is on measuring G_M^n at high Q^2 values in the range of approximately 5-12 GeV^2 , which is extracted using an unpolarized method.

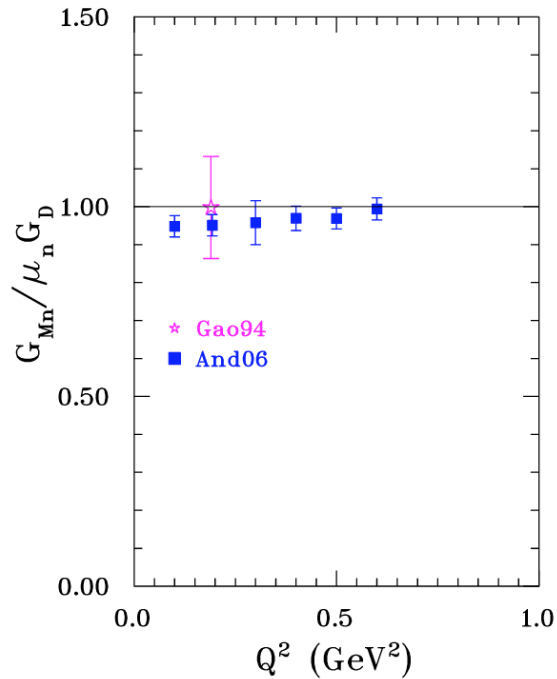


Figure 1.5: The measurements of G_M^n from polarized electron-deuteron experiments. Graph from Ref. [7].

1.4.2 Unpolarized Measurements

Most G_M^n measurements were extracted using an unpolarized electron beam incident on a deuterium target. Figure 1.6 shows the world data of the G_M^n measurements at different Q^2 values. Previous measurements of G_M^n were done by four methods:

- Inclusive quasielastic electron-deuterium scattering ${}^2\text{H}(e, e')$.
- Coincidence quasielastic electron-neutron cross-section ${}^2\text{H}(e, e'n)$ measurements.
- Anti-coincidence quasielastic electron-deuterium cross-section ${}^2\text{H}(e, e'\bar{p})$ measurements.
- The ratio of quasielastic electron-neutron to quasielastic electron-proton cross section ${}^2\text{H}(e, e'n)/{}^2\text{H}(e, e'p)$ measurements.

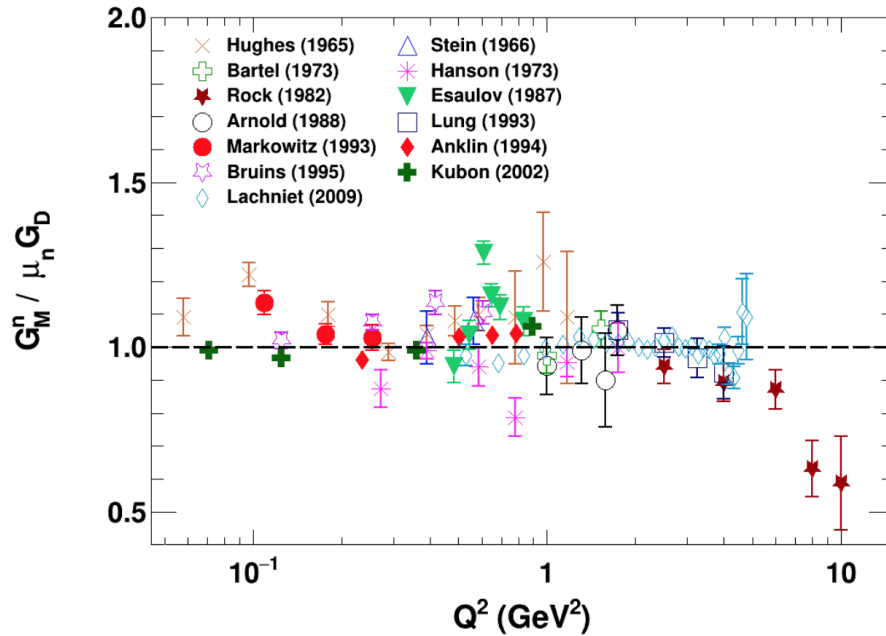


Figure 1.6: The world data on G_M^n from unpolarized electron-deuteron experiments. Graph from [27].

The first method requires subtraction of the proton contribution from the measured cross section and also a good knowledge of the deuterium model, which leads to

large systematic uncertainties. This method was done by Hughes *et al.* [28], Rock *et al.* [29], Esaulov *et al.* [30], Arnold *et al.* [31] and Lung *et al.* [32].

To avoid subtracting the proton contribution, Stein *et al.* [33], Bartel *et al.* [34] and Markowitz *et al.* [35] extracted G_M^n using coincidence ${}^2\text{H}(e, e'n)$ measurements, where the neutron is detected in this method. This method still requires a good knowledge of deuteron structure. In addition a precise measurement of the neutron detection efficiency is needed.

Due to the difficulties of detecting neutrons, Hanson *et al.* [36] measured G_M^n using an anti-coincidence ${}^2\text{H}(e, e'\bar{p})$ measurement, wherein one detects proton $D(e, e'p)$ and does not detect proton $D(e, e'\bar{p})$ which assumes to be equivalent to the detection of a neutron. Thus, it is possible to relate the experimental ratio $e\bar{p}/ep$ to the ratio of the elastic en/ep scattering cross sections. This method also requires good knowledge of the deuteron structure as well as accurate background subtraction to account for all the non-detected protons.

To minimize the uncertainties due to the nuclear effects in the deuterium model, the ratio method was used by Anklin *et al.* [37], Bruins *et al.* [38], Kubon *et al.* [39] and Lachniet *et al.* [40]. In this case, the protons and neutrons are detected in coincidence with scattered electrons from the deuterium target. This method only requires knowledge of neutron detection efficiency, which reduces the systematic uncertainties. There is still a nuclear model dependence as a function of Q^2 , but it is reduced in the ratio method especially at the higher Q^2 measured here.

The highest Q^2 measurement of G_M^n was primarily measured at SLAC by Rock *et al.* [29]. In this experiment, G_M^n was measured in the Q^2 range of 2.5 - 10 GeV² using the inclusive quasielastic electron-deuterium method. The results from this experiment are represented by the brown points in Fig. 1.7. Another SLAC experiment, performed by Lung *et al.* [32], used the same method to measure G_M^n in the

Q^2 range of 1.75 - 4 GeV², which is represented by the filled black triangles in the figure. The uncertainty in the G_M^n results from both the Rock and Lung experiments includes both statistical and systematic effects. The uncertainties associated with these measurements are large as shown in Fig. 1.7. This is mainly due to the proton subtraction and the deuteron model dependence.

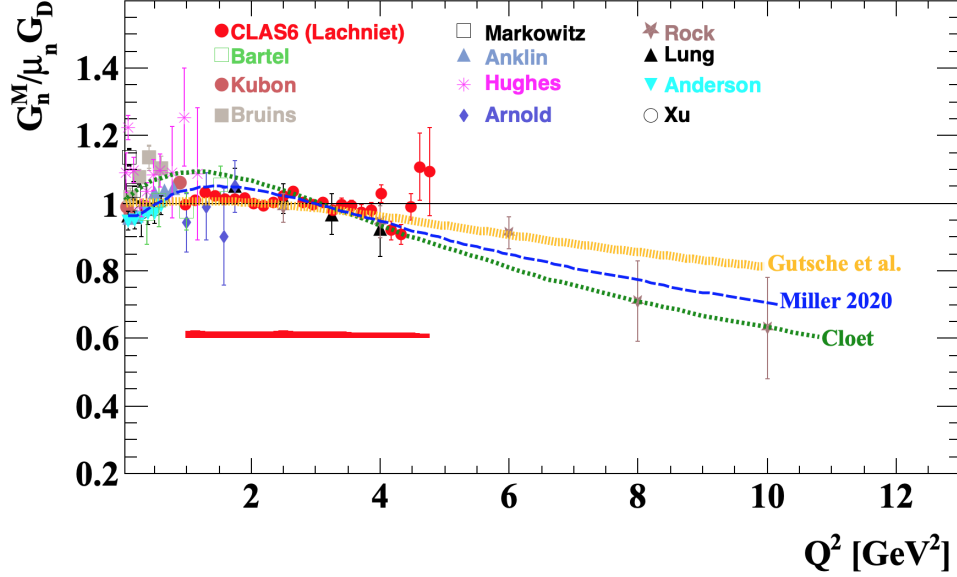


Figure 1.7: The world data on G_M^n from polarized and unpolarized electron-deuteron experiments at high Q^2 values. The red band shows the systematic uncertainty for the CLAS6 data. The theory curves are the Miller model (blue) [41], the Gutsche model (yellow) [42], and the Cloet model (green) [43].

The latest unpolarized measurements of G_M^n were done by Lachniet *et al.* [40] at JLab in Hall B using the CLAS detector. The CLAS result of G_M^n at $Q^2 = 1 - 4.8$ GeV² is shown as red points. The uncertainty in the G_M^n measurements represents the statistical error, while the red band illustrates the systematic uncertainty associated with the experiment. A unique feature of this experiment was a dual-cell target containing deuterium and hydrogen targets. This allowed measurement of the neutron detection efficiency by the $H(e, e'\pi^+)n$ reaction simultaneously with the cross-section measurements. The G_M^n results of CLAS data show a flat behavior

up to Q^2 around 4.8 GeV², while the SLAC data shows that G_M^n falls off at high Q^2 with large uncertainties. Measuring G_M^n at high Q^2 will extend our knowledge into the region where limited measurements currently exist. The next subsection will explain the ratio method that we used to extract G_M^n in this analysis.

Ratio Method

To extract G_M^n we use a method of measuring the ratio of quasi-elastic ${}^2\text{H}(e, e'n)$ to ${}^2\text{H}(e, e'p)$ cross sections in the deuteron target in the range $Q^2 = 5\text{-}12$ GeV². This ratio is proportional to the ratio of the free nucleon $e - n$ to $e - p$ cross section in Eq. 1.11 and is given by

$$R = \frac{\frac{d\sigma}{d\Omega} [{}^2\text{H}(e, e'n)_{QE}]}{\frac{d\sigma}{d\Omega} [{}^2\text{H}(e, e'p)_{QE}]} = a(Q^2)R_{free} = a(Q^2) \frac{\frac{(G_E^n)^2 + \tau(G_M^n)^2}{1+\tau} + 2\tau(G_M^n)^2 \tan^2(\frac{\theta}{2})}{\frac{(G_E^p)^2 + \tau(G_M^p)^2}{1+\tau} + 2\tau(G_M^p)^2 \tan^2(\frac{\theta}{2})}, \quad (1.32)$$

where $a(Q^2)$ is a nuclear correction to deviations from the free ratio and can be calculated by using standard models for the deuteron [40]. On the right side, the denominator contains electric, G_E^p , and magnetic, G_M^p , form factors for the proton; these quantities are well known from other measurements. The numerator contains the desired G_M^n value and the neutron electric G_E^n form factor, which is small over the range of this Q^2 measurement. Several parameterizations of G_E^n will be used to estimate the associated uncertainty. Therefore, the only unknown in Eq 1.32 is G_M^n and can be extracted. The advantage of using the ratio method is it reduces several systematic uncertainties that come from Fermi motion corrections, radiative corrections [5], and running conditions, which will be discussed in more detail in Chapter 4.

1.5 Theoretical predictions of G_M^n

Along with experimental attempts to measure the nucleon form factors, theorists have been developing nucleon models over the years to predict the elastic electromagnetic form factors. A good nucleon model should be able to describe and predict the electromagnetic form factors for both protons and neutrons. The following section describes some theoretical techniques.

1.5.1 Vector Meson Dominance Models

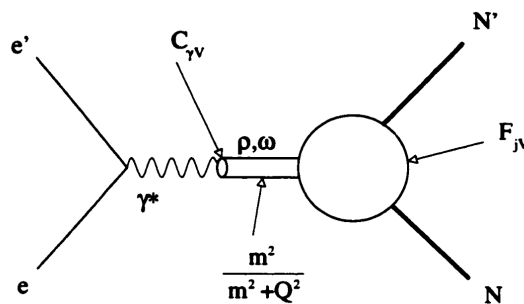


Figure 1.8: Photon-nucleon coupling in the VMD models.

The vector meson dominance model attempts to describe the interaction between hadrons and the virtual photon. In a series of papers investigating Vector Meson Dominance, Sakurai explored the nucleon form factors in the early 1960s [44]. In this model, the virtual photon is coupled to the nucleon through the exchange of vector mesons ρ , ω , and ϕ as shown in Fig 1.8. Hence, the Pauli and Dirac form factors in both isoscalar and isovector electromagnetic currents, $F_{1,2}^{is,iv}$, can be written as

$$F_j^{is,iv}(Q^2) = \sum_i \frac{m_i^2 C_{\gamma V_i}}{m_i^2 + Q^2} F_{jV_i}(Q^2), \quad (1.33)$$

where $C_{\gamma V}$ is a photon-meson coupling strength that can be determined experimentally or left as free parameters in a fit to the nucleon form factors, F_{jV} are

meson-nucleon vertex form factors and the sum is taken over the different vector mesons i of mass m_i . The meson-nucleon vertex form factor, F_{jV} , requires a functional form. For instance, the early literature frequently employs the monopole and dipole forms, or $F_{jV} = \left(1 + \frac{Q^2}{\Lambda^2}\right)^{-n}$ where $n = 1$ or 2 , respectively. The relations between the isoscalar and isovector electromagnetic currents and the electric and magnetic form factors are

$$G_E = \frac{1}{2}(F_1^{is} \pm F_1^{iv}) - \tau \frac{1}{2}(F_2^{is} \pm F_2^{iv}) \quad (1.34)$$

$$G_M = \frac{1}{2}(F_1^{is} \pm F_1^{iv}) + \frac{1}{2}(F_2^{is} \pm F_2^{iv}), \quad (1.35)$$

where the $+$ ($-$) sign is for the proton (neutron) form factor. The formulation in Eq. 1.33 neglects the widths of the vector mesons. Since earlier work ignored the width of the ρ -meson, Iachello, Jackson, and Lande (IJL) [45] in 1973 introduced a finite width for the ρ -meson by making the replacement in Eq. (1.33)

$$\frac{m_\rho^2}{m_\rho^2 + Q^2} \rightarrow \frac{m_\rho^2 + 6\Gamma_\rho m_\pi/\pi}{(m_\rho^2 + Q^2) + (4m_\pi^2 + Q^2)\Gamma_\rho\alpha(Q^2)/m_\pi}, \quad (1.36)$$

where $\Gamma_\rho = 112$ MeV and $\alpha(Q^2)$ is

$$\alpha(Q^2) = \frac{2}{\pi} \left[\frac{Q^2 + 4m_\pi^2}{Q^2} \right]^{1/2} \ln \left[\frac{(Q^2 + 4m_\pi^2)^{1/2} + (Q^2)^{1/2}}{2m_\pi} \right]. \quad (1.37)$$

The width of the ω and ϕ mesons were not included because they were much narrower compared to ρ . In 1985, Gari and Krümpelmann (GK) [46] extended this model for high Q^2 predictions to include perturbative QCD (pQCD). More recent work by Lomon in 2001 and 2002 [47, 48] where he extended the GK model by using 11 free fit parameters and included the $\rho'(1450)$, and the $\omega'(1419)$. He obtained reasonable fits to all four nucleon form factors. Lomon's fit was updated [49] when the G_E^n/G_M^n at $Q^2 = 3.4$ GeV² data set [50] from Hall A at Jefferson Lab became available. Figure 1.9 shows the recent fit from Lomon's extended GK for $G_M^n/\mu_n G_D$. Note, Lomon's fit didn't include the CLAS6 data (Lachniet).

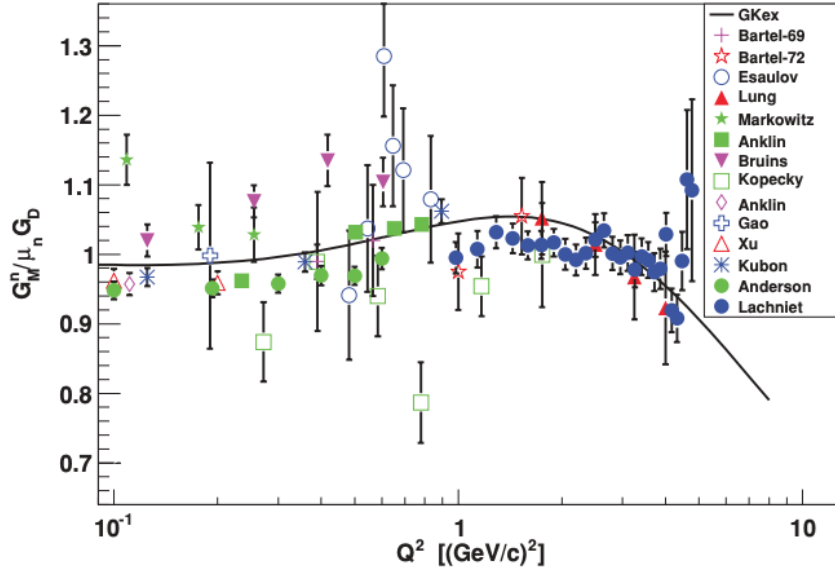


Figure 1.9: The fit of the extended GK model by Lomon’s work for the neutron magnetic form factor G_M^n scaled by $\mu_n G_D$ [49]. Graph from [51]

1.5.2 Constituent Quark Models

The constituent quark model (CQM) is a theoretical framework that describes the nucleon (proton and neutron) as composed of three valence constituent quarks. The early, nonrelativistic version of the CQM had significant success in defining the spectrum of baryons. In 2002, Gerald Miller [52] used the framework of describing the behavior of particles in relativistic quantum mechanics. He used the light-front dynamics to calculate the matrix elements of the electromagnetic current operator for nucleons, which describe the way in which nucleons interact with electromagnetic fields. Light-front dynamics is a particular approach to solving relativistic quantum field theories, where one chooses a specific reference frame known as the light-front frame. In this frame, the time variable is replaced by the light-front time, which is the time coordinate along the direction of the total momentum of the system. This choice of frame simplifies the equations of motion and allows for a more systematic

treatment of relativistic effects. By using light-front dynamics, Miller modeled the nucleon as the three bound constituent quarks surrounded by a cloud of pions. The pionic cloud is important to understand the behavior at low Q^2 , especially for the neutron electric form factor G_E^n . In a later study by Zhang, Hobbs and Miller [41] in 2020, they used a light-front quark model with a pion cloud to calculate the nucleon’s electromagnetic form factors. In this model, the nucleon is described as a composite particle made up of quarks and a diquark. The model includes the “pion cloud”, which represents the influence of pions in the nucleon’s structure. Pions are associated with the strong force and play a significant role in nuclear interactions. The result obtained from Zhang, Hobbs and Miller’s light front model for the neutron magnetic form factor, G_M^n , is shown in Fig. 1.7 (blue curve).

In addition, Gross *et al.* [53, 54] modeled the nucleon as a system of three valence constituent quarks using the covariant spectator formalism. The covariant spectator formalism is a theoretical framework for describing the structure of hadrons using quantum field theory. In this formalism, the hadron is represented as a composite system of constituent quarks, which interact via the exchange of virtual particles (gluons). The spectator formalism takes into account the fact that the quarks inside the hadron are not isolated, but are surrounded by a cloud of virtual particles, which affect their properties. By including the effects of this cloud of virtual particles in their model, Gross was able to obtain a better description of the structure of the nucleon. The results of their calculations were found to be in good agreement with the experimental measurements of the neutron magnetic form factor as shown in Fig. 1.10 (green curve).

Lastly, De Sanctis *et al.* [55] calculated the elastic electromagnetic form factors of the nucleon using a relativistic version of the hypercentral Constituent Quark Model (hCQM). Hypercentral refers to the specific form of the interaction potential

used to describe the interactions between constituent quarks within hadrons. The hCQM is an extension of the CQM, which incorporates a hypercentral potential, describing the interactions between the constituent quarks. The nucleon FFs were well fit by linear combinations of component quark FFs with monopole and dipole properties. Furthermore, Santopinto *et al.* [56] extended the calculations to higher values of Q^2 . The predictions of Santopinto for the neutron magnetic form factor is shown in Fig. 1.10 (black curve).

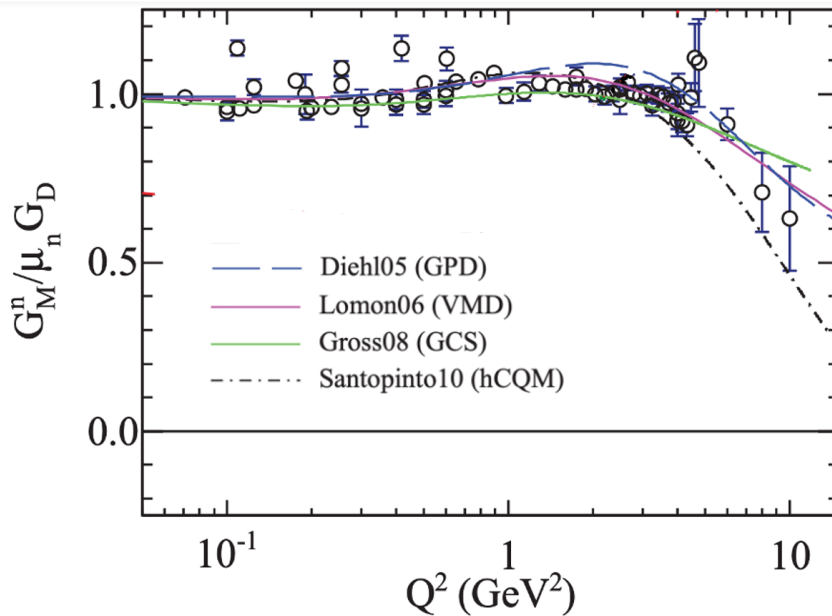


Figure 1.10: Comparison of theoretical predictions to G_M^n data. Theory curves are (Diehl05) [22], (Lomon06) [49], (Gross08) [54], and (Santopinto) [56]. Graph from [57] and G_M^n data are from Refs. [8, 26, 40]

1.5.3 Dyson-Schwinger Equations

One of the challenges in understanding hadrons is that quarks and gluons are confined within them, meaning they cannot be directly observed as free particles. Additionally, the effects of confinement and another phenomenon called dynamical chiral

symmetry breaking (DCSB) have a profound impact on the behavior of quarks and gluons within hadrons. Confinement refers to the fact that quarks and gluons are never found in isolation but are always bound together in hadrons. DCSB involves the generation of mass from interactions, leading to the majority of a nucleon’s mass being generated through these strong forces rather than from the masses of the individual quarks themselves [58]. To study these complex phenomena, Dyson–Schwinger equations (DSEs) are used. DSEs are the quantum-mechanical equations of motion that describe the interactions between particles within a quantum field theory, and they have been used successfully to study confinement, DCSB, and their effects on hadron properties.

Dyson-Schwinger equations have been applied to calculate the nucleon electromagnetic form factors. Cloët *et al.* [59] used the Dyson-Schwinger equations to calculate the electromagnetic form factors of the nucleon. The calculation was performed in the framework of a covariant and confining Nambu–Jona-Lasinio (NJL) model [43]. The NJL model describes the interactions among quarks using an effective four-fermion interaction term, and it has been used to study various properties of hadrons, including nucleons. The model takes into account both relativistic effects and the confinement of quarks and gluons. The result obtained from Cloët *et al.* [59, 43] for the neutron magnetic form factor G_M^n , is shown in Fig. 1.7 (green curve).

1.5.4 Generalized Parton Distributions (GPD)

Generalized Parton Distributions (GPD) describe the distribution of partons, such as quarks and gluons, within a hadron [60, 61]. GPDs provide us a 3D image of the quark and gluon structure of the nucleon. The Ji Sum Rule provides an important

key to understanding the origin of the spin of the nucleon, which relates the total angular momentum of the quarks to sums over some of the GPDs [60]. Knowledge of the nucleon elastic form factors is essential for the experimental determination of GPDs because their first moments are related to the elastic form factors through model-independent sum rules:

$$\int_{-1}^{+1} dx H_v^q(x, \xi, Q^2) = F_1^q(Q^2) \qquad \int_{-1}^{+1} dx E_v^q(x, \xi, Q^2) = F_2^q(Q^2), \quad (1.38)$$

where

$$H_v^q(x, \xi, Q^2) = H^q(x, 0, Q^2) + H^q(-x, 0, Q^2) \quad (1.39)$$

$$E_v^q(x, \xi, Q^2) = E^q(x, 0, Q^2) + E^q(-x, 0, Q^2) \quad (1.40)$$

where q is the quark flavor, x is the momentum fraction, ξ is the skewedness or asymmetry between the quark momenta and H^q and E^q are the flavor-dependent generalized parton distributions. Equations 1.39 and 1.40 are defined with $\xi = 0$ and include contributions from quarks as well as antiquarks. In the limit of $Q^2 \rightarrow 0$, $H_v^u(x, Q^2 = 0) = u_v(x)$ and $H_v^d(x, Q^2 = 0) = d_v(x)$, which are the valence quark densities of the proton. The v subscript refers to the ‘‘valence GPDs’’. The nucleon form factors can be constructed if the quark form factors are known using the calculations of Ref. [22]. Their results for both proton and neutron form factors are in good agreement with the available experimental data. The result of the GPD model of Ref [22] is compared to the G_M^n data shown in Fig 1.10 (blue curve).

1.5.5 Chiral Perturbation Theory

Chiral Perturbation Theory (ChPT) is a theoretical framework that provides a systematic way to describe the low-energy interactions of hadrons in terms of their underlying symmetries [62]. Faessler *et al.* [63] used a manifestly Lorentz covariant

chiral quark model to study baryons as composed of constituent quarks surrounded by a cloud of pseudoscalar mesons. This approach is based on a nonlinear chirally symmetric Lagrangian that involves two key components: constituent quarks and chiral fields representing pseudoscalar mesons. This Lagrangian plays a pivotal role in calculating dressed transition operators with proper chiral expansion, which describe how quarks interact with external fields in the presence of a virtual meson cloud. These dressed operators are then used to compute the momentum dependence of the nucleon's electromagnetic form factors. This approach allows insight into the structure and behavior of baryons by considering the interplay between constituent quarks and the surrounding pseudoscalar meson cloud within a consistent and covariant framework. Figure 1.11 shows a good agreement of the calculated neutron magnetic form factor G_M^n with the experimental data at high Q^2 before including CLAS6 data.

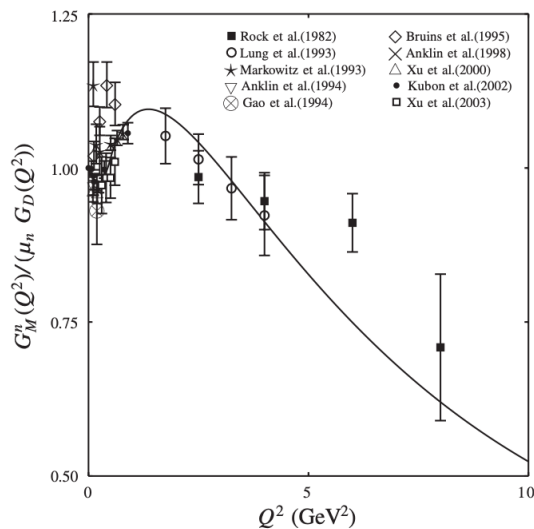


Figure 1.11: The result of predictions of the Faessler's model for the neutron magnetic form factor G_M^n scaled by $\mu_n G_D$ [63]

1.5.6 AdS/QCD Correspondence

An interesting way to calculate form factors is to use a holographic QCD or AdS/QCD correspondence, which describes the strong nuclear force QCD in terms of the anti-de Sitter/conformal field theory correspondence (AdS/CFT). AdS/CFT is a mapping between two physical theories: gravity in a negatively curved space called anti-de Sitter space (AdS) and a quantum field theory without gravity defined on the boundary of that space [64]. Gutsche *et al.* [65] have conducted a thorough analysis of the electromagnetic form factors of nucleons using a holographic soft-wall model. This method is based on an action that describes hadrons by accounting for broken conformal invariance and confinement through a background dilaton field. For cases where the number of colors (N_c) is equal to 3, they represent the nucleon's structure as a combination of a three-valence quark state and high Fock states that contain an adjustable number of partons (quarks, antiquarks, and gluons). This is accomplished by studying the behavior of 5D fermion fields with different scaling dimensions in anti-de Sitter space. The principle of gauge/gravity duality guides, indicating that these 5D fermion fields with distinct scaling dimensions correspond to specific Fock state components possessing a particular number of partons. In this study, they focus on the contribution of Fock state components containing 3 (which contains three valence quarks), 4 (which contains three valence quarks plus a gluon field), and 5 (which contains three valence quarks plus a $q\bar{q}$ pair of sea quarks or three valence quarks plus 2 gluons) partons within the nucleon's structure. Using a minimal set of independent parameters (including the dilaton scale parameter, mixing parameters for partial contributions from Fock states, and coupling constants in the effective Lagrangian), they achieved a level of agreement with experimental data that is not very reasonable as shown in the left of Fig. 1.12 for the neutron magnetic form factor.

In a later study by Gutsche *et al.* in 2018 [42], the soft-wall AdS/QCD action was expanded with new non-minimal terms. These terms play a critical role in influencing the momentum behavior of form factors and helicity amplitudes, which are important characteristics of the nucleon. This extended version of the soft-wall AdS/QCD model significantly improves its ability to describe the nucleon's form factors, as shown in the right-hand panel of Fig. 1.12. Also the Gutsche model is shown in Fig. 1.7 for G_M^n .

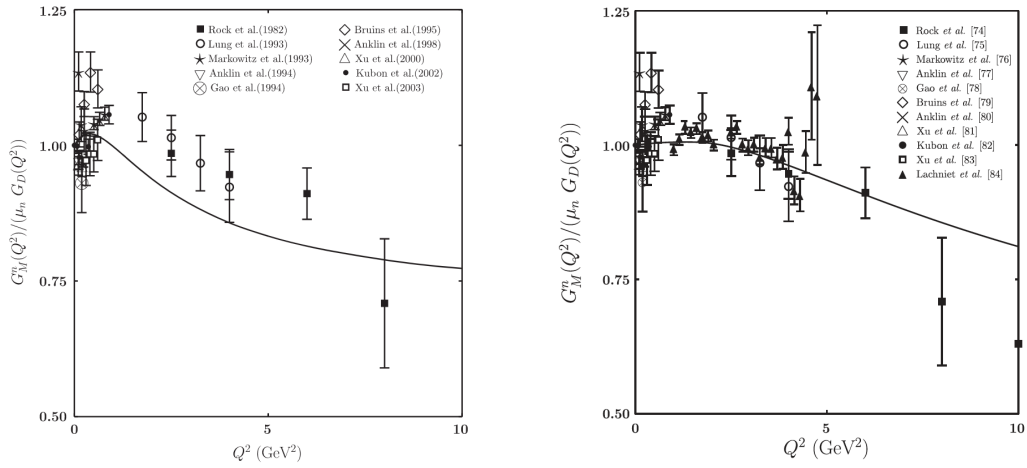


Figure 1.12: The prediction of soft-wall AdS/QCD model for the neutron magnetic form factor G_M^n . Left: With minimal number of parameters [65]. Right: Extended Gutsche's works [42]

CHAPTER 2

EXPERIMENTAL SETUP

The G_M^n experiment described in this dissertation was performed at the Thomas Jefferson National Accelerator Facility in Newport News, VA. In this chapter, the experimental setup is described. An overview of the laboratory, a detailed description of the CLAS12 detector and associated software is provided.



Figure 2.1: The Jefferson Lab CEBAF accelerator site and four experimental halls [66]. The electrons are emitted from the injector that is marked by the number (1) and accelerated through the two LINACs that are marked by the number (2), connected at each end with recirculating magnets represented by number (4). The electron beam is sent to four different experimental halls A, B, C and D that are marked by the numbers 5, 6, 7, and 8, respectively.

2.1 The Continuous Electron Beam Accelerator Facility (CEBAF)

The Thomas Jefferson National Accelerator Facility relies on the Continuous Electron Beam Accelerator Facility (CEBAF). It is designed in the form of a race track, which consists of two parallel linear accelerators (linacs), known as north and south linacs and dipole magnets at the ends to bend the beam around the arcs. The north and south linacs are represented by number 2 and the magnets are represented by number 4 in the Fig 2.1, respectively. Jefferson Lab houses four experimental halls, namely Halls A, B, C, and D, each of which receives a high-quality, high-luminosity, and polarized electron beam with an energy of up to 12-GeV in Hall D. These halls are represented by numbers 5, 6, 7, and 8 in the Fig 2.1, respectively. The electron beam is generated and accelerated and injected in the north linac (the injector of the beam shows by number 1 in Fig 2.1), then bent in a 180° arc and injected into the south linac. This acceleration process is done four and a half times more to achieve the final energy for Hall D and up to four times to get the desired delivery energies for Halls A, B, and C.

2.2 Hall B Beamline

The Hall B beamline allows the electron beam from CEBAF to be delivered safely and effectively to the physics target in the experimental hall. Over all, the beamline allows experimenters to monitor the beam quality in real time and allows operators to change the beam's characteristics as necessary. The Hall B beamline is divided into two segments: the “2C” line following beam extraction from the CEBAF accelerator to Hall B and the “2H” line inside the experimental hall. Accelerator

operators have access to several quadrupoles and corrector dipoles upstream of the CLAS12 detector that are used to keep the beam size within required tolerances and centered on the target as shown in Fig. 2.2. Hall B personnel control several beam position, polarization, current, and halo monitors [67].

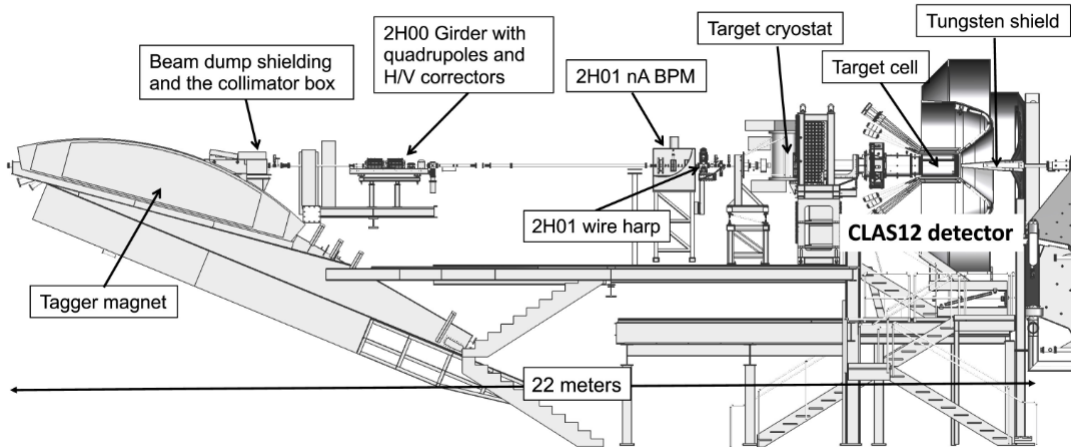


Figure 2.2: Hall B beamline upstream of the CLAS12 detector showing the tagger magnet yoke (in the left) that is energized during beam tuning and during polarization measurements, quadrupoles and corrector that are used to deliver beam to the target, beam position monitors (BPM) that consist of Radio Frequencies (RF) cavities to provide both the beam position in the $x - y$ plane and the relative beam intensity and wire harps that are used to measure the electron beam profile and position [67].

2.3 CEBAF Large Acceptance Spectrometer (CLAS12)

CLAS12 is a large acceptance spectrometer consisting of three major parts, a Forward Detector (FD) that detects particles within a polar angle from $5^\circ - 35^\circ$ a central detector (CD) that detects particles greater than 35° , see Fig. 2.3, and a Forward Tagger (FT) that detects particles within a polar angle from $2.5^\circ - 4.5^\circ$. The FD is based on the torus magnet, which provides the magnetic field used to

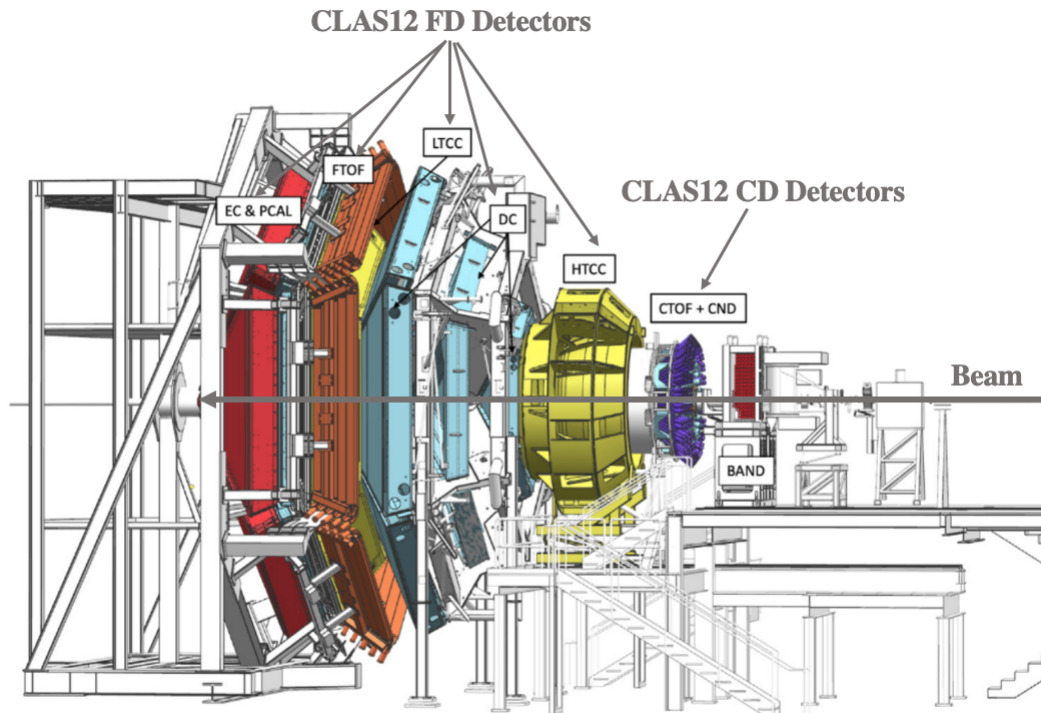


Figure 2.3: The CLAS12 spectrometer in Hall B at JLab. The electron beam is incident from the right side of this figure. The CLAS12 Forward (FD) and Central (CD) Detectors are identified [68].

determine the particle momentum and charge. Drift chambers (DC) are used to measure the track of the charged particles. A precise flight time of the traveling particles is measured in the forward time of flight (FTOF). The High and Low Threshold Cherenkov Counters (HTCC, LTCC) are used to differentiate between particle types. The HTCC is used to distinguish between electrons and pions at high momentum while the LTCC is used to distinguish between pions and kaons in the $3.5 - 9$ range GeV/c . The last parts of the FD are the preshower calorimeter (PCAL) and electromagnetic calorimeter (EC). They are used to stop the highest energy electrons and to identify electrons, photons, and neutrons. The second part

of the CLAS12 detector is the Central Detector (CD), which is comprised of Central Vertex Tracking (CVT) system [69], Central Time-Of-Flight system (CTOF) [70], Central Neutron Detector (CND) [71], and the solenoid magnet located inside the central detector that surrounds the target area and consists of five NbTi coils, producing a magnetic field of up to 5 T [72]. The last part of the CLAS12 detector, is the Forward Tagger (FT) located between the High Threshold Cerenkov Counter and the torus support that is located between the three regions of DCs. The FT is comprised of an electromagnetic calorimeter (FT-Cal), a tracker (FT-Trck), to measure the scattering angles $\theta_{e'}$ and $\phi_{e'}$, and a hodoscope (FT-Hodo) to provide e/γ separation. More details of FT can be found in [73].

In this analysis, the G_M^n measurement only used the CLAS12 forward detector. The following sections will describe each subsystem of the CLAS12 FD in more details.

2.3.1 Target

The G_M^n measurement used two types of cryogenic targets, liquid hydrogen (LH2) and liquid deuterium (LD2). The LH2 target is used to measure the neutron and proton detection efficiencies, while the LD2 target is used to measure the ratio of quasi-elastic $D(e, e'n)$ and $D(e, e'p)$ to extract G_M^n . The cryogenic target of CLAS12 is located within the Solenoid magnet. The target is a 50-mm long Kapton cone with a 23.66 mm upstream diameter and 15.08 mm downstream diameter. Figure 2.4 illustrates the design of the target cell located within the scattering chamber. The scattering chamber itself is constructed using Rohacell XT110 foam (density $\rho = 0.110 \text{ g/cm}^3$). The electron beam passes through entrance and exits windows at each end of the target that are made of 30- μm -thick aluminum [67]. The run groups

of the CLAS12 experimental program share many features, including the magnetic field setting, beam current, and the target. The first group that used the liquid hydrogen target was known as Run Group A (RG-A) while the second group used the liquid deuterium target known as Run Group B (RG-B).

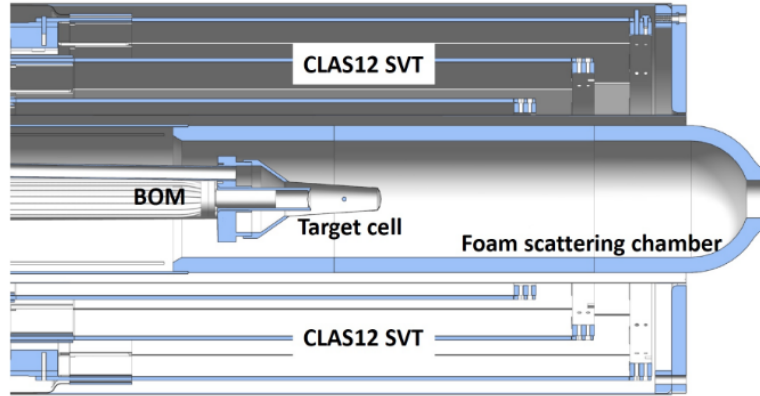


Figure 2.4: The design rendering of the target cell located within the scattering chamber [67].

2.3.2 Torus Magnets

The CLAS12 Torus magnet consists of six symmetrical trapezoidal super conducting coils located between each drift chamber (see Fig. 2.5). The purpose of the torus magnets is to provide a magnetic field to bend the charged particles toward or away from the beamline depending on the sign of the charge. The curvature of the tracks allows for a reconstruction of particle momenta. This magnetic field is oriented around the beam axis in the azimuthal direction. The six coils provide close to the same magnetic field in all the six sectors. The coils operate at a nominal current of 3770 A, producing a peak field of 3.6 T. At this current, the resulting integrated magnetic field $\int Bdl$ is 2.78 Tm at 5° and 0.54 Tm at 40° . The torus magnet can be operated with either field polarity, resulting in an “in-bending” configuration where

electrons are bent towards the beamline, or an “out-bending” configuration where electrons are bent away from the beamline. The acceptance for electrons differs significantly between in-bending and out-bending configurations. More detail can be found in Ref. [72].

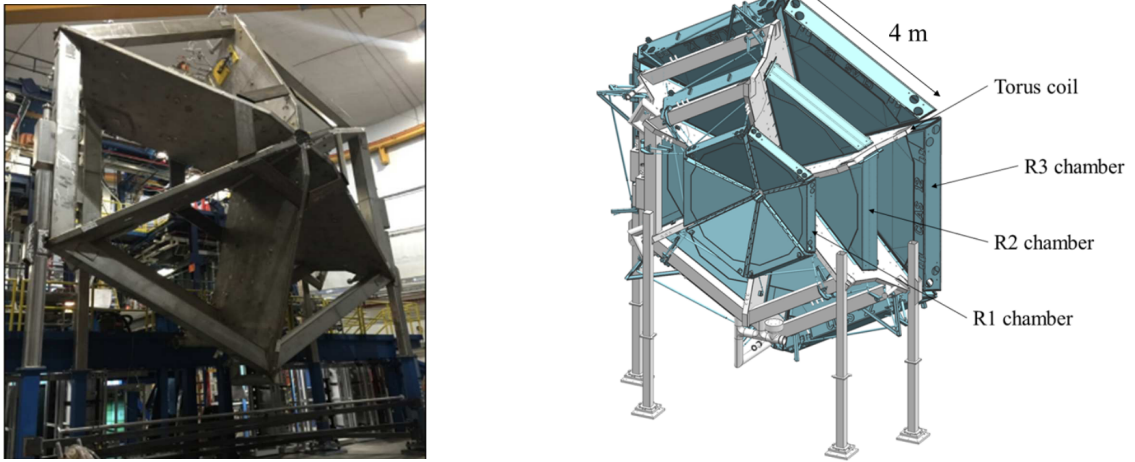


Figure 2.5: Left: The torus magnet in Hall B before the installation of drift chambers between the coils [72]. Right: The torus magnet between the drift chamber regions [74].

2.3.3 Drift Chambers

The drift chambers (DC) of CLAS12 are used to provide scattering angle and momentum reconstruction for charged particles by measuring their trajectory. The DC system is designed with 18 drift chambers arranged in three regions: Region 1 is located between the target and the torus; Region 2 is located within the magnetic field of the torus; Region 3 is located outside the torus magnet and before the TOF. Each region is divided into six sectors, as shown in Fig. 2.5. For each region, there are two superlayers with each containing six layer of sense wires. The wires within the superlayers are strung in stereo angles of $\pm 6^\circ$ relative to each other to

provide the azimuthal angle information of a track. Each sense wire is surrounded by two layers of field wires, forming a hexagonal cell as shown in Fig. 2.6.

The drift chambers are filled with mixture of a 90% of Argon and 10% of CO₂. When a charged particle passes through the drift chambers, it ionizes the atoms in the surrounding gas. Electrons and ions produced during the ionization process drift toward the cathode (field) and anode (sense) wires, respectively. As the electrons move closer to the sense wires, they experience a higher electric field and gain energy, which can lead to further ionization and electron multiplication. This creates a cascade of electrons that generates a detectable signal on the sense wires. The time it takes for ions created by the particle to drift to the sense wire is known as the drift time. The detected electric signals provide information about the particle's drift time which can be associated with the charged particles passing through the drift chambers. Then the track of the charge particles can be reconstructed by using information of the hit positions [74].

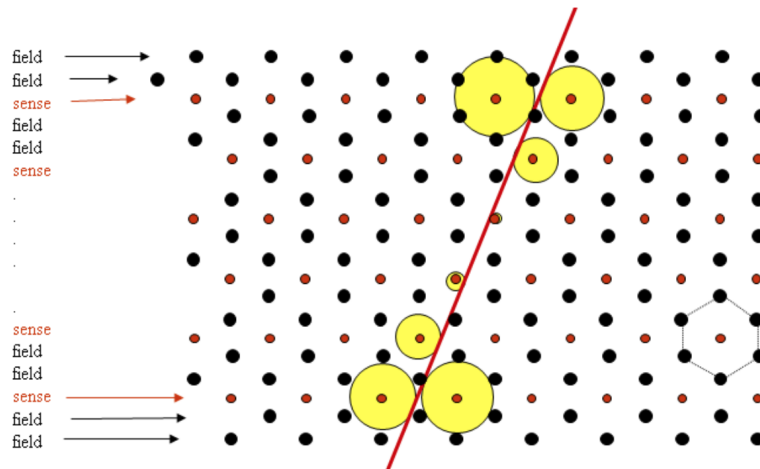


Figure 2.6: The wire layout of one superlayer of the CLAS12 drift chambers. A hexagonal cell is formed by surrounding the sense wire with two layers of field wires. The path of a charged particle detected in the chamber is represented by the red line. The drift distance (calculated from the drift time) between the track to the nearest signal wire (shown by yellow circles) constrains the track fit to reach the required momentum resolution of $\Delta p/p = 1\%$ [74].

2.3.4 Cherenkov Counters

CLAS12 uses three different Cherenkov counters, a high threshold Cherenkov counter (HTCC), a low threshold Cherenkov counter (LTCC), and a Ring Imaging Cherenkov detector (RICH), to provide particle identification for different ranges of momenta and particle species. The CLAS12 Cherenkov detectors are gas filled. When a charged particle passes through the gas with a velocity faster than the speed of light, it emits Cherenkov radiation in the form of a cone of light. The angle and intensity of the cone of light depend on the velocity and charge of the particle, allowing the Cherenkov counters to distinguish between different types of charged particles. It is only possible to emit light if the momentum of the particle is greater than a threshold momentum p_{th} , which is related to the speed of light in the medium given by

$$p_{th} = \frac{mc}{\sqrt{n^2 - 1}}, \quad (2.1)$$

where n is the refraction index of the gas and m is the mass of the particle. The Cherenkov light is collected by mirrors around the gas volume that focus the light on photomultiplier tubes (PMTs) for signal multiplication and readout.

The HTCC is located in front of the first region of drift chambers and filled with CO₂ gas to separate electrons from hadrons (pions, kaons, and protons) up to a momentum of 4 GeV/ c . The HTCC also provides a fast trigger signal for electron detection in the FD. The HTCC detector is shown in Fig. 2.7. More details can be found in reference [75].

The LTCC is designed to provide pion/kaon discrimination in the 4-8 GeV momentum range. It covers two sectors of the CLAS12 detector and is constructed from refurbished Cherenkov counters that were used in the previous CLAS6 detector. The LTCC uses a C₄F₁₀ radiator gas, with a lower refractive index than the

CO₂ gas used in the HTCC [76].

The RICH detector is located in sector four of the FD and is used for kaon identification in the 3-8 GeV momentum range. At the time of this work, the reconstruction algorithm for the RICH detector was still being developed, so the RICH is not used in this analysis. More information about the design, construction, and performance of the RICH detector can be found in Ref. [77].



Figure 2.7: Fully assembled High Threshold Cherenkov Counter [75].

2.3.5 Time of Flight System

The Forward Time Of Flight (FTOF) is placed after the DCs outside the torus magnetic field. The FTOF detector is divided into six sectors and each sector contains three panels of plastic scintillators: panel-1b and panel-1a cover the low polar angle, and panel-2 covers the larger polar angles as shown in Fig 2.8. When a charged particle passes through the scintillator material, it generates a flash of light. The light is collected by PMTs located at either end of the scintillator counters. The PMTs convert the light into an electrical signal, which is then amplified and recorded by data acquisition electronics. The FTOF is designed to measure the flight time of particles and the position of the hit along the paddle. Further details can be found at [70].

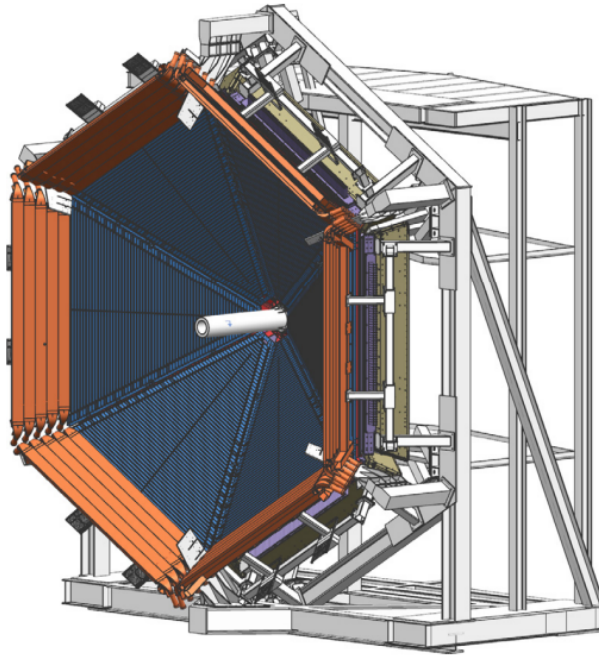


Figure 2.8: Forward Time Of Flight of CLAS12. It consists of three different counters: panel-1b counters (dark blue), panel-2 counters (orange), and panel-1a counters are located immediately downstream of the panel-1b counters which are not shown here [70].

2.3.6 Forward Electromagnetic Calorimeter

The Pre-shower Calorimeter (PCAL) and the Electromagnetic Calorimeter (EC) are the last subsystems of the forward CLAS12 detector, covering the polar angle range from $5^\circ - 35^\circ$ as shown in Fig. 2.9. The PCAL was added for the 12 GeV beam energy upgrade to extend the radiation length of the detector. This enhancement was necessary because the EC alone couldn't completely absorb the electromagnetic showers caused by the higher energy beam (12 GeV). The PCAL and EC together are referred to as the ECAL. The main purpose of the ECAL is to detect neutral particles, photons and neutrons, and to stop and measure the energy and positions of the electron.

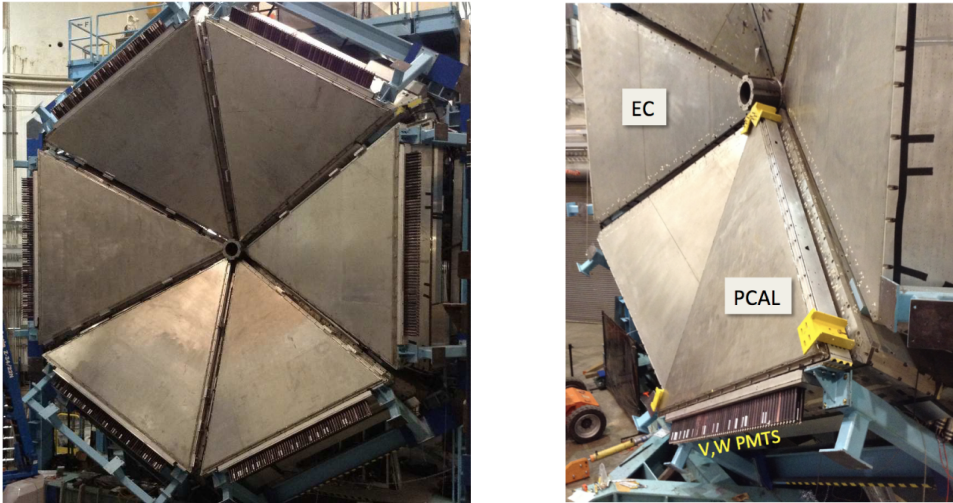


Figure 2.9: Left: 6 sectors of PCAL [68]. Right: A single PCAL sector located in front of the Sector 5 EC [78].

The ECAL is subdivided into six symmetrical triangles arranged around the beam line. Both the EC and the PCAL are made up of layers of plastic scintillator strips. In the EC, the layers are subdivided into EC inner consisting of 5 layers, and EC outer consisting of 8 layers [79]. While the PCAL consists of 5 layers [78]. Each layer, whether in the EC or PCAL, consists of a 10 mm thick scintillator followed by

a 2.2 mm thick lead sheet. These scintillators are made of strips arranged into sets of three, known as U, V, and W planes, each rotated by 120 degrees respective to each other, as shown in Fig. 2.10. This configuration allows for triangulation to determine the hit position, which is necessary for determining the direction of the particle that created the shower in the PCAL. There is one 2.2 mm thick lead sheet between each pair of scintillators. The lead sheets are used to initiate electromagnetic showers in the scintillators produced by the interaction of the incoming particles with the lead [78].

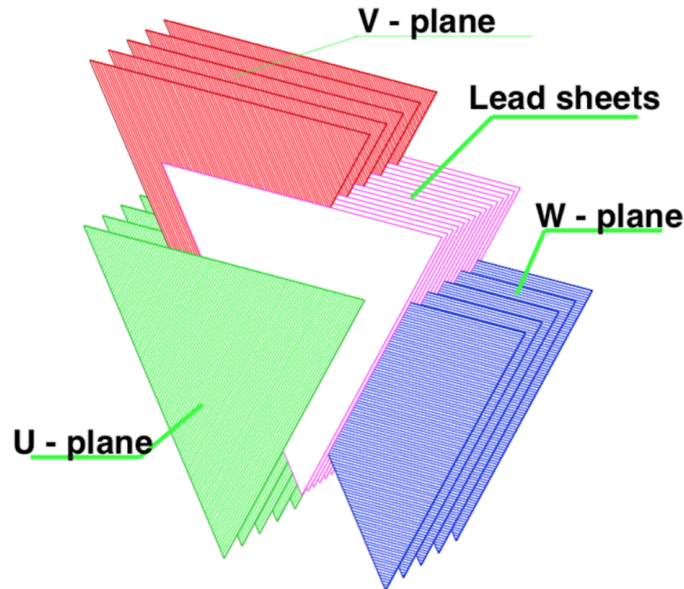


Figure 2.10: Visual representation of the PCAL configuration, showing five layers in each view (U, V, and W) and lead sheets placed between each scintillator layer [78].

The PCAL and EC are both sampling calorimeters. A sampling calorimeter measures the energy of particles by stopping them in an absorber material (such as lead) and measuring the resulting particle showers in an active medium (such as the scintillator material). The lead sheets absorb the energy of incoming particles and produce a shower of secondary particles that interact with the scintillator material,

producing scintillation light. The scintillation light is then detected by PMTs and the energy of the incoming particle is determined by measuring the amount of light produced.

The calorimeters play an important role in the G_M^n measurement since the reaction channel requires the detection of a neutron in its final state. The next chapter will discuss in more detail the method used for identifying neutrons and the efficiency of the calorimeter system.

2.4 Data Processing of CLAS12

The data processing in CLAS12 can be divided into two main steps: data acquisition (DAQ) and reconstruction software.

2.4.1 Data Acquisition of CLAS12

The CLAS12 data acquisition (DAQ) system plays a crucial role in collecting and organizing information from the various detectors, targets, and magnets of the CLAS12 experiment. The DAQ system consists of Analog-to-Digital Converters (ADCs) and Time-to-Digital Converters (TDCs) [80]. These components convert the analog signals into digital format, allowing for efficient data processing and storage. The digital signals are then transferred to the network-based DAQ system. The primary purpose of the DAQ system is to organize and store the event-by-event information generated by the CLAS12 detectors during the running of the experiment. Throughout data collection, data quality is monitored by showcasing a fraction of single events in the CLAS12 Event Display (CED), enabling prompt intervention by shift personnel in case of detector or electronics issues. In addition, monitoring histograms are consistently generated, encompassing information about the occu-

pancy of detector subsystem channels and basic analysis plots. These histograms are routinely compared with results collected earlier during the data taking.

The system responsible for determining whether or not to record data is the trigger system. Operating at Level 1 (L1), the CLAS12 fast trigger system is designed to identify and trigger events that have the physical topology of the desired events. It employs data from diverse detector systems (like HTCC, FTOF, EC, DC, etc.) to generate a global trigger signal, which is then distributed to all crates for detector readout and data collection.

In order to trigger on certain particle types using only an L1 trigger system, CLAS12 simulates the desired physics channels of the Run Group to understand the low-level detector architecture of such events. For example, a scattered electron's simulation in CLAS12 leaves hits in various detectors such as DCs, FTOF, EC, HTCC, etc. Within an L1 system, these hits form clusters and track segments that can be quickly identified with the desired physics channels, and clusters and track segments can be quickly identified by understanding the mapping between readout channels of different detectors. This simulation map is generated for electrons over a wide phase space.

For the purpose of identifying, creating and distributing triggers, the trigger system uses 69 VXS/VME crates with 111 readout controllers. Low-level detector information is transmitted to the VXS/VME crates, and established mappings (from simulations) between channels are utilized to form preliminary clusters and segments. If these clusters and segments align with each other, a trigger is produced and distributed. The CLAS12 DAQ and trigger system is shown in Fig 2.11. See Refs. [80] and [81] for more details.

The DAQ system of the CLAS12 detector is designed to handle trigger rates of up to 20 kHz and data rates of up to 1 GB/s with a livetime (the fraction of the

time during which data were recorded on tapes) up to 95%. The live-time drops with increasing trigger rates [68].

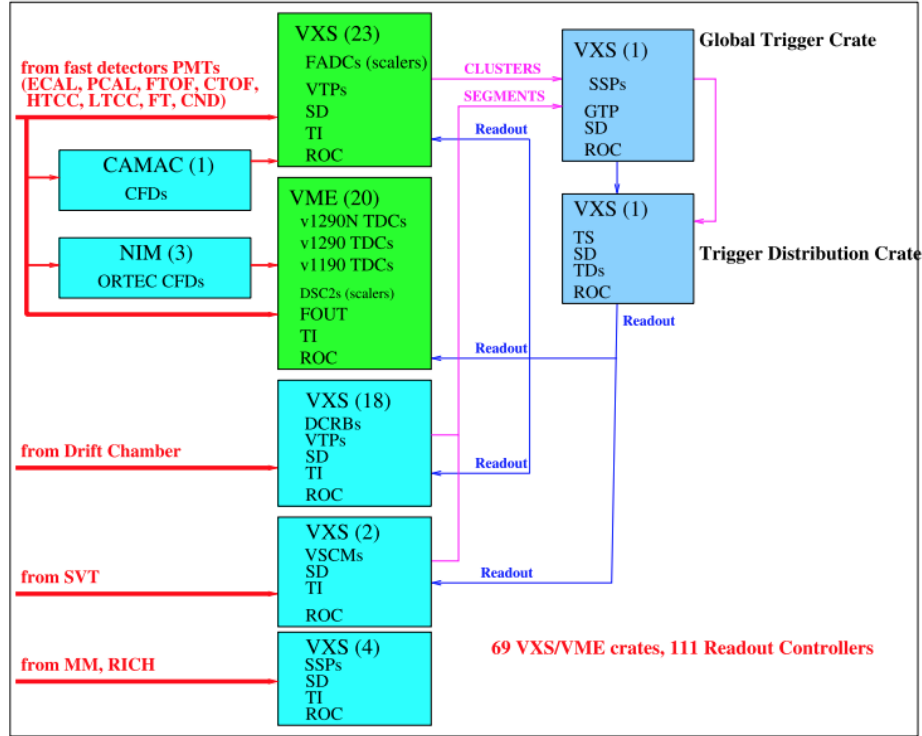


Figure 2.11: The DAQ and trigger system of CLAS12 [80].

2.4.2 Reconstruction Software of CLAS12

The CLAS12 reconstruction software proceeds in two stages: decoding and reconstruction [82]. The data from CLAS12 experiments are stored on data tapes in the EVIO (Event Input/Output) format. In the offline processing of CLAS12 data, the first step is decoding, which takes the input in the EVIO (Event Input/Output) format and produces the output in the HIPO (High Performance Output) format. During decoding, several tasks are performed. First, the signal waveforms recorded by the CLAS12 detectors are fitted to extract relevant information such as am-

plitudes, timings, and other parameters. This fitting process helps in extracting precise measurements from the recorded signals. The second step in the decoding process translates the electronic notation used by the DAQ system (crate/slot/channel) into the detector notation (sector/layer/component). The output HIPO files contain detector-related banks for each event, providing organized and structured data that can be used for calibration and reconstruction.

The reconstruction process utilizes the decoded HIPO file as input. The purpose of the reconstruction stage is to use the detector information to identify particles, extract their 3-momenta, the reaction vertex and assess the track status. The reconstruction of CLAS12 data is performed using the CLARA framework [82], which is a multi-threaded service-oriented software architecture designed for data processing and analysis. CLARA allows users to define a custom architecture for running various services that process input data and produce output data. The CLAS12 reconstruction architecture, shown in Fig. 2.12, follows the CLARA framework. Each micro-service (micro-services are software components that are small self-contained and designed to carry out specific tasks within a larger software application) takes specified detector subsystem information from the decoded HIPO file to perform reconstruction tasks with that information. For example, the ECAL reconstruction service requires the ADC and TDC information for the ECAL PMTs for each event in order to reconstruct a particle with position, timing, and energy deposition information.

The charged track reconstruction within the Forward Detector (FD) of CLAS12 occurs in two stages: a hit-based reconstruction followed by a time-based reconstruction. For hit-based tracking in the DCs, a segment can be formed by requiring four out of six connected DC cells within a super-layer, and a candidate track can be formed by requiring five out of six super-layers in a given sector. These candi-

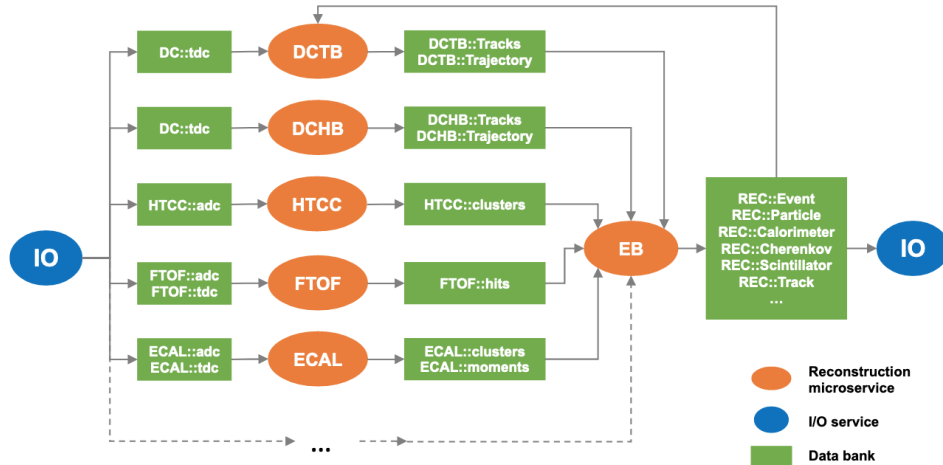


Figure 2.12: The CLARA framework for FD reconstruction. The information extracted from the decoded HIPO files is fed into the micro-services (represented by orange ovals) to produce transient information which is then used by the Event Builder (EB) [82].

date tracks are then matched with other detector elements like FTOF timing and position and ECAL shower clusters. For this preliminary step, the match is done just using the hit position of DC wires without considering time information since that information is not yet available for DC reconstruction. Unmatched hits associated with a track are stored as neutral particles. This information is passed to the Event Builder (EB), which can reconstruct the event start-time (the interaction time when the beam strikes a target nucleus). The start time is determined by the optimal charged particle candidate in the Forward Detector with associated time-of-flight timing. Once the event start time is assigned, a second iteration of forward tracking is performed, referred to as “time-based” tracking. The improved particle tracks obtained from time-based tracking are used in a second pass of the Event Builder process, which leads to the final event reconstruction. At this stage, the Event Builder (EB) utilizes the curvature of the tracks and information obtained from calorimetry and Cherenkov detectors to identify the charged particles.

The next stage is a basic charged particle identification. The charged particle is identified as a positron or an electron if the measured energy deposition is consistent with the expected value of the ECAL, which is more than 60 MeV deposited in the PCAL and the photoelectron response from the HTCC is consistent with more than 2 photo-electrons produced. Then the charged particle is assigned as an e^- or e^+ based on the curvature of the track caused by the torus magnetic field. The remaining charged particles are assumed to be hadrons and are identified solely using timing information. A mass hypothesis is selected for each hadron, and a time difference between the measured and expected times is assigned. The hadron candidate with the smallest time residual is chosen. More details for identifying hadrons can be found in Refs. [82] and [68].

Neutral particle identification involves differentiating between neutrons and photons based on timing and topological details. For the Forward Detectors, the ECAL is used to calculate the particle travel path from the event vertex, assuming a straight-line path. If the measured β is close to 1, the particle is assigned as a photon; otherwise, it is assigned as a neutron.

The Event Builder produces the final data output as data summary tapes (DSTs), which are a standardized selection of HIPO banks for physics analysis. The output data in the form of HIPO banks, and the names of these banks are prefixed with “REC”. These banks include the REC::Cherenkov, REC::Scintillator, REC::Calorimeter, REC::Particle banks, etc. The REC::Particle bank is organized by columns showing the reconstructed particles, and rows showing momentum, vertex, timing and status. The detailed detector responses for each track in REC::Particle are accessible via a mapping scheme that links the track index to each of the individual detector banks.

Because the EB produces large HIPO output files and to make the post recon-

struction analysis more efficient, “trains” are often used to manage the data. Trains involve event selecting or skimming (such as filtering out specific event patterns) and to accommodate various corrections and analysis plugins. The training process divides the data into several output files, each tailored for specific event selections optimized for different physics analyses. An example schematic for RGA is shown in Fig 2.13. We used the second output file that was labeled as $e\pi^+n$ to study the neutron detection efficiency that is described in the next chapter.

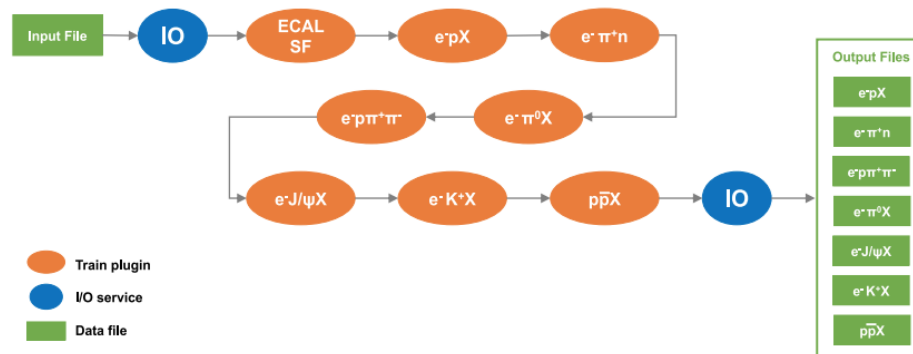


Figure 2.13: The schematic flow of analysis trains involves reading event data from HIPO files, applying corrections for the ECAL sampling fraction (SF) and filters through the analysis chain, labeling events based on filter criteria, and storing the labeled events in output files [82].

CHAPTER 3

NEUTRON DETECTION EFFICIENCY

This chapter will discuss the method used to calculate the neutron detection efficiency (NDE) in the calorimeter detector. This discussion will include the datasets used, the way of selecting a good neutron, and the cuts applied to these datasets. Additionally, the chapter will cover the fitting techniques to extract the NDE results and the parametrization of the NDE results.

3.1 Method of Measuring NDE

The method of measuring the efficiency involves using a hydrogen target to produce tagged neutrons from the reaction $p(e, e'\pi^+)n$. We can determine the tagged neutron missing momentum, P_{mm} , by identifying both the scattered electron and the π^+ detected in the CLAS12 Forward detector and assuming the missing particle is a single neutron. Once we know the neutron missing momentum, we check to see if it will strike the fiducial region of the CLAS12 calorimeters. That is done by calculating the neutron's path, which is a straight line starting from the electron vertex position, and continuing to an intersection point with either the pre-shower calorimeter (PCAL) or electromagnetic calorimeter (EC inner/ EC outer). If the missing neutron's calculated path intersects with the calorimeters, we call it an expected neutron. Otherwise, we skip the event. If we do count an expected neutron, we then loop over all neutral particle hits in the calorimeters to find a detected neutron near the path of the expected neutron. With appropriate kinematic cuts that are presented in Sec. 3.6.2, we can confirm that we have the detected neutron. This method is illustrated in Fig. 3.1 where the paths of expected and detected neutron are shown as a green and blue line, respectively. The intersection points of

expected and detected neutrons with the front face of the calorimeters are shown as green and gray points, respectively. The ratio of the number of detected to expected neutrons gives us the neutron detection efficiency ϵ :

$$\epsilon = \frac{N_{detected}}{N_{expected}}. \quad (3.1)$$

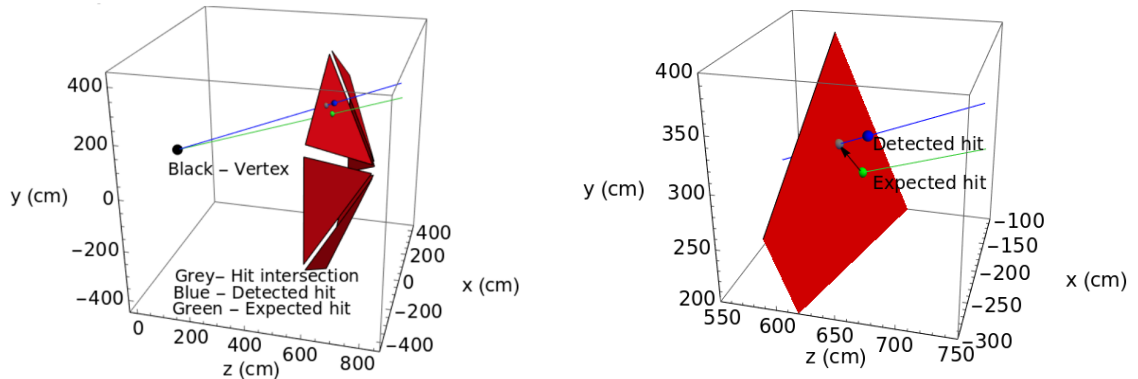


Figure 3.1: The front face of the calorimeter with 6 sectors on the left, and on the right is a close-up view of the single sector. The black point shows the electron vertex, the blue point shows the detected neutron measured by the calorimeter, and the gray and green points show the detected and expected neutron intersecting with the front face of the calorimeter. The blue line is the detected neutron’s path, which is calculated from the electron vertex in direction of the blue point while the green line is the expected neutron’s path starting from the electron vertex and moving in direction of the missing momentum of the neutron.

3.2 Dataset Used

We select the exclusive $ep \rightarrow e'\pi^+(n)$ events from RG-A datasets to extract the NDE. The analyzed datasets of RG-A were taken during Fall 2018 and Spring 2019 with two different beam energies 10.6 GeV and 10.2 GeV, respectively. The target used is unpolarized hydrogen (LH2). The beam current ranges from 40 nA to 75 nA. The torus magnet was set with two different polarities: outbending, where the track of a negative particle bends away from the beamline, and inbending, where

the track of a negative particle bends toward the beamline. The details of these three different datasets are shown in Table 3.1, where we analyzed each dataset separately.

Exp. Detail	In-bending	Out-bending	In-bending
Run Period	Fall 2018	Fall 2018	Spring 2019
Run Range	5032 - 5419	5422 - 5666	6616 - 6783
Number of runs	168 runs	170 runs	115 runs
Beam	10.6041 GeV	10.6041 GeV	10.1998 GeV
Current	40 - 55 nA	40 - 55 nA	50 nA
Target	Unpolarized LH2	Unpolarized LH2	LH2
Torus Field	-1	+1/+1.008	-1
Solenoid Field	-1	-1	-1

Table 3.1: RG-A taken on Fall 2018 and Spring 2019.

3.3 Event Selection

We are interested in the exclusive $ep \rightarrow e'\pi^+(n)$ reaction. Events with two charged particles, one electron and one pion, detected in Forward Detector were selected. The identification of both electron and pion follows the procedure of the approved RGA CLAS12 analysis note [83].

3.4 Electron Particle ID

Initially the electron was selected based on the standard CLAS12 Event Builder (EB) PID =11. The Event Builder assigns electron ID to tracks with responses in

the HTCC and ECAL satisfying the criteria in Table 3.2.

Cut	Limits
Charge	-1
Number of Photoelectrons	$N_{ph} > 2$
Minimum PCAL Energy Deposited	$E_{dep} > 60$ MeV
Sampling Fraction vs. E_{dep}	$\pm 5\sigma$

Table 3.2: EB electron (PID = 11) assignment requirements.

The following cuts were applied to improve electron selection criteria.

3.4.1 Electron Vertex Cut

The 5 cm long LH2 target was placed 3 cm upstream from the CLAS12 center for an inbending torus field and 5 cm upstream for an outbending torus field. Electrons that originated within the hydrogen target were selected by applying cuts on the electron vertex position as shown in Fig 3.2. The cut used is based on the RGA analysis note [83]; $-13 \text{ cm} < v_z < 12 \text{ cm}$ for the inbending torus and $-18 \text{ cm} < v_z < 10 \text{ cm}$ for outbending torus field. The cut used to reject electrons that were scattered at the window of the target cell.

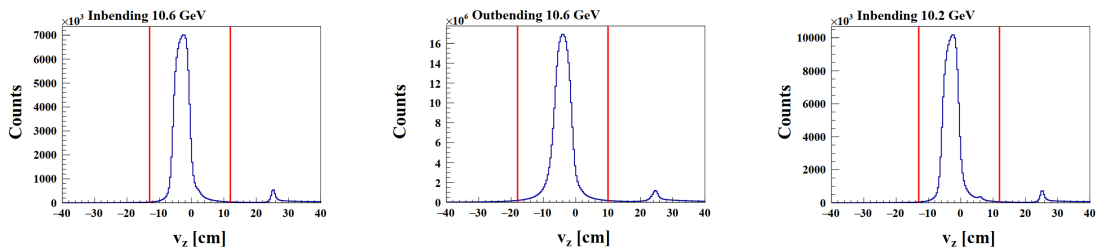


Figure 3.2: The electron z-vertex position for three different datasets. The events pass the EB cut that listed in Table 3.2.

3.4.2 HTCC Photoelectrons Cut

The High Threshold Cherenkov counter (HTCC) is used to reject negative pions up to 4.9 GeV. The track of charged electrons passing through the Cherenkov counter produces a number of photons via Cherenkov radiation. The electron produces more than 2 photoelectrons, which is a minimum threshold for this cut. Figure 3.3 shows the photoelectron distributions for the three different RGA datasets. The cut is defined in the Event Builder PID to select electrons in the Forward Detector.

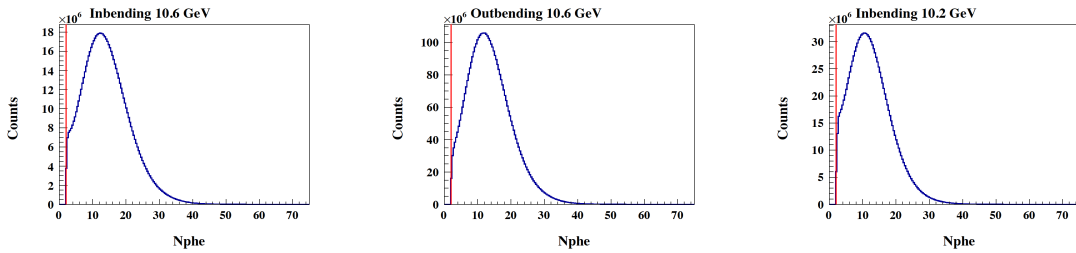


Figure 3.3: Number of photoelectrons produced in the HTCC. The events pass the EB cut that listed in Table 3.2.

3.4.3 PCAL Fiducial Cut

The fiducial region is the area inside the calorimeter that is considered reliable for making measurements. It is defined as the area away from the edges or boundaries of the calorimeter. The purpose of the fiducial cuts is to remove the regions of calorimeter where the shower from the event may not be fully contained within the calorimeter volume. This cut is applied to the local PCAL V and W coordinates in Fig. 2.10. There are three different cuts introduced at the RGA CLAS12 analysis note [83]: a looser cut with a distance of 9 cm from the edge, a medium cut with a distance of 14 cm, and a tighter cut with a distance of 19 cm. The medium cut is used for electrons where the distance from the edge of the V and W planes are greater than 14 cm ($V, W > 14.0$ cm). This cut is determined based on RGA

CLAS12 analysis note [83]. The effect of the PCAL fiducial cut can be shown in local x and y PCAL coordinates in Fig. 3.4.

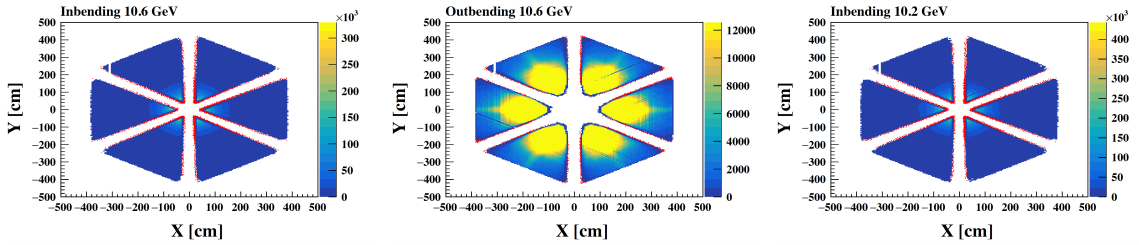


Figure 3.4: Effects of the PCAL fiducial cuts of electrons. Red shows all events. Non-red colors show the hits after applying the fiducial cut. The events pass the EB cut that listed in Table 3.2.

3.4.4 DC Fiducial Cuts

In a similar way, the DC regions where the electron trajectory is close to the edge of the chambers' volumes are removed. The DC fiducial cuts can be extracted in either the local $\theta - \phi$ or $x - y$ planes based on the distribution of the χ^2/NDF of the track. For this analysis, the DC fiducial cuts derived from the $x - y$ planes are used, however both methods yield very similar results. The procedure involves calculating the average tracking χ^2/NDF value separately for each particle type in bins of local x and y coordinates in each sector and DC region. The tracking χ^2 and NDF values are obtained from the corresponding tracking banks (REC::Track::chi2 and REC::Track::NDF). The x distribution of the averaged χ^2/NDF is sliced in each y bins. The center of the distributions in each y slice is fitted with a constant around $x = 0^\circ$. Then the final data points are fitted with a function of the form. More details can be found in the RG-A note [83]. Figure 3.5 shows the DC fiducial cuts for three regions of the DCs based on $x - y$ plane.

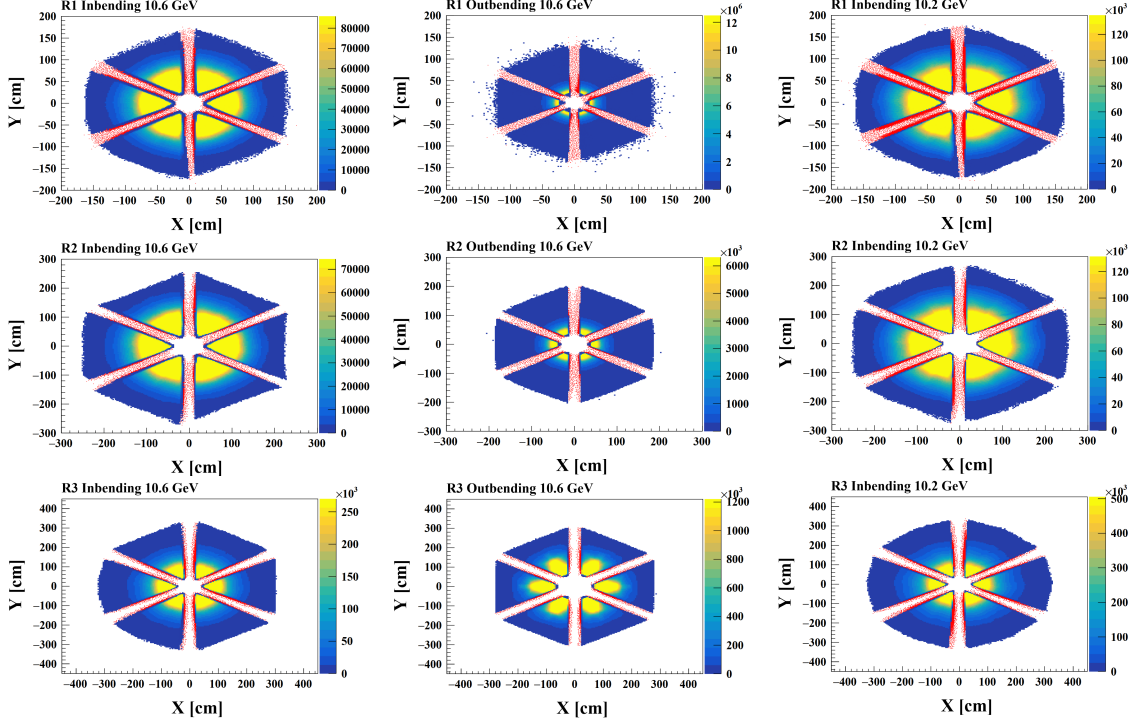


Figure 3.5: Effects on the three regions of DC fiducial cuts for electrons for each RGA dataset. The red points show the hits before the fiducial cuts and the color points show the hits after the fiducial cuts. The events pass the EB cut that listed in Table 3.2.

3.4.5 Calorimeter Cuts

The sampling calorimeters can be used to differentiate between pions and electrons. Electrons and pions deposit their energy in the calorimeter differently. Electrons interact in the EC producing electromagnetic showers and release all of their energy, E_{dep} , which is proportional to their momentum, p . On the other hand, charged pions are minimum ionizing particles, which means that regardless of their momentum, they deposit a constant and small amount of energy. The sampling fraction (SF) cut can be used to separate electrons and pions. The SF is defined as the ratio of a total deposited electron energy in all three calorimeter layers (PCAL+EC) to their momentum and given by:

$$E_{dep} \propto P_e \Rightarrow E_{dep}/P_e = constant = SF, \quad (3.2)$$

where SF is determined by the detector and is around ≈ 0.25 for electrons for CLAS12 at all momenta, see Fig. 3.6. The event builder has a default cut of the sampling fraction as a function of the total deposited energy of the electron E_{dep} . This cut with $\pm 5\sigma$ limit from the sampling fraction, as shown in Fig. 3.6. In order to improve pion rejection, the sampling fraction has been sliced and fitted with Gaussian function in each electron momentum bin to determine the mean and sigma per bin. Then the mean μ and sigma σ of the SF distribution for each P_e bin are fitted using the following forms:

$$\begin{aligned}\mu_{sf} &= A + B/1000 * (p - C)^2, \\ \sigma_{sf} &= a + b/(10 * (p - c)),\end{aligned}\tag{3.3}$$

where a , b , and c are the fit parameters that depend on the momentum bin and sector, shown in Table 3.3. A cut of $\mu \pm 3.5\sigma$ was applied based on [83], as shown in Fig. 3.6. It's important to note that the curly tail observed in the inbending 10.6 GeV dataset was a consequence of issues with the parameterization of the SF cut used by the event builder. The parameterization of SF vs. E_{dep} exhibited divergence as E_{dep} approached zero because the fit that was done was not well constrained at small energies, resulting in the observed curly tail when plotting SF as a function of momentum. When this was noticed, the fit was improved to avoid the divergence and for the other data sets there was no curl.

In addition, a cut on a minimum momentum of reconstructed electrons of 2 GeV and 1.5 GeV are applied for 10.6 GeV and 10.2 GeV beam energies, respectively, to reject pion contamination in this region. Furthermore, a cut on the chi2pid are applied. The chi2pid value is a quality factor used by the event builder to assess how closely the calculated and expected sampling fractions align. The chi2pid value

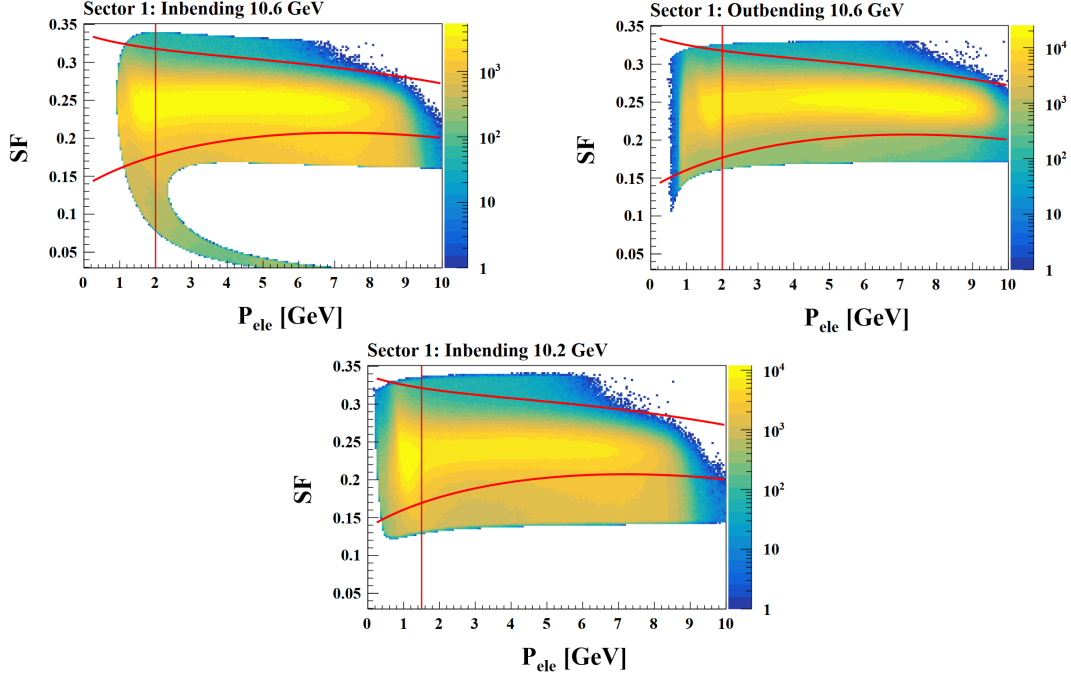


Figure 3.6: The sampling fraction for electron candidates in sector 1 as a function of momentum with the $\pm 5\sigma$ cut applied by the event-builder on SF as a function of E_{dep} . The red lines are the cut on the SF as a function of P_{ele} with the $\pm 3.5\sigma$ and a vertical line indicating the minimum electron momentum cut. The distributions have the EB cut that listed in Table 3.2. The curly tail that appears in the inbending 10.6 GeV dataset was a result of an issue with the parameterization of SF vs. E_{dep} cut, see text for explanation.

	μ_{sf}			σ_{sf}		
	A	B	C	a	b	c
Sector 1	0.25310	-0.6502	4.939	2.726e-3	1.062	-4.089
Sector 2	0.2550	-0.7472	5.350	4.157e-3	0.859	-3.318
Sector 3	0.2514	-0.7674	5.102	5.222e-3	0.5564	-2.078
Sector 4	0.2494	-0.4913	6.440	5.398e-3	0.6576	-2.565
Sector 5	0.2528	-0.3988	6.149	8.453e-3	0.3242	-0.8223
Sector 6	0.2521	-0.703	4.957	6.533e-3	0.4423	-1.274

Table 3.3: Parameters for sampling fraction cut on electron identification.

is determined using the following formula:

$$\chi^2 = \frac{SF_{\text{meas}}(E) - SF_{\text{calc}}(E)}{\sigma_p}, \quad (3.4)$$

where σ_p is the resolution of the sampling fraction. The cut used was $|\chi^2| < 3$ as shown in Fig 3.7.

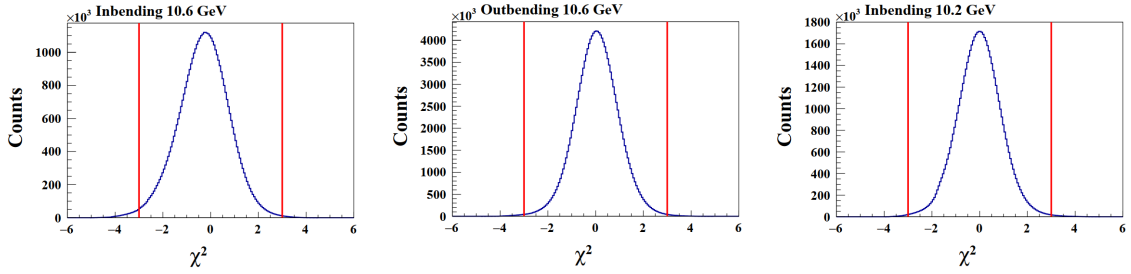


Figure 3.7: The chi2pid distribution of reconstructed electron. The events pass the EB cuts listed in Table 3.2, $\pm 3.5\sigma$ SF cut and the minimum momentum of 2 GeV and 1.5 GeV for 10.6 GeV and 10.2 GeV beam energies, respectively.

The last cut related to the sampling fraction we used is a diagonal cut. The correlation between the inner calorimeter sampling fractions and the PCAL sampling fractions cuts can be applied in order to avoid electrons/pions misidentification above the HTCC threshold at 4.5 GeV. A diagonal cut is defined as

$$\frac{E_{\text{inner}}}{p_e} < 0.2 - \frac{E_{\text{PCAL}}}{p_e}, \quad (3.5)$$

and is shown in Fig. 3.8. The cut is applied to particles with momentum above 4.5 GeV [83].

3.4.6 Energy Deposited Cuts

The selection of electrons can be improved by cutting out the pion based on energy deposited in PCAL layer at 0.06 GeV, as shown on Fig. 3.9. The band below the 60 MeV red line corresponds to pions. This cut is automatically implemented by the

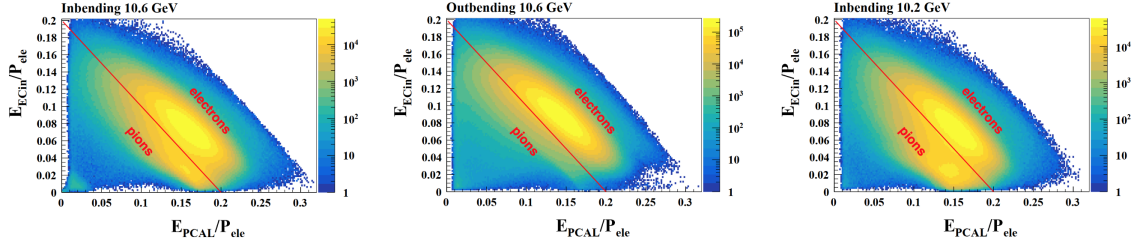


Figure 3.8: The correlation of the sampling fraction using the E_{inner} vs. the PCAL. The events pass the EB cuts listed in Table 3.2 and $P_{ele} > 4.5$ GeV. The diagonal cut removes the events below the red lines, which are pions.

Event Builder when selecting electrons with PID =11. Figure 3.10 shows the same distribution after the PCAL energy cut.

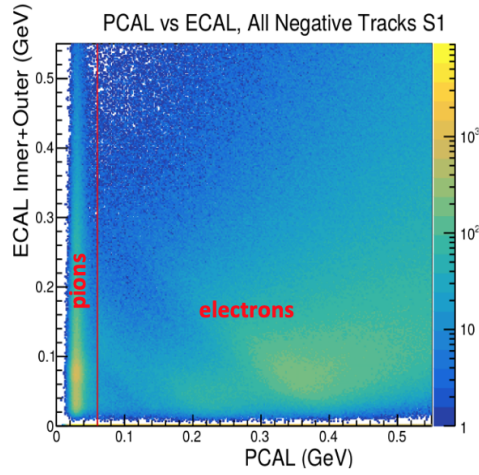


Figure 3.9: Energy is deposition in $EC_{in} + EC_{out}$ layers versus energy deposited in the PCAL layer. The red line is at 60 MeV. Plot is for all negative tracks for Sector 1.

All cuts applied for identification electron are summarized in Table 3.4.

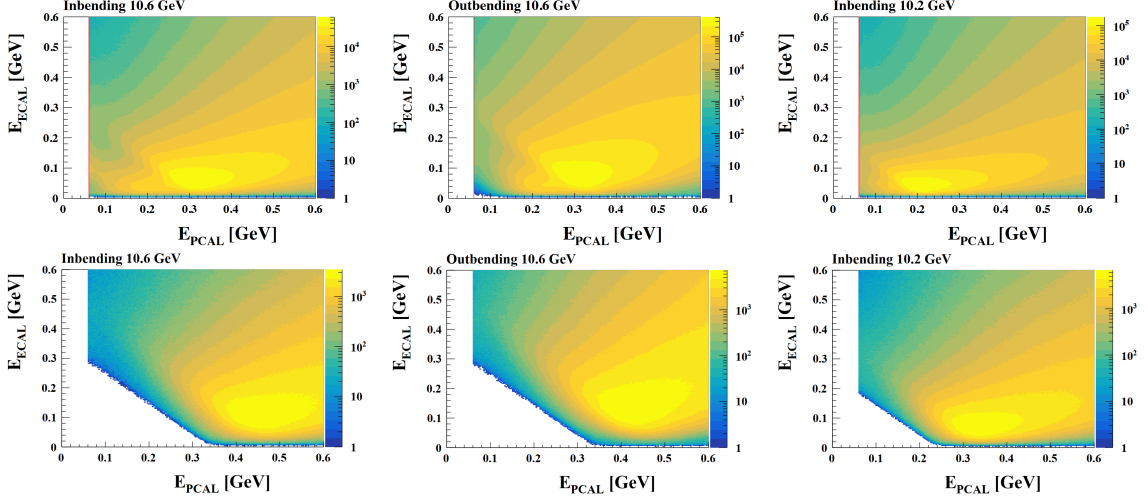


Figure 3.10: Top: Energy deposition in $EC_{in} + EC_{out}$ layers versus energy deposited in the PCAL layer. The $PCAL > 0.06$ GeV cut is defined in the Event Builder. The events pass the EB cuts listed in Table 3.2. Bottom: Same distribution but with $\pm 3.5\sigma$ cut on SF as a function of P_{ele} , diagonal cut, and the minimum momentum of 2 GeV and 1.5 GeV for 10.6 GeV and 10.2 GeV beam energies, respectively.

3.5 π^+ Particle ID

3.5.1 Vertex Difference Cut

To reject pions produced outside of the target region a cut on the difference between the reconstructed electron z-vertex position and the pion vertex is applied. A loose cut of $|v_z(ele) - v_z(\pi^+)| < 20$ cm is placed for all three different datasets, as shown in Fig. 3.11. The cut used is based on the RGA analysis note [83].

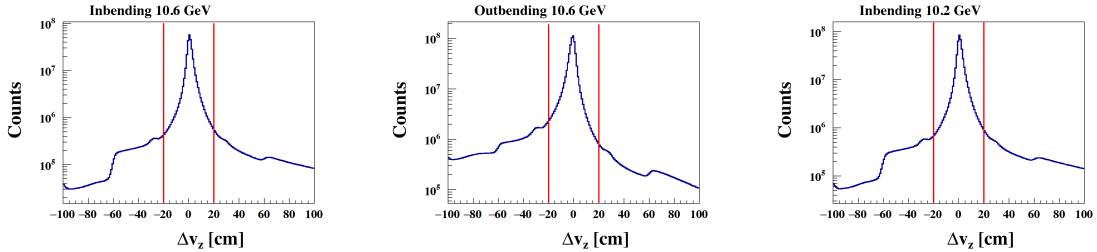


Figure 3.11: Vertex difference between the electron and π^+ . The events pass the EB cuts listed in Table 3.2.

Cut	Limits
PID	11
vertex cut	v_z vertex position
Number of Photoelectrons	$N_{ph} > 2$
PCAL Fiducial Cut	V, W > 14 cm
DC Fiducial Cut for 3 DC regions	$x - y$ plane cuts
SF vs. P_{ele}	$\pm 3.5\sigma$
Diagonal cut	
chi2pid cut	$ \chi^2 < 3$ cut
Minimum PCAL Energy Deposited	$E_{dep} > 60$ MeV

Table 3.4: Cuts used for electron identification.

3.5.2 χ^2 PID Cut

The Event Builder determines the charged hadrons including π^+ by minimizing the difference between the electron vertex time t_{st} and the π^+ start time $t_0^{\pi^+}$. The electron vertex time is determined by the electron vertex position, which is the position where the electron beam hits the nucleus target. The π^+ start time is calculated with the absolute timing from FTOF (t_{FTOF}) and the path length of the π^+ to the FTOF(L):

$$\begin{aligned} \Delta t &= t_{st} - t_0^{\pi^+} \\ &= t_{st} - \left[t_{FTOF} - \frac{L}{\beta_{\pi^+}} \right], \end{aligned} \quad (3.6)$$

where β_{π^+} is

$$\beta_{\pi^+} = \frac{p_{\pi^+}}{\sqrt{p_{\pi^+}^2 + m_{\pi^+}^2}}, \quad (3.7)$$

where $m_{\pi^+}^2$ is the known mass of the π^+ and p_{π^+} is the track momentum of the π^+ . The variable chi2pid in Event Builder is assigned as the number of σ 's from the

expected vertex time for the best hypothesis [83]:

$$\chi_{pid}^2 = \frac{\Delta t}{\sigma}. \quad (3.8)$$

The distribution of chi2pid values for π^+ as a function of pion momentum is shown in Fig. 3.12. There is a significant kaon contamination on the positive side of the chi2pid distribution above 2.44 GeV. To remove the kaon contribution the following cut is used:

$$\begin{aligned} \chi_{pid} < 3 \cdot 0.88 & \quad \text{for } p_{\pi^+} < 2.44 \text{ GeV} \\ \chi_{pid} < 0.88 \cdot (0.00869 + 14.98587 \cdot \exp(-p/1.18236) \\ & + 1.81751 \cdot \exp(-p/4.86394)) & \quad \text{for } p_{\pi^+} > 2.44 \text{ GeV}. \end{aligned} \quad (3.9)$$

More details on this cut can be found in [83].

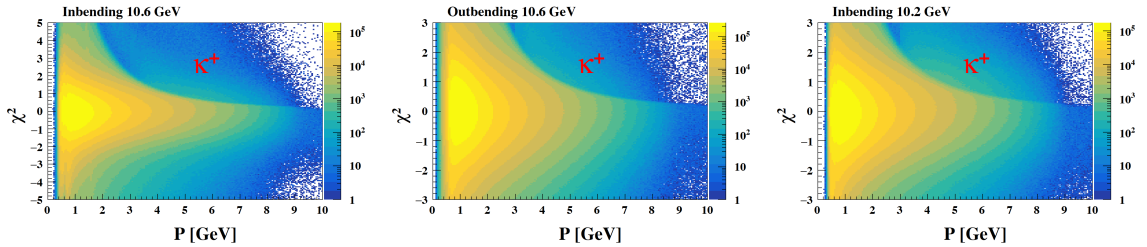


Figure 3.12: Top: The chi2pid vs momentum distribution after the Event Builder applied Δt to assign a particle as the pions.

3.5.3 Fiducial Cuts for DC

The drift-chamber fiducial cuts for positive pions have been applied based on the $x - y$ plane, similar to the cut for electrons. The result of this cut in the three drift chamber regions is shown in Fig. 3.13. More details of the DC fiducial cuts including the exact parametrizations can be found in the RGA analysis note [83]. The summary of the cuts applied for identification of pion is shown in Table 3.5.

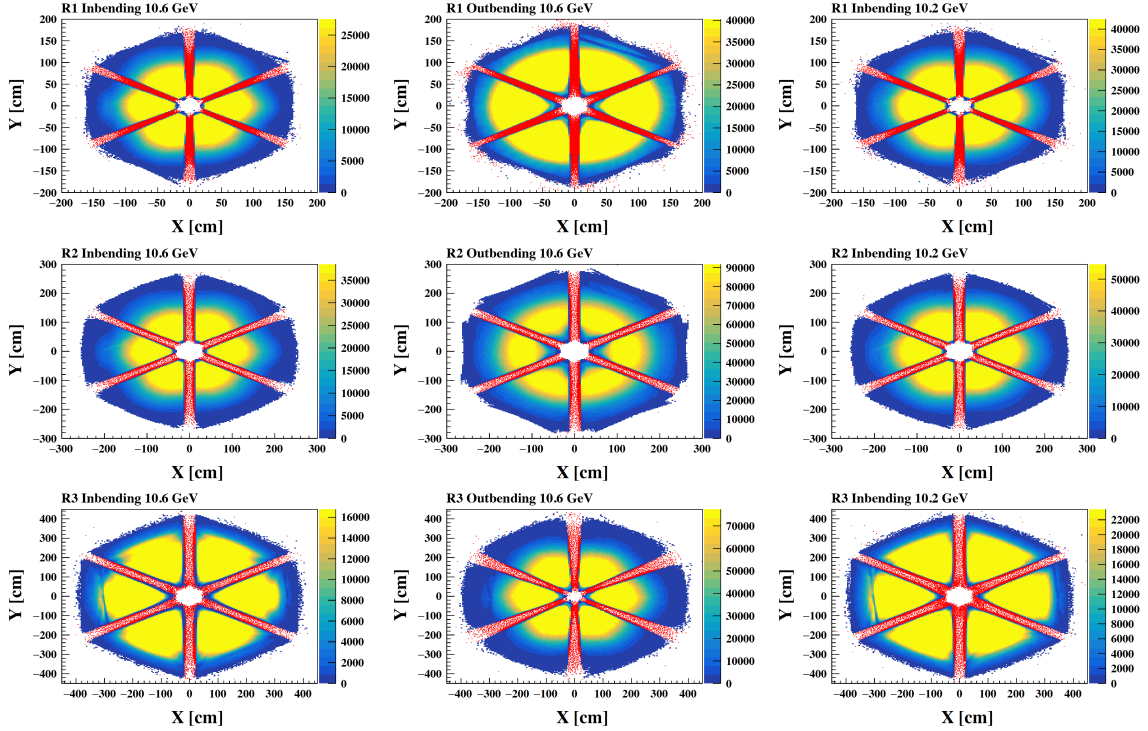


Figure 3.13: The effect of fiducial cuts on the three regions of the drift chambers on the π^+ . The red points show the hits before the cuts were applied and the overlaid colored points show the hits that survive the fiducial cut. Top is region 1, middle is region 2 and bottom is region 3.

3.6 Neutron Selection

Neutral hits are identified as a cluster in the PCAL/ EC with no associated charged-particle track reconstructed in the DC. Photons and neutrons are identified in the Event Builder based on a beta cut at 0.9: $\beta > 0.9$ for photons and $\beta < 0.9$ for neutrons. In this analysis, both photons and neutrons are combined to select final neutrons. The neutrons are selected in two ways: (1) Expected neutrons are in events where the trajectory in the direction of the missing-momentum vector of the $p(e, e'\pi^+)X_n$ reaction intersects the calorimeters. (2) Detected neutrons are found as neutral hits in the calorimeters near an expected neutron.

Cut	Limits
PID	211
vertex cut	$ v_z(ele) - v_z(\pi^+) < 20$ cm
DC Fiducial Cut for 3 DC regions	$x - y$ plane cuts
chi2pid cut	$ \chi^2 < 3$ cut

Table 3.5: Cuts used for pion identification.

3.6.1 Identification of the Reaction $p(e, e'\pi^+)n$

Once a scattered electron and a π^+ have been identified, the missing mass and missing momentum of the $p(e, e'\pi^+)n$ reaction can be calculated by considering 4-momentum conservation:

$$P_e^\mu + P_p^\mu = P_{e'}^\mu + P_{\pi^+}^\mu + P_{mm}^\mu, \quad (3.10)$$

where $P^\mu = (\vec{P}, E)$ for each particle and $P_{mm}^\mu = (\vec{P}_{mm}, E_{mm})$ is the missing neutron 4-momentum. The 3-momentum vector \vec{P}_e of the incoming electron is zero in the x and y directions (beam moves along z -axis) and the 3-momentum vector \vec{P}_p of the target proton is zero (initially at rest). The missing mass can be calculated as

$$P_{mm}^\mu P_{\mu mm} = E_{mm}^2 - P_{mm}^2 = MM^2. \quad (3.11)$$

The magnitude of the missing neutron 3-momentum is

$$\vec{P}_{mm} = \sqrt{P_{xmm}^2 + P_{ymm}^2 + P_{zmm}^2} = P_{mm}, \quad (3.12)$$

where: $P_{xmm}, P_{ymm}, P_{zmm}$ are the missing neutron momentum components in the x , y and z direction, respectively, and calculated as:

$$P_{xmm} = -P_{x_{e'}} - P_{x_{\pi^+}}, \quad (3.13)$$

$$P_{ymm} = -P_{y_{e'}} - P_{y_{\pi^+}}, \quad (3.14)$$

$$P_{z_{mm}} = E_{beam} - P_{z_{e'}} - P_{z_{\pi^+}}. \quad (3.15)$$

The missing neutron energy can be calculated as:

$$E_{mm} = E_{beam} + E_p - E_{e'} - E_{\pi^+}, \quad (3.16)$$

where $E = \sqrt{\vec{P}^2 + m^2}$ for each particle and E_{beam} is the energy of the incoming electron beam. Figure 3.14 shows the missing mass distribution as a function of the missing momentum of $p(e, e'\pi^+)X_n$, where X_n in this stage can be one or more particles with a charge of zero. The missing momentum of the neutron, P_{mm} , can reach up to 7 GeV. The missing mass distribution of $p(e, e'\pi^+)X_n$ shows two prominent peaks with a large high-mass background in Fig. 3.15. The first peak corresponds to the neutron mass at 0.939 GeV and the second peak corresponds to the Δ^0 at 1.2 GeV.

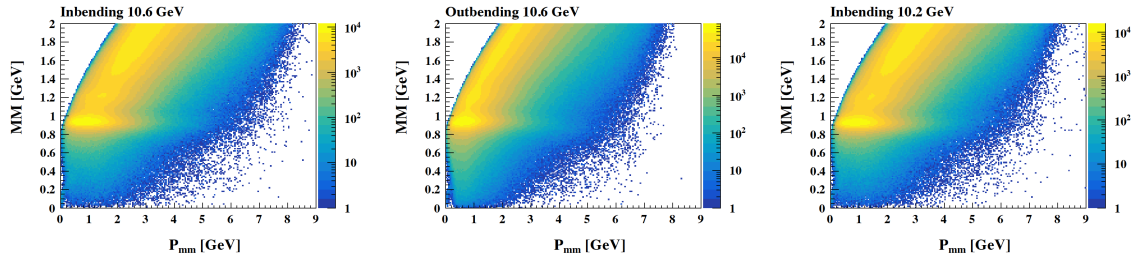


Figure 3.14: The missing mass distribution as function of missing momentum of $ep \rightarrow e'\pi^+X_n$.

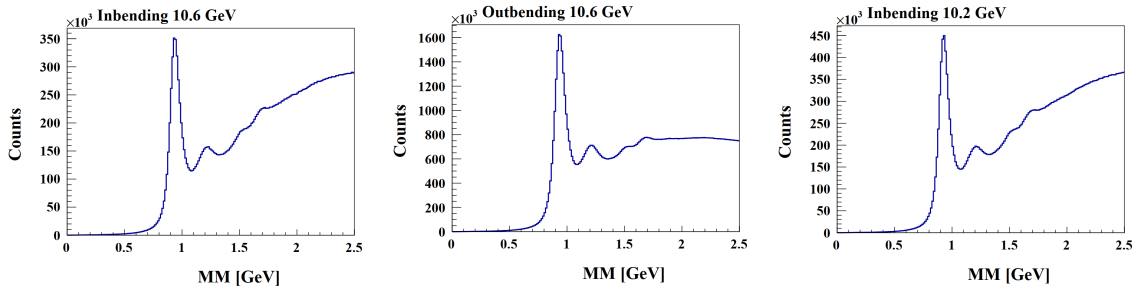


Figure 3.15: The missing mass distribution of $ep \rightarrow e'\pi^+X_n$.

To identify the expected neutron $p(e, e'\pi^+)n$, we swim the neutron through the CLAS12 detector to the calorimeter. The neutron's path is a straight line starting

from the electron vertex position and pointing in the missing 3-momentum direction. If the neutron's path intersects with the calorimeters, it counts as an expected neutron. If the intersection point lies outside the calorimeters, the event is dropped. An additional fiducial cut is applied for the expected neutron to be more than 10 cm from the edge of the calorimeters. The fiducial cut is defined by rotating $x - y$ of the expected neutron by $(s - 1)60^\circ$ where s is the sector number as shown in the upper plots of Fig. 3.16. Bottom plots in Fig. 3.16 show the result of the fiducial cut in all sectors.

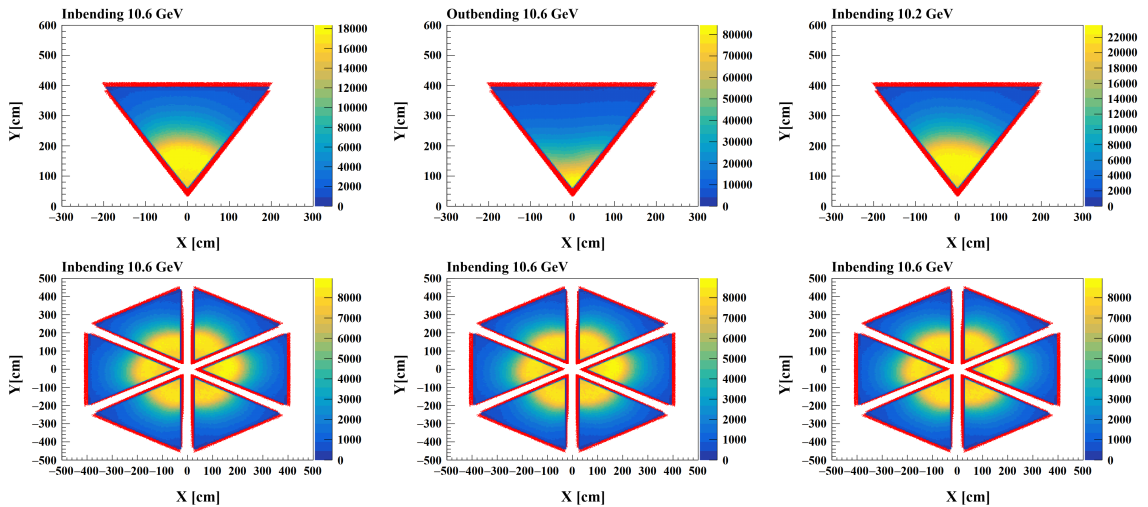


Figure 3.16: PCAL/ECAL hit position Y vs. X of expected neutrons intersecting with the calorimeters. The red points show the events before applying the fiducial cut. Top row shows an overlay of all sectors rotated by $(s - 1)60^\circ$ and the bottom row shows each sector individually.

3.6.2 Identification of the Reaction $p(e, e'\pi^+n)$

Once the expected missing neutron intersects the calorimeters and satisfies the fiducial cut, a tight MM cut on the expected missing neutron is applied to select the actual neutron measured in the calorimeter. The cut used on the expected neutron

corresponds to a 2σ cut on the Gaussian as shown in Fig. 3.17.

$$\begin{aligned}
0.8565 \text{ GeV} < MM < 1.0339 \text{ GeV} & \quad \text{Inbending 10.6 GeV} \\
0.8685 \text{ GeV} < MM < 1.0407 \text{ GeV} & \quad \text{Outbending 10.6 GeV} \\
0.8491 \text{ GeV} < MM < 1.0237 \text{ GeV} & \quad \text{Inbending 10.2 GeV}
\end{aligned} \tag{3.17}$$

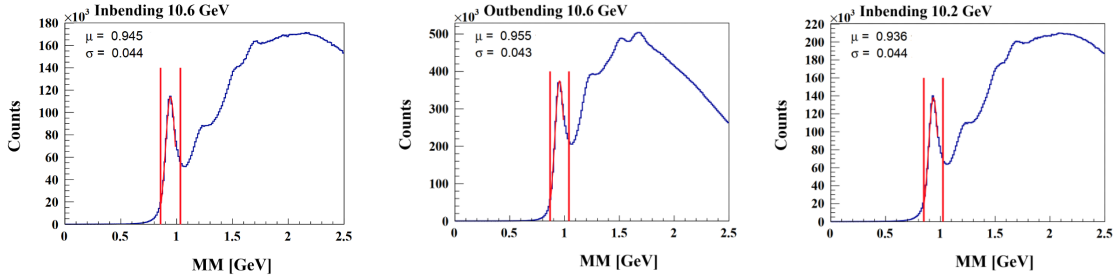


Figure 3.17: The missing mass distribution of the expected neutron $p(e, e'\pi^+)n$ that intersects with the calorimeters and passes the fiducial cut. The red vertical lines show the cut applied within 2σ .

If the expected neutron passes the 2σ cut above, we loop over all neutral hits in the calorimeters to select the candidate neutrons. Candidate neutrons are identified by considering the direction in which the missing 3-momentum of the expected neutron should coincide with the direction of the detected neutral particles. The detected neutral hit position in the calorimeter is defined by drawing a line starting from the electron vertex position in the direction of the measured hit in the calorimeter coordinates x , y , and z to the intersection with calorimeter face plane. Therefore the direction of detected neutral particles is defined as:

$$\begin{aligned}
C_{x\text{neut}} &= x/r, \\
C_{y\text{neut}} &= y/r, \\
C_{z\text{neut}} &= z/r,
\end{aligned} \tag{3.18}$$

where $r = \sqrt{x^2 + y^2 + z^2}$ and x , y and z are the position of the detected neutral hit on the face plane of the calorimeters. The direction cosines of the expected neutrons

in the x , y and z directions can be determined by dividing each component of the missing 3-momentum of the expected neutron by the magnitude of the missing 3-momentum of the expected neutron vector:

$$\begin{aligned} C_{x_{mm}} &= P_{x_{mm}}/P_{mm}, \\ C_{y_{mm}} &= P_{y_{mm}}/P_{mm}, \\ C_{z_{mm}} &= P_{z_{mm}}/P_{mm}. \end{aligned} \tag{3.19}$$

The difference between the transverse direction cosines ($\Delta C_i = C_{i_{mm}} - C_{i_{\text{neut}}}$, where $i = x$ or y) is shown in Fig. 3.18. A cut on the difference in direction cosines between the missing momentum of the expected neutron and the detected neutral hit is applied to select the detected neutron. This cut is defined based on fitting $\Delta C_{i_{mm}}$ with a Gaussian and applying a 2σ cut as

$$\begin{aligned} \sqrt{(\Delta C_x)^2 + (\Delta C_y)^2} &< 0.1174 \quad \text{Inbending 10.6 GeV,} \\ &< 0.1308 \quad \text{Outbending 10.6 GeV,} \\ &< 0.1195 \quad \text{Inbending 10.2 GeV.} \end{aligned} \tag{3.20}$$

The cut is shown in Fig. 3.18 as a red circle. If there are multiple neutral hits, the smallest value of $\sqrt{(\Delta C_x)^2 + (\Delta C_y)^2}$ is selected. The missing mass of the detected neutron that satisfy the 2σ cut on the ΔC_x and ΔC_y is shown in Fig. 3.19.

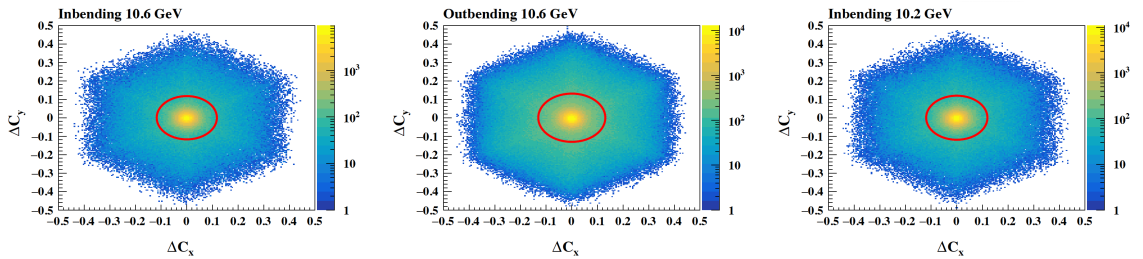


Figure 3.18: Differences in direction cosines ΔC_y vs. ΔC_x . The red circle shows the cut used to eliminate the background.

Most of the background under the detected missing mass of neutron is due to the photons contribution as shown in Fig. 3.20. The beta of the neutral particle, β_{neut} ,

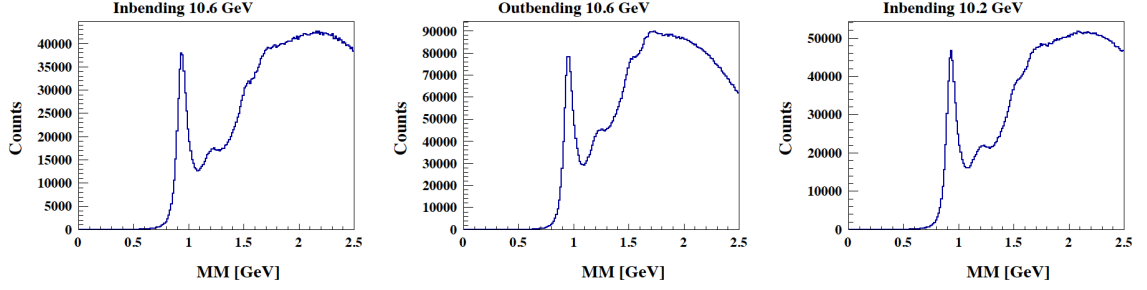


Figure 3.19: The missing mass distribution of detected $p(e, e'\pi^+n)$ neutron satisfied $\Delta C_x, \Delta C_y$ cut. From left to right inbending 10.6 GeV, outbending 10.6 GeV and inbending 10.2 GeV.

detected in the calorimeter as a function of P_{mm} shows two bands that correspond to photons and detected neutrons, where the β_{neut} is given by:

$$\beta_{\text{neut}} = \frac{l_{\text{neut}}}{c\Delta t_{\text{neut}}}, \quad (3.21)$$

where c is the speed of light, l_{neut} is the path length of the neutral particles measured to the front face of the calorimeters. The Δt_{neut} is defined as the difference of the time measured by the calorimeters t_{neut} and the event start time t_0^n

$$\Delta t_{\text{neut}} = t_{\text{neut}} - t_0^n, \quad (3.22)$$

where t_0 is the difference between a hit measured and the ToF for particle

$$t_0^n = t - \frac{l}{c}, \quad (3.23)$$

where t and l are the time and path length, respectively of electron, measured by the TOF. The clear separation between photons and neutrons is observed below 1.5 GeV. These photons have not been removed in order to treat the detected neutron as the expected neutron to subtract the background in Sec 3.8.

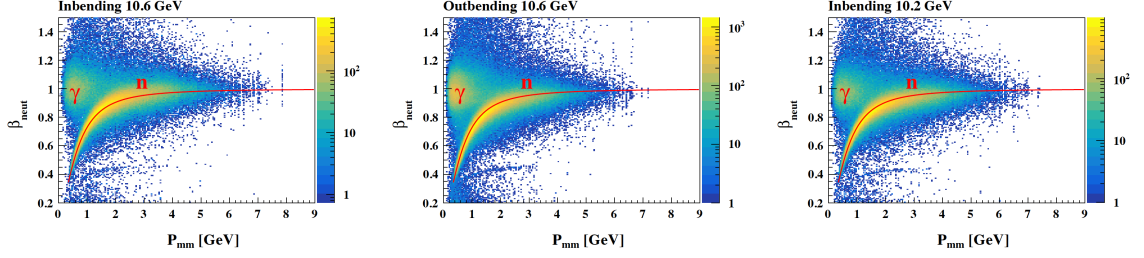


Figure 3.20: β_{neut} of neutral particles measured in calorimeters vs. missing momentum that satisfied ΔC_x , ΔC_y cut. The red line is the theoretical curve for neutrons.

3.7 Efficiency Measurement in the Calorimeter

The efficiency ϵ is defined as the ratio of detected neutrons $p(e, e'\pi^+n)$ to the number of expected neutrons $p(e, e'\pi^+)n$ as:

$$\epsilon = \frac{\#p(e, e'\pi^+n)}{\#p(e, e'\pi^+)n} \quad (3.24)$$

Below is the summary of the cuts applied to the expected and the detected neutrons:

1) Expected neutron events $p(e, e'\pi^+)n$:

- Intersect with the face plane of the calorimeters.
- Pass fiducial cut.

2) Detected neutron events $p(e, e'\pi^+n)$:

- All cuts listed in 1.
- The difference in direction cosines, $\sqrt{(\Delta C_x)^2 + (\Delta C_y)^2} < 2\sigma$.

Figure 3.21 shows that both the expected and detected missing mass have background events that must be taken into account when measuring efficiency.

3.8 Background Subtraction

Generally, the neutron efficiency is calculated as a function of the missing momentum, P_{mm} . The procedure used to extract the neutron yield involves fitting the

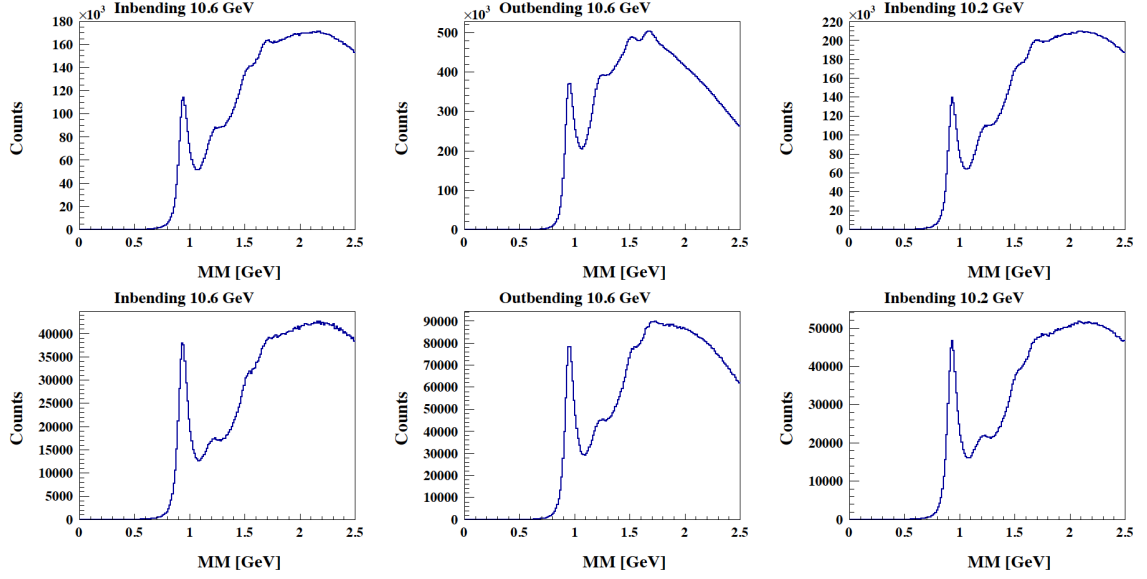


Figure 3.21: The missing mass distribution of expected $p(e, e'\pi^+)n$ (top) and detected $p(e, e'\pi^+)n$ (bottom) neutron satisfied above cuts. From left to right, inbending 10.6 GeV, outbending 10.6 GeV and inbending 10.2 GeV.

missing mass distribution of both expected and detected neutrons at different P_{mm} bins with two different functions:

- **Gaussian plus a fourth-order polynomial.**

$$f(x) = Ae^{-\frac{1}{2}\left(\frac{x-\mu}{\sigma}\right)^2} + P_0 + P_1x + P_2x^2 + P_3x^3 + P_4x^4, \quad (3.25)$$

- **Crystal Ball plus a fourth-order polynomial.**

$$f(x) = f_{CB}(x; A, \mu, \sigma, a, n) + P_0 + P_1x + P_2x^2 + P_3x^3 + P_4x^4, \quad (3.26)$$

where the Crystal Ball function is defined as [84]

$$\begin{aligned} f_{CB}(x; A, \mu, \sigma, a, n) &= Ae^{-\frac{1}{2}\left(\frac{x-\mu}{\sigma}\right)^2} && \text{for } \frac{x-\mu}{\sigma} > -a \\ &= \left(\frac{n}{|a|}\right)^n e^{-\frac{|a|^2}{2}} \left(\frac{n}{|a|} - |a| - \frac{x-\mu}{\sigma}\right)^{-n} && \text{for } \frac{x-\mu}{\sigma} \leq -a. \end{aligned} \quad (3.27)$$

The Crystal Ball (CB) function combines a Gaussian function with a power-law times an exponential tail, which is described by the parameters a and n . The parameter a controls the location of the transition point between the Gaussian and power-law parts of the function and n determines the steepness of the power-law tail. The parameters A , μ and σ are the amplitude, mean (centroid), and width (standard deviation) of the Gaussian part of the CB or Gaussian, respectively. The parameters P_0 , P_1 , P_2 , P_3 and P_4 are the polynomial coefficients.

The main reason for using the CB function is that the Gaussian function alone is not appropriate for describing the missing mass distributions. The distributions can be distorted by resolution and radiative effects, where the radiative effects are due to electron target interactions before or after the hard electron-proton scattering leading to low energy photons that are not accounted for in the MM calculation. The Crystal Ball function provides a better fit to the shape of the missing mass distributions, including the presence of a tail, and can effectively describe the effects of resolution and radiative contributions. The tail of the CB function is investigated using the semi-inclusive deep inelastic scattering (SIDIS) Monte Carlo (MC) simulation. The SIDIS MC is generated using the clasdis generator, which is based on the LEPTO generator [85]. More details on SIDIS MC can be found in [83]. The tail of the missing mass distribution of $(e, e'\pi^+n)$ for inbending 10.6 GeV is shown at high missing mass distribution in Fig. 3.22. It extends to higher missing mass.

The fitting procedure for the missing mass distributions of expected and detected neutrons is described as follows. The first step is to fit the cleanest missing mass distribution, which is the detected neutron by a Gaussian and polynomial function. The Gaussian function is used to model the neutron signal, while a fourth-order polynomial is used to describe the background. The fitting is performed for each of P_{mm} bins, allowing all parameters (amplitude, mean, width, and polynomial

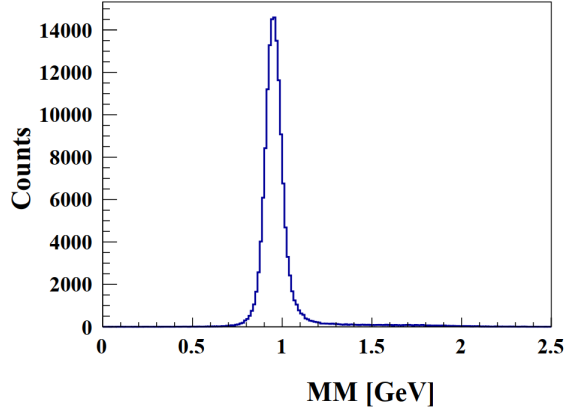


Figure 3.22: The missing mass distribution of $p(e, e'\pi^+n)$ for incident 10.6 GeV, generated from SIDIS MC.

coefficients) to vary. This step gives us the width and the mean of the neutron MM peak. Next, the same mean and width obtained from the detected neutron Gaussian fitting are applied to the expected neutron distribution. The Gaussian amplitude and polynomial coefficients for the expected neutron distribution are allowed to vary.

The range of the Gaussian fitting is limited to $MM < 1.1$ GeV for both expected and detected neutrons at $P_{mm} < 2$ GeV. For higher values of P_{mm} , the upper limit of the fitting range is gradually extended to $MM < 1.2$ GeV.

After that, we fit both expected and detected neutrons for each P_{mm} bin using the CB function. The mean and width obtained from the Gaussian fitting of the detected neutron are used as fixed values in the CB function for both the expected and detected neutrons. The high MM tail parameters of the CB function for detected neutron are used for the expected neutron distribution. However, if a large χ^2 value is observed for the fitting of the expected neutron distribution, the tail parameters are varied for both expected and detected neutron and fixed at the same values that give the lowest χ^2 .

The range of the fitting in the CB function is extended to $MM < 1.2$ GeV for all P_{mm} bins.

The fitting of the expected and detected neutrons for different P_{mm} bins using a Gaussian and CB functions is shown in Fig 3.23 and 3.24, respectively. The fitting is shown for three P_{mm} bins for inbending 10.6 GeV dataset, the fitting of the all P_{mm} bins and other datasets can be found in the Appendix A for Gaussian function and Appendix B for CB function. The CB function can fit a higher range of missing mass (MM) and provides a similar fit quality to the Gaussian function for the detected neutron. However, for the expected neutron, the Gaussian function shows a better fit quality with a lower average χ^2 value. The average χ^2 of the expected and detected neutron for the two functions is shown in Table. 3.6.

The values of the mean and width obtained from the Gaussian fitting of detected neutron are shown in Fig. 3.25 for each P_{mm} bin for the three datasets. Ideally, the mean values of the neutrons peak should be centered at 0.939 GeV. For inbending 10.6 GeV dataset the peaks are centered between $\simeq 0.939$ and 0.94 GeV. However, for inbending 10.2 GeV dataset the mean values of the neutrons peak are centered at $\simeq 0.929$ to 0.930 GeV except for the last two P_{mm} bins. For outbending 10.6 GeV dataset the peak position is shifted and centered at $\simeq 0.959$ to 0.960 GeV below 3 GeV then they start to decrease at high P_{mm} bins. This shift of the peak position is due to the imperfections in the magnetic field map and the drift chamber misalignments. We have applied the momentum correction of both electrons and pions particles developed by RGA group for the three datasets. At this stage, the momentum corrections look good for only inbending 10.6 GeV.

In the right-hand panel of Fig. 3.25, the width of the neutron peak is almost constant below 1 GeV, then it starts to increase smoothly from one bin to the next. Also, we used the similar width for all three datasets under the assumption that the width of the peak should remain the same in each bin. The fit parameters of the three data sets using Gaussian and CB function is shown in the Appendix A and

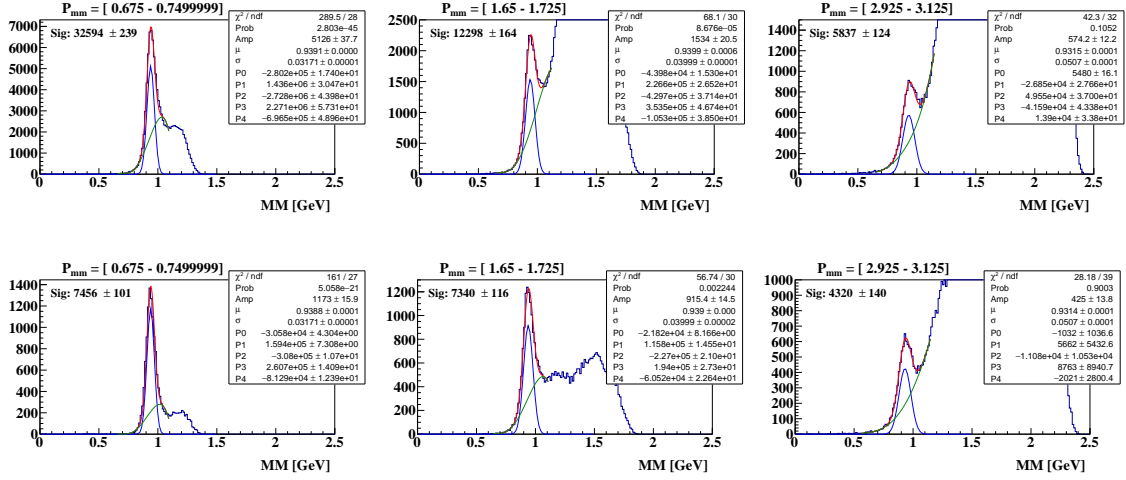


Figure 3.23: The missing mass distribution of expected (top) and detected (bottom) neutron for three different P_{mm} bins. The distribution is fitted with a Gaussian plus polynomial background. The blue curve is the signal distribution after subtraction of the background distribution, the green is the background, and the red is the sum of the two. The fitting is shown for inbending 10.6 GeV dataset. See Appendix A for other P_{mm} bins and other datasets.

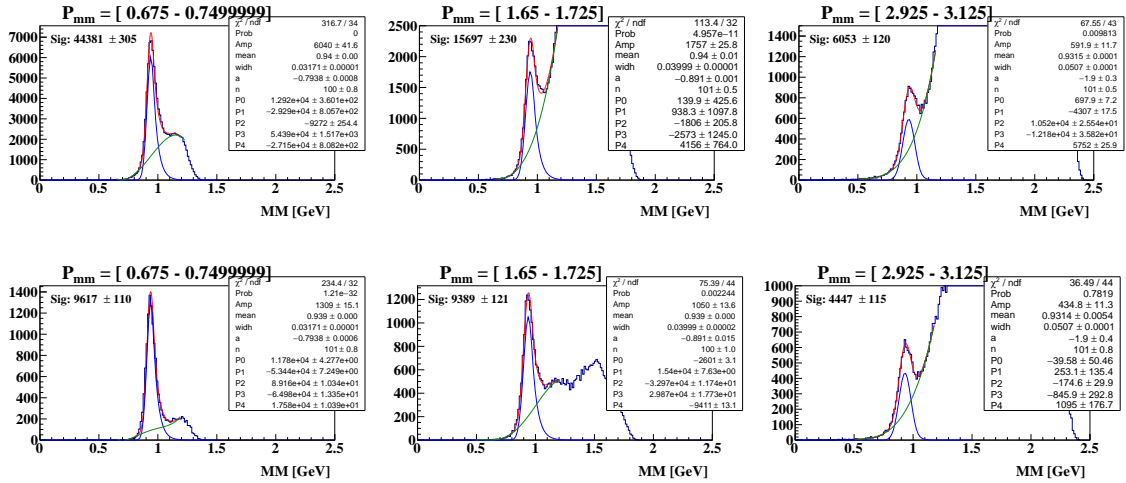


Figure 3.24: The missing mass distribution of expected (top) and detected (bottom) neutron for three different P_{mm} bins. The distribution is fitted with a Crystal ball polynomial background. The blue curve is the signal distribution after subtraction of the background distribution, the green is the background, and the red is the sum of the two. The fitting is shown for inbending 10.6 GeV dataset. See Appendix B for other P_{mm} bins and other datasets.

B, respectively.

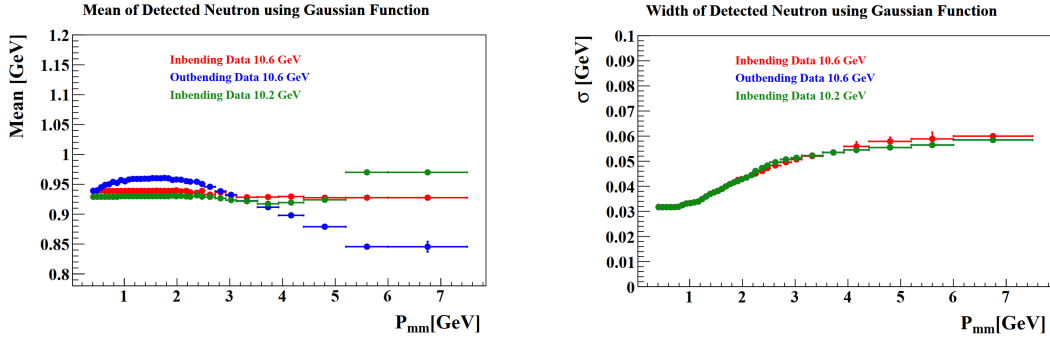


Figure 3.25: Left: The mean values of the signal distribution for both expected and detected neutrons for each P_{mm} bin. Right: The width values of the signal distribution for both expected and detected neutrons for each P_{mm} bin.

	Gaussian Function		Crystal Ball Function	
	Detected MM	Expected MM	Detected MM	Expected MM
Inbending 10.6 GeV	2.42	2.63	2.83	4.82
Outbending 10.6 GeV	4.22	7.49	5.43	12.68
Inbending 10.2 GeV	2.31	5.94	2.59	5.98

Table 3.6: The average χ^2 of both expected and detected neutrons for Gaussian and CB functions.

3.9 NDE Results

Once the missing mass of expected and detected neutrons are fitted in each missing momentum bin P_{mm} , the yields of the neutron signal can be calculated by integrating either Gaussian or Crystal Ball function. The detection efficiency in each momentum bin can be calculated as:

$$\epsilon_i = \frac{N_{deti}}{N_{exp_i}}, \quad (3.28)$$

where ϵ_i is the efficiency in the i^{th} missing momentum bin, N_{deti} is the yield of the detected neutron signal in the i^{th} missing momentum bin, and N_{exp_i} is the yield of

the expected neutron signal in the i^{th} missing momentum bin. An uncertainty to the efficiency in the i^{th} bin is calculated based on the binomial distribution

$$\sigma_i = \sqrt{\frac{\epsilon_i (1 - \epsilon_i)}{N_{exp_i} - 1}}. \quad (3.29)$$

A comparison of the neutron efficiency calculated by the Gaussian function and the Crystal ball function, binned in missing momentum of the neutron, is shown in Fig. 3.26. The comparison is shown for each dataset individually, inbending and outbending 10.6 GeV, and inbending 10.2 GeV. The agreement between the two functions is very good for missing momentum P_{mm} greater than about 1.5 GeV. Below this value, the results extracted from the Gaussian is slightly above the Crystal ball function. Overall, the discrepancy between the two functions is within 3%. Figure 3.27 shows the results, of the present analysis, for the CLAS12 neutron detection efficiency compared to the CLAS6 data. The CLAS12 results show that all three datasets, inbending and outbending 10.6 GeV and inbending 10.2 GeV, are consistent to each other in both functions. The CLAS12 results are a higher compared to the CLAS6 result over all P_{mm} bins because of the additional PCAL detector. The efficiency result of the CLAS12 data increase with increasing the missing momentum of the neutron, and plateaus at about 78%, while the plateaus of the CLAS6 at about 60%.

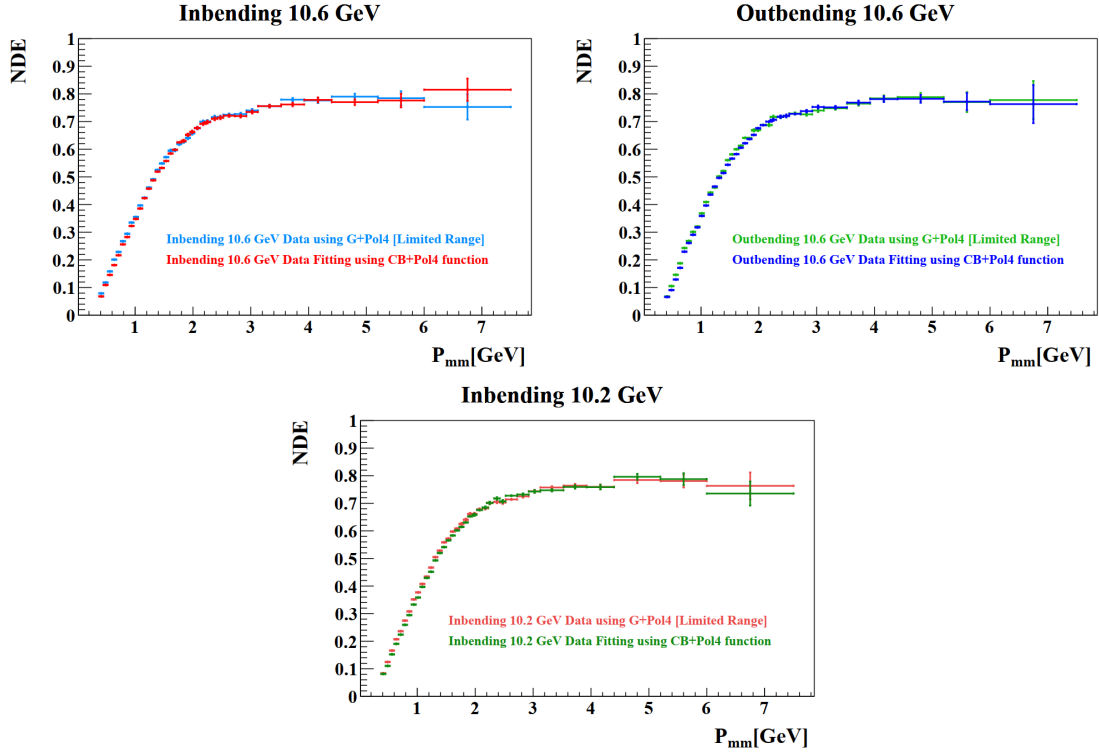


Figure 3.26: A comparison of the neutron detection efficiency in the CLAS12 calorimeters detector between the Gaussian and the Crystal Ball fitting, binned in missing momentum of neutron. The comparison shows inbending 10.6 GeV (Top Left), outbending 10.6 GeV (Top Right) and inbending 10.2 GeV (Bottom).

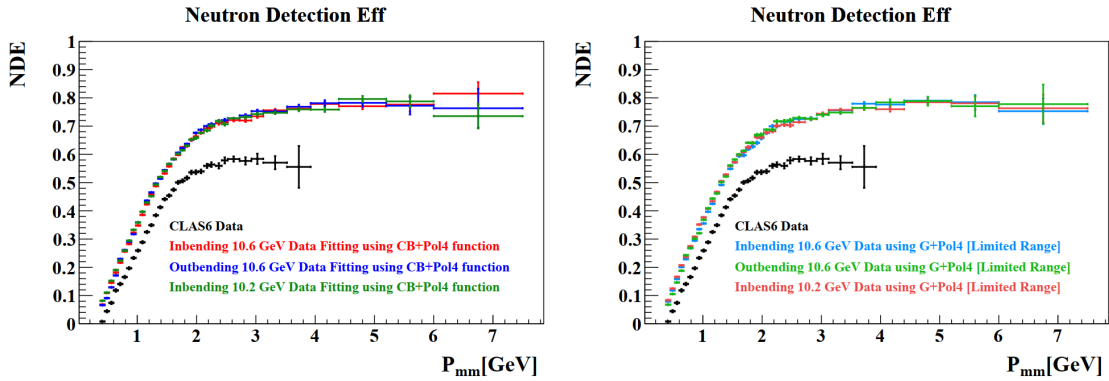


Figure 3.27: The neutron detection efficiency in the calorimeter detector was extracted from the Gaussian (Right) and the Crystal Ball function (Left), binned in missing momentum of the neutron, for each dataset and compared with the CLAS6 result.

3.10 NDE Parameterization

In order to use the NDE results for G_M^n , we need a functional form that can describe these results. The neutron detection efficiency as a function of the missing momentum, P_{mm} , is fitted using a least-squares method with the following function:

$$\begin{aligned} \eta(P_{mm}) &= a_0 + a_1 P_{mm} + a_2 P_{mm}^2 + a_3 P_{mm}^3 && \text{for } P_{mm} < p_t \\ &= a_4 \left(1 - \frac{1}{1 + \exp \frac{P_{mm} - a_5}{a_6}} \right) && \text{for } P_{mm} \geq p_t, \end{aligned} \quad (3.30)$$

where a_0 , a_1 , a_2 , a_3 , a_4 , a_5 , a_6 and p_t are the parameters of the fit. The boundary between the two parts of the fitting, p_t , is varied to find the best connection between them. The uncertainty of the fit at a given missing momentum can be calculated from the error matrix:

$$\sigma_\eta^2 = \sum_{i,j} \epsilon_{ij} \frac{\partial \eta}{\partial a_i} \frac{\partial \eta}{\partial a_j}, \quad (3.31)$$

where η is the value of the fitted function, a_i and a_j are the i^{th} and j^{th} parameters of the fit, respectively, and ϵ_{ij} is the value of the error matrix.

The fits and associated uncertainties are shown in Fig. 3.28 for a Crystal Ball function in the top and for a Gaussian function in the bottom. The black line shows the fit for the NDE result using the functions in Eq. 3.30. The right plots in Fig. 3.28 show the band of the uncertainty on the fits for both Crystal Ball (top) and Gaussian functions (bottom). Bottom plot in each panel shows the residuals, which lies close to zero as expected. Table. 3.7 summarizes the parameters of the fit results for the two functions.

Since two different functions are used to determine the NDE, the difference between the results can be considered as systematic uncertainty.

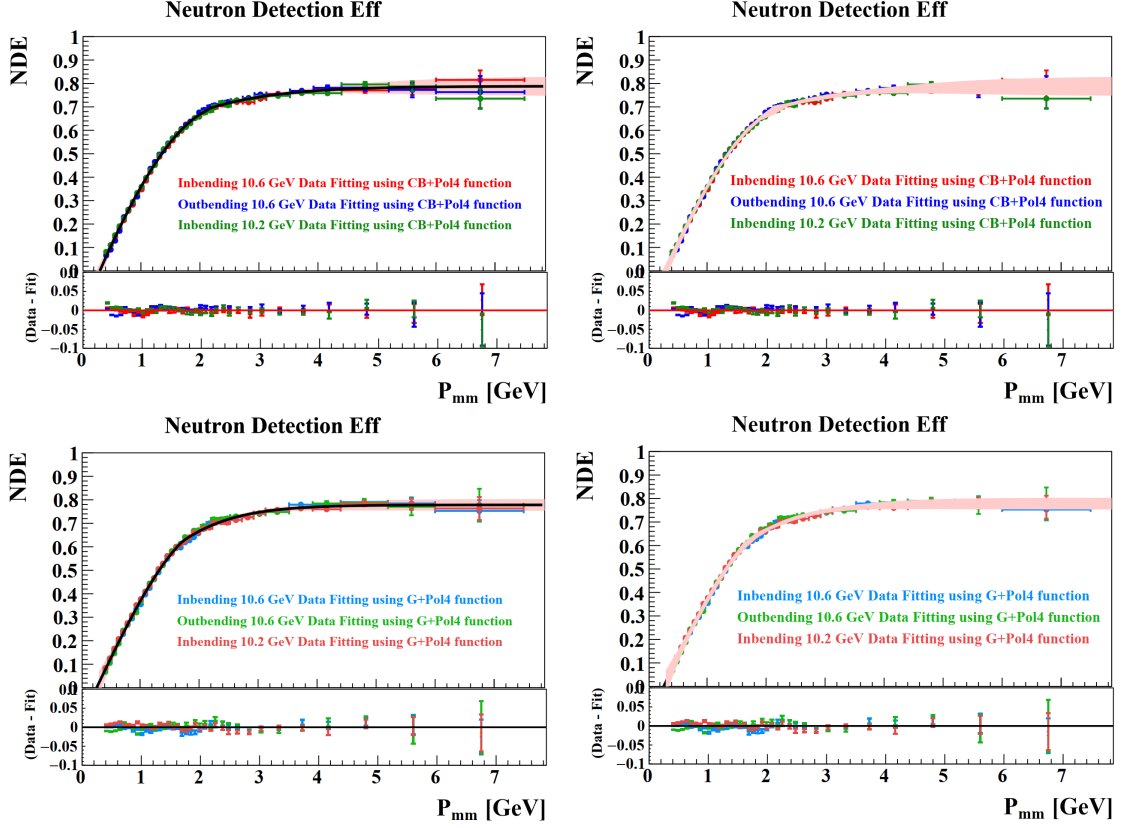


Figure 3.28: A fit of the neutron detection efficiency for the Crystal Ball function (top) and the Gaussian (bottom) according to Eq. 3.30. The uncertainty on the fit is shown as a band in the right hand side plots for the Crystal Ball function (top) and the Gaussian (bottom).

Fit Parameters	Gaussian Function	Crystal Ball Function
χ^2	0.7976	0.4813
a_0	-0.1404 ± 0.0172	-0.1817 ± 0.0136
a_1	0.5282 ± 0.0035	0.6187 ± 0.0375
a_2	0.01837 ± 0.0179	-0.0605 ± 0.0332
a_3	-0.0392 ± 0.0015	-0.0179 ± 0.0090
a_4	0.7784 ± 0.0044	0.7884 ± 0.0087
a_5	0.7057 ± 0.0698	0.0086 ± 0.3067
a_6	0.7278 ± 0.0507	1.0796 ± 0.1876
p_t	$1.7628 \pm 5.9e^{-0.8}$	2.146 ± 0.0001

Table 3.7: The fit parameters of the neutron detection efficiency.

CHAPTER 4

QUASI-ELASTIC RATIO MEASUREMENT

In this chapter, we focus on the measurement of the ratio used to extract G_M^n . We will start by discussing the data sets that have been used for this measurement. Next, we will describe the procedure used to select quasi-elastic $D(e, e'p)$ and $D(e, e'n)$. Finally, we will present the results of the ratio measurement.

4.1 RGB Run Period

The CLAS12 Run Group B (RG-B) data were taken over three periods: Spring of 2019, Fall of 2019 and Spring of 2020. A 5-cm-long liquid deuterium target were used with a polarized electron beam operating at three different beam energy (10.6, 10.2 and 10.4 GeV). Two different polarities of the torus magnet was used: outbending, where the track of a negative particle bends away from the beamline, and inbending, where the track of a negative particle bends toward the beamline. A summary of the run conditions are shown in Table 4.1. We analyzed each dataset separately. The outbending dataset was excluded from the analysis due to limited statistics.

Exp. Detail	In-bending	Out-bending	In-bending
Run Period	Spring 2019	Fall 2019	Spring 2020
Run Range	6156 - 6603	11093 - 11300	11323 - 11571
Number of runs	117 runs 106 runs	97 runs	171 runs
Beam	10.6 GeV 10.2 GeV	10.4 GeV	10.4 GeV
Target	Unpolarized LD2	Unpolarized LD2	Unpolarized LD2
Current	35-50 nA	40 nA	35-50 nA
Torus Field	-1	+1/+1.008	-1
Solenoid Field	-1	-1	-1

Table 4.1: RG-B run period conditions.

4.2 Events Selection

The data files analyzed are referred to as “gmn” files, which contain events of two channels: $D(e, e'n)$ and $D(e, e'p)$. In the $D(e, e'n)$ channel, the file included events where an electron was detected and all neutral particles are in the forward detector, while for $D(e, e'p)$ channel, the file contained events with both an electron and a positive charged particle detected in the forward detector. In both $D(e, e'n)$ and $D(e, e'p)$ channels, the electron identification requires the cuts discussed in Sec. 3.4 and summarized in Table. 4.2. For nucleon identification, different selections were made depending on the channel. In the $D(e, e'p)$ channel, a positively charged particle that hit the calorimeter was selected as a proton candidate, while in the $D(e, e'n)$ channel, neutral particles that hit the calorimeter were considered as neutron candidates as shown in Table. 4.2.

electron	proton	neutron
pid = 11 v_z vertex position $N_{ph} > 2$ PCAL fiducial V, W > 14 cm cut DC fiducial cut for 3 DC regions SF vs. $P_{ele} \pm 3.5\sigma$ Diagonal cut chi2pid $ \chi^2 < 3$ cut Minimum PCAL $E_{dep} > 60$ MeV	Positive charge particle hit calorimeter	Neutral charge particle hit calorimeter

Table 4.2: Cuts used for electron and nucleon identification.

Once a scattered electron has been identified in the $D(e, e'n)$ and $D(e, e'p)$ channels, the 4-momentum of a recoil nucleon (proton or neutron) can be calculated

assuming QE scattering as

$$\begin{aligned}
 P_e^\mu + P_N^\mu &= P_{e'}^\mu + P_{N'}^\mu, \\
 P_{N'}^\mu &= P_e^\mu + P_N^\mu - P_{e'}^\mu = h^\mu,
 \end{aligned}
 \tag{4.1}$$

where $P^\mu = (\vec{P}, E)$ is the 4-momentum for each particle, and N refers to either a proton or neutron. The square of the invariant mass of the nucleon can be written as

$$W^2 = h^\mu h_\mu,
 \tag{4.2}$$

where h_μ is the 4-momentum of the recoil nucleon.

4.3 Quasi-elastic Selection

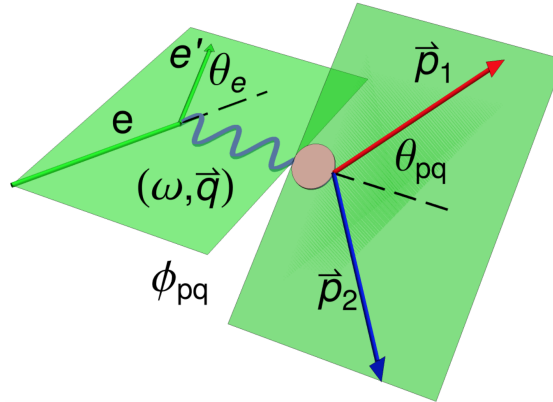


Figure 4.1: The kinematic quantities for $D(e, e'p)/D(e, e'n)$ shows the scattering plane that is defined by the 3-momenta of the incoming and scattered electrons and the reaction plane that is determined by the 3-momentum transfer, $\vec{q} = \vec{p}_{e'} - \vec{p}_e$, and the final proton/neutron 3-momentum, \vec{p}_1 . θ_{pq} is the angle between the direction of the detected nucleon \vec{p}_1 and the direction of the virtual photon \vec{q} .

In order to measure the ratio σ_n/σ_p and extract G_M^n , the Quasi-elastic peak of the $D(e, e'n)$ and $D(e, e'p)$ channels is selected. For the $D(e, e'p)$ channel, we required at least one electron in the forward detector and a positive charged particle hit

in the calorimeter. For the $D(e, e'n)$ channel, we required at least one electron in the forward detector and a neutron hit in the calorimeter. The distribution of the invariant mass W as a function of θ_{pq} (see Fig. 4.1), which is the angle between the direction of the detected nucleon (proton or neutron) and the direction of the virtual photon is shown in Fig. 4.2.

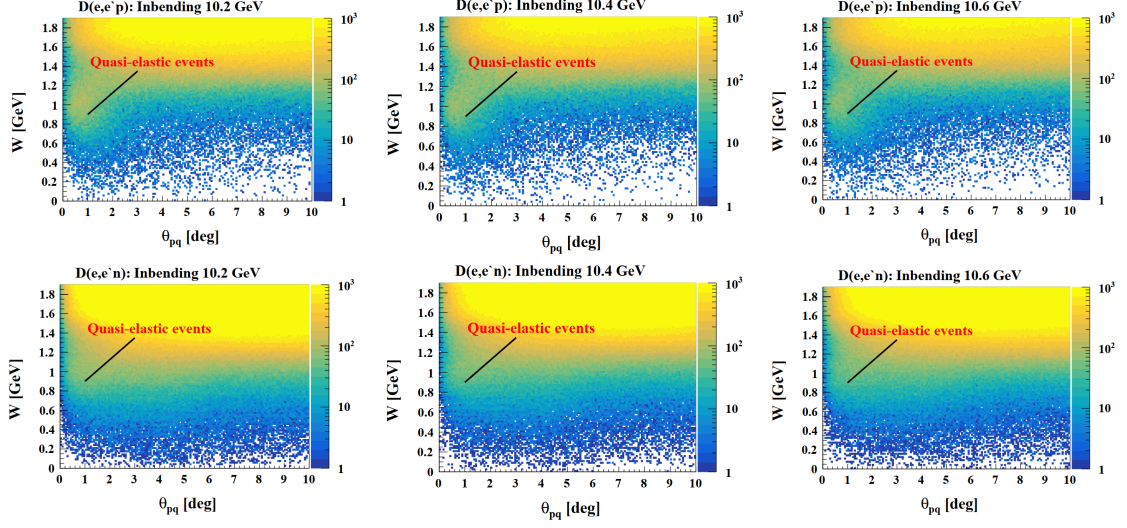


Figure 4.2: The invariant mass W distribution as a function of θ_{pq} for $D(e, e'p)$ (top) and $D(e, e'n)$ (bottom) for each data set.

The quasi-elastic events tend to be emitted close to the direction of the momentum transfer \vec{q} ($\theta_{pq} \sim 0^\circ$), while inelastic events are not. It is hard to observe the quasi-elastic peak of the $D(e, e'n)$ events compared to the $D(e, e'p)$ channel at this stage due to a large neutral background. The invariant mass W distribution of $D(e, e'p)$ and $D(e, e'n)$ channels, shown in Fig 4.3, show a significant amount of inelastic background events, which obscures the quasi-elastic peak of the nucleon. Therefore, several cuts need to be applied to reduce the inelastic background and make the peak of the proton and neutron masses visible. There are three cuts applied to select quasi-elastic events:

1. Incident electron beam energy cut.

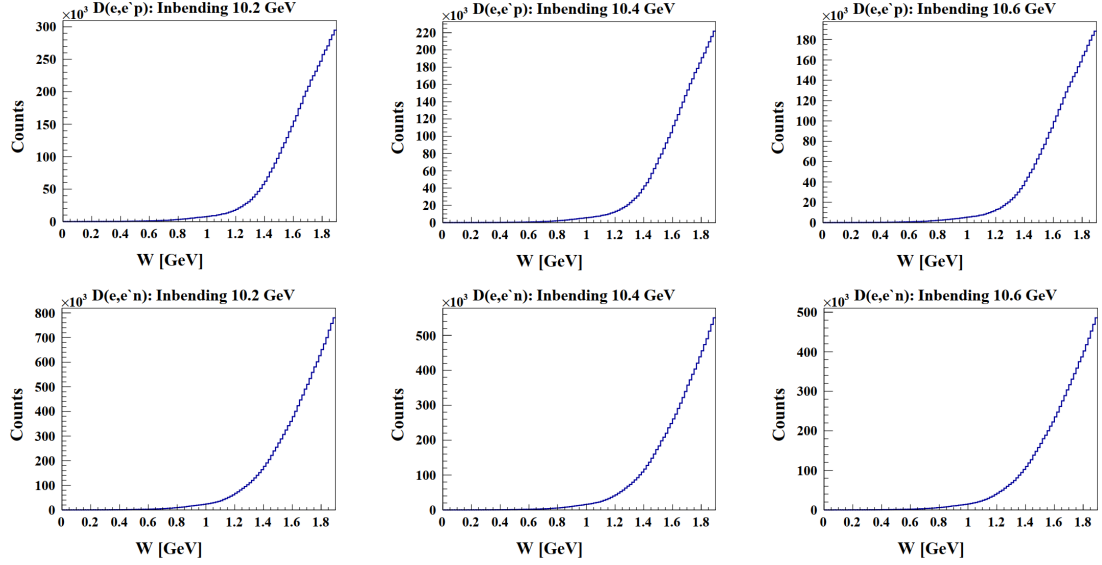


Figure 4.3: The invariant mass W distribution of $D(e, e'p)$ (top) and $D(e, e'n)$ (bottom) for each dataset.

2. $\Delta\phi$ cut
3. θ_{pq} cut.

Below we will discuss each cut in detail.

4.3.1 Incident Electron Beam Energy Cut

The incident electron beam energy can be calculated from the measured events in two different ways:

1. $E_{\text{beam}}^{\text{angles}}$: Using the scattering polar angles of the electron and the nucleon, measured by the CLAS12 forward detector, the beam energy is [86]:

$$E_{\text{beam}}^{\text{angles}} = \frac{m_N}{1 - \cos \theta_{e'}} \left(\cos \theta_{e'} + \cos \theta_{N'} \frac{\sin \theta_{e'}}{\sin \theta_{N'}} - 1 \right), \quad (4.3)$$

where m_N is the nucleon mass, $\theta_{e'}$, $\theta_{N'}$ are polar angles of scattered electron and nucleon, either proton or neutron, respectively.

2. $E_{\text{beam}}^{\text{from ele}}$: Using the scattering momentum and polar angle of the electron, measured by the CLAS12 forward detector, the beam energy is [87]:

$$E_{\text{beam}}^{\text{from ele}} = \frac{P_{e'}}{1 - 2P_{e'} \sin^2(\frac{\theta_{e'}}{2})/m_N}, \quad (4.4)$$

where $P_{e'}$ is the momentum of the scattered electron.

The correlation between $E_{\text{beam}}^{\text{angles}}$ and $E_{\text{beam}}^{\text{from ele}}$ for events satisfying $\theta_{pq} < 10^\circ$ is shown in Fig. 4.4. It is observed that the quasi-elastic events in the $D(e, e'n)$ channel exhibit a wider spread compared to the $D(e, e'p)$ channel, making it difficult to discern the peak in the $E_{\text{beam}}^{\text{angles}}$ distribution. To address this, a cut is applied on the invariant mass around the known nucleon mass, $0.85 < W < 1.05$ GeV, in order to reduce the inelastic background under the $E_{\text{beam}}^{\text{angles}}$ distribution. Subsequently, quasi-elastic events are selected by applying sector-dependent cuts on the $E_{\text{beam}}^{\text{angles}}$ distribution. Figures 4.5 and 4.6 show the $E_{\text{beam}}^{\text{angles}}$ distributions for $D(e, e'p)$ and $D(e, e'n)$ for each sector, respectively. These distributions satisfied the criteria of $0.85 < W < 1.05$ GeV, and $\theta_{pq} < 10^\circ$ cuts, thereby capturing the peak corresponding to the incident beam energy. It is clearly seen that the $E_{\text{beam}}^{\text{angles}}$ distribution is wider for neutrons compared to protons because of the better angle resolution for charged particles due to the drift-chamber angle measurement that is not available for neutral particles. The cut used for quasi-elastic selection corresponds to 1σ on the Gaussian function fit to the central peak.

4.3.2 $\Delta\phi$ Cut

It is expected for quasi-elastic scattering that the electron and nucleon will lie in or nearly in the same plane. The difference in the lab azimuthal angle between the nucleon and the scattered electron ($\Delta\phi = \phi_{N'} - \phi_{e'}$) is used to select the quasi-elastic events. This particular cut becomes necessary for the $D(e, e'n)$ channel, where some

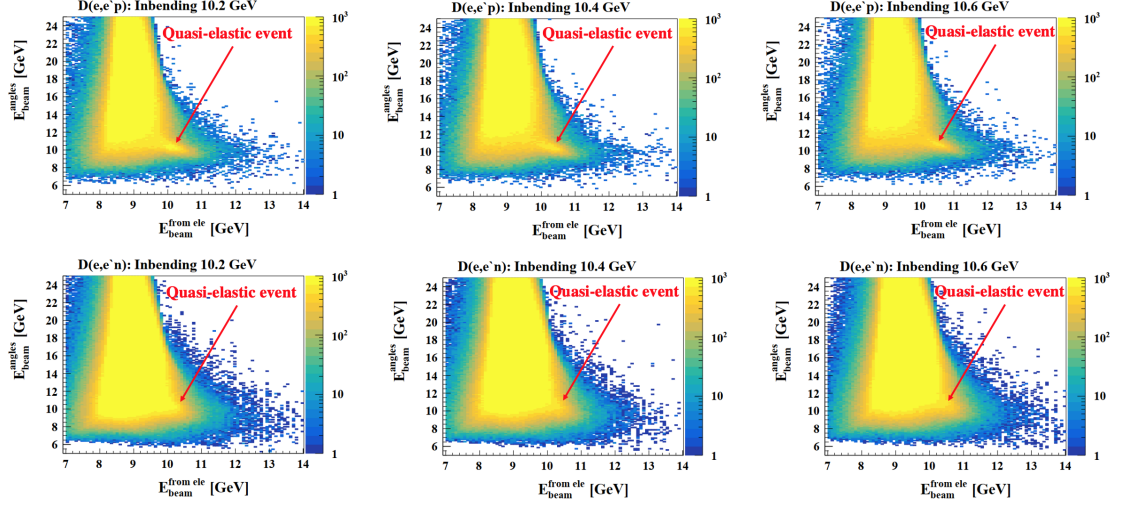


Figure 4.4: The $E_{\text{beam}}^{\text{angles}}$ vs. $E_{\text{beam}}^{\text{from ele}}$ distributions for $D(e, e'p)$ (top) and $D(e, e'n)$ (bottom) that satisfied $\theta_{pq} < 10^\circ$ cut for each dataset.

background remains even after applying the incident beam energy cut ($E_{\text{beam}}^{\text{angles}}$), as shown in Fig. 4.7. This background is most likely due to photon contamination. The cut applied corresponds to 1σ on the Gaussian function fit to the central peak. These cuts are tight in order to select as clean of a sample of quasi-elastic events as possible for $D(e, e'n)$ channel. For consistency, the same cut (1σ on the Gaussian) is applied for the $D(e, e'p)$ channel.

4.3.3 θ_{pq} Cut

The distribution of the Q^2 as a function of θ_{pq} for $D(e, e'p)$ and $D(e, e'n)$ events that satisfied $0.85 < W < 1.05$ GeV, $\theta_{pq} < 10^\circ$, $E_{\text{beam}}^{\text{angles}}$ and $\Delta\phi$ cuts are shown in Fig 4.8. The quasi-elastic events depend on the Q^2 value, where the distribution of quasi-elastic events is narrow at higher Q^2 values and becoming broader as the Q^2 range decreases.

To select quasi-elastic events while minimizing background contamination in the

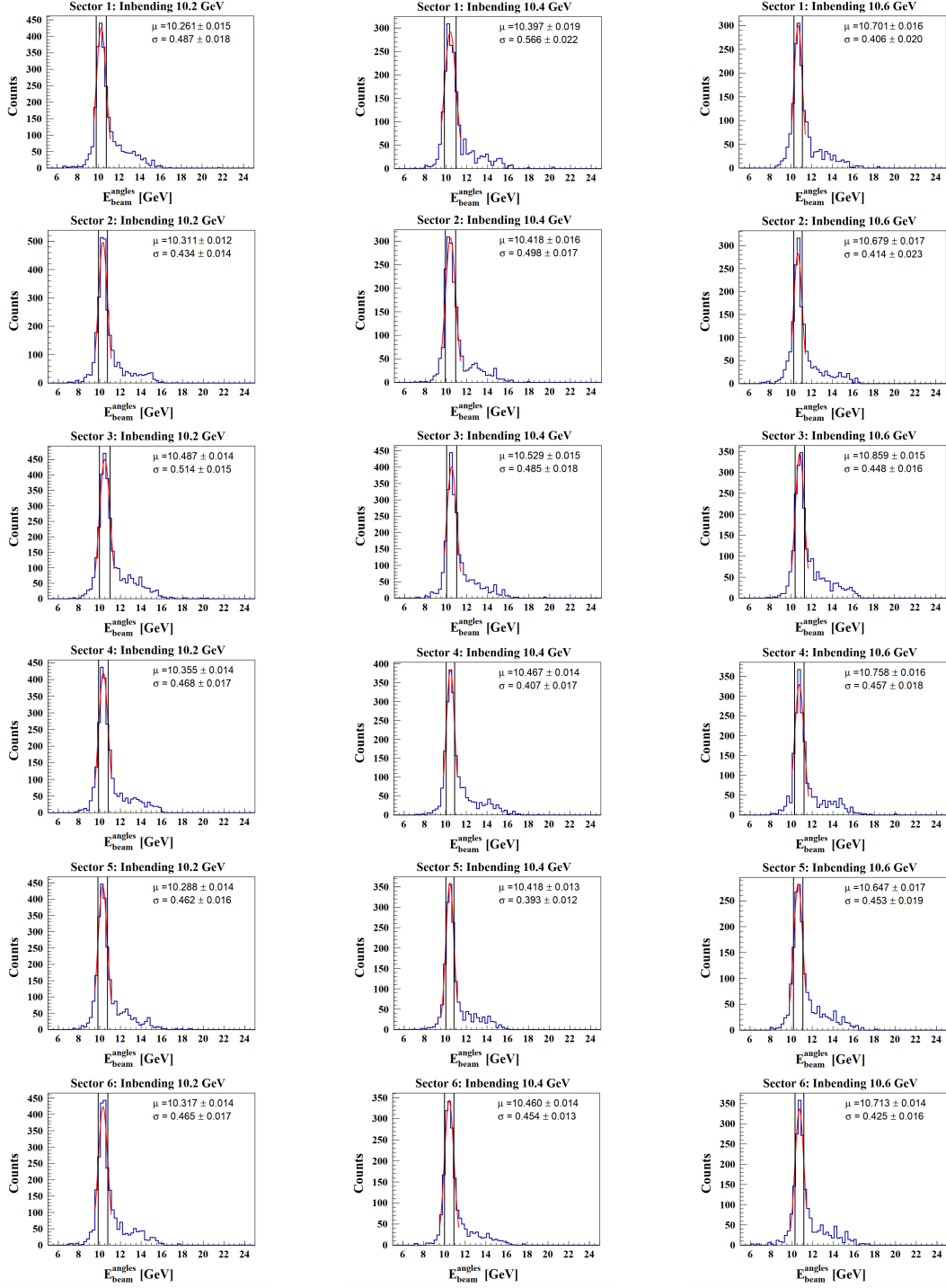


Figure 4.5: The $E_{\text{beam}}^{\text{angles}}$ distributions of $D(e, e'p)$ events that satisfied $0.85 < W < 1.05$ GeV and $\theta_{pq} < 10^\circ$ cut for each sector. The black vertical lines show the cut applied within 1σ .

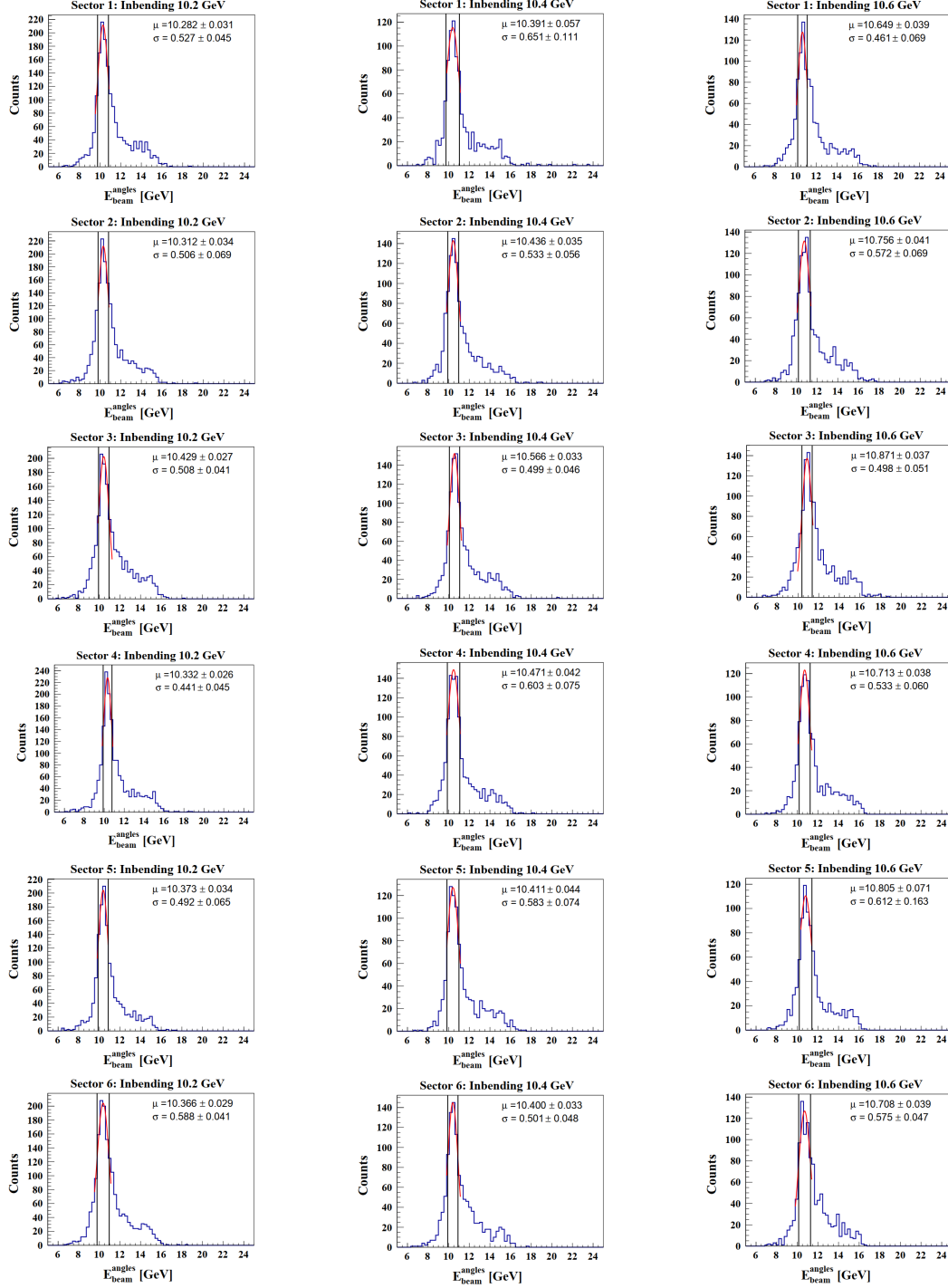


Figure 4.6: The $E_{\text{beam}}^{\text{angles}}$ distributions of $D(e, e'n)$ events that satisfied $0.85 < W < 1.05$ GeV and $\theta_{pq} < 10^\circ$ cut for each sector. The black vertical lines show the cut applied within 1σ .

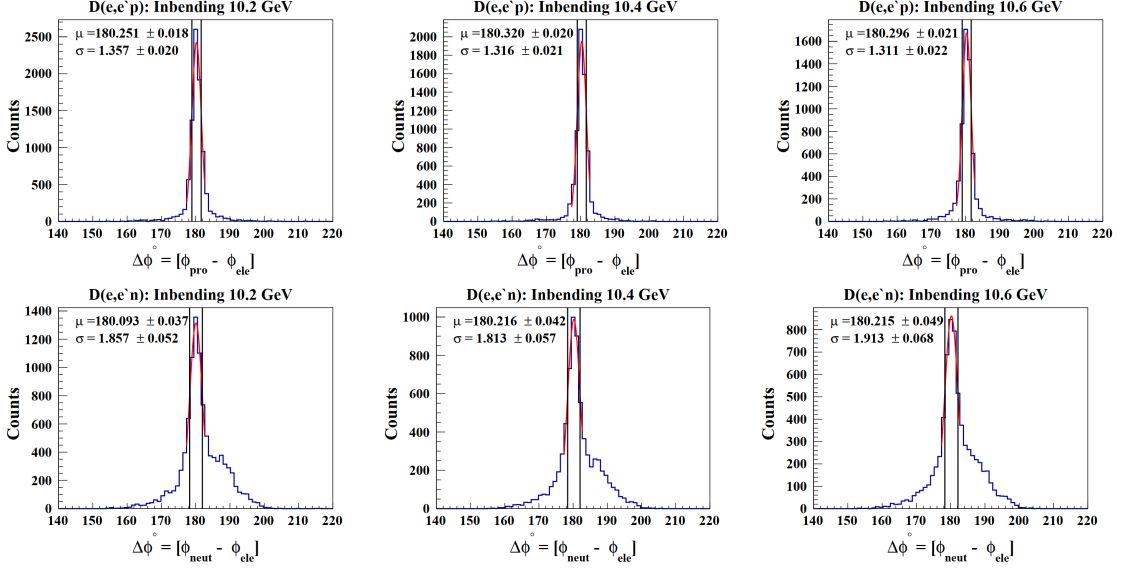


Figure 4.7: The $\Delta\phi$ distributions for events passing cut on $0.85 < W < 1.05$ GeV, $\theta_{pq} < 10^\circ$ and $E_{\text{beam}}^{\text{angles}}$ cuts for $D(e, e'p)$ (top) and $D(e, e'n)$ (bottom) for each datasets. The black vertical lines show the cut applied within 1σ .

absence of the W cut, a function is introduced as follows:

$$f(\theta_{pq}) = 2.5204 + \frac{6.2127}{\theta_{pq}^{0.9003}}. \quad (4.5)$$

This function, defined using the TCut feature of the ROOT data analysis framework, is used as a cut in both $D(e, e'p)$ and $D(e, e'n)$ channels. The cuts applied are $Q^2 < f(\theta_{pq})$ and $\theta_{pq} < 2^\circ$ and is shown in Fig. 4.8 as a red curve. It's important to mention that the selection of the $\theta_{pq} < 2^\circ$ cut was done visually. However, it should be noted that this cut will be varied during the systematic uncertainty analysis.

The W distribution of the quasi-elastic events for both $D(e, e'p)$ and $D(e, e'n)$ that satisfied $E_{\text{beam}}^{\text{angles}}$, $\Delta\phi$ and θ_{pq} cuts are shown in Fig 4.9. These distributions clearly show the clean quasi-elastic peaks for both the $D(e, e'p)$ and $D(e, e'n)$ channels.

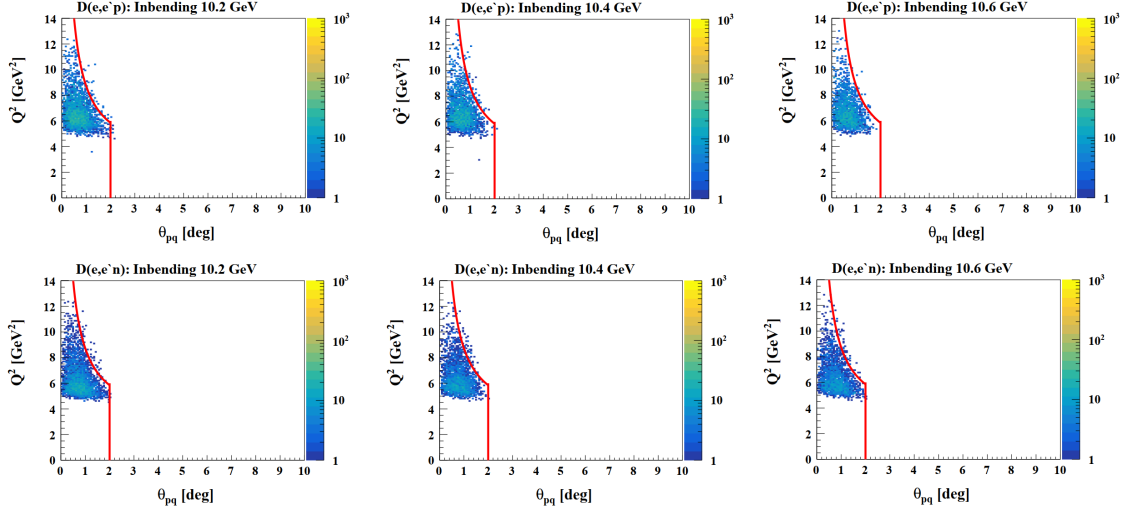


Figure 4.8: The Q^2 as a function of θ_{pq} distribution for $D(e, e'p)$ (top) and $D(e, e'n)$ (bottom) for each datasets that satisfied $0.85 < W < 1.05$ GeV, $E_{\text{beam}}^{\text{angles}}$ and $\Delta\phi$ cuts. The red curve is the cut used to select the quasi-elastic events.

4.4 Acceptance Matching

To measure the ratio of neutron to proton cross sections, σ_n/σ_p , correctly, it is important to account for the geometric acceptance for each $D(e, e'p)$ and $D(e, e'n)$ channel. To ensure that both neutrons and protons have the same acceptances, a common fiducial region is required. This can be done by using the acceptance matching technique as shown in Fig. 4.10 and described as follows.

1. In each event, the expected 3-momentum of the nucleon (either neutron or proton) is determined based on the measured electron kinematics and assuming elastic scattering and nothing else.
2. For each event we start with a good electron and assume the nucleon is a neutron first. Then, we swim it through the CLAS12 detector system by drawing a straight line from the electron vertex in the direction of the expected 3-momentum of the neutron. This path is “swum” through the CLAS12 detector system to see if the track strikes the fiducial volume of the calorimeter.

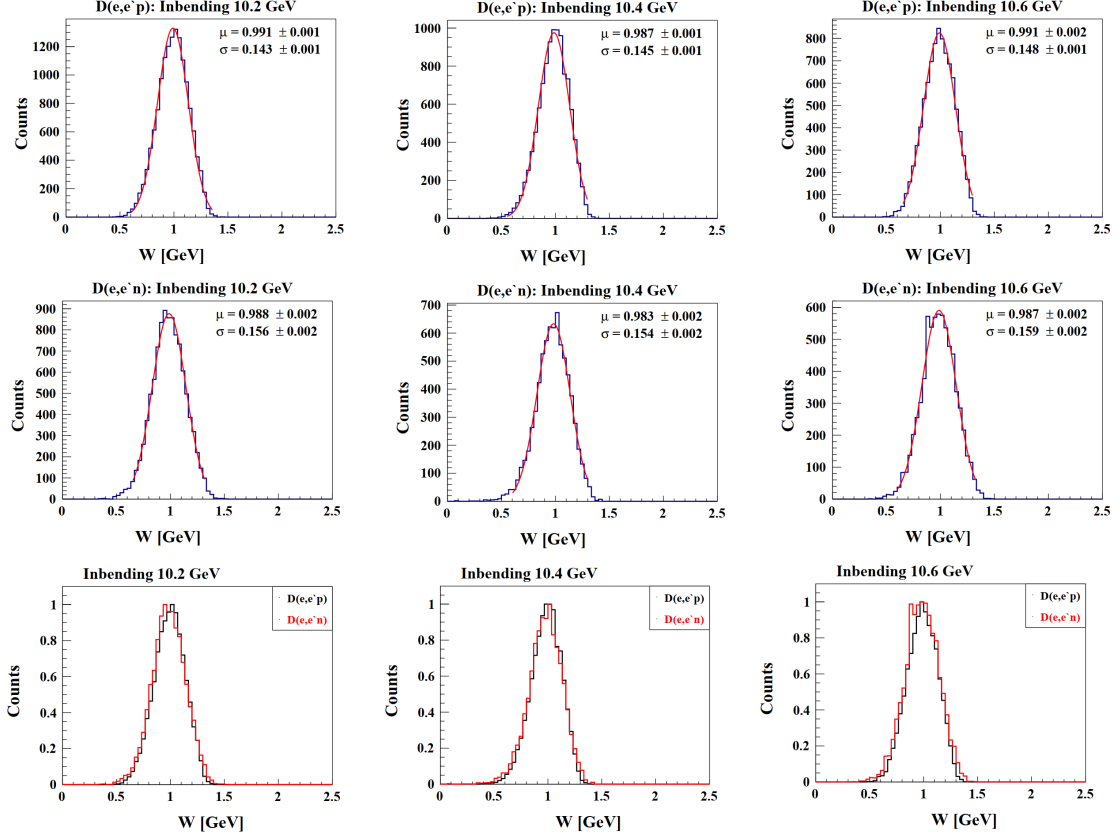


Figure 4.9: The W distribution for $D(e, e'p)$ (top) and $D(e, e'n)$ (middle) for each dataset that satisfied $E_{\text{beam}}^{\text{angles}}$, $\Delta\phi$ and θ_{pq} cuts. The bottom plots shows the comparison between $D(e, e'p)$ and $D(e, e'n)$ channels. The counts are scaled by normalizing the peak of the $D(e, e'p)$ and $D(e, e'n)$ events.

If it hits the ECAL and is at least 10 cm away from the edge of the calorimeter the analysis continues. If it misses, the entire event is dropped.

3. If the event passes step 2 above, we then assume the expected nucleon is a proton. The charged particle track of the proton is “swum” from the electron vertex through the magnetic field of CLAS12 towards the calorimeter. If this charged track also strikes the ECAL fiducial volume and is at least 10 cm away from the edge, the entire event is kept. Otherwise the event is dropped.

The acceptance matching technique described above is performed twice, once for the $D(e, e'p)$ channel and once for the $D(e, e'n)$ channel. The hit position of the swum

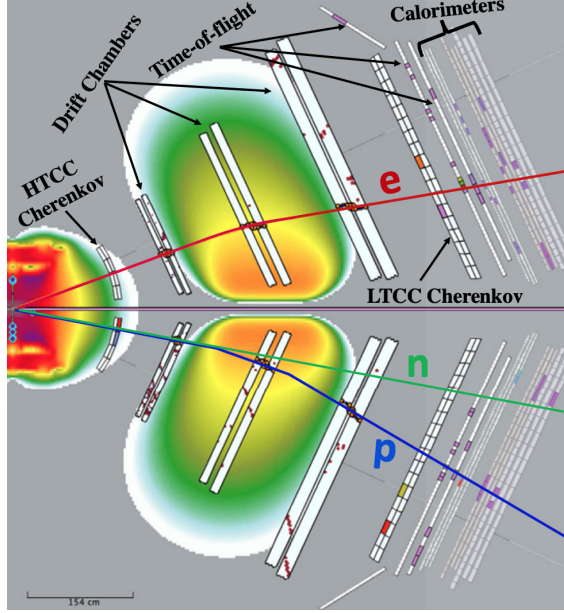


Figure 4.10: Acceptance matching using the “swimming” technique for negative torus polarity “inbending” field, where the electron is bent toward the beam line. By requiring both swum-neutron and swum-proton tracks to hit the calorimeters, the geometric acceptance of $D(e, e'p)$ and $D(e, e'n)$ are equal.

particles within the fiducial region of the calorimeter is shown in Fig. 4.11 for these channels. The different hit positions of protons and neutrons within the fiducial region of the calorimeter are due to the protons being deflected by the magnetic field in the detector, while neutrons are not affected by the magnetic field.

4.5 Uncorrected Ratio Results

Events that satisfy the quasi-elastic selection cuts and pass acceptance matching are used to fill two histograms, one for neutron events and one for proton events. They are binned in Q^2 , and each bin in the histogram contains the count of events (either proton or neutron). The ratio measurement is calculated by dividing each

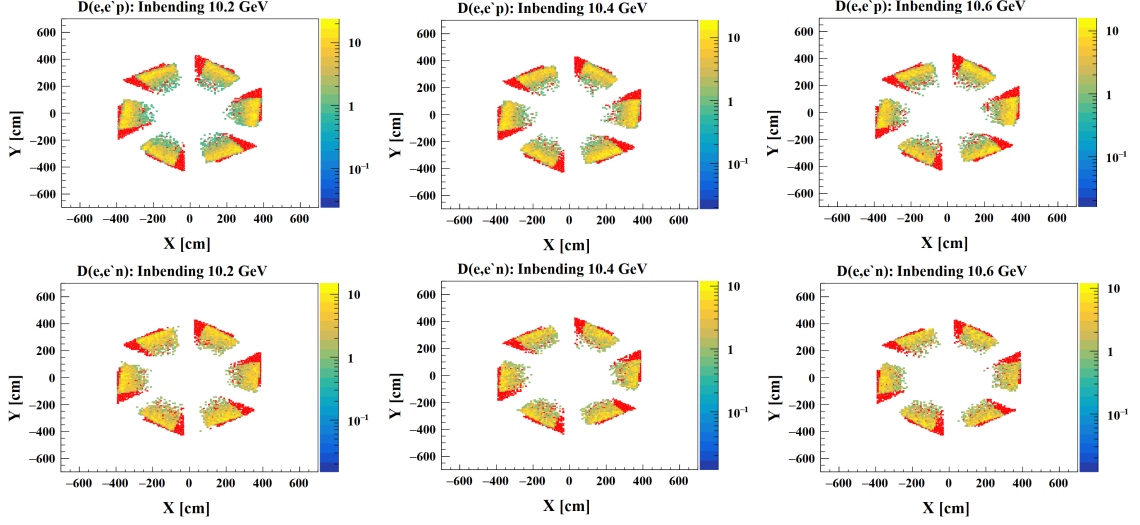


Figure 4.11: The distribution of the swum neutron (yellow points) and swum proton (red points) in the $x-y$ plane of the ECAL for $D(e, e'p)$ (top) and $D(e, e'n)$ (bottom) for each data set.

bin in the neutron histogram by the corresponding bin in the proton histogram:

$$R_{\text{meas}}^i = \frac{b_{\text{neut}}^i}{b_{\text{pro}}^i}, \quad (4.6)$$

where b_{neut}^i and b_{pro}^i are the number of neutron and proton events found in the i^{th} Q^2 bin, respectively. The uncertainty on each bin in the ratio histogram is given by the propagation of errors formula:

$$\sigma_{R_{\text{meas}}^i} = \sqrt{\left(\frac{\partial R_{\text{meas}}^i}{\partial b_{\text{neut}}^i}\right)^2 \sigma_{b_{\text{neut}}^i}^2 + \left(\frac{\partial R_{\text{meas}}^i}{\partial b_{\text{pro}}^i}\right)^2 \sigma_{b_{\text{pro}}^i}^2}, \quad (4.7)$$

where R_{meas}^i represents the value of the ratio measurement in the i^{th} bin, $\sigma_{b_{\text{pro}}^i}^2$ and $\sigma_{b_{\text{neut}}^i}^2$ are the uncertainties of the number of proton and neutron entries in that bin, respectively. Fig. 4.12 shows the ratio measurements from different data sets, showing the consistency of the ratio results at different beam energies.

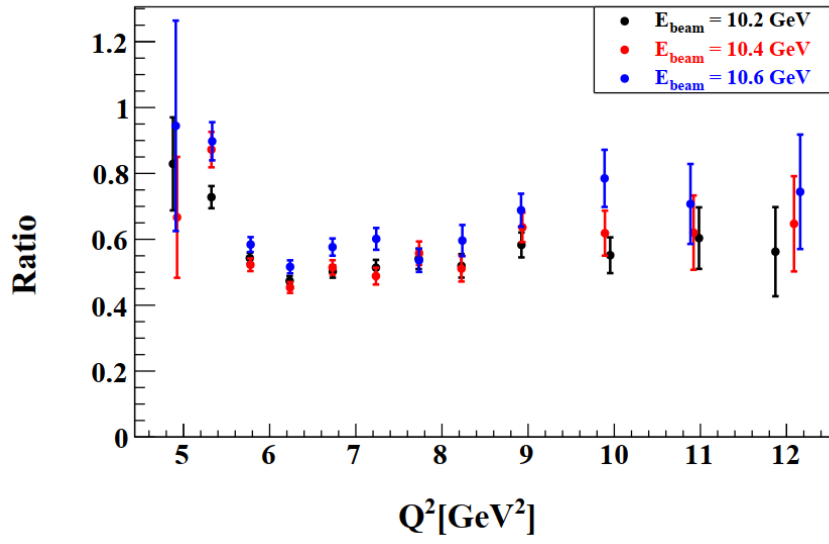


Figure 4.12: The σ_n/σ_p ratio results from different data sets at three different beam energies 10.2, 10.4, and 10.6 GeV binned in Q^2 .

CHAPTER 5

CORRECTIONS TO QUASI-ELASTIC RATIO

This chapter will discuss the corrections to the ratio measurements. These corrections include neutron efficiency (NDE), Fermi motion of the nucleons within the deuteron, and radiative effects. At the present time, we do not have corrections for the proton detection efficiency or for nuclear-interaction effects.

5.1 NDE Corrections to the Ratio

The neutron detection efficiency (NDE) was calculated and detailed in Chapter 3. To implement NDE correction, we used the functional form in Eq 3.30, that is discussed in Sec. 3.10. At this stage, we used the Crystal Ball parametrization in Table 3.7 due to its ability to fit a higher range of missing mass values. However, it's important to note that the Gaussian parametrization will also be taken into consideration as part of the systematic uncertainty analysis.

The $D(e, e'n)$ events that satisfy both the quasi-elastic selection cuts in Sec 4.3 and pass acceptance matching are used to fill a histogram. This histogram is binned in Q^2 and the entries are weighted by the reciprocal of the neutron detection efficiency calculated from the Crystal Ball function. The R_{Cor}^i ratio histogram is calculated by dividing each bin in the neutron weighted histogram by the corresponding bin in the proton $D(e, e'p)$ histogram:

$$R_{\text{Cor}}^i = \frac{b_{\text{neut}_w}^i}{b_{\text{pro}}^i}. \quad (5.1)$$

where R_{Cor}^i is the ratio corrected for the NDE in the i^{th} Q^2 bin, $b_{\text{neut}_w}^i$ is the efficiency-weighted number of neutron events found in that bin and b_{pro}^i is the number of proton events found in that bin. The uncertainty on each bin in this ratio histogram is given

by the propagation of errors formula:

$$\sigma_{R_{\text{Cor}}^i} = \sqrt{\left(\frac{\partial R_{\text{Cor}}^i}{\partial b_{\text{neut}_w}^i}\right)^2 \sigma_{b_{\text{neut}_w}^i}^2 + \left(\frac{\partial R_{\text{Cor}}^i}{\partial b_{\text{pro}}^i}\right)^2 \sigma_{b_{\text{pro}}^i}^2}, \quad (5.2)$$

Fig. 5.1 shows the R_{Cor}^i ratio in each Q^2 bin including the NDE correction from different data sets, showing the consistency of the ratio results at different beam energies. The results show that the NDE correction increases the ratio values by approximately 15% – 20%.

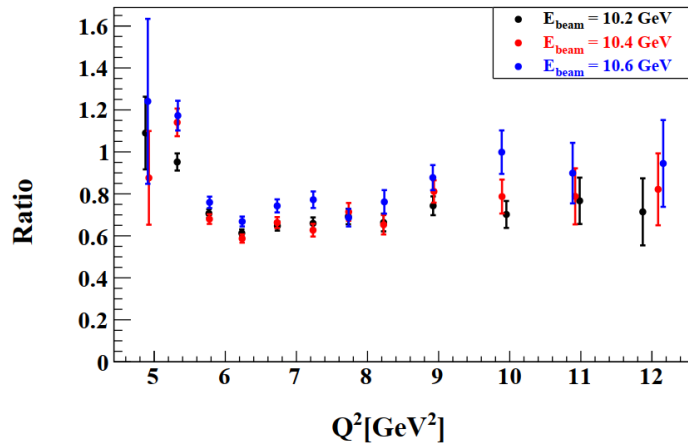


Figure 5.1: The σ_n/σ_p ratio results including NDE correction from different data sets at three different beam energies 10.2, 10.4, and 10.6 GeV binned in Q^2

5.2 Correction due to Fermi motion of the Target

In experiments where scattering involves a target nucleon in motion, such as in the case of the deuteron, the Fermi motion of nucleons within the deuteron can result in losses or migrations of scattered particles outside the acceptance region of the detector. For instance, if a scattered nucleon is expected to hit near the edge of the detector's acceptance region, the motion of the target nucleon due to Fermi motion may cause the scattered particle to move out of the acceptance region. This

can have an impact on the measured σ_n/σ_p ratio. To address and correct for these effects, Monte Carlo simulations are used. These simulations enable the estimation of the fraction of scattered nucleons expected to be removed from the acceptance by Fermi effects.

5.2.1 Simulating Quasielastic Scattering on Deuterium

The QUasi-Elastic Event Generator (QUEEG) is an event generator developed by J. D. Lachniet and used for the CLAS measurement of the neutron magnetic form factor and later extended by G. Gilfoyle in preparation of this experiment. It is designed to simulate quasielastic scattering events in the $D(e, e'p)$ and $D(e, e'n)$ reactions on a deuterium target. In QUEEG, the deuterium target is treated as a system composed of two on-shell nucleons. One nucleon acts as a spectator, while the other participates in the elastic scattering with the target nucleon. The generator uses the Hulthen distribution, which is a theoretical model that describes the bound state of the deuterium. QUEEG estimates the effects of Fermi motion, which is the motion of nucleons inside the nucleus. The Fermi-motion distribution inside the deuteron is calculated with the Hulthen distribution, as shown in Figure 5.2. More detail on the QUEEG generator can be found in [88].

In both quasi-elastic $D(e, e'p)$ and $D(e, e'n)$ channels, a total of 3.5 million events were generated using the QUEEG event generator, with incident beam energies of 10.2, 10.4, and 10.6 GeV. The simulated events are passed through the GEant4 Monte-Carlo (GEMC) and the CLAS12 reconstruction software [89]. The GEMC framework uses the GEant4 simulation toolkit for simulating the passage of particles through various materials and the CLAS12 detector components by considering the physical geometry, materials, and response characteristics.

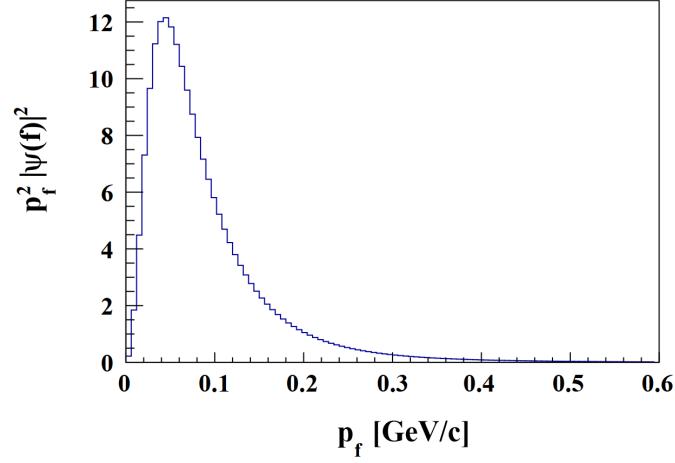


Figure 5.2: Fermi momentum distribution of nucleons inside the deuteron given by Hulthen model and generated by QUEEG.

5.2.2 Comparison to Data

The MC data has been analyzed in the same way as the experimental data. All cuts and corrections were made for the MC data in the same way as the experimental data. The comparison between the experimental data and the simulated events of electron kinematics for the $D(e, e'p)$ and $D(e, e'n)$ is shown in Fig. 5.3 and Fig. 5.4.

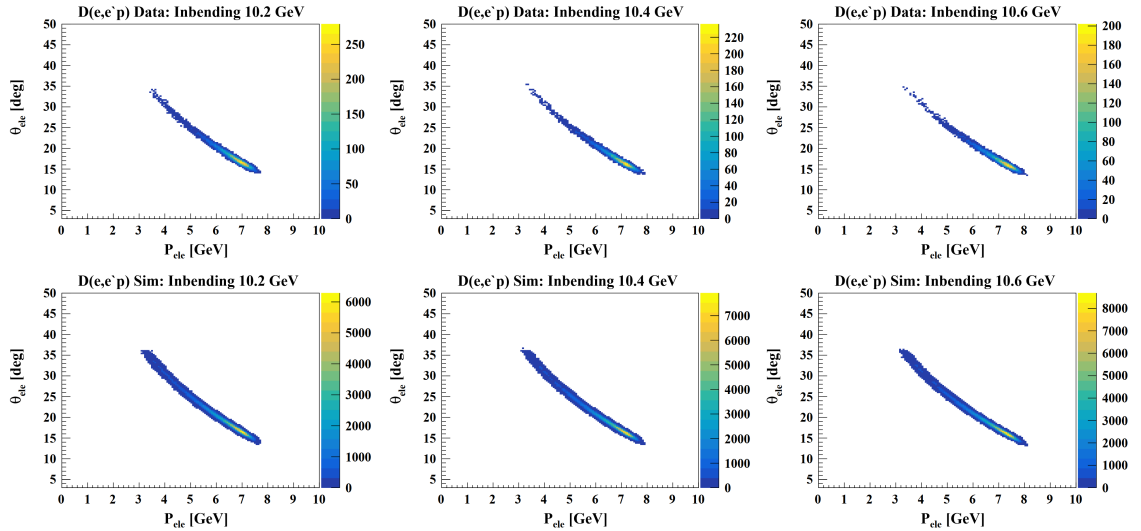


Figure 5.3: The polar angle of the reconstructed electron as a function of the momentum of electron for $D(e, e'p)$ quasi-elastic events for each data set. Top row is the data and bottom is the simulation.

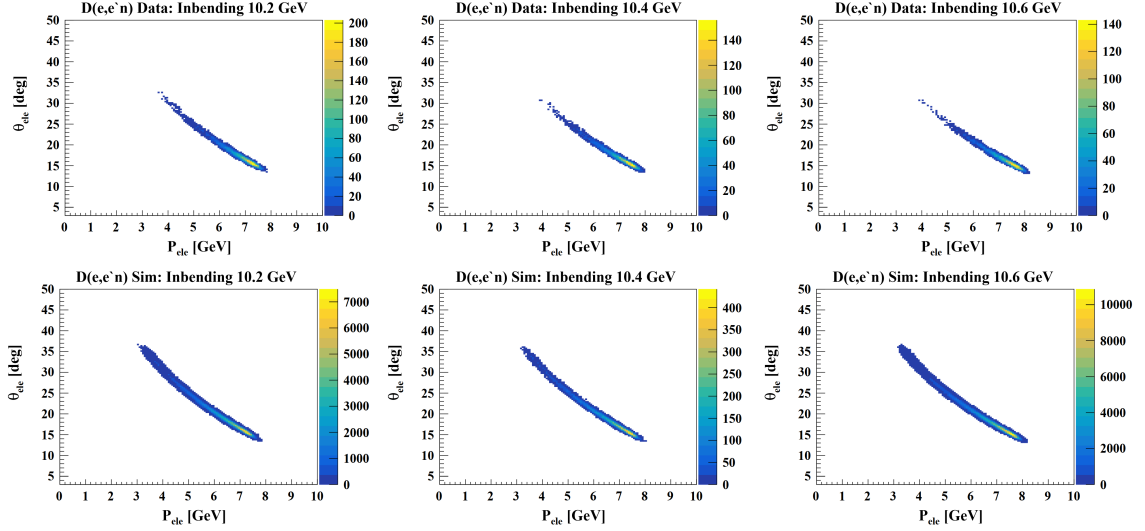


Figure 5.4: The polar angle of reconstructed electron as a function of the momentum of electron for $D(e, e'n)$ quasi-elastic events for each data set. Top row is the data and bottom is the simulation.

The comparison between the experimental and the simulated data of the invariant mass W that satisfy the quasi-elastic selection cuts and pass acceptance matching is shown in Fig. 5.5. The counts are scaled by normalizing the maximum histogram of both experimental and simulated data. Good agreement between the W distributions of the Monte Carlo results and data is found for each dataset.

5.2.3 Fermi-Loss Correction to the Ratio

The correction for the effects of Fermi loss in the R_{meas}^i ratio histogram is determined by filling two histograms. The first histogram consists of events where the nucleon is expected to be found inside the acceptance of the PCAL/ECAL detector. The expected nucleon location is determined using only the kinematic information of the scattered electron (this is the only available information in real data) and assuming elastic scattering off a stationary target. The second histogram consists of events where the scattered nucleon is actually found inside the acceptance of

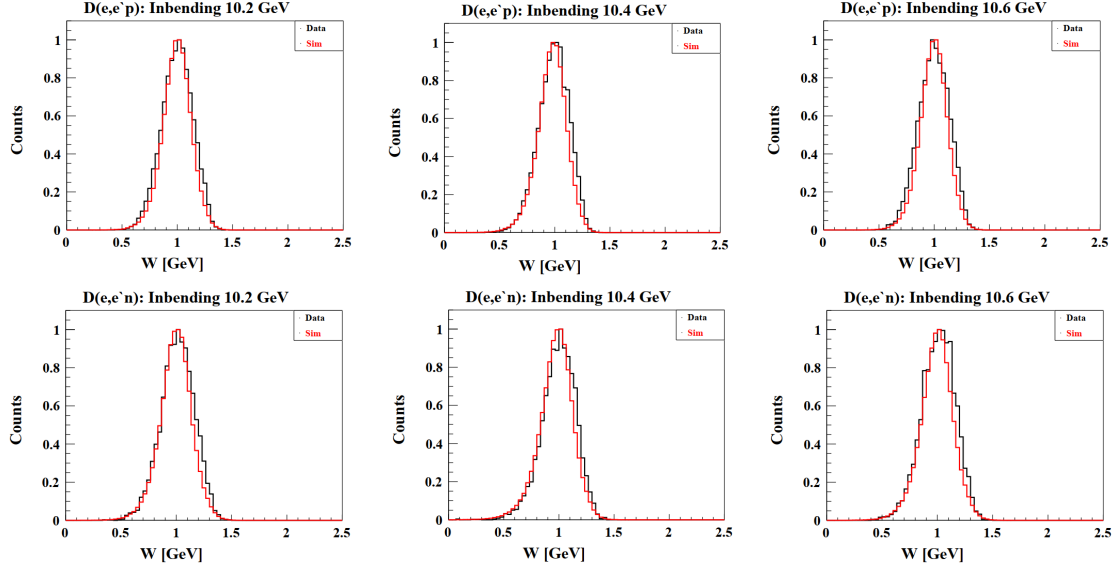


Figure 5.5: The W distribution for $D(e, e'p)$ (top) and $D(e, e'n)$ (bottom) for both experimental (black) and simulated (red) data that satisfied the quasi-elastic selection cuts and pass acceptance matching. The counts are scaled by normalizing the maximum histogram of both experimental and simulated data. The comparison is shown for incident beam energies of 10.2, 10.4 and 10.6 GeV.

the PCAL/ECAL detector and satisfies the θ_{pq} cuts described in Sec. 4.3.3. This determination uses the information about the scattered nucleon's momentum from the event generator, which is not available in real data. The ratio of these two histograms provides the fraction of nucleons that are lost due to the effects of Fermi motion, which moves the scattered nucleons outside the acceptance. The loss factor is calculated separately for neutrons and protons as a function of Q^2 and shown in Fig. 5.6.

To correct for the Fermi loss effects, each Q^2 bin in the R_{meas}^i ratio histogram is multiplied by the corresponding correction factor determined from the Fermi loss histograms:

$$R_{\text{Cor}}(Q^2) = \frac{f_{\text{pro}}(Q^2)}{f_{\text{neut}}(Q^2)} R_{\text{meas}}(Q^2) = f_{\text{fermi}}(Q^2) R_{\text{meas}}(Q^2), \quad (5.3)$$

where f_{pro} , f_{neut} are taken from the histograms in Fig. 5.6. The correction factor

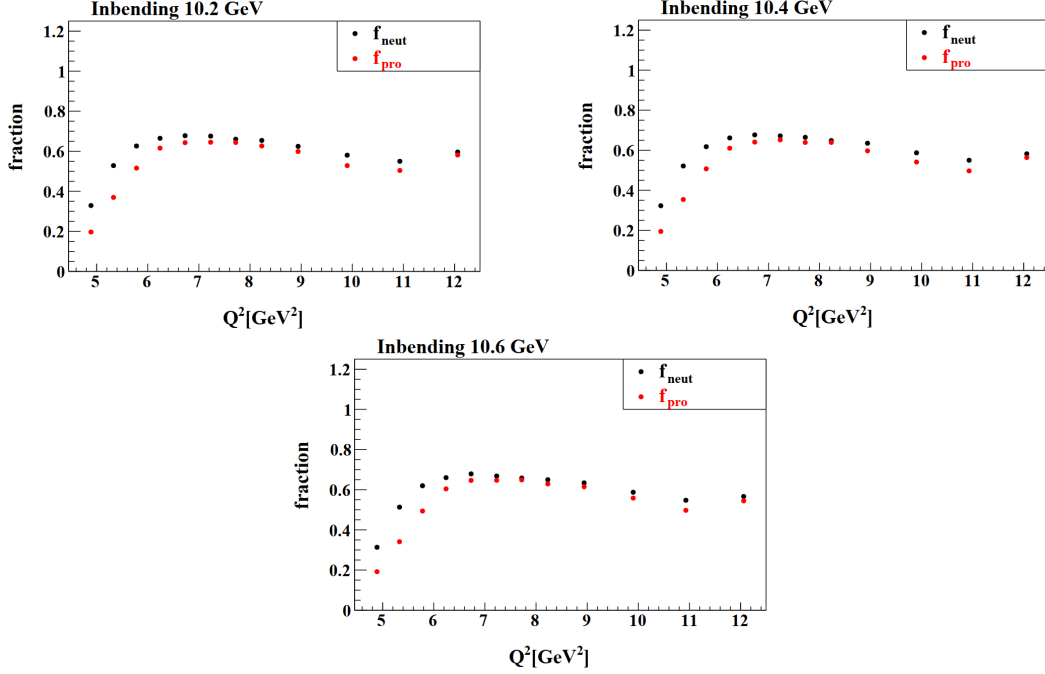


Figure 5.6: The fraction of nucleons at different Q^2 bins that scattered into the PCAL/ECAL acceptance and satisfied the θ_{pq} cuts and acceptance matching, as determined by simulation. The black points on the plot represent the neutron fraction, while the red points represent the proton fraction. These points were generated using an incident beam energy of 10.2, 10.4 and 10.6 GeV. The error bars on the plot are quite small and may not be easily observed.

for the R_{meas}^i ratio, which is $f_{\text{fermi}}(Q^2) = \frac{f_{\text{pro}}(Q^2)}{f_{\text{neut}}(Q^2)}$ is shown in Fig. 5.7 for the three different beam energy 10.2, 10.4 and 10.6 GeV. It's close to 1.0 above 6 GeV and its the same for all data sets.

The impact of applying Fermi loss corrections on the R_{meas}^i ratio histograms is shown in Figure 5.8 for each dataset. The results show that the Fermi correction has a varying impact on the ratio. For Q^2 values above 6 GeV 2 , the Fermi correction causes the ratio to decrease by approximately 1% to 5%, while for Q^2 values below 6 GeV 2 , the effect varies significantly, ranging from 10% to 40%.

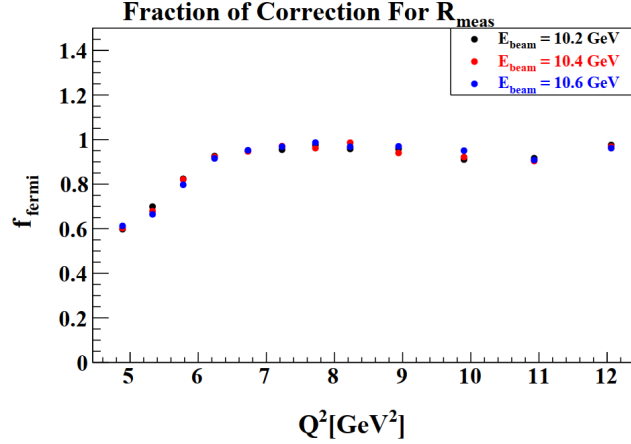


Figure 5.7: The correction factor, $f_{fermi}(Q^2) = \frac{f_{pro}(Q^2)}{f_{neut}(Q^2)}$, to the σ_n/σ_p ratio for Fermi loss in the PCAL/ECAL has been determined for the 10.2, 10.4 and 10.6 GeV data. The error bars on the plot are quite small and may not be easily observed.

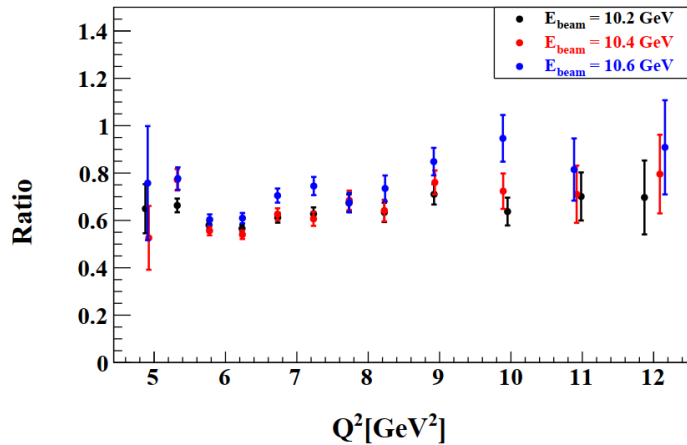


Figure 5.8: The σ_n/σ_p ratio results including NDE and Fermi corrections from data at three different beam energies 10.2, 10.4, and 10.6 GeV binned in Q^2

5.3 Radiative Correction

The desired cross section measurement assumes a single-photon exchange, which is known as Born scattering. However, there are other processes that effect the total measured cross sections. The electron in particular can emit photons when it is accelerated in the field of the target. Photons can be emitted before or after

the collisions and alter the final, detected electron energy. This effect on R_{meas}^i is considered here. The Feynman diagrams of the radiative effects for the electron are shown in Fig. 5.9. These diagrams illustrate the following radiative processes that are present in the measured events:

- the Bremsstrahlung, in which a photon is emitted by the incoming or outgoing electron, Fig. 5.9 b).
- the vertex correction, in which the photon is emitted by the incoming electron and absorbed by the outgoing electron, Fig. 5.9 c).
- the vacuum polarization, in which the virtual photon produces temporarily an e^+e^- pair, Fig. 5.9 d).

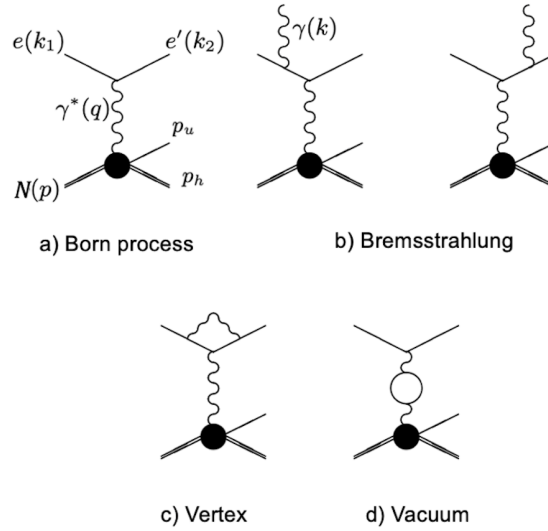


Figure 5.9: Feynman diagrams for Born term and lowest order radiative processes for the electron. The p_h and p_u are the momentum of the detected and undetected hadrons, respectively.

Including these other processes in the cross section can be done by multiplying the Born cross section by a radiative correction factor:

$$\frac{d\sigma}{d\Omega} = (1 + \delta) \left(\frac{d\sigma}{d\Omega} \right)_{\text{Born}}, \quad (5.4)$$

where $(\frac{d\sigma}{d\Omega})_{Born}$ is the single-photon-exchange cross section in Eq. 1.11, and the radiative correction factor $(1+\delta)$ comes from the bremsstrahlung, vacuum polarization and vertex corrections.

The radiative corrections (RC) for G_M^n were calculated by the program EXCLURAD. The EXCLURAD program is written by A. Afanasev [90] for exclusive pion electroproduction $p(e, e'\pi^+)n$, and it has been further modified by G. Gilfoyle [91] to include the radiative effects in the $D(e, e'p)n$ and $D(e, e'n)p$ channels. The response functions at the deuteron-virtual photon vertex, which describe the deuteron's response to the virtual photon, were calculated by W. Van Orden [92] and incorporated into the code. The EXCLURAD code contains the radiative correction for the electron only which is shown in the left of Fig. 5.9 and does not take into account the nucleon's radiative correction or the two-photon exchange.

The EXCLURAD code is used to generate the ratio of the radiated cross section to the cross section that would be measured if there were no radiative effects for specific kinematic variables. These variables include Q^2 (the square of the four-momentum transfer), W (the invariant mass of the hadronic final state), $\cos\theta_{pq}$ (the cosine of the polar angle between the virtual photon direction and the direction of the detected hadron), and ϕ_{pq} (the azimuthal angle between these directions).

The EXCLURAD code calculates the radiative correction factor for different values of Q^2 in $\cos\theta_{pq}$ and ϕ_{pq} surfaces. These surfaces represent the dependence of the radiative correction factor on the angles $\cos\theta_{pq}$ and ϕ_{pq} . To obtain the overall radiative correction factor at a specific Q^2 value, the generated surface is integrated over the experimental range of $\cos\theta_{pq}$ for that particular Q^2 value. The calculation is performed twice, once for the proton detection, channel $D(e, e'p)n$, and once for the neutron detection, channel $D(e, e'n)p$. Figures 5.10, 5.11, and 5.12 show the comparison of the radiative corrections factor for $D(e, e'p)n$ (red curve) and

$D(e, e'n)p$ (green curve) channels at $W = 2.60$ GeV, $\cos \theta_{pq} = 0.998^\circ$ at different Q^2 values for the 10.2 GeV, 10.4 GeV and 10.6 GeV data sets, respectively. There is a significant factor of correction in each $D(e, e'p)n$ and $D(e, e'n)p$ channel. However, the curves are close to each other and the difference between them is very small over the full range of the ϕ_{pq} values.

In the G_M^n measurement we are interested in the ratio of $D(e, e'p)n$ to $D(e, e'n)p$ corrections

$$f_{rad}(Q^2) = \frac{1 + \delta_p(Q^2)}{1 + \delta_n(Q^2)} = \frac{RC_p}{RC_n}, \quad (5.5)$$

where the subscripts (n, p) indicate the neutron and proton, respectively. Figure 5.13 shows the ratio of radiative corrections (f_{rad}), RC_p to RC_n , at various Q^2 values for the 10.2 GeV, 10.4 GeV, and 10.6 GeV data sets. This ratio varies from 1.0 by approximately 0.20% on average at low ϕ_{pq} values to 0.35% on average at high ϕ_{pq} values at each Q^2 bin. The differences between the smallest and the largest of the ratio of radiative corrections at each value of Q^2 in Fig. 5.13 will be considered as a systematic uncertainty.

To apply radiative corrections to the R_{meas}^i measurement, we used the average radiative correction over ϕ_{pq} values at each Q^2 point ($R_{cor} = f_{rad} \times R_{meas}^i$). The average radiative correction factors for RC_p and RC_n and the ratio of the average radiative correction f_{rad} over the ϕ_{pq} values at each Q^2 point for the 10.2 GeV, 10.4 GeV, and 10.6 GeV data sets are shown in Table 5.1. The radiative correction applied to the R_{meas}^i ratio measurement is shown in Fig. 5.14 for the three different beam energies (10.2, 10.4, and 10.6 GeV). These results show that the radiative correction does not significantly impact the ratio measurements.

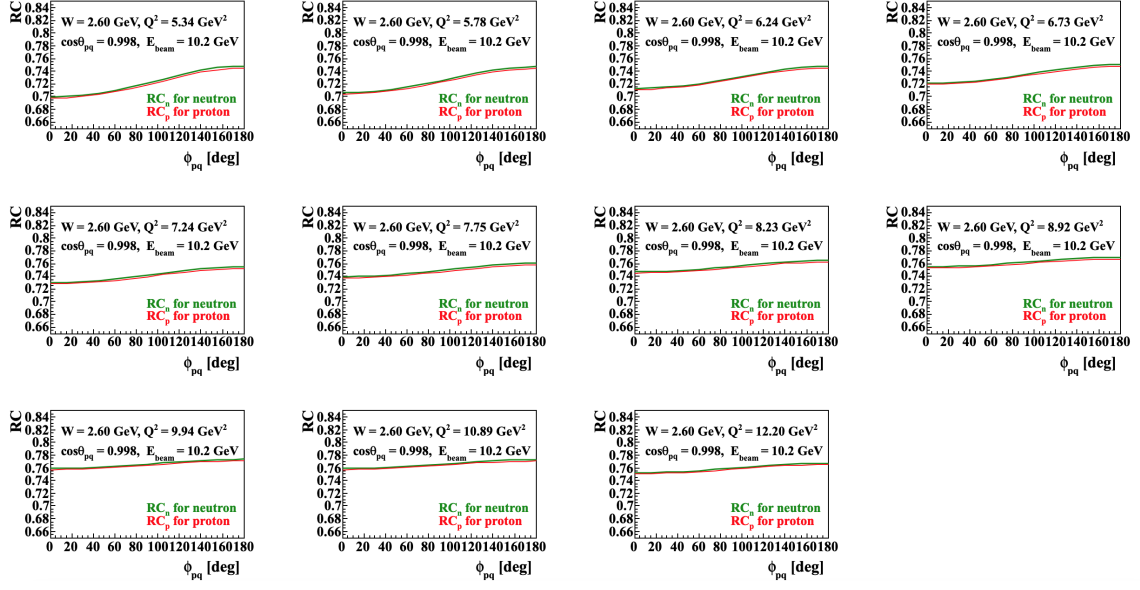


Figure 5.10: A comparison of the radiative correction factor, RC, for $D(e, e'p)n$ (red curve) and $D(e, e'n)p$ (green curve) as a function of ϕ_{pq} . The curves shown were generated for a beam energy of 10.2 GeV and $W = 2.60$ GeV at different Q^2 values.

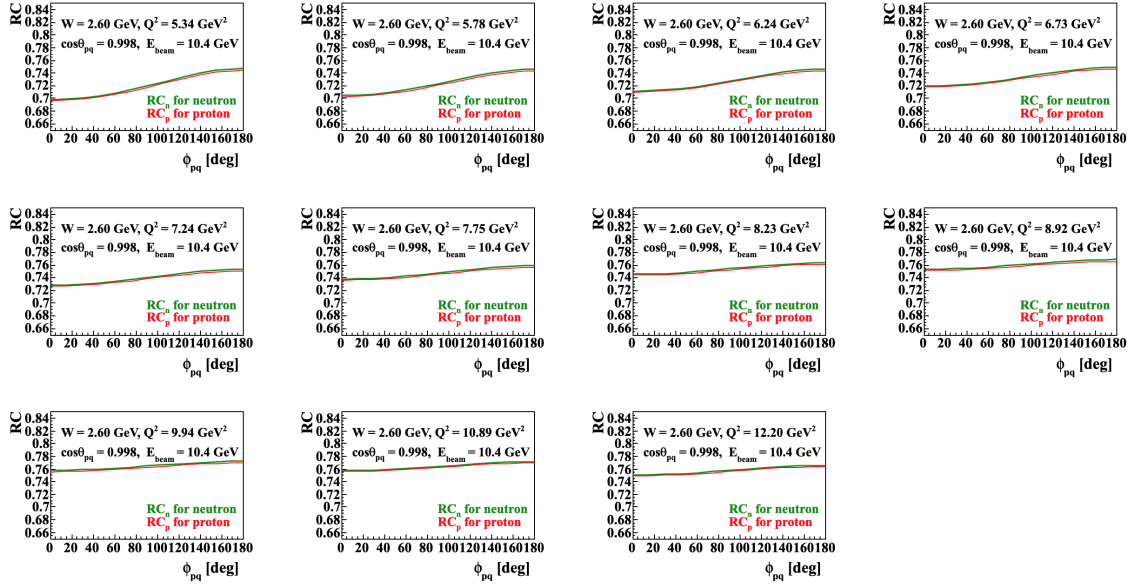


Figure 5.11: A comparison of the radiative correction factor, RC, for $D(e, e'p)n$ (red curve) and $D(e, e'n)p$ (green curve) as a function of ϕ_{pq} . The curves shown were generated for a beam energy of 10.4 GeV and $W = 2.60$ GeV at different Q^2 values.

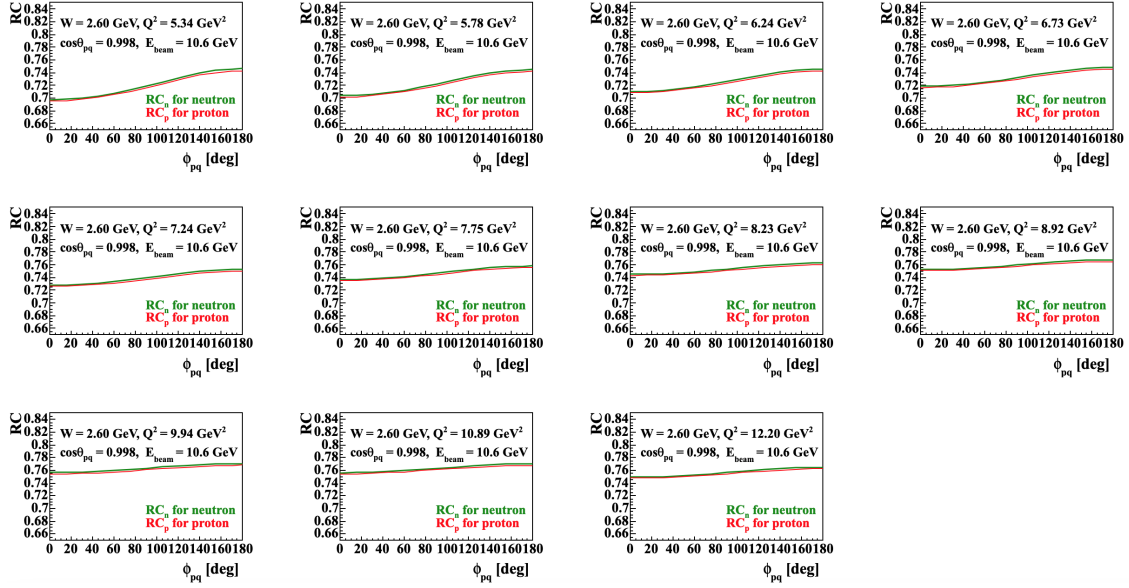


Figure 5.12: A comparison of the radiative correction factor, RC, for $D(e, e'p)n$ (red curve) and $D(e, e'n)p$ (green curve) as a function of ϕ_{pq} . The curves shown were generated for a beam energy of 10.6 GeV and $W = 2.60$ GeV at different Q^2 values.

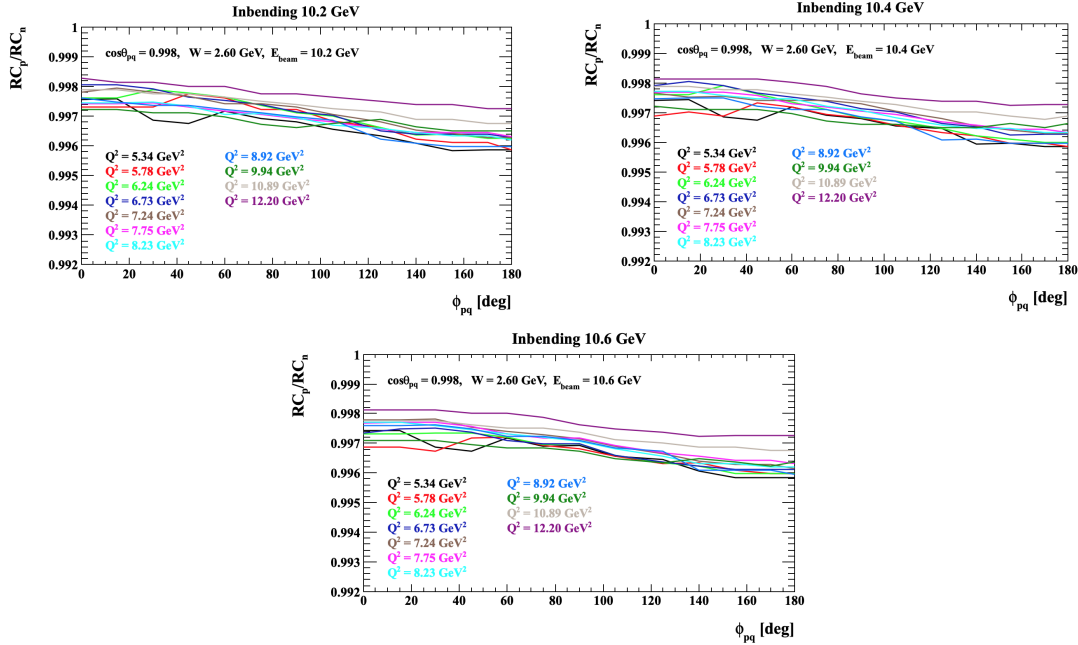


Figure 5.13: The ratio of the radiative correction of $D(e, e'p)n$ to $D(e, e'n)p$ at different Q^2 values for 10.2 GeV (top left), 10.4 GeV (top right) and 10.6 GeV (bottom middle). The average over the ϕ_{pq} values of these radiative correction are used to correct the ratio measurement in each Q^2 point.

Q^2 GeV ²	Inbending 10.2 GeV			Inbending 10.4 GeV			Inbending 10.6 GeV		
	RC _p	RC _n	f_{rad}	RC _p	RC _n	f_{rad}	RC _p	RC _n	f_{rad}
5.34	0.7205	0.7230	0.9966	0.7193	0.7218	0.9966	0.7181	0.7206	0.9966
5.78	0.7236	0.7259	0.9969	0.7222	0.7246	0.9966	0.7210	0.7234	0.9966
6.24	0.7277	0.7299	0.9971	0.7263	0.7286	0.9969	0.7250	0.7274	0.9967
6.73	0.7333	0.7354	0.9971	0.7320	0.7341	0.9971	0.7305	0.7328	0.9968
7.24	0.7402	0.7423	0.9971	0.7389	0.7411	0.9970	0.7376	0.7398	0.9970
7.75	0.7474	0.7497	0.9969	0.7462	0.7484	0.9970	0.7449	0.7471	0.9971
8.23	0.7537	0.7561	0.9969	0.7525	0.7548	0.9970	0.7512	0.7535	0.9970
8.92	0.7601	0.7625	0.9968	0.7587	0.7612	0.9967	0.7575	0.7599	0.9969
9.94	0.7638	0.7663	0.9968	0.7624	0.7649	0.9968	0.7610	0.7635	0.9967
10.89	0.7638	0.7659	0.9974	0.7624	0.7645	0.9973	0.76105	0.7631	0.9973
12.20	0.7578	0.7595	0.9977	0.7563	0.7581	0.9977	0.7549	0.7567	0.9977

Table 5.1: The average radiative correction values for 10.2, 10.4 and 10.6 GeV data set. These values are used to correct the ratio measurement in each Q^2 bin.

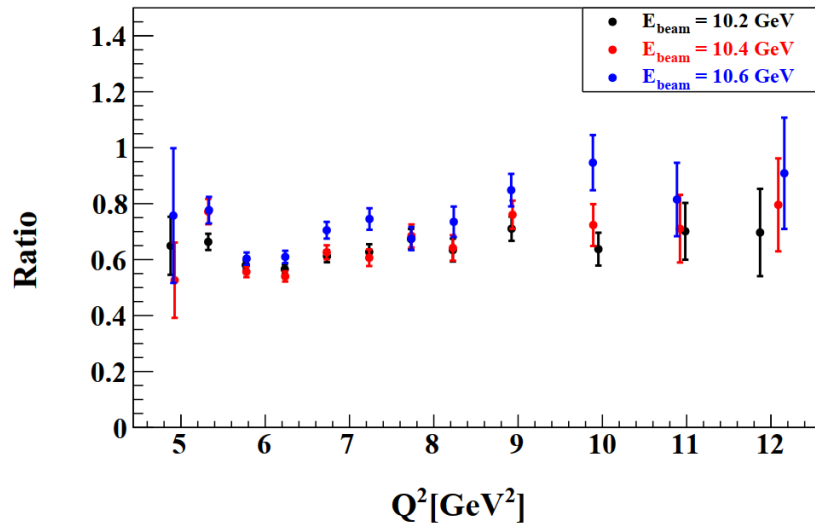


Figure 5.14: The σ_n/σ_p ratio results including NDE, Fermi and radiative corrections from different data sets at three different beam energies 10.2, 10.4, and 10.6 GeV binned in Q^2 .

CHAPTER 6

G_M^n RESULTS

In this chapter, we will extract G_M^n from the ratio of quasi-elastic $D(e, e'p)$ to $D(e, e'n)$ scattering. Then we will discuss the sources of systematic uncertainties that might impact the accuracy of the G_M^n result.

6.1 G_M^n Extraction from Ratio

To extract the neutron magnetic form factor (G_M^n) from the ratio of $D(e, e'n)$ to $D(e, e'p)$ scattering, we begin with the cross-section expression in Eq. 1.11:

$$\frac{d\sigma}{d\Omega} = \sigma_{Mott} \left(G_E^2 + \frac{\tau}{\epsilon} G_M^2 \right) \left(\frac{1}{1 + \tau} \right), \quad (6.1)$$

where ϵ and τ are defined as:

$$\epsilon = \frac{1}{1 + 2(1 + \tau) \tan^2(\frac{\theta_e}{2})} \quad \text{and} \quad \tau = \frac{Q^2}{4M^2}. \quad (6.2)$$

The measured ratio R_{meas} is given by:

$$R_{\text{meas}} = \frac{\frac{d\sigma}{d\Omega}[D(e, e'n)]}{\frac{d\sigma}{d\Omega}[D(e, e'p)]} = \frac{\sigma_{Mott}^n \left(G_E^{n2} + \frac{\tau_n}{\epsilon_n} G_M^{n2} \right) \left(\frac{1}{1 + \tau_n} \right)}{\sigma_{Mott}^p \left(G_E^{p2} + \frac{\tau_p}{\epsilon_p} G_M^{p2} \right) \left(\frac{1}{1 + \tau_p} \right)}, \quad (6.3)$$

where the sub-/super-scripts p and n refer to protons and neutrons, respectively.

Solving Eq. 6.3 for G_M^n leads to

$$G_M^n = \pm \sqrt{\left[R_{\text{cor}} \left(\frac{\sigma_{mott}^p}{\sigma_{mott}^n} \right) \left(\frac{1 + \tau_n}{1 + \tau_p} \right) \left(G_E^{p2} + \frac{\tau_p}{\epsilon_p} G_M^{p2} \right) - G_E^{n2} \right] \frac{\epsilon_n}{\tau_n}}, \quad (6.4)$$

where R_{cor} takes into account various corrections including neutron detection efficiency (NDE), proton detection efficiency (PDE), nuclear, Fermi, and radiative corrections

$$R_{\text{cor}}(Q^2) = f_{NDE}(Q^2) f_{PDE}(Q^2) f_{Nuclear}(Q^2) f_{Fermi}(Q^2) f_{Radiative}(Q^2) R_{\text{meas}}(Q^2). \quad (6.5)$$

At this stage, the proton detection efficiency correction and the nuclear correction have not been included.

To simplify Eq. 6.4, we make approximations:

$$\frac{\sigma_{mott}^p}{\sigma_{mott}^n} \approx 1, \quad \frac{1 + \tau_n}{1 + \tau_p} \approx 1. \quad (6.6)$$

Thus, the neutron magnetic form factor G_M^n becomes

$$G_M^n = \sqrt{\left[\left(G_E^p{}^2 + \frac{\tau_p}{\varepsilon_p} G_M^p{}^2 \right) R_{cor} - G_E^n{}^2 \right] \frac{\varepsilon_n}{\tau_n}} = \sqrt{[\sigma_p R_{cor} - G_E^n{}^2] \frac{\varepsilon_n}{\tau_n}}, \quad (6.7)$$

where $\sigma_p = G_E^p{}^2 + \frac{\tau_p}{\varepsilon_p} G_M^p{}^2$ represents the reduced proton cross section. The standard propagation of errors for the extracted value of G_M^n is determined as

$$(\delta G_M^n)^2 = \left(\frac{\partial G_M^n}{\partial \sigma_p} \right)^2 (\delta \sigma_p)^2 + \left(\frac{\partial G_M^n}{\partial R_{cor}} \right)^2 (\delta R_{cor})^2 + \left(\frac{\partial G_M^n}{\partial G_E^n} \right)^2 (\delta G_E^n)^2. \quad (6.8)$$

To extract G_M^n , the Arrington parametrization [93] is used to calculate the proton form factors (G_E^p and G_M^p) as well as the neutron electric form factor G_E^n . This parametrization is shown in Fig 6.1 as black solid curves. The details of the fit function and the procedure of the fitting that Arrington used can be found in [93]. The Arrington parametrization of G_E^p , G_M^p and G_E^n that we used to extract G_M^n is shown in Fig 6.2.

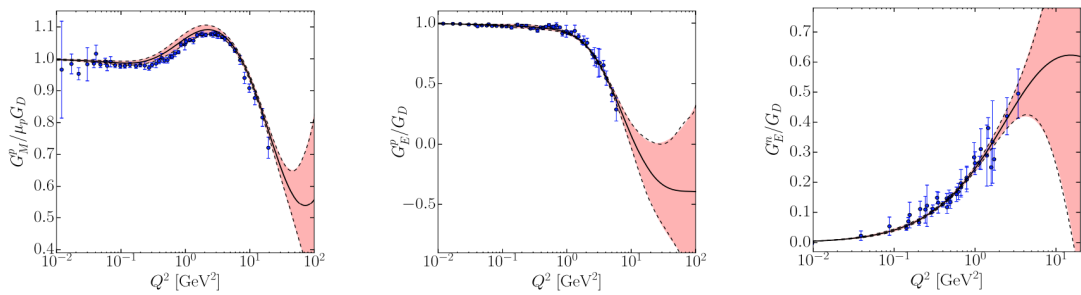


Figure 6.1: Arrington parameterizations of $G_M^p/\mu_p G_D$ (left), G_E^p/G_D (middle) and $G_E^n/\mu_n G_D$ (right) shown as black solid curves. The error band within the dashed curves and highlighted in red represent the fit uncertainty from the parameterization. The plot from Ref. [93].

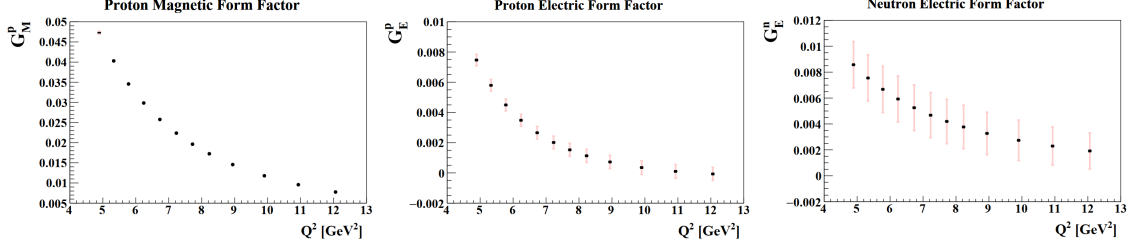


Figure 6.2: Arrington parameterizations of G_M^p (left), G_E^p (middle) and G_E^n (right) that correspond to the Q^2 values of our experiment.

The results of G_M^n as a function of Q^2 for three different beam energies 10.2, 10.4 and 10.6 GeV are shown in Fig 6.3. The results show that all three data sets are consistent with each other.

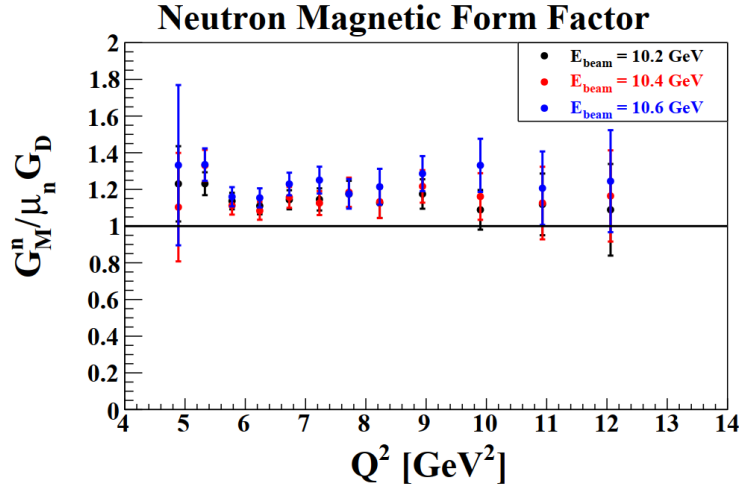


Figure 6.3: The G_M^n as a function of Q^2 for three different beam energies of 10.2, 10.4 and 10.6 GeV. The black line showing $G_M^n = \mu_N G_D$.

The weighted average of G_M^n in each Q^2 bin is obtained by merging the results from these three different beam energies. The calculation of the weighted average involves minimizing the χ^2 value, following the formula [94]

$$\chi^2 = \sum_j \frac{(x_j - \bar{x})^2}{\sigma_j^2}, \quad (6.9)$$

where x_j represents the G_M^n value and σ_j is the statistical error associated with the j^{th} measurement contributing in that Q^2 bin (with j being an integer between 1 and

3). By setting $\partial\chi^2/\partial\bar{x}$ to 0 in Eq. 6.9 and solving for \bar{x} , we find

$$\bar{x} = \frac{\sum_j \frac{x_j}{\sigma_j^2}}{\sum_j \frac{1}{\sigma_j^2}}. \quad (6.10)$$

The statistical error for each point within the weighted average is determined using the following formula:

$$\begin{aligned} \sigma_{\bar{x}}^2 &= \sum_j \left(\frac{\partial\bar{x}}{\partial x_j} \right)^2 \sigma_j^2, \\ &= \frac{1}{\sum_j \frac{1}{\sigma_j^2}}. \end{aligned} \quad (6.11)$$

The result of the weighted average for G_M^n is shown in Fig 6.4. The G_M^n results of CLAS12 show a flat behavior over the range of $Q^2 = 5 - 12 \text{ GeV}^2$. The numerical values of the three individual measurements and the weighted average of G_M^n as a function of Q^2 can be found in Appendix C.

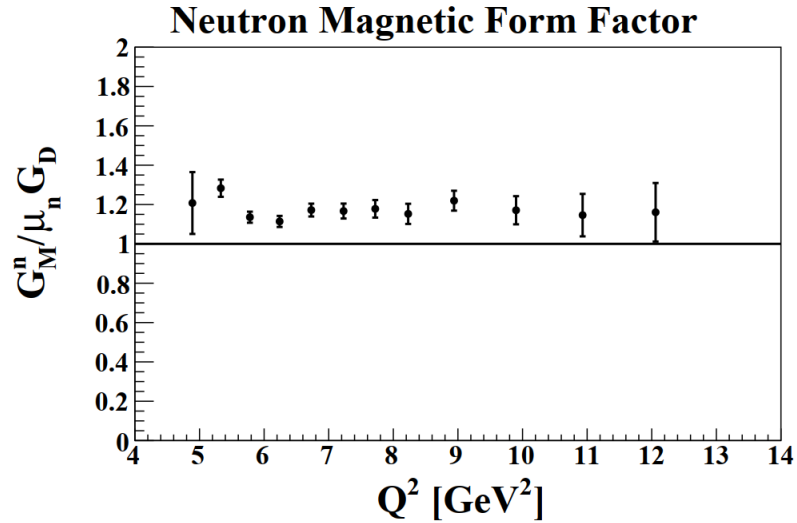


Figure 6.4: G_M^n weighted average as a function of Q^2 obtained by combining data from three different beam energy 10.2, 10.4 and 10.6 GeV. The black line shows $G_M^n = \mu_n G_D$.

6.2 Systematic Uncertainties

There are multiple sources of systematic uncertainties that can affect the accuracy of the G_M^n measurement. To determine the total systematic uncertainty, the following sources have been considered:

- Systematic uncertainty due to neutron detection efficiency (δ_{syst}^{NDE})
- Systematic uncertainty due to electron identification cuts:
 - vertex cut (δ_{syst}^{vz})
 - fiducial cut ($\delta_{syst}^{fiducial}$)
 - Sampling Fraction cut (δ_{syst}^{SF})
- Systematic uncertainty due to quasi-elastic selection cuts:
 - $E_{\text{beam}}^{\text{angles}}$ cut ($\delta_{syst}^{\text{beam}}$).
 - $\Delta\phi$ cut ($\delta_{syst}^{\Delta\phi}$)
 - θ_{pq} cut ($\delta_{syst}^{\theta_{pq}}$)
- Systematic uncertainty due to radiative effects ($\delta_{syst}^{\text{rad}}$)

These uncertainties are determined by making small variations to a particular source while keeping others constant, and observing how the G_M^n results change. The formula used to calculate the relative systematic uncertainty associated with the variation in the i^{th} source is given by

$$\begin{aligned}\delta_{syst}^i &= \frac{|G_M^n - G_M^{n \text{ alt}}|}{G_M^n} \times 100, \\ &= \frac{\Delta G_M^n}{G_M^n} \times 100,\end{aligned}\tag{6.12}$$

where $\Delta G_M^n = |G_M^n - G_M^{n \text{ alt}}|$, G_M^n represents the reference measurement and $G_M^{n \text{ alt}}$ corresponds to the measurement with an alternate cut.

6.2.1 Systematic Uncertainty due to Neutron Detection Efficiency

The neutron detection efficiency (NDE) was calculated using two different functions, Gaussian and Crystal Ball functions, as described in Section 3.8. The difference between the results obtained by these two functions is less than 3% as shown in Fig 6.5.

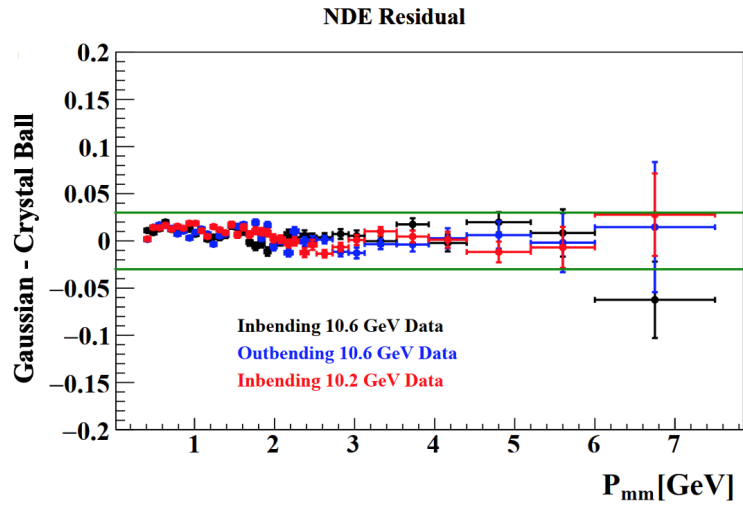


Figure 6.5: The difference of the neutron detection efficiency between fitting the neutron peak with a Gaussian function and a Crystal Ball function, binned in missing momentum of neutron for inbending and outbending 10.6 GeV and inbending 10.2 GeV datasets.

The uncertainty associated with the NDE is determined by recalculating G_M^n using the Gaussian parametrization listed in Table 3.7. The result of the G_M^n using both the Gaussian and Crystal Ball parametrizations is shown in the left panel of Fig 6.6. The relative systematic uncertainty is shown in the right panel of Fig. 6.6, which is determined by using Eq. 6.12.

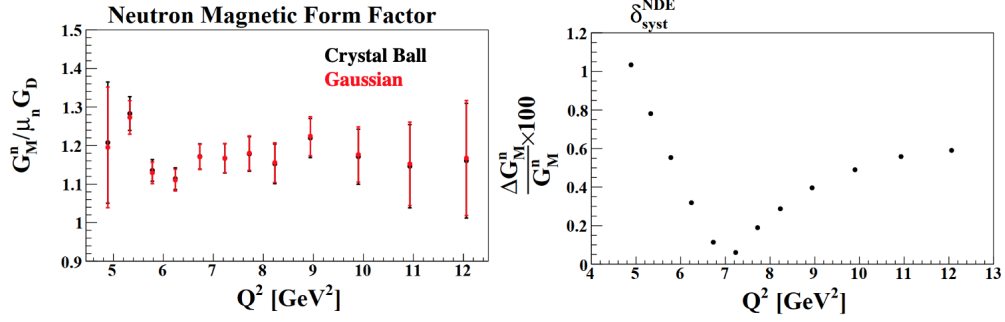


Figure 6.6: Left: Comparison of the G_M^n measurements with Crystal Ball (black) and Gaussian (red) functions used to determine the NDE correction. Right: The estimated relative systematic uncertainty on G_M^n due to the NDE fitting procedure.

6.2.2 Systematic Uncertainty due to Electron Identification

Cuts

Below is a detailed description of the relative systematic uncertainties related to electron identification:

Electron Vertex Cut: To assess the uncertainty associated with the electron vertex cut, we conducted an analysis without applying this particular cut. Figure 6.7 shows a comparison between G_M^n measurements with and without the electron vertex cut. The right panel of Fig. 6.7 shows the estimated relative systematic uncertainty due to the electron vertex cut. It's important to note that the difference is zero for $Q^2 > 7.6$ GeV². Consequently, the relative systematic uncertainty associated with the vertex cut is determined to be less than 0.06%.

Fiducial Cuts: Similarly, we disabled the PCAL and DC fiducial cuts during electron ID selection to investigate their impact. The comparison between G_M^n measurements with and without these fiducial cuts is shown in the left panel of Fig. 6.8. The right panel of the same figure shows the estimated relative systematic uncertainty due to the fiducial cuts. The relative systematic uncertainty due to fiducial cut is determined to be less than 1.4%.

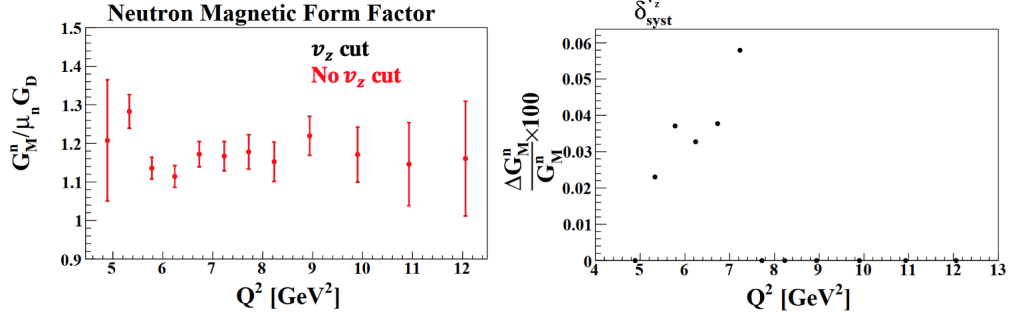


Figure 6.7: Left: Comparison of the G_M^n measurements with (black) and without (red) electron vertex cut applied during particle identification. Right: The estimated relative systematic uncertainty on G_M^n due to electron vertex cut.

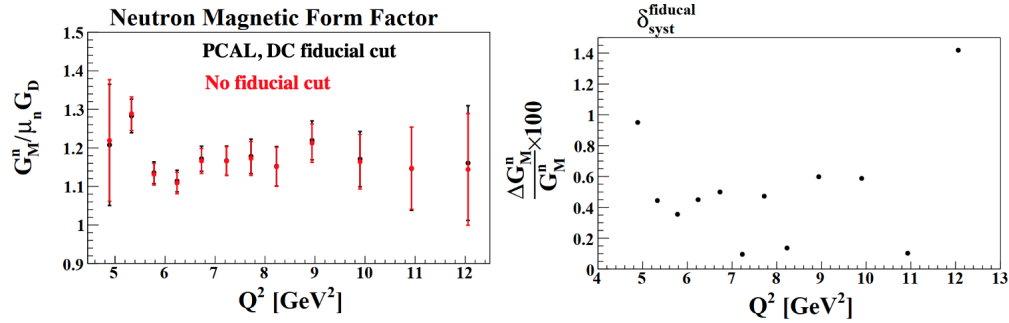


Figure 6.8: Left: Comparison of G_M^n measurements with (black) and without (red) fiducial cuts applied during particle identification. Right: The estimated relative systematic uncertainty on G_M^n due to fiducial cuts.

Sampling Fraction Cut: For the sampling fraction (SF), we initially selected $\mu \pm 3.5\sigma$ from the fitted distribution versus momentum, as detailed in Section 3.4.5. We then modified this cut to $\mu \pm 3.0\sigma$ and recalculated G_M^n . Figure 6.9 shows a comparison of G_M^n results with the $\mu \pm 3.5\sigma$ and $\mu \pm 3.0\sigma$ cuts on the sampling fraction. The right panel of Fig. 6.9 shows the corresponding relative systematic uncertainty associated with the sampling fraction cut. The relative systematic uncertainty associated with the SF cut is determined to be less than 0.6%.

Given that similar electron ID cuts were applied to both $D(e, e'p)$ and $D(e, e'n)$ channels, the relative systematic effect on the G_M^n due to electron identification is

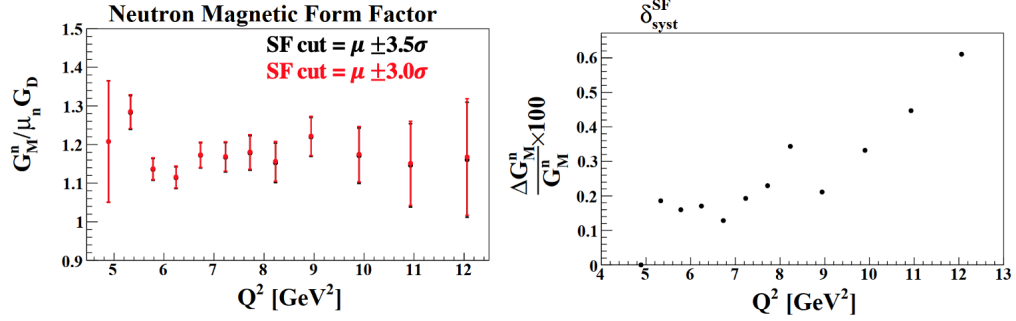


Figure 6.9: Left: Comparison of G_M^n measurements with different SF cut applied during electron identification. Right: The estimated relative systematic uncertainty on G_M^n due to SF cut.

expected to be small (less than 1.6%) in most Q^2 values as shown in Fig 6.10.

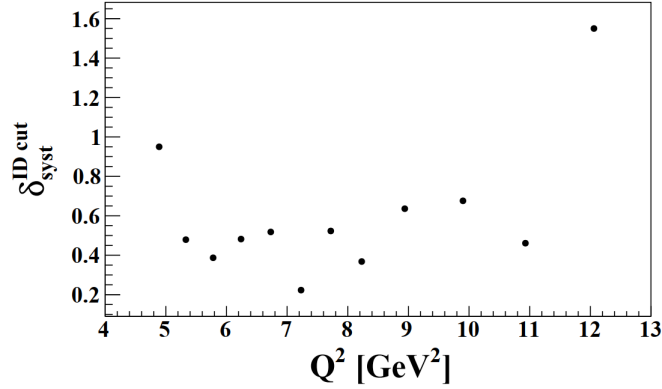


Figure 6.10: The estimated relative systematic uncertainty on G_M^n due to electron ID cuts in added quadrature.

6.2.3 Systematic Uncertainty due to Quasi-elastic Selection

Cuts

Below is a detailed description of the systematic uncertainties related to quasi-elastic selection:

Incident Electron Beam Energy Cut: In the quasi-elastic event selection, we

applied a $\mu \pm 1.0\sigma$ cut on the incident electron beam energy $E_{\text{beam}}^{\text{angles}}$, as described in Section 4.3. To assess the systematic uncertainty, we altered this cut to $\mu \pm 1.25\sigma$ and recalculated G_M^n . The reason for the small variation is to avoid regions where the background becomes significant, especially for the $D(e, e'n)$ channel. The comparison between G_M^n measurements with the $\mu \pm 1.0\sigma$ and $\mu \pm 1.25\sigma$ cuts on $E_{\text{beam}}^{\text{angles}}$ is shown in the left panel of Fig. 6.11. The right panel of the same figure shows the estimated relative systematic uncertainty due to the incident electron beam energy $E_{\text{beam}}^{\text{angles}}$, which is determined to be less than 2.5%.

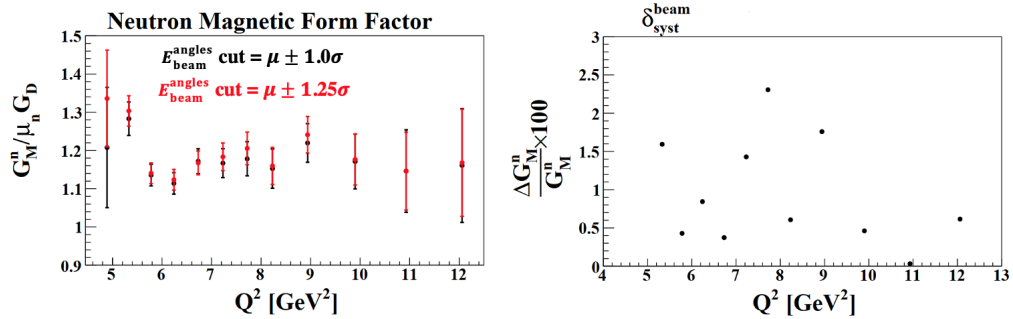


Figure 6.11: Left: Comparison of G_M^n measurements with different $E_{\text{beam}}^{\text{angles}}$ cut applied during quasi-elastic events selection. Right: The estimated relative systematic uncertainty on G_M^n due to $E_{\text{beam}}^{\text{angles}}$ cut.

$\Delta\phi$ Cut: Another crucial cut for quasi-elastic event selection was a $\mu \pm 1.0\sigma$ cut on the $\Delta\phi$ distribution. We modified this cut to $\mu \pm 1.25\sigma$ and recalculated G_M^n . The comparison between G_M^n measurements with the $\mu \pm 1.0\sigma$ and $\mu \pm 1.25\sigma$ cuts on $\Delta\phi$ is depicted in the left panel of Fig. 6.12. The right panel of the same figure shows the estimated relative systematic uncertainty due to the $\Delta\phi$ cuts, which is determined to be less than 3.5% over Q^2 values, except at the $Q^2 = 10.93$ GeV².

θ_{pq} Cuts: The final cut used for quasielastic event selection was the θ_{pq} cut. We considered θ_{pq} cuts that are 10% larger and 10% smaller than the cut we initially used, as shown by the black curves in Fig. 6.13. These variations in the θ_{pq} cut are

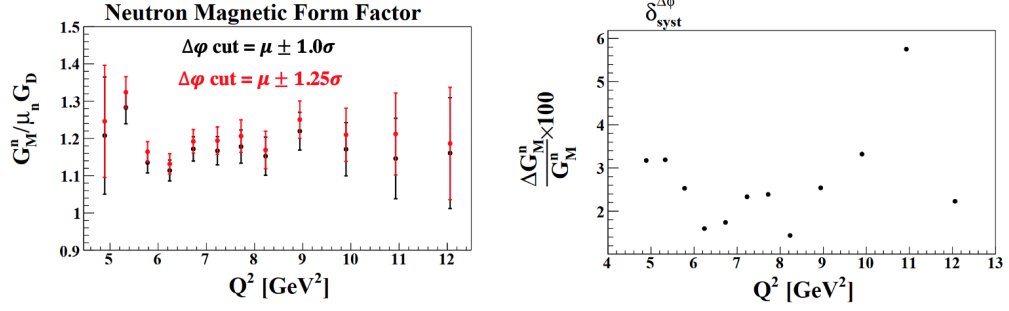


Figure 6.12: Left: Comparison of G_M^n measurements with different $\Delta\phi$ cut applied during quasi-elastic events selection. Right: The estimated relative systematic uncertainty on G_M^n due to $\Delta\phi$ cut.

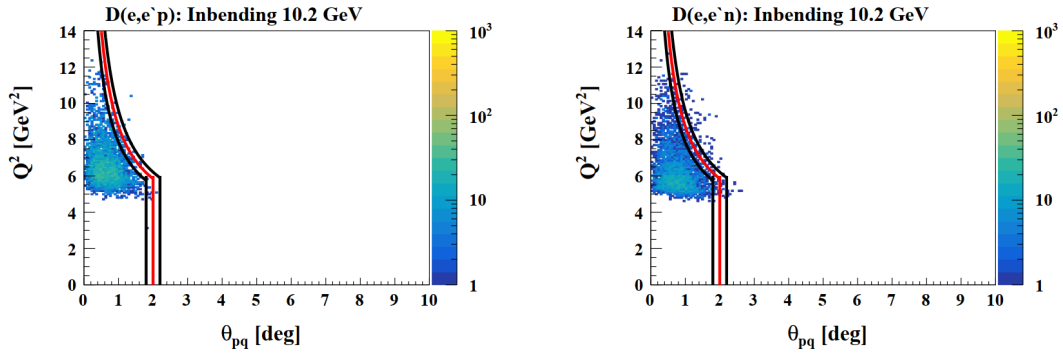


Figure 6.13: The Q^2 as a function of θ_{pq} distribution for $D(e, e'p)$ (left) and $D(e, e'n)$ (right) for 10.2 GeV dataset. The red curve represents the initial θ_{pq} cut applied to select quasi-elastic events. The black curves represent θ_{pq} cuts that are 10% larger and smaller than the original cut.

used to understand how different θ_{pq} cut values affect the G_M^n measurements. The comparison between G_M^n measurements with the the original θ_{pq} cut and the 10% larger and smaller than the original cut are shown in the left panel of Fig. 6.14 and Fig. 6.15, respectively. The right panel of the same figures show the estimated relative systematic uncertainty due to the variations in the θ_{pq} cut, which is determined to be less than 3% over Q^2 values, except at the $Q^2 = 4.89$ GeV².

The major source of systematic uncertainties in the G_M^n analysis is expected to be related to the quasi-elastic event selection procedure. The total relative systematic uncertainty in quadrature due to the quasi-elastic cut is less than 6 % in most Q^2

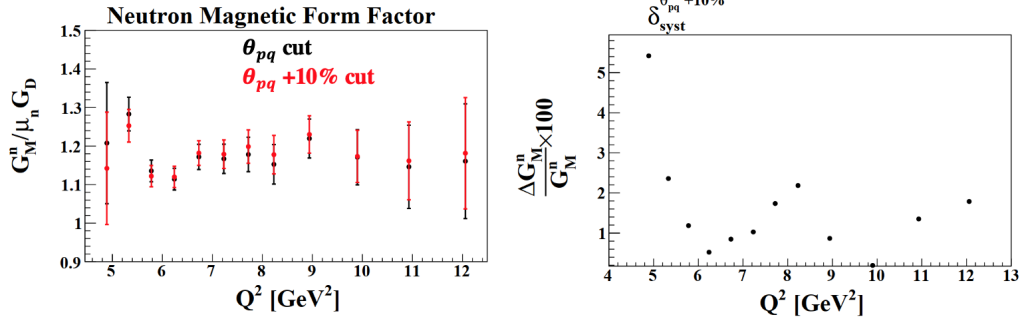


Figure 6.14: Left: Comparison of G_M^n measurements with different θ_{pq} cut applied during quasi-elastic events selection. Right: The estimated relative systematic uncertainty on G_M^n due to a 10% larger than the original θ_{pq} cut.

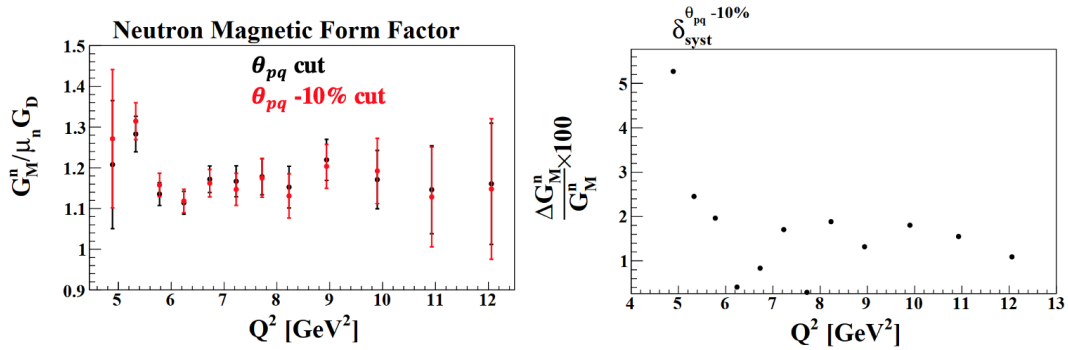


Figure 6.15: Left: Comparison of G_M^n measurements with different θ_{pq} cut applied during quasi-elastic events selection. Right: The estimated relative systematic uncertainty on G_M^n due to a 10% smaller than the original θ_{pq} cut.

values, except at the $Q^2 = 4.89$ GeV² as shown in Fig 6.16.

6.2.4 Systematic Uncertainty due to Radiative Effects

As mentioned in section 5.3, the systematic uncertainty associated with the radiative correction is determined by considering the differences between the smallest and largest values of the ratio of radiative corrections at each Q^2 value (see Fig. 5.13). In this procedure, G_M^n is calculated twice: once using the smallest value of the ratio of radiative corrections at each Q^2 value and then using the largest value of the ratio of radiative corrections at each Q^2 value. The comparison between the

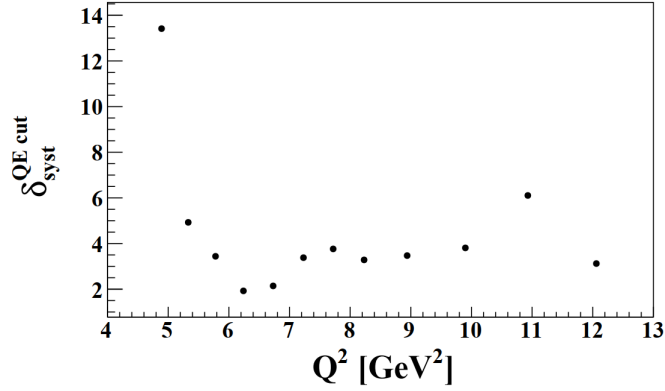


Figure 6.16: The estimated relative systematic uncertainty on G_M^n due to the quasi-elastic cuts in added quadrature.

resulting G_M^n measurements, based on the smallest and largest values of the ratio of radiative corrections, is shown in the left panel of Fig. 6.17. The right panel of the same figure show the estimated relative systematic uncertainty due to the radiative correction. The relative systematic uncertainty due to radiative correction is at 0.08%.

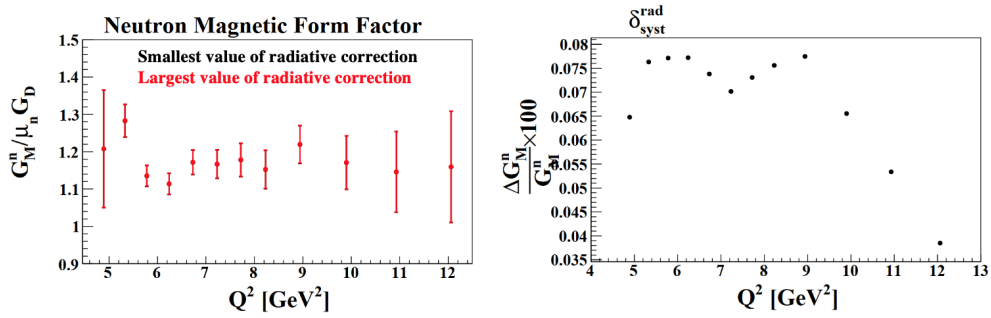


Figure 6.17: Left: Comparison of G_M^n measurements with smallest and largest value of the ratio of radiative corrections. Right: The estimated relative systematic uncertainty on G_M^n due to the radiative correction.

6.3 Total Systematic Uncertainty

The relative systematic uncertainty is computed individually for each Q^2 bin and for each source. Figure 6.18 provides an overview of how the different sources contribute to the relative systematic uncertainty across various Q^2 values. The figure shows that the uncertainty associated with $\Delta\phi$ is the dominant factor in most Q^2 bins. The other sources generally remain at or below a level of 1-2.5% over Q^2 values, except at the $Q^2 = 4.89 \text{ GeV}^2$, where there is a noticeable increase in the systematic uncertainty. The total relative systematic uncertainty δ_{syst}^{total} is determined by adding

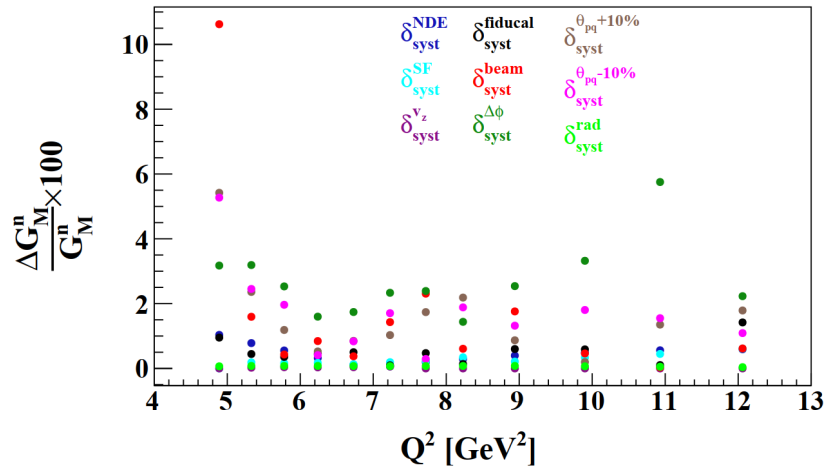


Figure 6.18: The estimated relative systematic uncertainty on the weighted average of G_M^n for the individual contributing sources as a function of Q^2 values.

the individual contributions in quadrature:

$$\delta_{syst}^{total} = \sqrt{\sum_i \delta_{syst}^i{}^2}. \quad (6.13)$$

Figure 6.19 shows the total relative systematic uncertainty in the G_M^n measurement as a function of various Q^2 values. This figure shows that the total relative systematic uncertainty generally falls within the range of 2-6%. The calculated relative

systematic uncertainties due to various sources at different Q^2 bins are listed in Table 6.1.

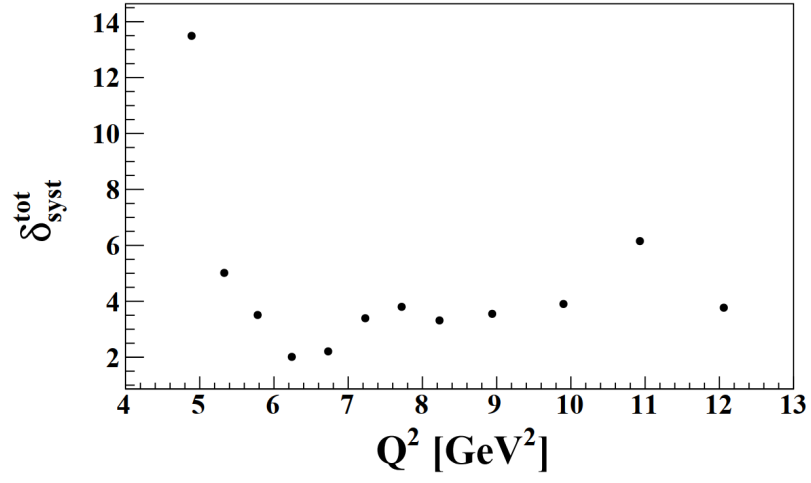


Figure 6.19: The total estimated relative systematic uncertainty on the weighted average value of G_M^n in added quadrature.

Q^2	δ_{syst}^{NDE}	$\delta_{syst}^{v_z}$	$\delta_{syst}^{fiducial}$	δ_{syst}^{SF}	δ_{syst}^{beam}	$\delta_{syst}^{\Delta\phi}$	$\delta_{syst}^{\theta_{pq}+10\%}$	$\delta_{syst}^{\theta_{pq}-10\%}$	δ_{syst}^{rad}	δ_{syst}^{total}	δ_{stat}
4.89	1.03	0.00	0.95	0.00	10.62	3.17	5.42	5.27	0.06	13.49	15.72
5.33	0.78	0.02	0.44	0.19	1.59	3.19	2.36	2.45	0.08	5.02	4.37
5.78	0.55	0.04	0.35	0.16	0.43	2.53	1.19	1.96	0.08	3.51	2.81
6.24	0.32	0.03	0.45	0.17	0.84	1.60	0.52	0.41	0.08	2.01	2.81
6.73	0.11	0.04	0.50	0.13	0.37	1.74	0.85	0.84	0.07	2.21	3.26
7.23	0.06	0.06	0.10	0.19	1.43	2.33	1.03	1.70	0.07	3.39	3.79
7.72	0.19	0.00	0.47	0.23	2.31	2.39	1.74	0.29	0.07	3.80	4.46
8.23	0.29	0.00	0.14	0.34	0.61	1.44	2.19	1.88	0.08	3.31	5.13
8.94	0.40	0.00	0.60	0.21	1.76	2.54	0.87	1.32	0.08	3.55	5.06
9.90	0.49	0.00	0.59	0.33	0.46	3.32	0.19	1.80	0.07	3.90	7.16
10.93	0.56	0.00	0.10	0.45	0.03	5.75	1.35	1.55	0.05	6.15	10.80
12.06	0.59	0.00	1.42	0.61	0.62	2.23	1.79	1.09	0.04	3.77	14.88

Table 6.1: Relative systematic uncertainties due to various sources and relative statistic uncertainties at different Q^2 bins.

CHAPTER 7

PRELIMINARY G_M^n RESULT AND DISCUSSION

This chapter provides an overview of the preliminary results for the neutron magnetic form factor, G_M^n . These results have been compared with previous measurements and various theoretical models. In addition, we will briefly discuss the goals for the immediate future of this work toward publication.

7.1 Comparison to Previous Measurements and Models

A comparison of the weighted average determination of G_M^n , scaled to the dipole parametrization, with previous measurements and some theoretical predictions discussed in Section 1.5 is shown in Fig.7.1. In this plot, the grey error band represents the weighted average systematic uncertainty and a black line showing the standard dipole form factor $G_M^n = \mu_N G_D$. A similar plot is presented in Fig.7.2, where the error bars show the statistical and systematic errors combined in quadrature. The CLAS12 result shows a flat behavior of $G_M^n = \mu_N G_D$ within the Q^2 range of 5 to 12 GeV^2 , with systematic uncertainty 2 – 6%. A significant disagreement is seen when comparing CLAS12 result to the Rock *et al.* [29] measurement. The Rock results shows that G_M^n falls off at high Q^2 with large uncertainties (4-15%) while the CLAS12 data is consistent with the standard dipole form factor within 12-20%.

Moreover, there are significant differences between our results and various theoretical models, and these differences are expected to persist even after applying the missing corrections (PDE and nuclear corrections).

The CLAS12 results are currently derived from RG-B pass1 data. However, we expect that once we transition to using RG-B pass2 data, G_M^n will align more closely with the dipole form factor. The RG-B pass2 analysis in CLAS12 holds

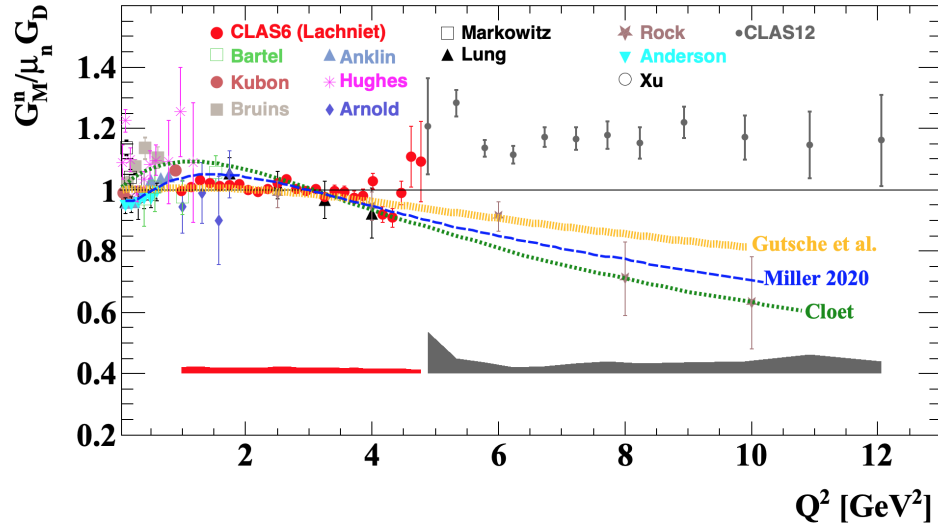


Figure 7.1: Final G_M^n results scaled to the dipole parametrization. A selection of previous measurements is shown. The grey points indicate the results of this analysis. The weighted average systematic error is shown as a grey band. The black line indicates $G_M^n = \mu_n G_D$. The theory curves are the Miller model (blue) [41], the Gutsche model (yellow) [42], and the Cloet model (green) [43].

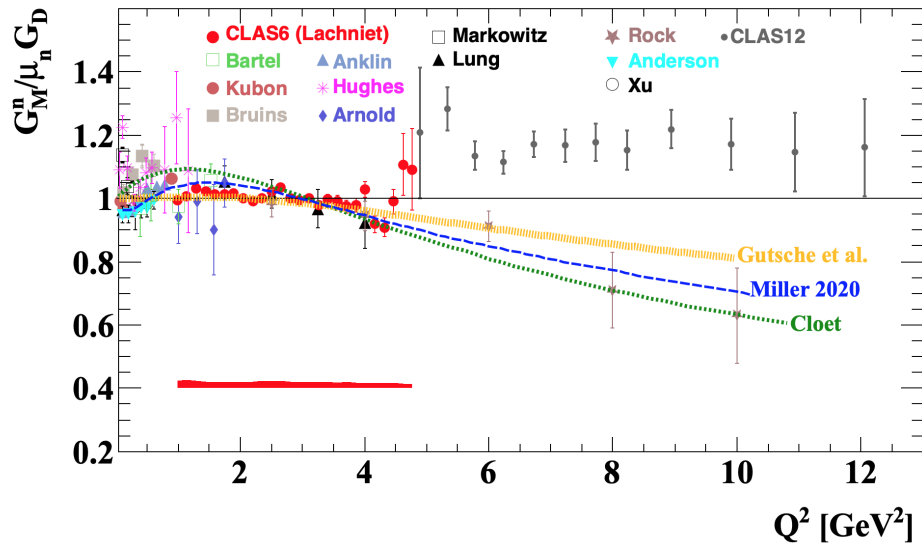


Figure 7.2: Same as Fig. 7.1 but with error bars being the quadrature sum of systematic and statistical uncertainty for our results.

the promise of significant improvement. This improvement is achievable through the collaborative efforts directed at refining various aspects, including tracking ef-

efficiency, momentum correction, calibration, and alignment. These combined efforts are expected to result in significantly improved experimental resolution of $e - p$ and $e - n$ events in comparison to the current stage of our study. In addition, the results shown in this thesis included a significant statistical uncertainty that may be reduced with the RG-B pass 2 data.

7.2 Conclusion

The elastic electromagnetic form factors are important observables for understanding the structure of the nucleon. Measuring all four elastic form factors, G_E^p , G_E^n , G_M^p , and G_M^n , at high Q^2 is one of the central goals of the physics programs at Jefferson Lab. This thesis focused on the measurement of neutron magnetic form factor, G_M^n , at $Q^2 = 5-12 \text{ GeV}^2$ using the Forward Detector in CLAS12. G_M^n has been extracted from the ratio of quasi-elastic $e - n$ to $e - p$ scattering from a deuteron target. The results have shown that G_M^n is approximately 12-20% higher than the predictions of the dipole form factor across the considered range of Q^2 , based on RG-B pass1 data. However, it is expected that G_M^n will closely align with the dipole form factor when RG-B pass2 data is used.

Ongoing research efforts are focused on calculating the proton detection efficiency in the forward calorimeter. Preliminary insights show that this efficiency ranges from 97% to 99% for Q^2 values above 6 GeV^2 . However, for Q^2 values below 6 GeV^2 , there is considerable variability, with the proton efficiency fluctuating between 35% and 80%. It's important to note that these results will undergo validation and further analysis in upcoming work. Despite these variations, the current expectation is that G_M^n will continue to show consistent behavior to the dipole form factor even after applying the proton detection efficiency correction.

The results presented in Fig.7.2 have the potential to pose a fundamental challenge to various theoretical models. The observed behavior may necessitate a reconsideration of existing theoretical frameworks by physicists. A notable example is the flavor decomposition of proton form factors, as illustrated in Fig.1.4, which relies on the fitting of experimental data for G_E^n , G_M^n , G_E^p , and G_M^p . It's important to note that the fitting for G_M^n at high Q^2 is currently based solely on Rock data, where the data shows a decline at high Q^2 . Our results suggest the potential for a modification in the fitting of G_M^n at high Q^2 , thereby influencing the flavor decomposition of proton form factors within the high Q^2 regime.

In physical terms, the neutron's magnetic form factor, G_M^n , provides insights into how magnetic properties are distributed within the neutron. If the neutron's magnetic form factor aligns with the dipole model, it implies a uniform or symmetric distribution of magnetic properties within the neutron. If experimental data closely matches this expected behavior, it signifies that the magnetic properties of the neutron will decrease as the momentum transfer Q^2 increases. Our results have the potential to pose a fundamental challenge to various theoretical models. The theoretical physicists may need to reassess and reconsider their existing models based on these results. The result of the flavor decomposition of proton form factors that are shown in Fig. 1.4 is calculated based on the fitting of all four form factors, G_E^n , G_M^n , G_E^p , and G_M^p . The fitting that is used for G_M^n to calculate the contributions of the up and down quarks relies on the Rock data only at high Q^2 . Our result can modify the fitting of the G_M^n at high Q^2 and might influence the flavor decomposition of proton form factors at high Q^2 .

Conversely, if the neutron's magnetic form factor decreases as Q^2 increases (as shown in the theoretical model), it could indicate the effect of asymptotic freedom. Asymptotic freedom signifies that quarks and gluons essentially become free particles

at high Q^2 . This observation offers insights into the transition between confinement, where quarks are bound together within the nucleon, and asymptotic freedom, where they behave as free particles. Additionally, a decrease in the magnetic form factor with increasing Q^2 might suggest the presence of a resonance structure within the neutron as shown in Miller's calculations [41]. Miller's model takes into account a pion cloud and within this pion cloud he calculated the delta resonance to provide valuable insights into the internal dynamics of the neutron.

Finally, there is an interest in expanding this research by studying G_M^n using the Central detector. This would allow for overlapping results with CLAS6 data, providing improved measurements of the neutron magnetic form factor at these values of Q^2 .

BIBLIOGRAPHY

- [1] J. Manners. *Quantum Physics: An Introduction*, volume 7. CRC Press, 2000.
- [2] F. Halzen and A. D. Martin. *Quark and Leptons: An Introductory Course in Modern Particle Physics*. John Wiley and Sons, 1984.
- [3] S. J. Brodsky and G. R. Farrar. Scaling Laws at Large Transverse Momentum. *Physical Review Letters*, 31(18):1153, 1973.
- [4] S. J. Brodsky and G. R. Farrar. Scaling Laws for Large-Momentum-Transfer Processes. *Physical Review D*, 11(5):1309, 1975.
- [5] K. De Jager J. Arrington and C. F. Perdrisat. Nucleon Form Factors—a Jefferson Lab Perspective. In *Journal of Physics: Conference Series*, volume 299, page 012002. IOP Publishing, 2011.
- [6] V. Punjabi, C. F. Perdrisat, M. K. Jones, E. J. Brash, and C. E. Carlson. The Structure of the Nucleon: Elastic Electromagnetic Form Factors. *Eur. Phys. J. A*, 51:79, 2015.
- [7] C. F. Perdrisat *et al.* Nucleon Electromagnetic Form Factors. *Progress in Particle and Nuclear Physics*, 59(2):694–764, 2007.
- [8] G. D. Cates *et al.* Flavor Decomposition of the Elastic Nucleon Electromagnetic Form Factors. *Physical Review Letters*, 106(25):252003, 2011.
- [9] Jefferson Lab. Experiment Proposal, 2007-2009. Available on-line at <https://hallaweb.jlab.org/12GeV>, https://www.jlab.org/exp_prog/generated/12GeV/apphallb.html, https://www.jlab.org/exp_prog/generated/12GeV/apphallc.html.

- [10] M. E. Peskin and D. V. Schroeder. *An Introduction to Quantum Field Theory Addison*. Wesley Publishing Company, 1995.
- [11] F. J. Ernst *et al.* Electromagnetic Form Factors of the Nucleon. *Physical Review*, 119(3):1105, 1960.
- [12] J. Binney and D. Skinner. *The Physics of Quantum Mechanics*. Oxford University Press, 2013.
- [13] B. Friedrich and H. Schmidt-Böcking. Otto Stern’s Molecular Beam Method and Its Impact on Quantum Physics. In *Molecular Beams in Physics and Chemistry; From Otto Stern’s Pioneering Exploits to Present-Day Feats*, pages 37–88. 2021.
- [14] L. W. Alvarez and F. Bloch. A Quantitative Determination of the Neutron Moment in Absolute Nuclear Magnetons. *Physical Review*, 57(2):111, 1940.
- [15] S. Galster *et al.* Elastic Electron-Deuteron Scattering and the Electric Neutron Form Factor at Four-Momentum Transfers $5 \text{ fm}^{-2} < q^2 < 14 \text{ fm}^{-2}$. *Nuclear Physics B*, 32(1):221–237, 1971.
- [16] R. G. Sachs. High-Energy Behavior of Nucleon Electromagnetic Form Factors. *Physical Review*, 126(6):2256, 1962.
- [17] J. J. Kelly. Nucleon Charge and Magnetization Densities from Sachs Form Factors. *Physical Review C*, 66(6):065203, 2002.
- [18] J. J. Kelly. Simple Parametrization of Nucleon Form Factors. *Physical Review C*, 70(6):068202, 2004.
- [19] G. A. Miller. Charge Densities of the Neutron and Proton. *Physical Review Letters*, 99(11):112001, 2007.

- [20] M. J. Musolf and T. W. Donnelly. The Interpretation of Parity-Violating Electron-Scattering Experiments. *Nuclear Physics A*, 546(3):509–587, 1992.
- [21] D. Borisyuk. Proton Charge and Magnetic RMS Radii From the Elastic ep Scattering Data. *Nuclear Physics A*, 843(1–4):59–67, October 2010.
- [22] M. Diehl *et al.* Generalized Parton Distributions From Nucleon Form Factor Data. *The European Physical Journal C-Particles and Fields*, 39(1):1–39, 2005.
- [23] H. Gao *et al.* Measurement of the Neutron Magnetic Form Factor from Inclusive Quasielastic Scattering of Polarized Electrons from Polarized ^3He . *Physical Review C*, 50(2):R546, 1994.
- [24] B. Anderson *et al.* Extraction of the Neutron Magnetic Form Factor from Quasielastic $^3\text{He}(\vec{e}, e')$ at $Q^2 = 0.1\text{--}0.6 \text{ (GeV/c)}^2$. *Physical Review C*, 75(3), March 2007.
- [25] W. Xu *et al.* Transverse $A_{T'}$ Asymmetry from the Quasielastic $A_{T'}$ Process and the Neutron Magnetic Form Factor. *Physical Review Letters*, 85(14):2900, 2000.
- [26] W. Xu *et al.* Plane-Wave Impulse Approximation Extraction of the Neutron Magnetic Form Factor from Quasielastic at $Q^2 = 0.3 \text{ to } 0.6 \text{ (GeV/c)}^2$. *Physical Review C*, 67(1):012201, 2003.
- [27] R. F. Obrecht. Electric Form Factor of the Neutron from Asymmetry Measurements. 2019.
- [28] E. B. Hughes *et al.* Neutron Form Factors from Inelastic Electron-Deuteron Scattering. *Physical Review*, 139(2B):B458, 1965.

- [29] S. Rock *et al.* Measurement of Elastic Electron-Neutron Cross Sections up to $Q^2 = 10 \text{ (GeV)}^2$. *Physical Review Letters*, 49(16):1139, 1982.
- [30] A. S. Esaulov *et al.* Measurement of the Neutron Magnetic Form-factor in the $D(e, e')np$ Reaction for Momentum Transfers $0.48\text{-GeV}^2 \leq Q^2 \leq 0.83\text{-GeV}^2$. *Sov. J. Nucl. Phys.*, 45:258–262, 1987.
- [31] R. G. Arnold *et al.* Measurements of Transverse Quasielastic Electron Scattering From the Deuteron at High Momentum Transfers. *Physical Review Letters*, 61(7):806, 1988.
- [32] A. Lung *et al.* Measurements of the Electric and Magnetic Form Factors of the Neutron from $Q^2 = 1.75$ to 4.00 (GeV/c)^2 . *Physical Review Letters*, 70(6):718, 1993.
- [33] P. Stein *et al.* Measurements of Neutron Form Factors. *Physical Review Letters*, 16(13):592, 1966.
- [34] W. Bartel *et al.* Measurement of Proton and Neutron Electromagnetic Form Factors at Squared Four-Momentum Transfers up to 3 (GeV/c)^2 . *Nuclear Physics B*, 58(2):429–475, 1973.
- [35] P. Markowitz *et al.* Measurement of the Magnetic Form Factor of the Neutron. *Physical Review C*, 48(1):R5, 1993.
- [36] K. M. Hanson *et al.* Large-Angle Quasielastic Electron-Deuteron Scattering. *Physical Review D*, 8(3):753, 1973.
- [37] H. Anklin *et al.* Precision Measurement of the Neutron Magnetic Form Factor. *Physics Letters B*, 336(3-4):313–318, 1994.

- [38] E. E. W. Bruins *et al.* Measurement of the Neutron Magnetic Form Factor. *Physical Review Letters*, 75(1):21, 1995.
- [39] G. Kubon *et al.* Precise Neutron Magnetic Form Factors. *Physics Letters B*, 524(1-2):26–32, 2002.
- [40] J. Lachniet *et al.* Precise Measurement of the Neutron Magnetic Form Factor G_M^n in the Few-GeV² Region. *Physical Review Letters*, 102(19):192001, 2009.
- [41] X. Zhang *et al.* Unified Model of Nucleon Elastic Form Factors and Implications for Neutrino-Oscillation Experiments. *Physical Review D*, 102(7):074026, 2020.
- [42] T. Gutsche *et al.* Electromagnetic Structure of Nucleon and Roper in Soft-Wall AdS/QCD. *Physical Review D*, 97(5):054011, 2018.
- [43] I.C. Cloët *et al.* Role of Diquark Correlations and the Pion Cloud in Nucleon Elastic Form Factors. *Physical Review C*, 90(4):045202, 2014.
- [44] J. J. Sakurai. Vector-Meson Dominance and High-Energy Electron-Proton Inelastic Scattering. *Physical Review Letters*, 22(18):981, 1969.
- [45] F. Iachello, A. D. Jackson and A. Lande. Semi-Phenomenological Fits to Nucleon Electromagnetic Form Factors. *Physics Letters B*, 43(3):191–196, 1973.
- [46] M. Gari and W. Krümpelmann. Semiphenomenological Synthesis of Meson and Quark Dynamics and the EM Structure of the Nucleon. *Zeitschrift für Physik A Atoms and Nuclei*, 322(4):689–693, 1985.
- [47] E. L. Lomon. Extended Gari-Krümpelmann Model Fits to Nucleon Electromagnetic Form Factors. *Physical Review C*, 64(3):035204, 2001.

- [48] E. L. Lomon. Effect of Recent R_p and R_n Measurements on Extended Gari-Krümpelmann Model Fits to Nucleon Electromagnetic Form Factors. *Physical Review C*, 66(4):045501, 2002.
- [49] E. L. Lomon. Effect of Revised R_n Measurements on Extended Gari-Krümpelmann Model Fits to Nucleon Electromagnetic Form Factors. *arXiv preprint nucl-th/0609020*, 2006.
- [50] R. Madey. E02-013 for G_E^n/G_M^n at Q^2 up to 3.4 (GeV/c)^2 .
- [51] C. Crawford *et al.* Role of Mesons in the Electromagnetic Form Factors of the Nucleon. *Physical Review C*, 82(4):045211, 2010.
- [52] G. A. Miller. Light Front Cloudy Bag Model: Nucleon Electromagnetic Form Factors. *Physical Review C*, 66(3):032201, 2002.
- [53] F. Gross and P. Agbakpe. Shape of the Nucleon. *Physical Review C*, 73(1):015203, 2006.
- [54] F. Gross, G. Ramalho and M. T. Pena. Pure S-wave Covariant Model for the Nucleon. *Physical Review C*, 77(1):015202, 2008.
- [55] M. De Sanctis *et al.* Electromagnetic Form Factors and the Hypercentral Constituent Quark Model. *Physical Review C*, 76(6):062201, 2007.
- [56] E. Santopinto *et al.* High Q^2 Behavior of the Electromagnetic Form Factors in the Relativistic Hypercentral Constituent Quark Model. *Physical Review C*, 82(6):065204, 2010.
- [57] A. J. R. Puckett *et al.* Final Analysis of Proton Form Factor Ratio Data at $Q^2 = 4.0, 4.8, \text{ and } 5.6 \text{ GeV}^2$. *Physical Review C*, 85(4):045203, 2012.

- [58] A. Bashir *et al.* Collective Perspective on Advances in Dyson—Schwinger Equation QCD. *Communications in Theoretical Physics*, 58(1):79–134, July 2012.
- [59] I. C. Cloët *et al.* Survey of Nucleon Electromagnetic Form Factors. *Few-Body Systems*, 46(1):1–36, 2009.
- [60] X. Ji. Generalized Parton Distributions. *Annual Review of Nuclear and Particle Science*, 54(1):413–450, 2004.
- [61] A. V. Belitsky and A. V. Radyushkin. Unraveling Hadron Structure with Generalized Parton Distributions. *Physics Reports*, 418(1-6):1–387, 2005.
- [62] G. Ecker. Chiral Perturbation Theory. *Progress in Particle and Nuclear Physics*, 35:1–80, 1995.
- [63] A. Faessler *et al.* Chiral Dynamics of Baryons in a Lorentz Covariant Quark Model. *Physical Review D*, 73(11):114021, 2006.
- [64] S. J. Brodsky and G. F. de Téramond. AdS/CFT and light-front QCD. In *Search For The “Totally Unexpected” In The LHC Era*, pages 139–183. World Scientific, 2010.
- [65] T. Gutsche *et al.* Nucleon Structure Including High Fock States in AdS/CFT. *Physical Review D*, 86(3):036007, 2012.
- [66] Jefferson Lab. CEBAF at Jefferson Lab, 2022. Available online at <https://www.jlab.org/brochures>.
- [67] N. Baltzell *et al.* The CLAS12 Beamline and its Performance. *Nuclear Instruments and Methods in Physics Research Section A: Accelerators, Spectrometers, Detectors and Associated Equipment*, 959:163421, 2020.

- [68] V. D. Burkert *et al.* The CLAS12 Spectrometer at Jefferson Laboratory. *Nuclear Instruments and Methods in Physics Research Section A: Accelerators, Spectrometers, Detectors and Associated Equipment*, 959:163419, 2020.
- [69] M. A. Antonioli *et al.* The CLAS12 Silicon Vertex Tracker. *Nuclear Instruments and Methods in Physics Research Section A: Accelerators, Spectrometers, Detectors and Associated Equipment*, 962:163701, 2020.
- [70] D. S. Carman *et al.* The CLAS12 Forward Time-of-Flight System. *Nuclear Instruments and Methods in Physics Research Section A: Accelerators, Spectrometers, Detectors and Associated Equipment*, 960:163629, 2020.
- [71] P. Chatagnon *et al.* The CLAS12 Central Neutron Detector. *Nuclear Instruments and Methods in Physics Research Section A: Accelerators, Spectrometers, Detectors and Associated Equipment*, 959:163441, 2020.
- [72] R. Fair *et al.* The CLAS12 Superconducting Magnets. *Nuclear Instruments and Methods in Physics Research Section A: Accelerators, Spectrometers, Detectors and Associated Equipment*, 962:163578, 2020.
- [73] A. Acker *et al.* The CLAS12 Forward Tagger. *Nuclear Instruments and Methods in Physics Research Section A: Accelerators, Spectrometers, Detectors and Associated Equipment*, 959:163475, 2020.
- [74] M. D. Mestayer *et al.* The CLAS12 Drift Chamber System. *Nuclear Instruments and Methods in Physics Research Section A: Accelerators, Spectrometers, Detectors and Associated Equipment*, 959:163518, 2020.
- [75] Y. G. Sharabian *et al.* The CLAS12 High Threshold Cherenkov Counter. *Nuclear Instruments and Methods in Physics Research Section A: Accelerators, Spectrometers, Detectors and Associated Equipment*, 968:163824, 2020.

- [76] M. Ungaro *et al.* The CLAS12 Low Threshold Cherenkov Detector. *Nuclear Instruments and Methods in Physics Research Section A: Accelerators, Spectrometers, Detectors and Associated Equipment*, 957:163420, 2020.
- [77] M. Contalbrigo *et al.* The CLAS12 Ring Imaging Cherenkov Detector. *Nuclear Instruments and Methods in Physics Research Section A: Accelerators, Spectrometers, Detectors and Associated Equipment*, 964:163791, 2020.
- [78] G. Asryan *et al.* The CLAS12 Forward Electromagnetic Calorimeter. *Nuclear Instruments and Methods in Physics Research Section A: Accelerators, Spectrometers, Detectors and Associated Equipment*, 959:163425, 2020.
- [79] M. Amarian *et al.* The CLAS Forward Electromagnetic Calorimeter. *Nuclear Instruments and Methods in Physics Research Section A: Accelerators, Spectrometers, Detectors and Associated Equipment*, 460(2-3):239–265, 2001.
- [80] S. Boyarinov, B. Raydo *et al.* The CLAS12 Data Acquisition System. *Nuclear Instruments and Methods in Physics Research Section A: Accelerators, Spectrometers, Detectors and Associated Equipment*, 966:163698, 2020.
- [81] B. Raydo *et al.* The CLAS12 Trigger System. *Nuclear Instruments and Methods in Physics Research Section A: Accelerators, Spectrometers, Detectors and Associated Equipment*, 960:163529, 2020.
- [82] V. Ziegler *et al.* The CLAS12 Software Framework and Event Reconstruction. *Nuclear Instruments and Methods in Physics Research Section A: Accelerators, Spectrometers, Detectors and Associated Equipment*, 959:163472, 2020.
- [83] CLAS Collaboration at Jefferson Laboratory. CLAS12 RG-A - Analysis Note Overview and Procedures, 2020. <https://clas12-docdb.jlab.>

[org/DocDB/0009/000949/001/RGA_Analysis_Overview_and_Procedures-08172020.pdf](https://www.jlab.org/DocDB/0009/000949/001/RGA_Analysis_Overview_and_Procedures-08172020.pdf).

- [84] S. Das. A Simple Alternative to the Crystal Ball Function. *arXiv preprint arXiv:1603.08591*, 2016.
- [85] G. Ingelman, A. Edin, and J. Rathsman. LEPTO 6.5 — A Monte Carlo generator for deep inelastic lepton-nucleon scattering. *Computer Physics Communications*, 101(1–2):108–134, April 1997.
- [86] S. Stepanyan. Beam Energy Measurement with Elastic Scattering on CLAS, 2002. https://www.jlab.org/Hall-B/notes/clas_notes02/02-008.pdf.
- [87] K. Alexei and S. Kuhn. Momentum Corrections for E6, 2003. https://www.jlab.org/Hall-B/notes/clas_notes03/03-005.pdf.
- [88] G. P. Gilfoyle and O Alam. QUEEG: A Monte Carlo Event Generator for Quasielastic Scattering on Deuterium, 2014.
- [89] M. Ungaro *et al.* The CLAS12 Geant4 Simulation. *Nuclear Instruments and Methods in Physics Research Section A: Accelerators, Spectrometers, Detectors and Associated Equipment*, 959:163422, 2020.
- [90] A. Afanasev, I. Akushevich, V. Burkert, and K. Joo. Qed radiative corrections in processes of exclusive pion electroproduction. *Physical Review D*, 66(7), October 2002.
- [91] G. P. Gilfoyle and A. Afanasev. Radiative Corrections for Deuteron Electro disintegration, 2005.

- [92] J. Adam *et al.* Covariant description of inelastic electron-deuteron scattering: Predictions of the relativistic impulse approximation. *Phys. Rev. C*, 66:044003, Oct 2002.
- [93] Z. Ye, J. Arrington *et al.* Proton and neutron electromagnetic form factors and uncertainties. *Physics Letters B*, 777:8–15, February 2018.
- [94] J. Lachniet. *A High Precision Measurement of the Neutron Magnetic Form Factor using the CLAS Detector*. PhD Thesis: Carnegie Mellon University, 2005.

APPENDIX A
FIT MISSING MASS DISTRIBUTION USING GAUSSIAN
FUNCTION

The following plots show the fitting of the expected and detected neutrons using Gaussian plus a 4th order Polynomial function. Also it shows the parameters of the fit as a function of P_{mm} .

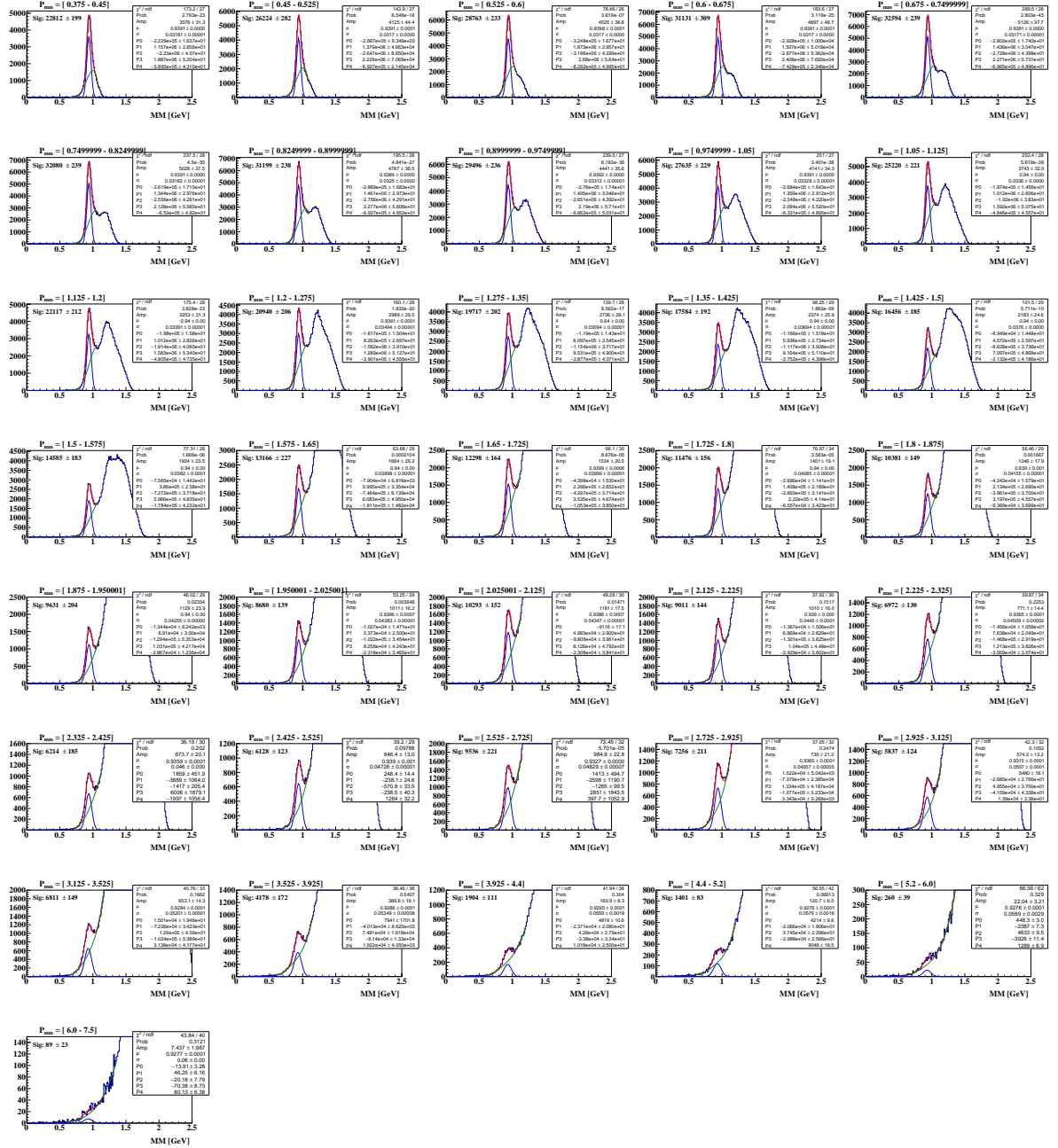


Figure A.1: The missing mass distribution of expected neutron $p(e, e'\pi^+)n$ for different P_{mm} bin. The distribution is fitted with a Gaussian plus polynomial background. The blue curve is the signal distribution after subtraction of the background distribution, the green is the background, and the red is the sum of the two. The fitting is shown for inbending 10.6 GeV dataset.

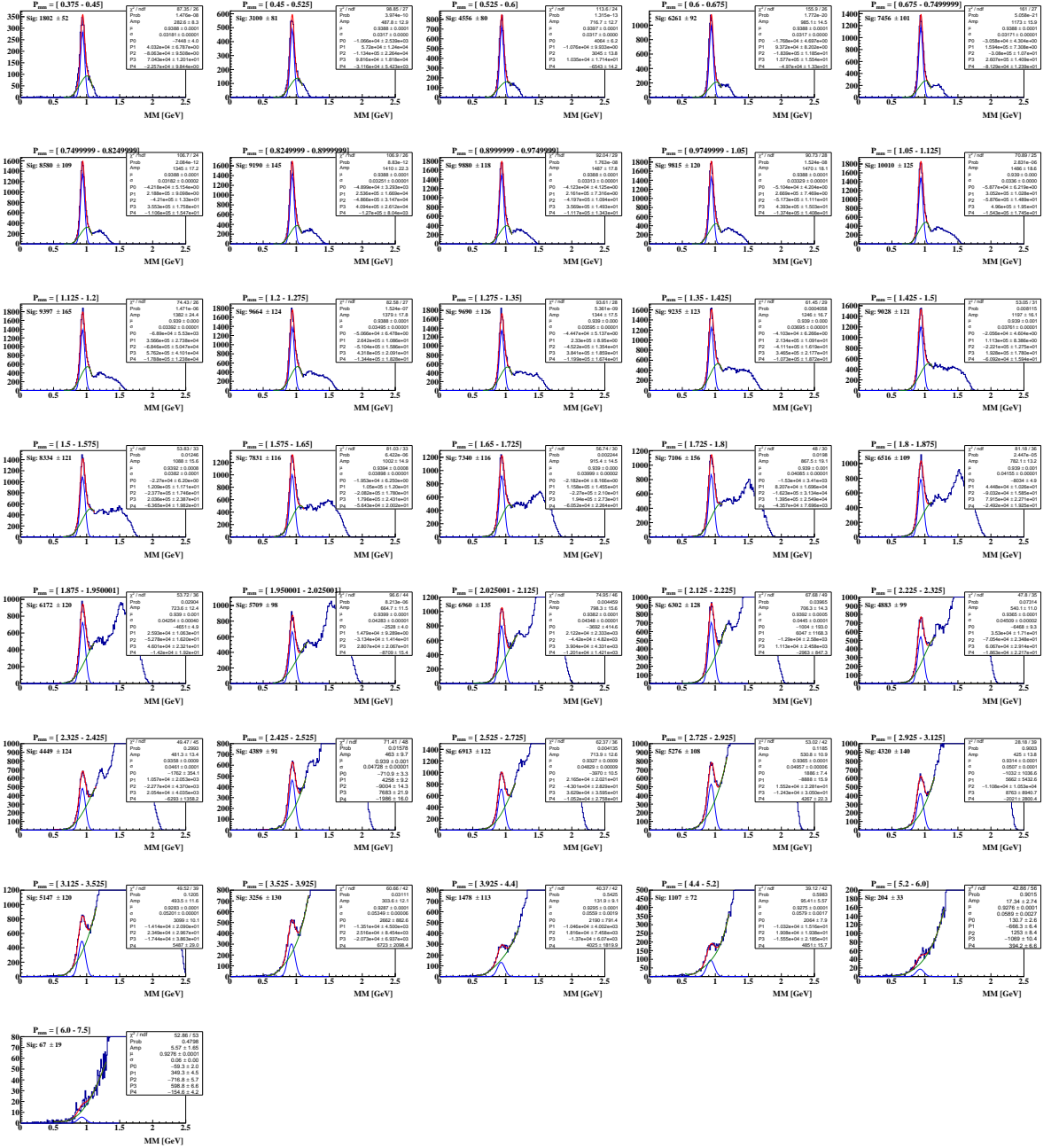


Figure A.2: The missing mass distribution of detected neutron $p(e, e'\pi^+n)$ for different P_{mm} bin. The distribution is fitted with a Gaussian plus polynomial background. The blue curve is the signal distribution after subtraction of the background distribution, the green is the background, and the red is the sum of the two. The fitting is shown for inbending 10.6 GeV dataset.

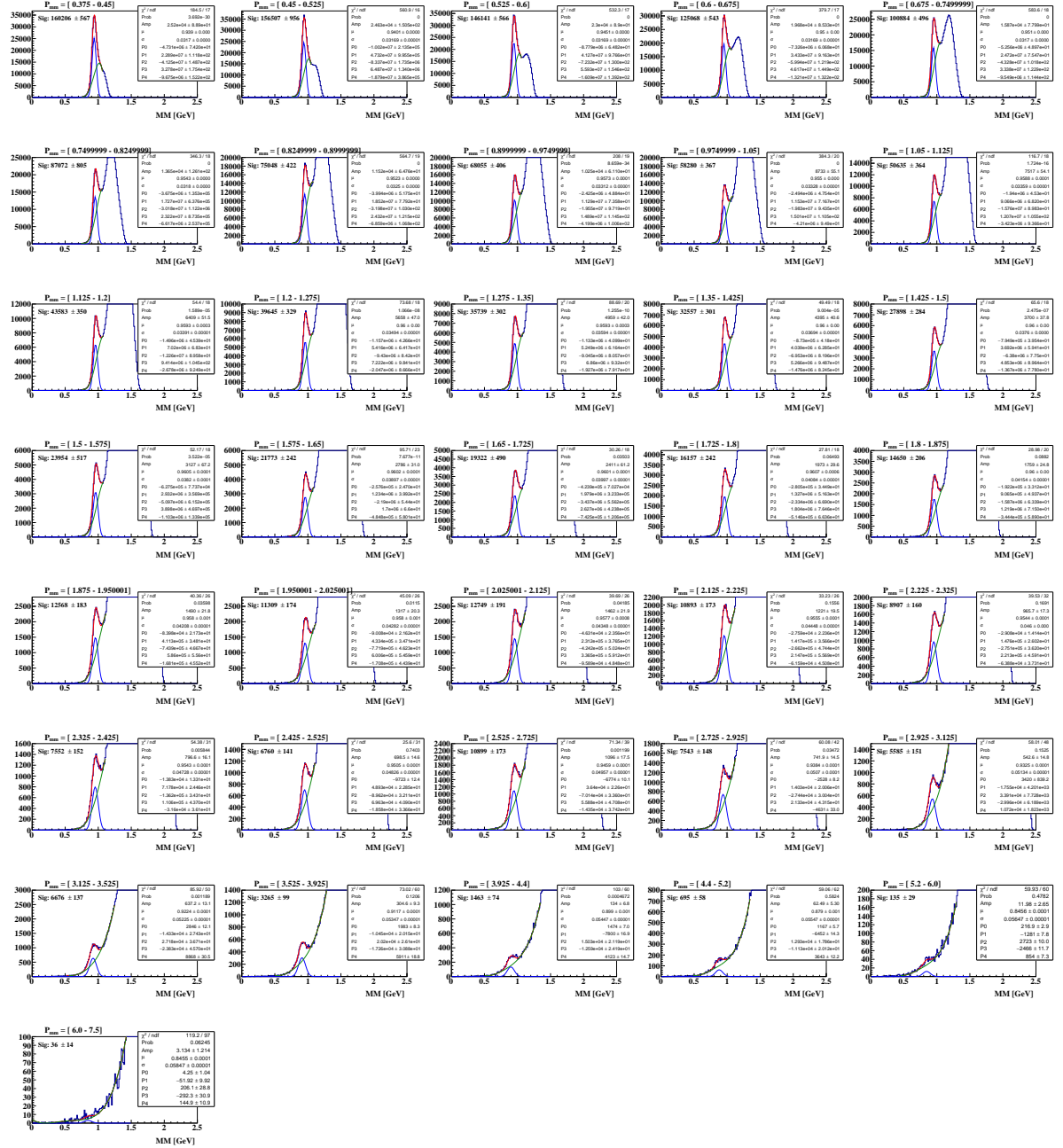


Figure A.3: Missing mass distribution of expected neutron $p(e, e'\pi^+)n$ for different P_{mm} bin. The distribution is fit with a gaussian + polynomial background. The blue curve is the signal distribution after subtraction of the background distribution, the green is the background, and the red is the sum of the two. The fitting is shown for outbending 10.6 GeV dataset.

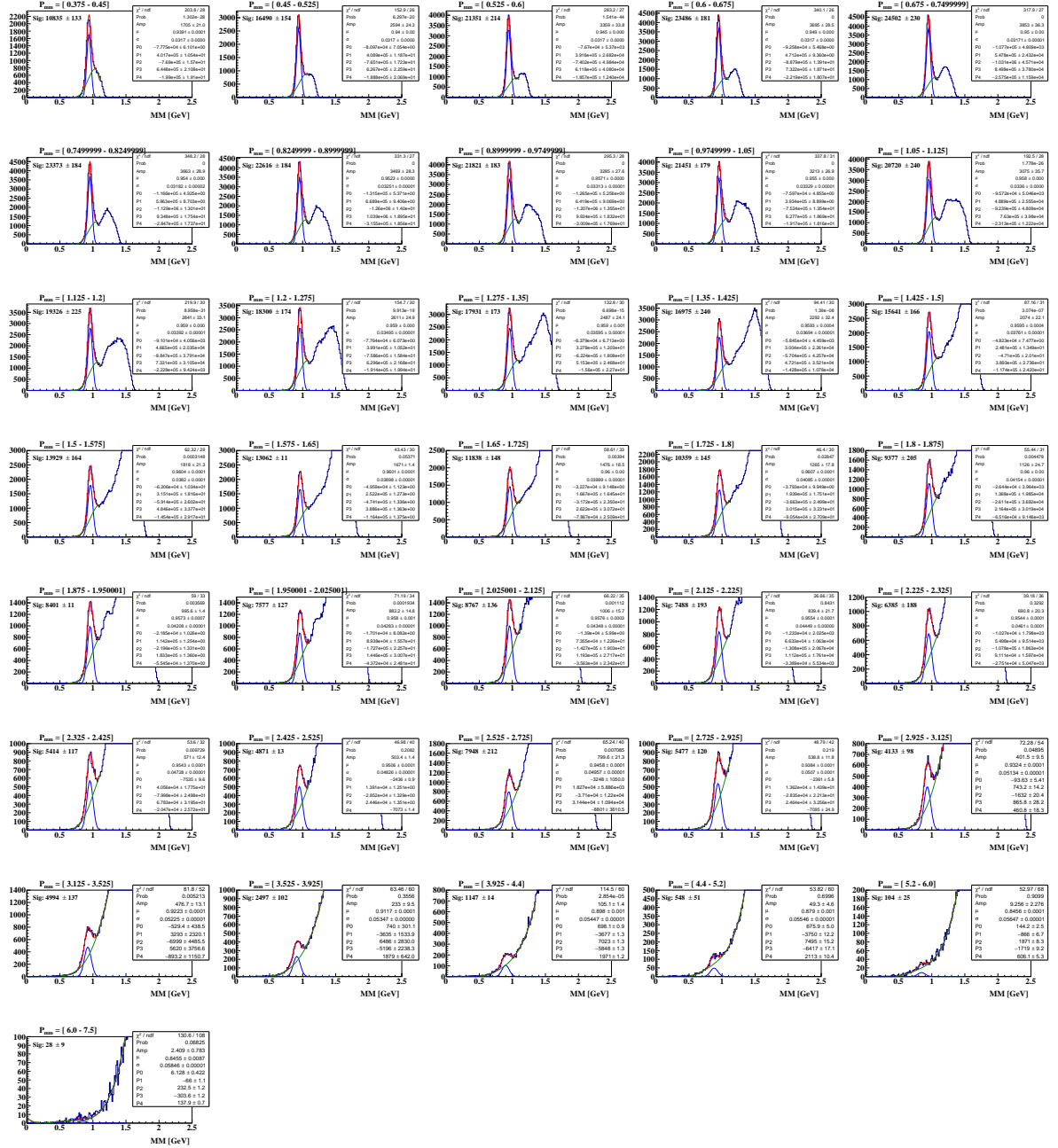


Figure A.4: Missing mass distribution of detected neutron $p(e, e' \pi^+ n)$ for different P_{mm} bin. The distribution is fit with a gaussian + polynomial background. The blue curve is the signal distribution after subtraction of the background distribution, the green is the background, and the red is the sum of the two. The fitting is shown for outbending 10.6 GeV dataset.

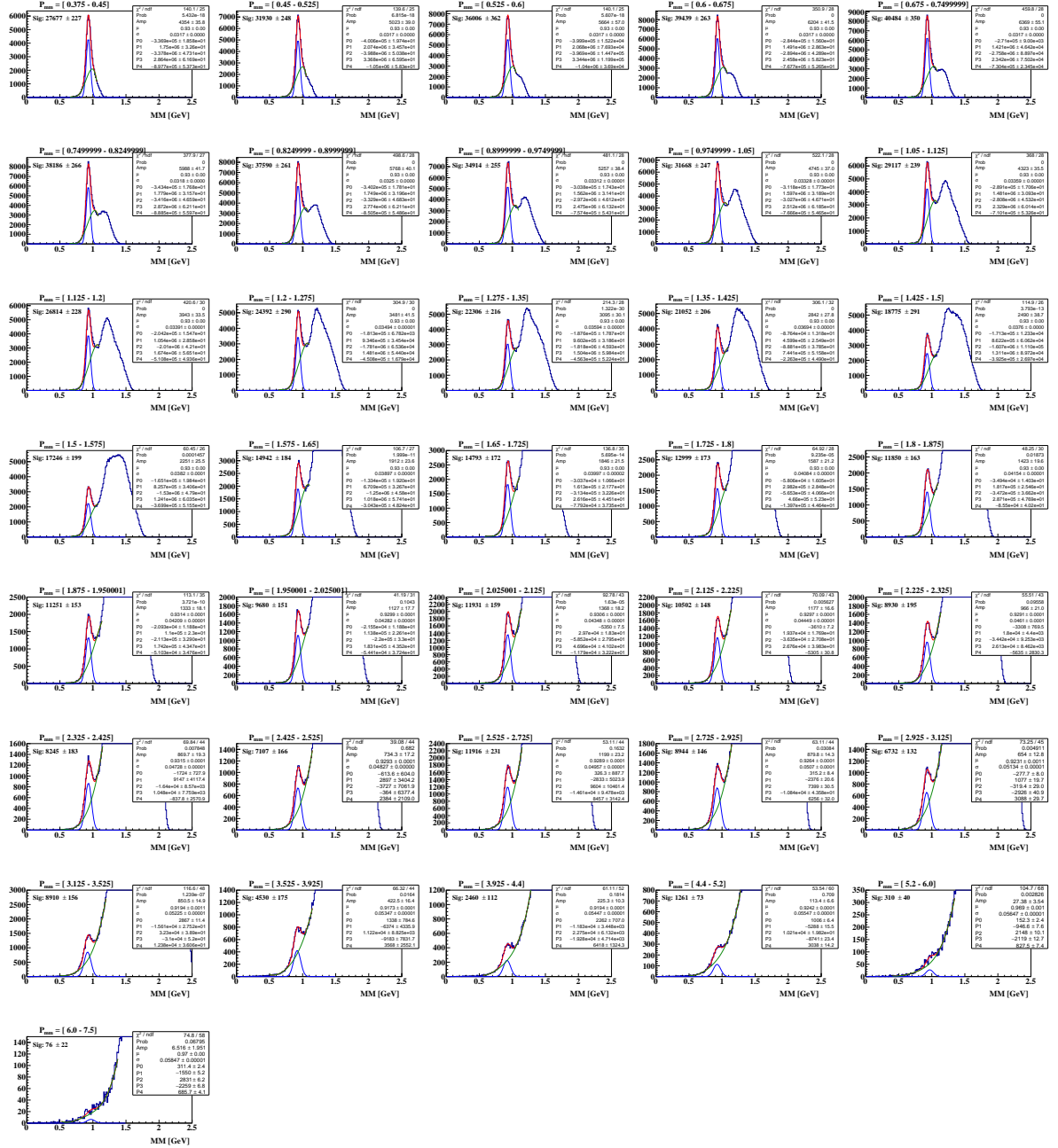


Figure A.5: Missing mass distribution of expected neutron $p(e, e'\pi^+n)$ for different P_{mm} bin. The distribution is fit with a Gaussian + polynomial background. The blue curve is the signal distribution after subtraction of the background distribution, the green is the background, and the red is the sum of the two. The fitting is shown for inbending 10.2 GeV dataset.

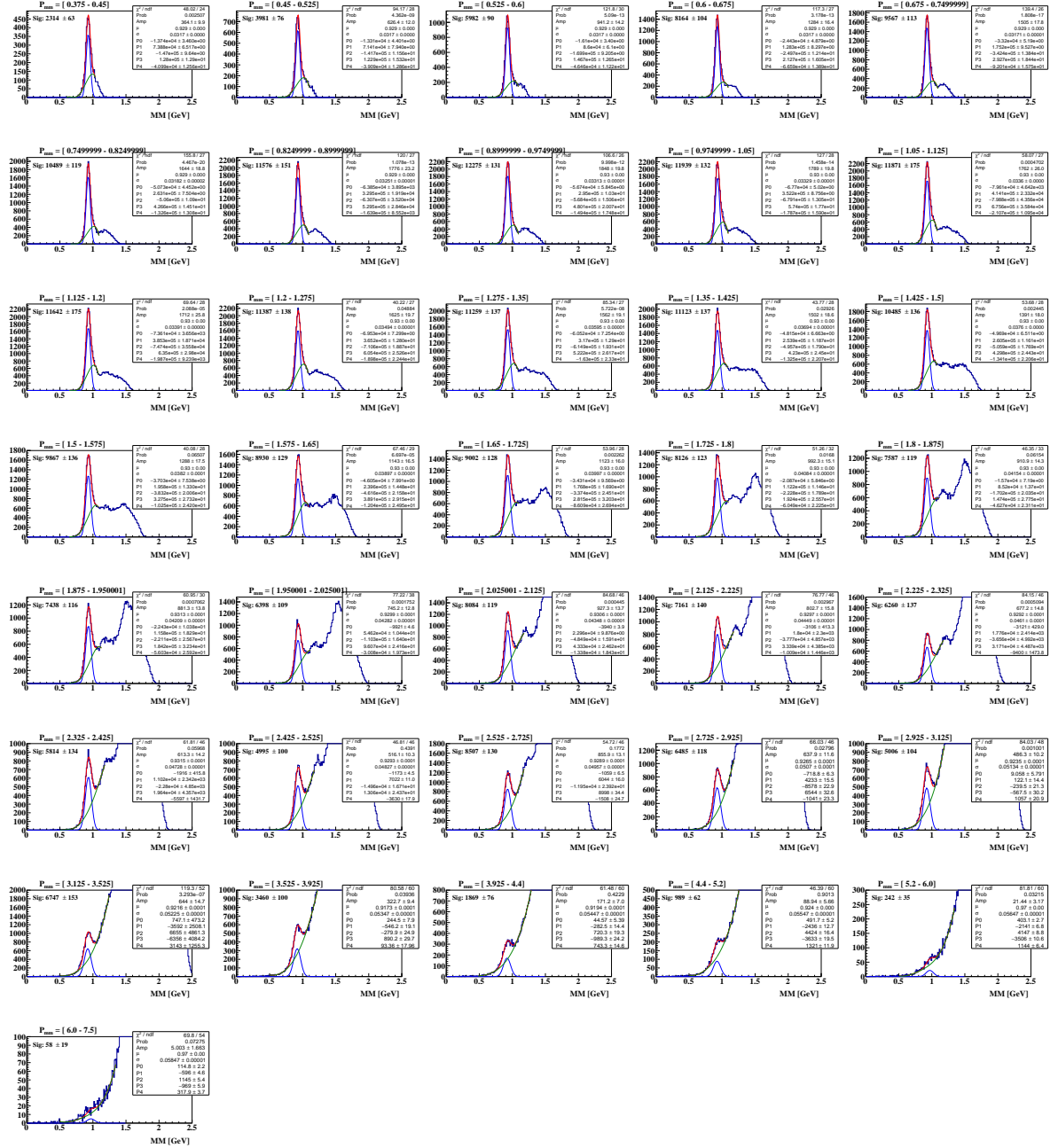


Figure A.6: Missing mass distribution of detected neutron $p(e, e'\pi^+n)$ for different P_{mm} bin. The distribution is fit with a Gaussian + polynomial background. The blue curve is the signal distribution after subtraction of the background distribution, the green is the background, and the red is the sum of the two. The fitting is shown for inbending 10.2 GeV dataset.

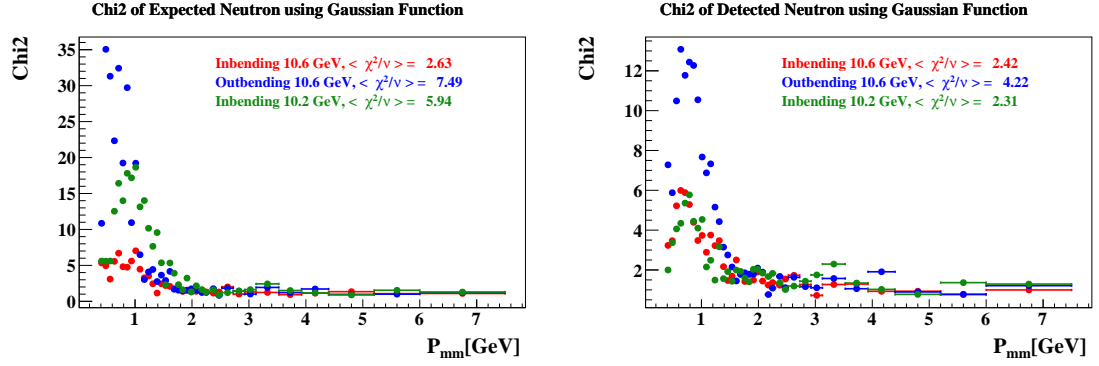


Figure A.7: The χ^2 of the expected (left) and detected (right) neutron as a function of P_{mm} using Gaussian + polynomial background.

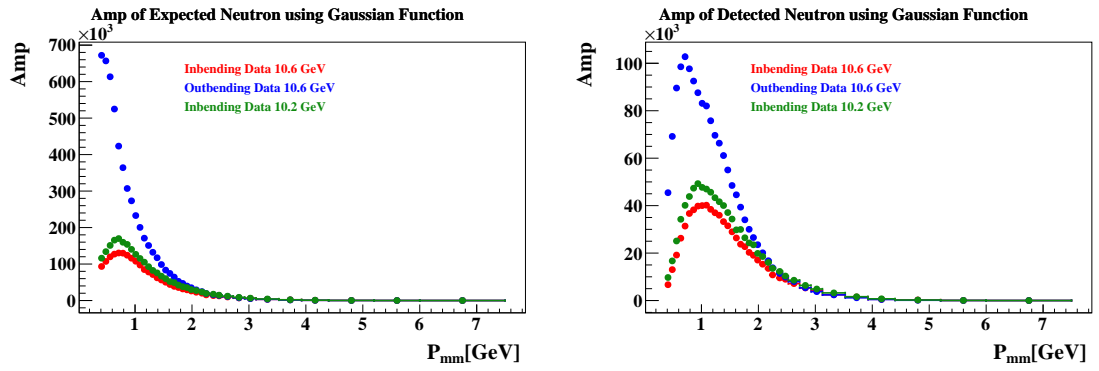


Figure A.8: The amplitude of the expected (left) and detected (right) neutron as a function of P_{mm} using Gaussian + polynomial background.

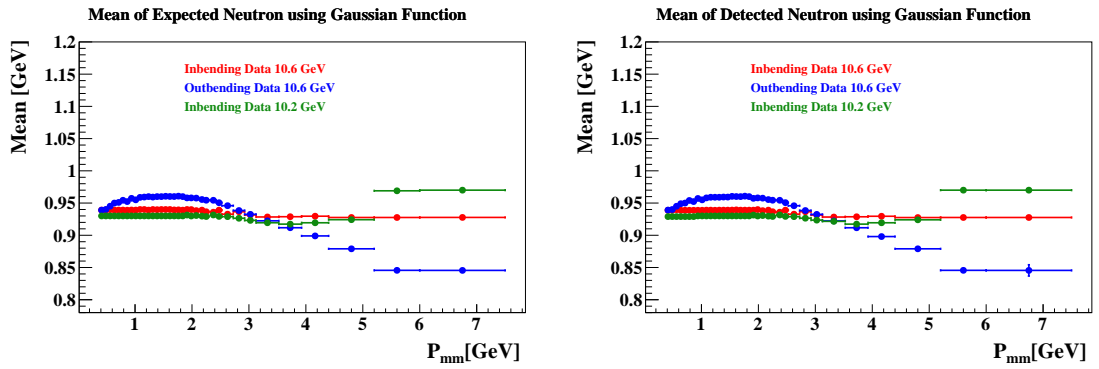


Figure A.9: The mean of the expected (left) and detected (right) neutron as a function of P_{mm} using Gaussian + polynomial background.

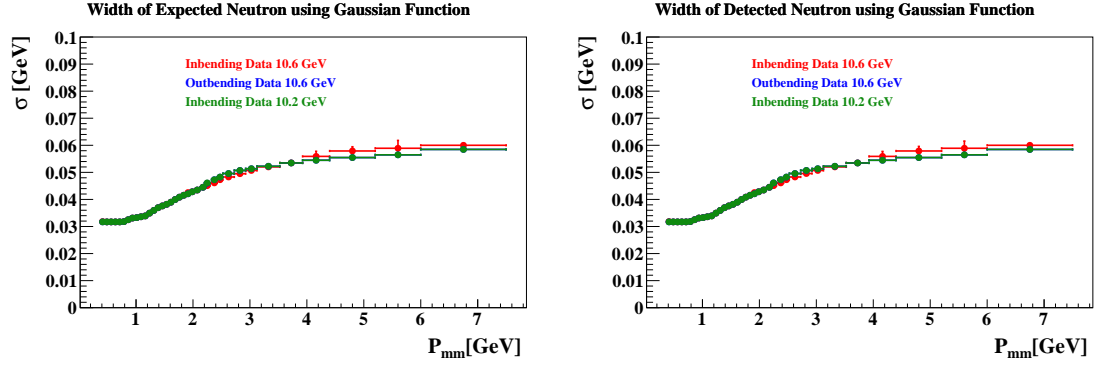


Figure A.10: The width of the expected (left) and detected (right) neutron as a function of P_{mm} using Gaussian + polynomial background.

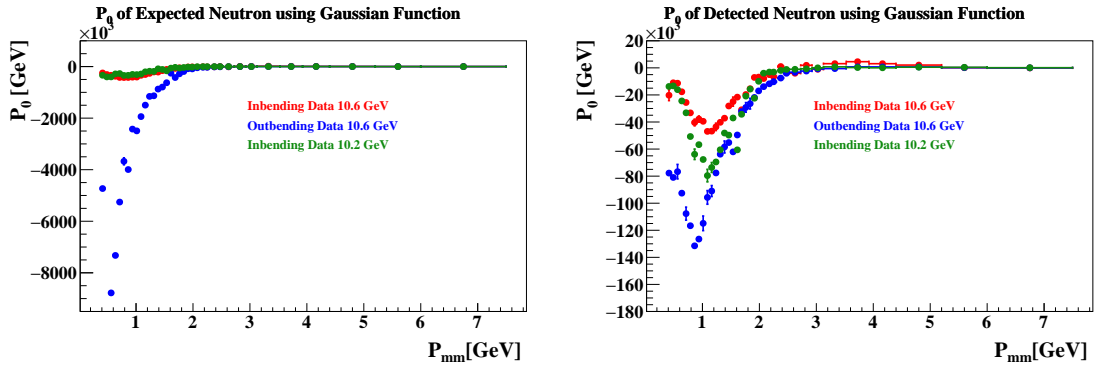


Figure A.11: The P_0 parameter of the expected (left) and detected (right) neutron as a function of P_{mm} using Gaussian + polynomial background.

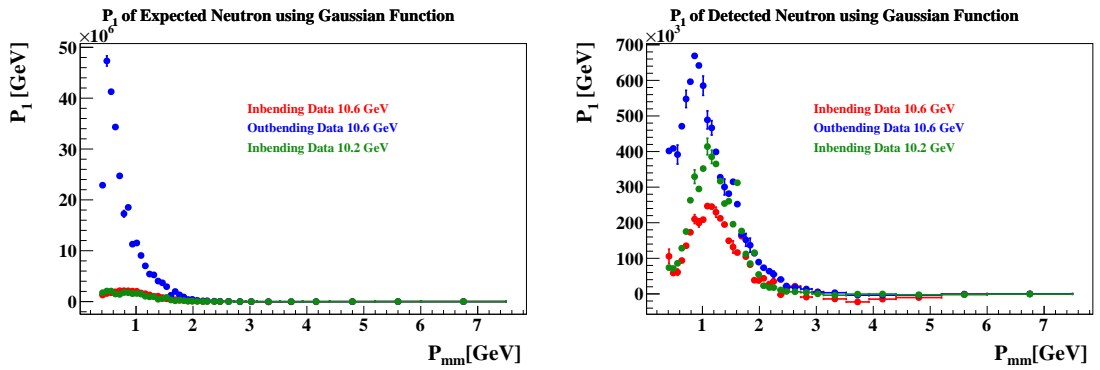


Figure A.12: The P_1 parameter of the expected (left) and detected (right) neutron as a function of P_{mm} using Gaussian + polynomial background.

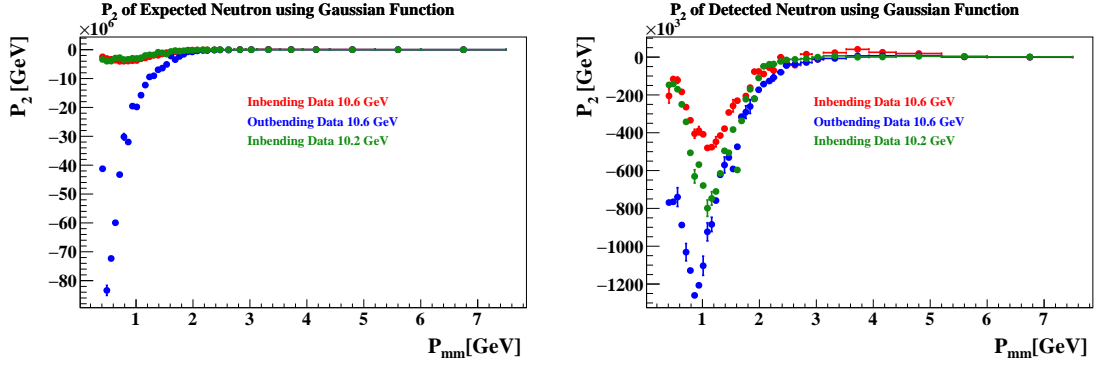


Figure A.13: The P_2 parameter of the expected (left) and detected (right) neutron as a function of P_{mm} using Gaussian + polynomial background.

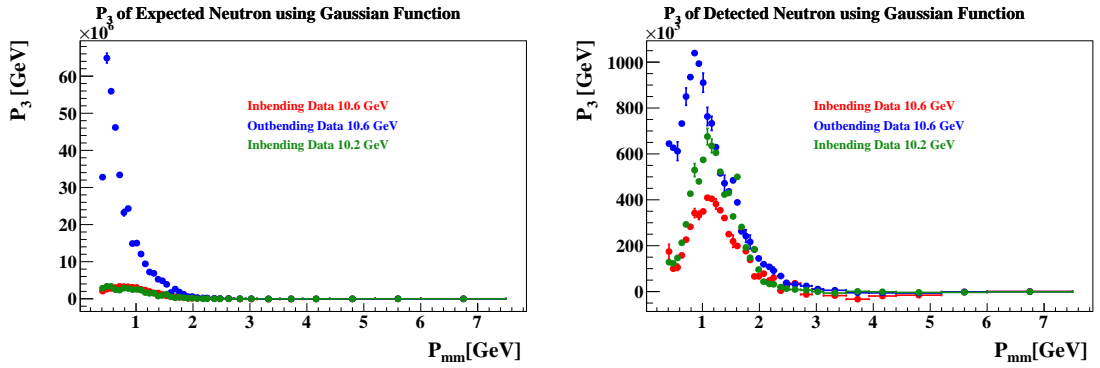


Figure A.14: The P_3 parameter of the expected (left) and detected (right) neutron as a function of P_{mm} using Gaussian + polynomial background.

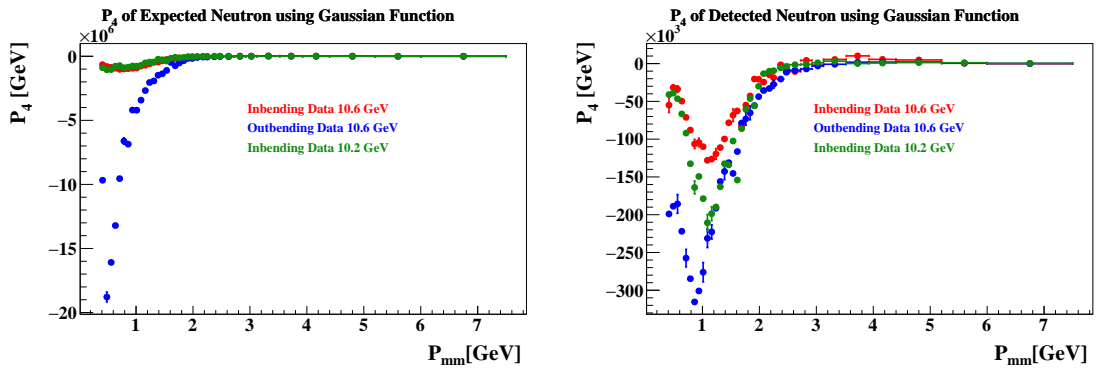


Figure A.15: The P_4 parameter of the expected (left) and detected (right) neutron as a function of P_{mm} using Gaussian + polynomial background.

APPENDIX B
FIT MISSING MASS DISTRIBUTION USING CRYSTAL BALL
FUNCTION

The following plots show the fitting of the expected and detected neutrons using Crystal Ball plus a 4th order Polynomial function. Also it shows the parameters of the fit as a function of P_{mm} .

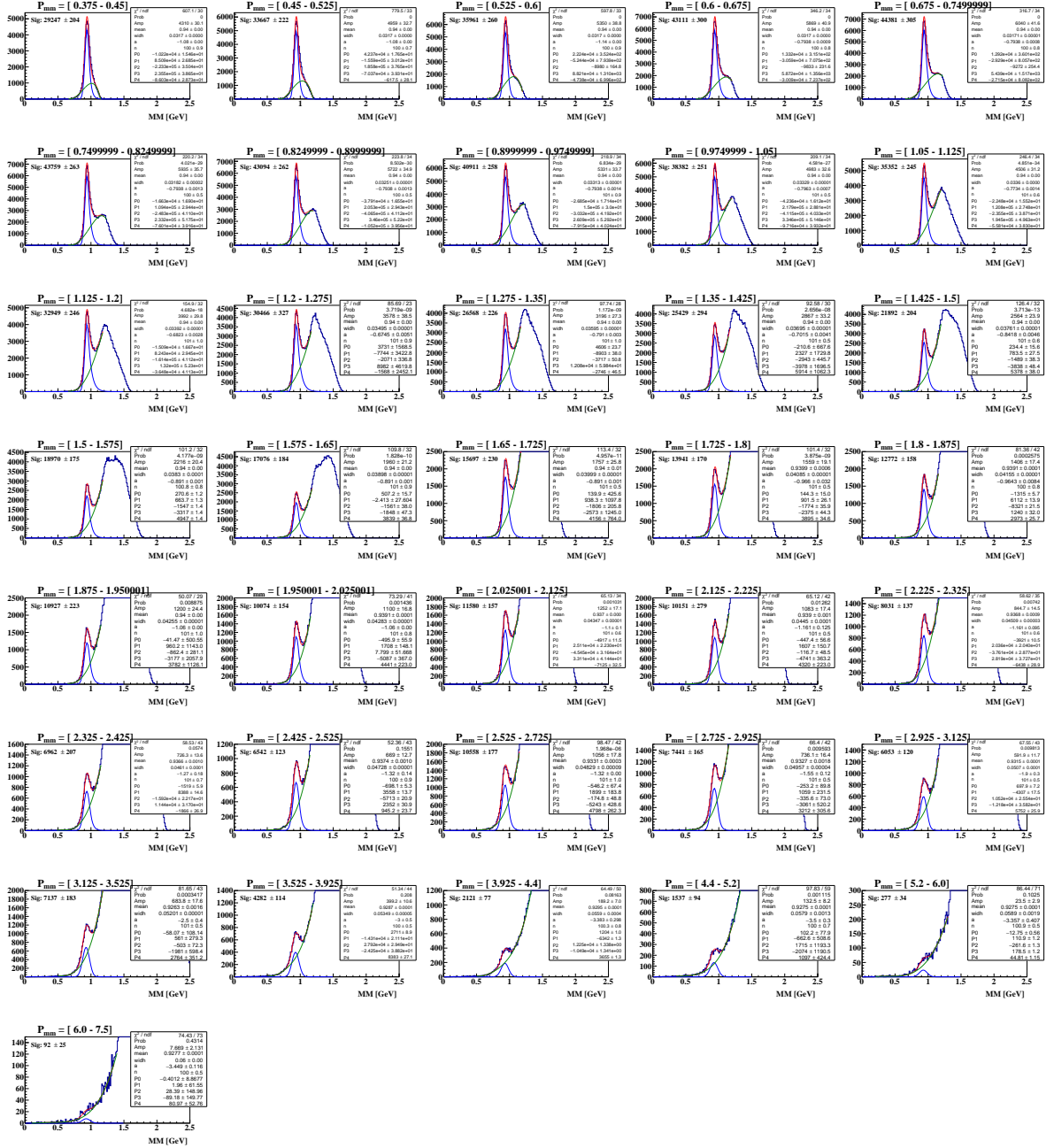


Figure B.1: The missing mass distribution of expected neutron $p(e, e'\pi^+)n$ for different P_{mm} bin. The distribution is fitted with a Crystal Ball + polynomial background. The blue curve is the signal distribution after subtraction of the background distribution, the green is the background, and the red is the sum of the two. The fitting is shown for inbending 10.6 GeV dataset.

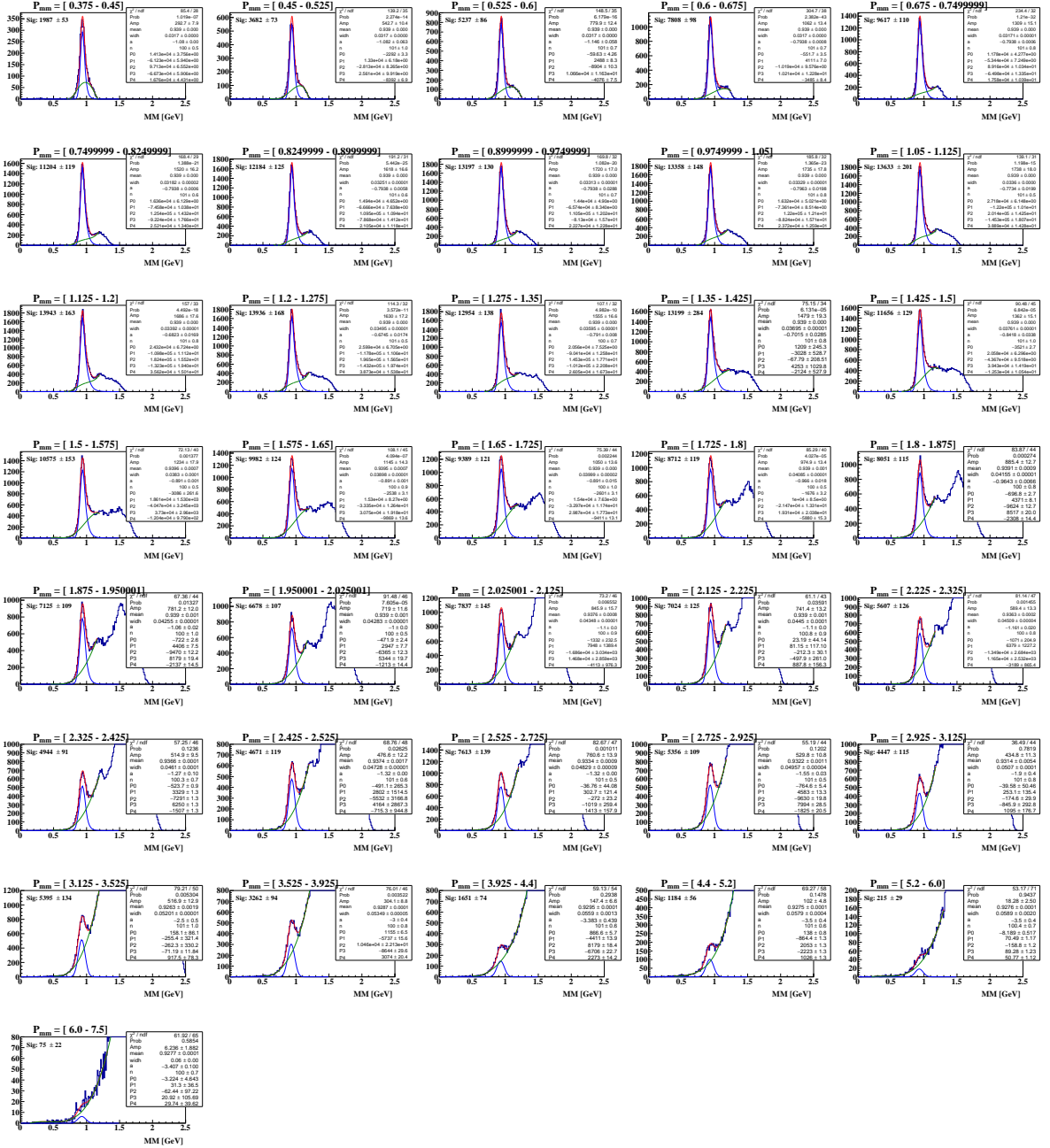


Figure B.2: The missing mass distribution of detected neutron $p(e, e' \pi^+ n)$ for different P_{mm} bin. The distribution is fitted with a Crystal Ball + polynomial background. The blue curve is the signal distribution after subtraction of the background distribution, the green is the background, and the red is the sum of the two. The fitting is shown for inbending 10.6 GeV dataset.

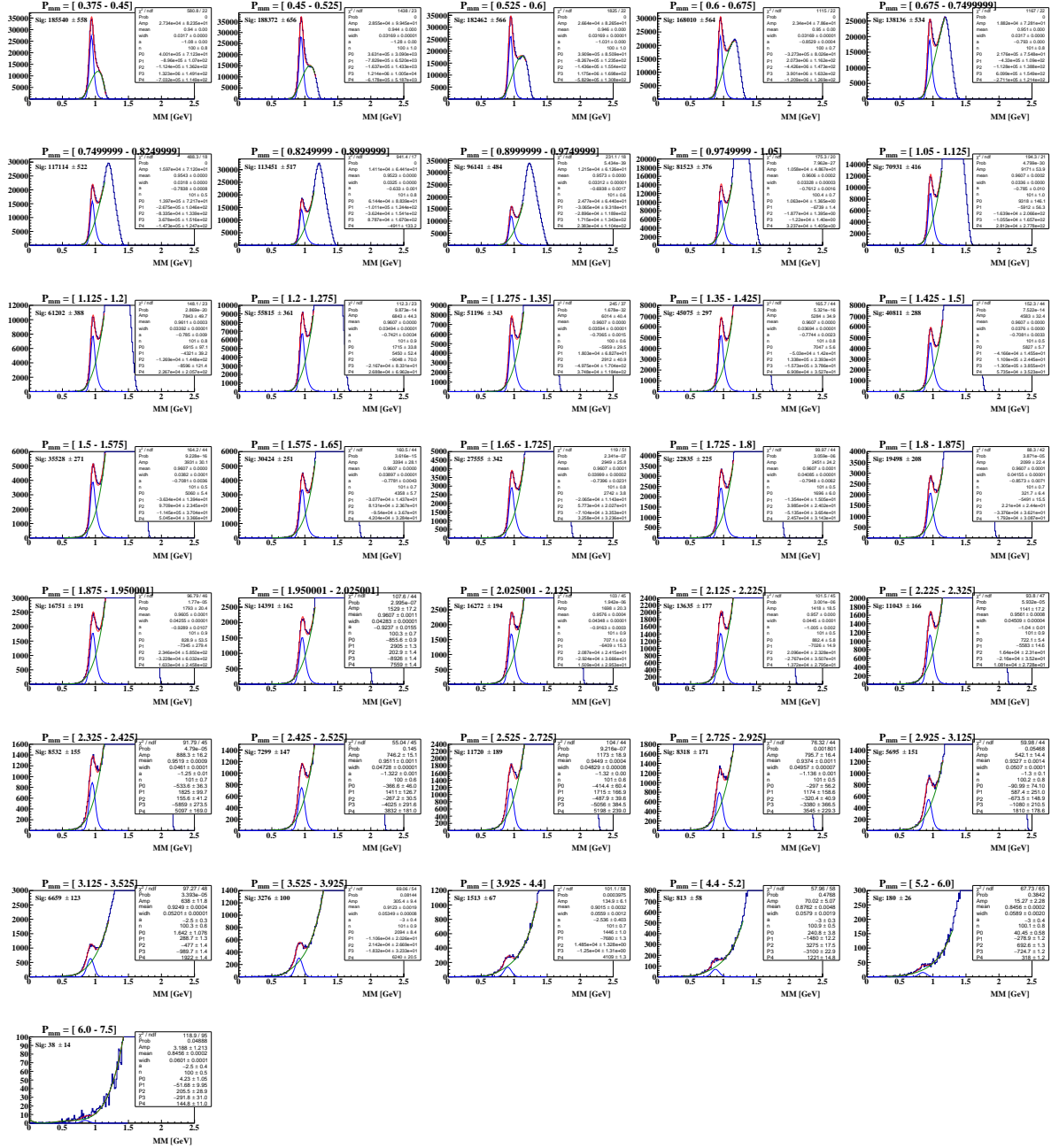


Figure B.3: Missing mass distribution of expected neutron $p(e, e'\pi^+)n$ for different P_{mm} bin. The distribution is fit with a Crystal ball + polynomial background. The blue curve is the signal distribution after subtraction of the background distribution, the green is the background, and the red is the sum of the two. The fitting is shown for outbending 10.6 GeV dataset.

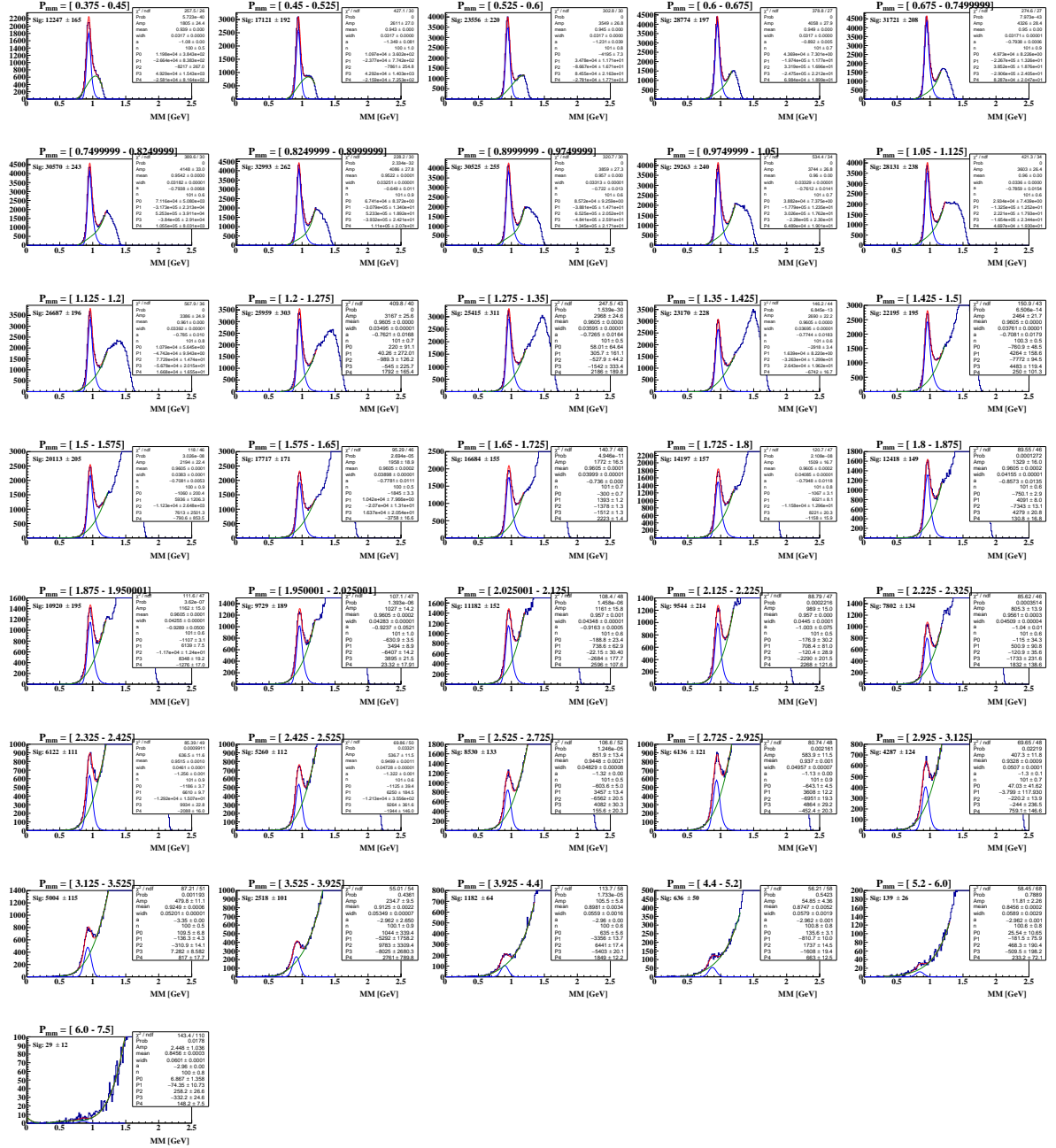


Figure B.4: Missing mass distribution of detected neutron $p(e, e'\pi^+)n$ for different P_{mm} bin. The distribution is fit with a Crystal ball + polynomial background. The blue curve is the signal distribution after subtraction of the background distribution, the green is the background, and the red is the sum of the two. The fitting is shown for outbending 10.6 GeV dataset.

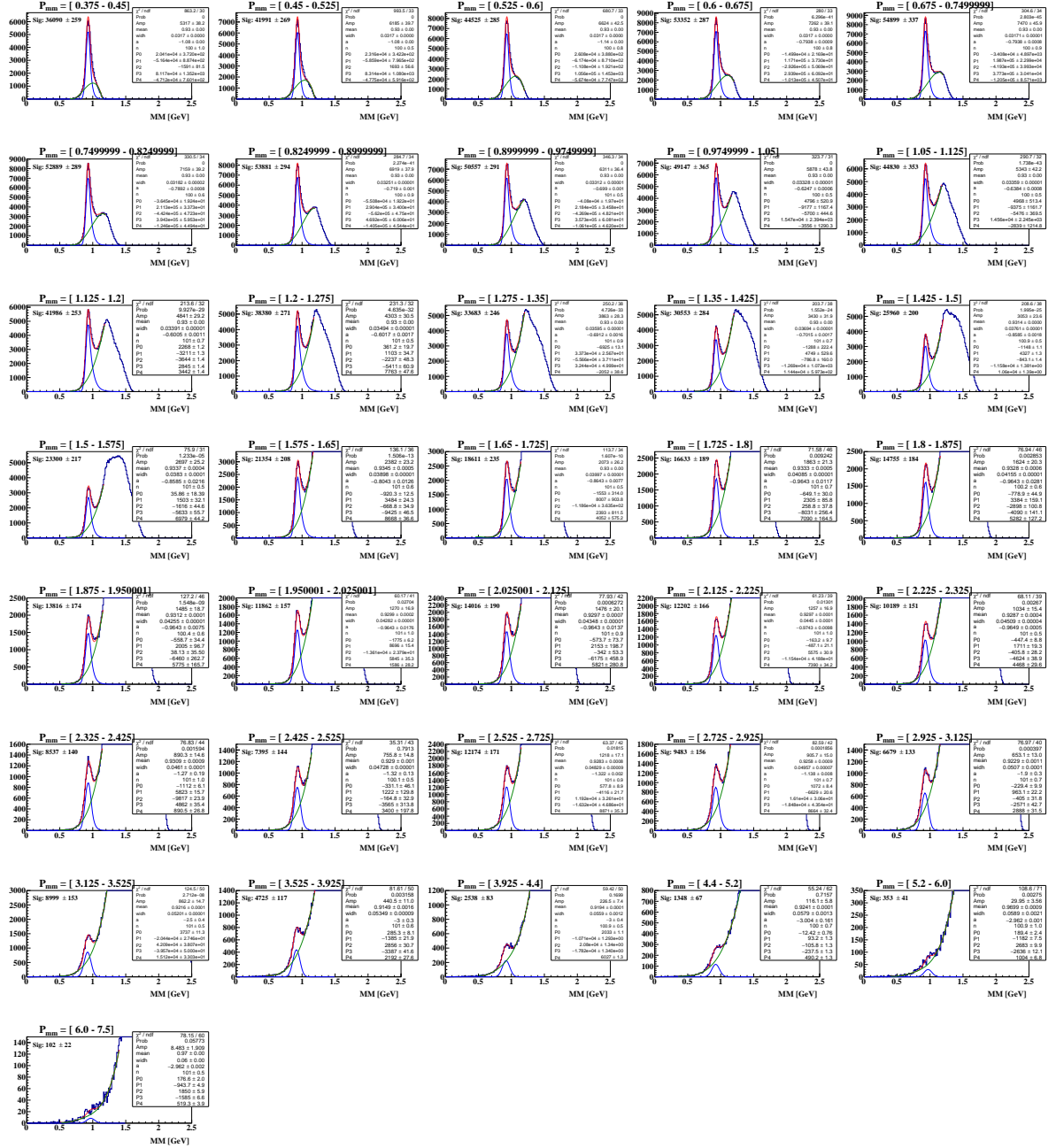


Figure B.5: Missing mass distribution of expected neutron $p(e, e'\pi^+)n$ for different P_{mm} bin. The distribution is fit with a Crystal ball + polynomial background. The blue curve is the signal distribution after subtraction of the background distribution, the green is the background, and the red is the sum of the two. The fitting is shown for inbending 10.2 GeV dataset.

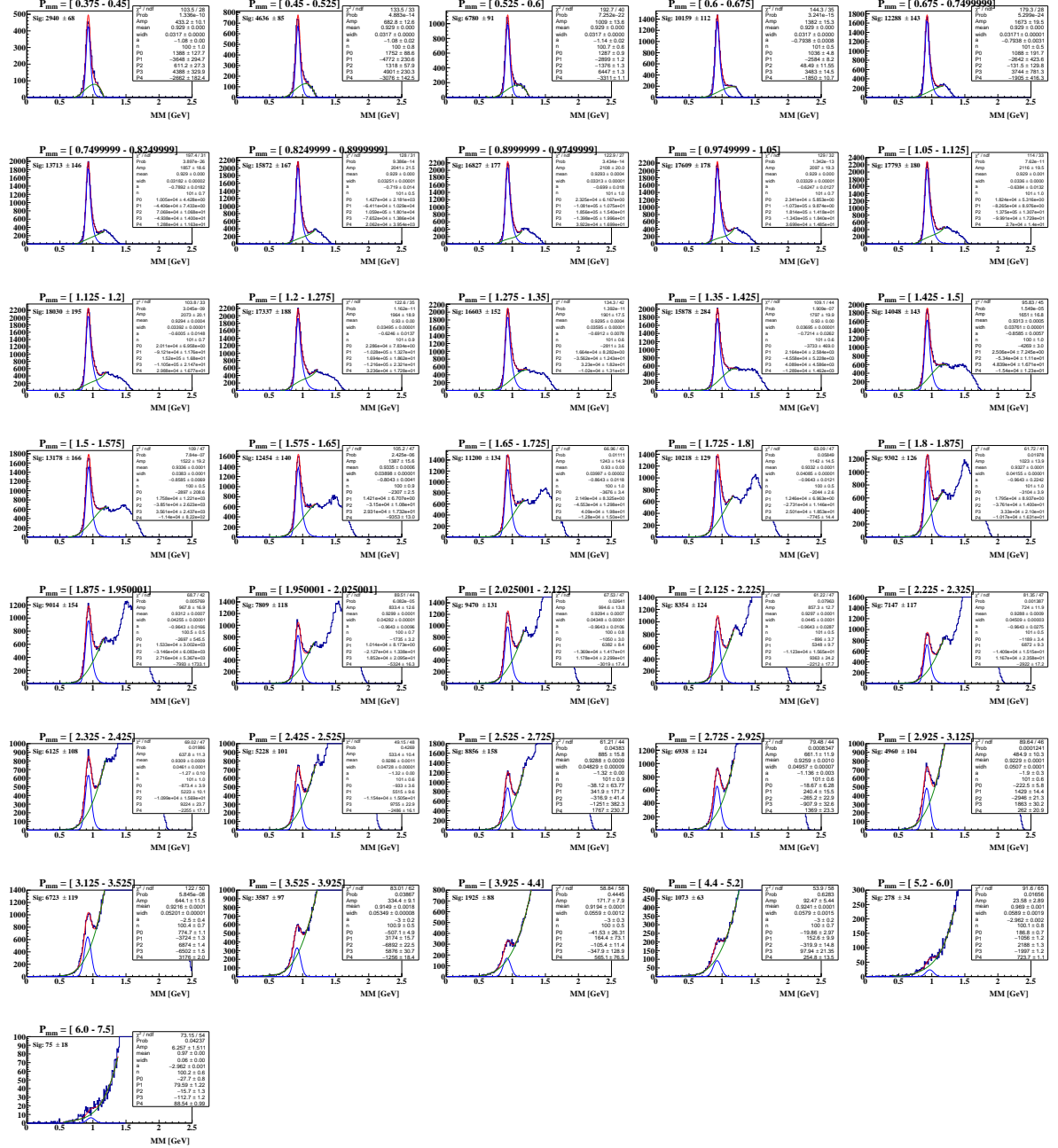


Figure B.6: Missing mass distribution of detected neutron $p(e, e'\pi^+)n$ for different P_{mm} bin. The distribution is fit with a Crystal ball + polynomial background. The blue curve is the signal distribution after subtraction of the background distribution, the green is the background, and the red is the sum of the two. The fitting is shown for inbending 10.2 GeV dataset.

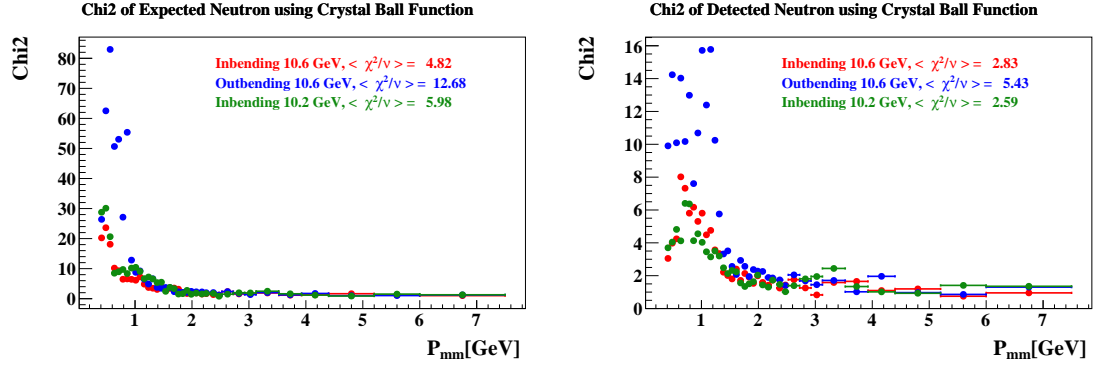


Figure B.7: The χ^2 of the expected (left) and detected (right) neutron as a function of P_{mm} using Crystal ball + polynomial background.

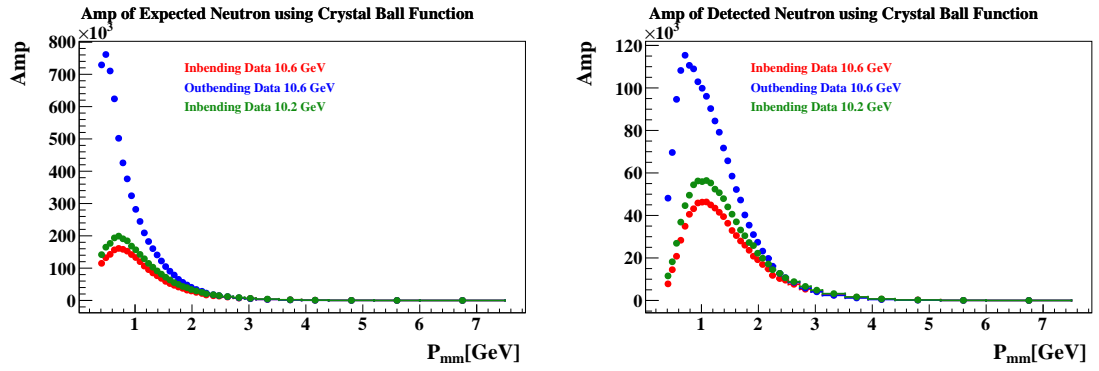


Figure B.8: The amplitude of the expected (left) and detected (right) neutron as a function of P_{mm} using Crystal ball + polynomial background.

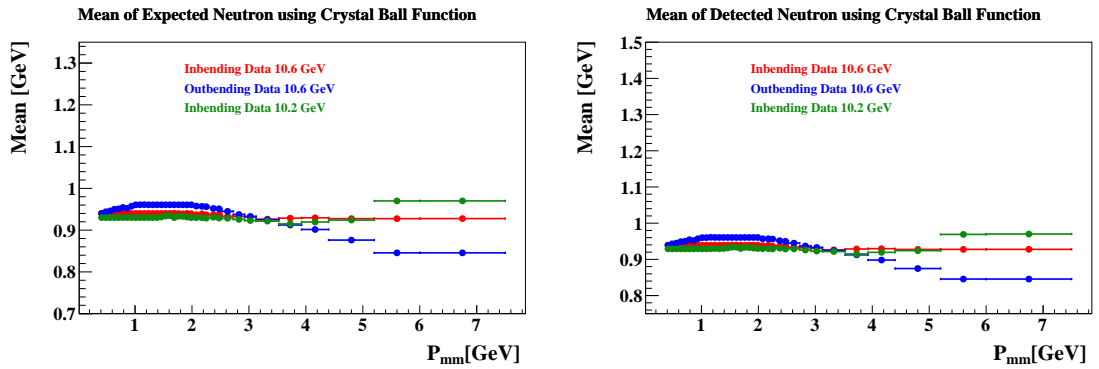


Figure B.9: The mean of the expected (left) and detected (right) neutron as a function of P_{mm} using Crystal ball + polynomial background.

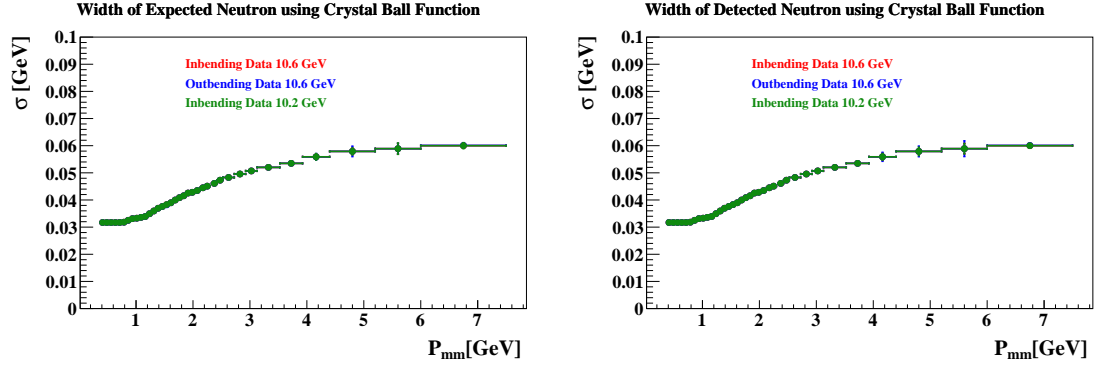


Figure B.10: The width of the expected (left) and detected (right) neutron as a function of P_{mm} using Crystal ball + polynomial background.

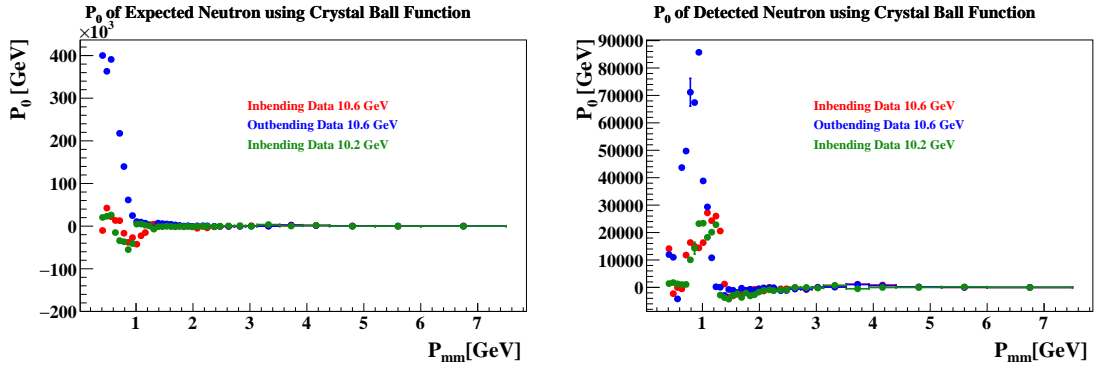


Figure B.11: The P_0 parameter of the expected (left) and detected (right) neutron as a function of P_{mm} using Crystal ball + polynomial background.

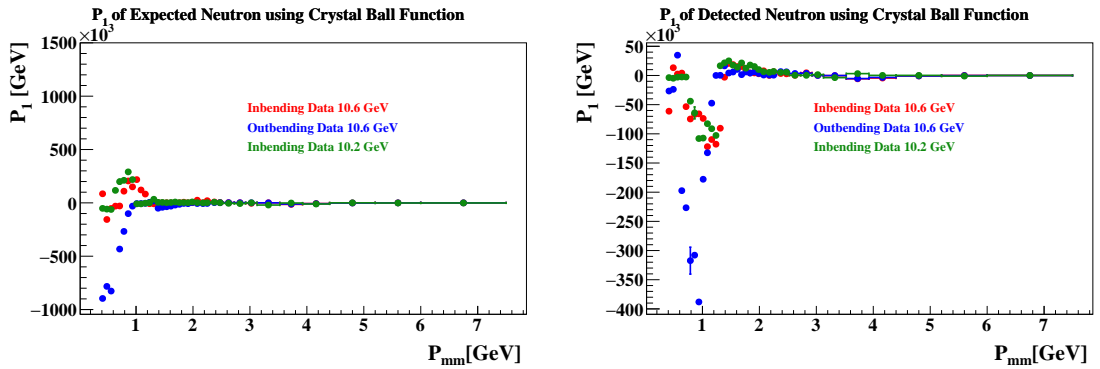


Figure B.12: The P_1 parameter of the expected (left) and detected (right) neutron as a function of P_{mm} using Crystal ball + polynomial background.

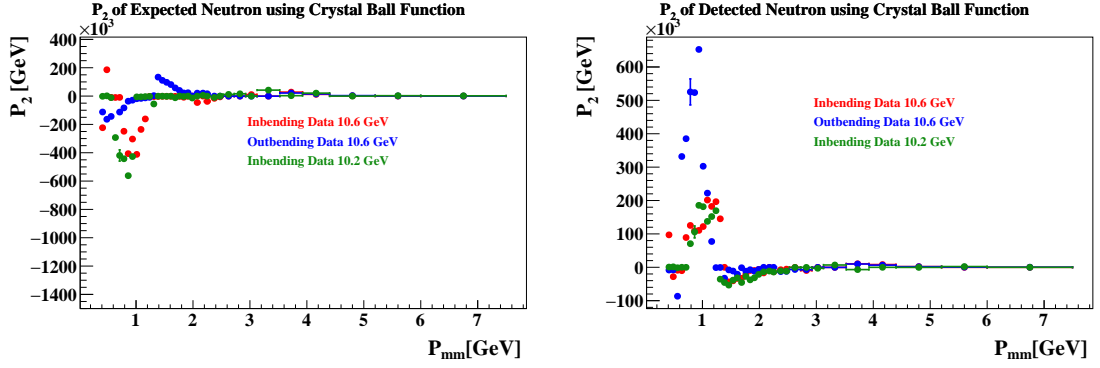


Figure B.13: The P_2 parameter of the expected (left) and detected (right) neutron as a function of P_{mm} using Crystal ball + polynomial background.

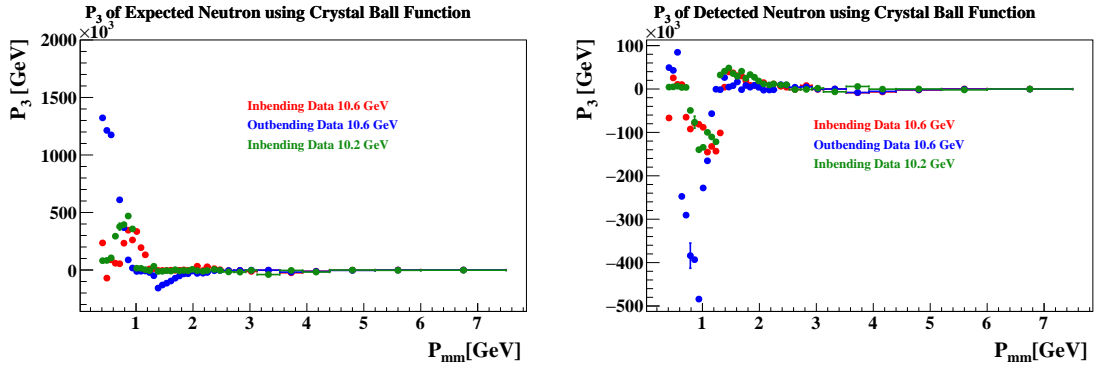


Figure B.14: The P_3 parameter of the expected (left) and detected (right) neutron as a function of P_{mm} using Crystal ball + polynomial background.

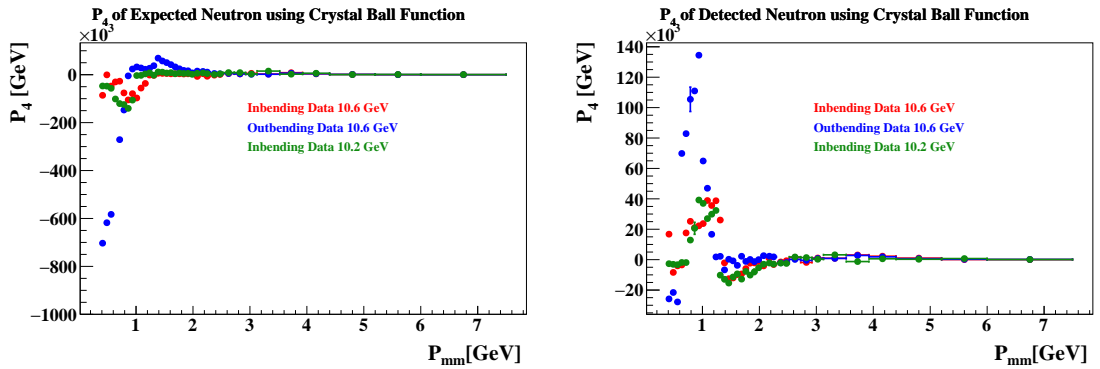


Figure B.15: The P_4 parameter of the expected (left) and detected (right) neutron as a function of P_{mm} using Crystal ball + polynomial background.

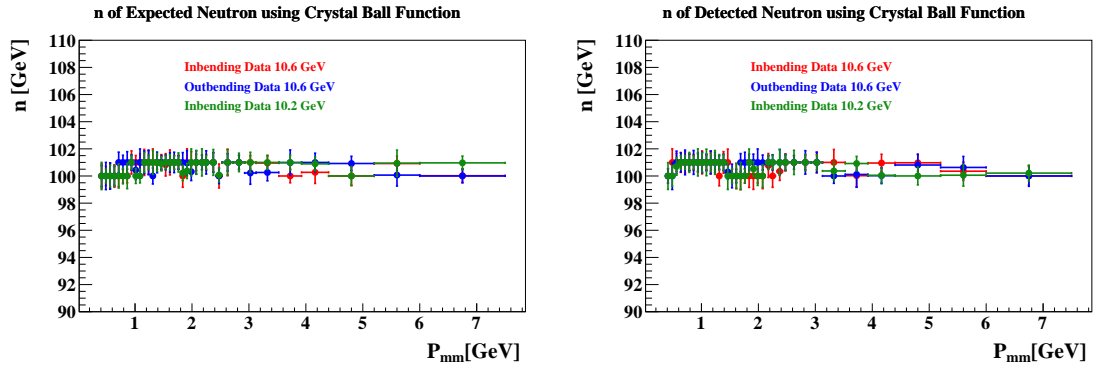


Figure B.16: The n parameter of the expected (left) and detected (right) neutron as a function of P_{mm} using Crystal ball + polynomial background.

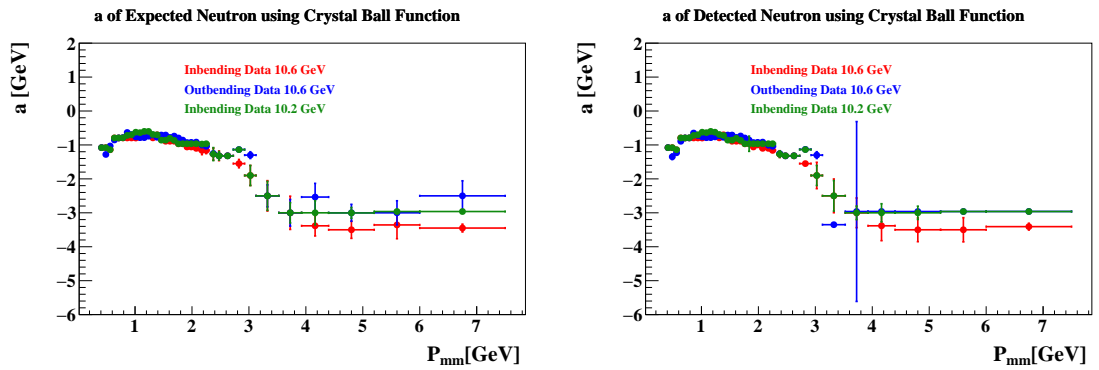


Figure B.17: The a parameter of the expected (left) and detected (right) neutron as a function of P_{mm} using Crystal ball + polynomial background.

APPENDIX C

MEASURED G_M^n VALUES AND ERRORS

A table will be added that shows the final result of G_M^n and the statistical uncertainty for the three different beam energies individual as well as the weighted average of G_M^n and the statistical and systematic uncertainty

Q^2	10.2 GeV		10.4 GeV		10.6 GeV	
[GeV ²]	$G_M^n/\mu_n G_D$	σ_{stat}	$G_M^n/\mu_n G_D$	σ_{stat}	$G_M^n/\mu_n G_D$	σ_{stat}
4.89	1.2305	0.2051	1.1034	0.2956	1.3321	0.4369
5.33	1.2311	0.0624	1.3308	0.0849	1.3354	0.0885
5.78	1.1366	0.0450	1.1122	0.0495	1.1601	0.0524
6.24	1.1101	0.0457	1.0835	0.0489	1.1539	0.0522
6.73	1.1436	0.0519	1.1568	0.0569	1.2295	0.0617
7.23	1.1455	0.0603	1.1254	0.0651	1.2508	0.0732
7.72	1.1746	0.0723	1.1846	0.0797	1.1760	0.0809
8.23	1.1260	0.0815	1.1329	0.0893	1.2144	0.0979
8.94	1.1751	0.0803	1.2166	0.0887	1.2861	0.0957
9.90	1.0889	0.1080	1.1614	0.1270	1.3313	0.1449
10.93	1.1183	0.1682	1.1257	0.1979	1.2066	0.2004
12.06	1.0890	0.2497	1.1644	0.2486	1.2450	0.2780

Table C.1: Measured values of $G_M^n/\mu_n G_D$ and statistical errors for each dataset. The Q^2 values given are the central value of each Q^2 bin.

Q^2 [GeV ²]	$G_M^n/\mu_n G_D$	σ_{stat}	σ_{syst}	σ_{Total}
4.89	1.2077	0.1572	0.1349	0.2071
5.33	1.2830	0.0437	0.0512	0.0673
5.78	1.1355	0.0281	0.0351	0.0450
6.24	1.1140	0.0281	0.0201	0.0345
6.73	1.1719	0.0326	0.0221	0.0394
7.23	1.1669	0.0379	0.0339	0.0508
7.72	1.1782	0.0446	0.0380	0.0586
8.23	1.1526	0.0513	0.0331	0.0611
8.94	1.2195	0.0506	0.0355	0.0618
9.90	1.1710	0.0716	0.0390	0.0815
10.93	1.1462	0.1080	0.0615	0.124
12.06	1.1607	0.1488	0.0377	0.1535

Table C.2: Measured values of $G_M^n/\mu_n G_D$, statistical and systematic uncertainties from the weighted average. The Q^2 values given are the central value of each Q^2 bin.

VITA

Lamya Baashen

2004 - 2008 B.S., Physics

King Saud University

Riyadh, Saudi Arabia

2009 - 2013 M.S., Physics

King Saud University

Riyadh, Saudi Arabia

2016 - 2019 M.S., Physics

Florida International University

Miami, Florida

2016 - 2023 Ph.D. Candidate, Physics

Florida International University

Miami, Florida

PUBLICATIONS AND PRESENTATIONS

L. Baashen, B. Raue, G. P. Gilfoyle et al. (CLAS Collaboration), “*Neutron Magnetic Form Factor G_M^n Measurement at High Q^2 with CLAS12*”, the CLAS collaboration meeting(2022).

L. Baashen, B. Raue, G. P. Gilfoyle et al. (CLAS Collaboration), “*Neutron Detection Efficiency in the Forward Calorimeter*”, the CLAS collaboration meeting(2023).

L. Baashen, B. Raue, G. P. Gilfoyle et al. (CLAS Collaboration), “*Neutron Magnetic Form Factor G_M^n Measurement at High Q^2 with CLAS12*”, DNP meeting, Bulletin of the American Physical Society 66(2022).

L. Baashen, B. Raue, G. P. Gilfoyle et al. (CLAS Collaboration), “*Neutron Magnetic Form Factor G_M^n Measurement at High Q^2 with CLAS12*”, DNP meeting, Bulletin of the American Physical Society 66(2020).

C. Kim et al. (CLAS Collaboration), “*Measurements of the Helicity Asymmetry E for the $\gamma p \rightarrow p\pi^0$ Reaction in the Resonance Region*”, arXiv:2305.08616, submitted to Eur. Phys. J. A. (2023).

S. Diehl et al. (CLAS Collaboration), “*First Measurement of Hard Exclusive $\pi^- \Delta^{++}$ Electroproduction Beam Spin Asymmetries off the Proton*”, Phys. Rev. Lett. 131, 021901 (2023).

G. Christiaens et al. (CLAS Collaboration), “*First CLAS12 Measurement of DVCS Beam-Spin Asymmetries in the Extended Valence Region*”, Phys. Rev. Lett. 130, 211902 (2023).

T. Chetry et al. (CLAS Collaboration), “*First Measurement of λ Electroproduction off Nuclei in the Current and Target Fragmentation Regions*”, Phys. Rev. Lett. 130, 14 (2023).

S. Diehl et al. (CLAS Collaboration), “*A Multidimensional Study of the Structure Function Ratio $\sigma_{LT'}/\sigma^0$ from Hard Exclusive π^+ Electroproduction off Protons in the GPD Regime*”, Phys. Lett. B 839, 137761 (2023).

H. Avakian et al. (CLAS Collaboration), “*Observation of Correlations Between Spin and Transverse Momenta in Back-to-Back Dihadron Production at CLAS12*”, Phys. Rev. Lett. 130, 022501 (2023).

S. Paul et al. (CLAS Collaboration), “*Observation of Azimuth-Dependent Suppression of Hadron Pairs in Electron Scattering off Nuclei*”, Phys. Rev. Lett. 129, 182501 (2022).

J. Rowley et al. (CLAS Collaboration), “*Improved λp Elastic Scattering Cross Sections Between 0.9 and 2.0 GeV/c and Connections to the Neutron Star Equation of State*”, Phys. Rev. Lett. 127, 272303 (2021).